

Formation and Evolution of Magnetised and Turbulent Molecular Clouds

Varying Initial Conditions and the Role of Stellar Feedback

Dissertation zur Erlangung des Doktorgrades
an der Fakultät für Mathematik,
Informatik und Naturwissenschaften

Fachbereich Physik
der Universität Hamburg

vorgelegt von
Bastian Körtgen

Hamburg, 2015

Tag der Disputation: 12.02.2016

Folgende Gutachter empfehlen die Annahme der Dissertation:

Prof. Dr. Robi Banerjee

Prof. Dr. Stefanie Walch-Gassner, Universität zu Köln

Gutachter der Dissertation:

Prof. Dr. Robi Banerjee
Prof. Dr. Stefanie Walch–Gassner

Leiter des Fachbereiches Physik:

Prof. Dr. Peter Hauschildt

Dekan der Fakultät für Mathematik,
Informatik und Naturwissenschaften:

Prof. Dr. Heinrich Graener

FÜR MEINEN OPA.

Formation and Evolution of Magnetised and Turbulent Molecular Clouds Varying Initial Conditions and the Role of Stellar Feedback

ABSTRACT

I present results from high resolution numerical simulations studying the formation and subsequent evolution of molecular clouds driven by the convergence of warm neutral medium flows. The results highlight the importance of magnetic fields in the diffuse interstellar medium as well as the initial conditions of the formation process. I show that magnetic field strengths consistent with recent observational results do not lead to gravitationally collapsing clumps within the clouds. Non-ideal magnetohydrodynamic effects, which increase the diffusion of the magnetic field show only minor difference compared to ideal magnetohydrodynamics. I conclude that the issue of how stars form in highly magnetised environments still persists.

In a second step, I study the evolution of star forming molecular clouds subject to supernova feedback from high-mass stars. I show that this feedback process is too inefficient to disrupt the parental molecular cloud. The long-term energy and momentum input are not sufficient to disperse the gas. On spatial scales of $\sim 10 - 20$ pc, however, supernova feedback is seen to be much more efficient than corresponding other feedback mechanisms prior to the supernova. The impact on the star formation rate and efficiency is rather limited. Both quantities are reduced by a minimum factor of ~ 2 , but do not come to a halt.

ZUSAMMENFASSUNG

Mittels hochaufgelöster numerischer Simulationen untersuche ich die Entstehung und Entwicklung von Molekülwolken, welche durch die Kollision zweier Gasströme im interstellaren Medium hervorgerufen wird. In einer ersten Studie untersuche ich den Einfluss des interstellaren Magnetfeldes auf den resultierenden Entstehungsprozess, sowie den weiteren zeitlichen Verlauf. Ich zeige, dass starke Magnetfelder – wie sie derzeit beobachtet werden – zu einer Unterdrückung des Gravitationskollaps und damit der Sternentstehung führen. Auf Basis von nicht-idealer Magnetohydrodynamik führe ich weitere Studien durch. Die Ergebnisse zeigen jedoch keine signifikante Änderung, was letztendlich zu der Frage führt, wie Sterne in kalten, stark magnetisierten Wolken entstehen.

Weiterhin gehe ich die Frage an, welchen Effekt Supernova-Explosionen massereicher Sterne auf

die elterliche Molekülwolke haben. Ich zeige, dass das Lebensende eines massereichen Sterns nur einen sehr lokal begrenzten Effekt aufweist. Die globale Stabilität der Wolke wird dabei nur kurzweilig durch die Supernova dominiert. Auf Skalen von $\sim 10 - 20$ pc jedoch erweisen sich Supernova-Explosionen als äußerst effizient im Vergleich zu anderen Rückkopplungsmechanismen. Hinsichtlich der Sternentstehungsrate und -effizienz kann eine Verringerung um einen Faktor 2 vermerkt werden. Ein vollständiges Ende der Sternentstehung wird jedoch nicht beobachtet.

LIST OF PUBLICATIONS

Data presented in this work has been partially used for the following publications.

1. **Körtgen, B.** & Banerjee, R., Impact of magnetic fields on molecular cloud formation and evolution, 2015, MNRAS, 451, 3340
2. Stanchev, O.; Veltchev, T. V.; Kauffmann, J.; Donkov, S.; Shetty, R.; **Körtgen, B.**; Klessen, R. S., Tracing the general structure of Galactic molecular clouds using Planck data - I. The Perseus region as a test case, 2015, MNRAS, 451, 1056

Contents

1	INTRODUCTION	1
2	OVERVIEW	5
2.1	The Interstellar Medium	6
2.1.1	Composition and Phases	7
2.1.2	Energy Densities	9
2.1.3	Magnetic Fields	10
2.1.4	Turbulence	16
2.1.5	Heating and Cooling	22
2.1.6	The Galactic Cycle	23
2.2	Molecular Clouds	25
2.2.1	Properties of Molecular Clouds	25
2.2.2	Formation of Molecular Clouds	26
2.2.3	Scaling Relations of Molecular Clouds	31
2.2.4	Molecular Cloud Lifetimes	32
2.2.5	Star Formation Rate and Efficiency	34
2.3	Formation of Stars	36
2.3.1	Jeans Analysis	36
2.3.2	Free-Fall Timescale	37
2.3.3	Magnetic Fields and Star Formation	38
2.3.4	Collapse of Individual Cloud Cores	40
2.3.5	Star Formation in Filaments	45
2.3.6	Gravoturbulent Star Formation	46
2.3.7	Formation of a Protostar	47
2.3.8	Models of High-Mass Star Formation	48
2.4	Stellar Initial Mass Function	50
2.5	Protostellar and Stellar Feedback	52
2.5.1	Protostellar Jets	52
2.5.2	Stellar Winds	53
2.5.3	H II Regions	56
2.5.4	Supernovae	59

3	THEORY AND NUMERICAL METHOD	65
3.1	Magnetohydrodynamics	65
3.1.1	The Vlasov–Maxwell–Poisson–System	65
3.1.2	The Magnetohydrodynamic (MHD) Equations	69
3.1.3	Validity of the MHD Approach	71
3.1.4	Heating and Cooling Source Terms	72
3.1.5	The Maxwell Equations	72
3.1.6	The Poisson Equation	73
3.1.7	Non–Ideal Effects	74
3.1.8	Wave Modes in MHD	75
3.1.9	MHD Summary	76
3.2	The FLASH Code	77
3.2.1	Basics	78
3.2.2	Sink Particles	79
3.2.3	Grid Refinement	80
3.3	Initial Conditions	81
3.4	The Supernova–Model	83
3.5	Chapter Summary	85
4	IMPACT OF MAGNETIC FIELDS ON THE FORMATION AND EVOLUTION OF MOLECULAR CLOUDS	87
4.1	Introduction	88
4.2	Molecular Cloud Formation by Head-On Colliding Flows	91
4.2.1	Varying the Turbulent Velocity	91
4.2.2	Dependence on the Magnetic Field Strength	94
4.3	Inclined WNM flows	97
4.3.1	The Setup	97
4.3.2	Magnetic Flux Reduction and Star Formation	100
4.3.3	Comparing Cloud Dynamics in Magnetically Differing Environments	102
4.3.4	Dynamics of Dense Cores	107
4.3.5	Analysis of the Densest Cores	110
4.4	Chapter Summary & Discussion	112
4.4.1	Discussion: Influence of Ambipolar Diffusion	112
4.4.2	Summary	113
5	THE INFLUENCE OF SUPERNOVA FEEDBACK ON THE EVOLUTION AND LIFETIME OF MOLECULAR CLOUDS	117
5.1	Introduction	118
5.2	Evolution of Cloud Masses	121
5.2.1	Evolution of the Densest Parts	122
5.3	Cloud Dynamics	123

5.3.1	Thermal State of the Cloud	127
5.3.2	Long-Term Dynamical Evolution of the Dense Gas	130
5.3.3	Evolution of Energy Ratios of the Dense Gas	131
5.4	Star Formation	132
5.4.1	Number and Mass of Sinks	132
5.4.2	Star Formation Efficiency & Rate	133
5.5	The One-Dimensional Velocity Dispersion	134
5.6	Lifetimes of Individual Regions within the Clouds	135
5.7	Chapter Summary and Discussion	136
5.7.1	Discussion: Missing Physics	136
5.7.2	Summary	138
6	SUMMARY AND OUTLOOK	141
6.1	Summary: Magnetic Fields in the ISM	141
6.2	Summary: Supernova Feedback in Molecular Clouds	142
6.3	Outlook: Magnetic Fields in the ISM	143
6.4	Outlook: Supernova Feedback in Molecular Clouds	144
	APPENDIX A APPENDIX	145
A.1	The Magnetised ISM: Estimate of the Effective Magnetic Diffusion	145
A.2	SN Feedback: Resolution Study	146
A.3	Notes on the Supernova Rate	147
	BIBLIOGRAPHY	151

1

Introduction

Stars are crucial for our understanding of the interstellar medium. Through their mechanical and radiative energy input they control the remote dynamics of the gas between the stars. The injection process drives random motions in the gas, accelerates energetic particles and indirectly amplifies ambient magnetic fields. The hot bubbles surrounding high-mass stars yield the escape of material from the Galactic disc and provide the source for Galactic winds or fountain flows. Low-mass stars, in contrast, only act upon their immediate surrounding. However, the combined effects of all stars provide a significant source of energy for the dynamical processes in the interstellar medium.

Stars are important for our understanding of molecular clouds. Beside their impact on the large scales, the stars couple to their parental cloud also via feedback processes. Already in the phase of stellar birth, the feedback is accomplished via stellar jets and outflows. During the star's time on the main-sequence it drives powerful winds, which shape the surrounding material. High-mass stars with $M \gtrsim 8 M_{\odot}$ also ionise the surrounding gas by the release of energetic photons. In the end of the stellar life, the low-mass stars interact with the surrounding material by ejecting their outer shells. The high-mass stars, in contrast, end their short lives in a powerful supernova,

thereby injecting a large amount of energy in a very short period of time. All these stellar feedback processes shape the morphological and dynamical picture of their birthplaces. The amount of energy and momentum, which is transferred to the molecular cloud, is crucial for the cloud's further evolution and whether it is dispersed or not.

Stars are vital for our understanding of planet formation. Through their continuous fusion processes, high-mass stars generate elements heavier than Lithium. When these stars end their lives in a supernova, they enrich the surrounding interstellar medium with those heavy elements. The new chemical elements provide the seeds for the formation of dust particles, which themselves serve as the origin of large sized objects in the dense discs surrounding young stars.

State-of-the-art observational techniques are able to disentangle the complex interplay of stars, molecular clouds, and the interstellar medium. Observations have revealed that the interstellar gas is pervaded by strong magnetic fields, which influence the formation and evolution of molecular clouds and the formation of stars. The observations also provide us with unprecedented data of the sites of contemporary star formation. The role of interstellar filaments is being re-emphasised since the first results from the *Herschel* space telescope. It is acknowledged that supersonic turbulence shapes these filaments. The role of magnetic fields, in contrast, is still subject to discussion.

The latest observational studies also provide a wealth of high-resolution data on the distribution, morphology, and dynamics of regions of stellar feedback. From these data, the coupling of the star to the surrounding cloud can be estimated and compared to theoretical predictions. The theoretical predictions are based to a large extent on the results from numerical simulations. The complex interplay of magnetic fields, radiation, hydrodynamics, etc. cannot be described analytically. However, even numerical simulations concentrate on different aspects of the galactic lifecycle and provide small pieces for the large puzzle of star formation.

In this work I will contribute to the following questions:

What is the influence of the magnetic field on the formation and evolution of molecular clouds?

How does feedback from high-mass stars influence the evolution and lifetime of molecular clouds?

To accomplish these tasks, chapter 2 describes the basics of the interstellar medium, thereby emphasising the role of magnetic fields and interstellar turbulence. Molecular clouds and their properties will also be discussed. A description of the formation of stars as well as their mass distribu-

tion and feedback closes this chapter. This study makes extensively use of a simulation code. This numerical tool and its underlying equations are introduced in chapter 3. The following chapters 4 and 5 discuss the results of this study. Concluding remarks and a brief outlook are given in chapter 6.

2

Overview

The following chapter is dedicated to the establishment of a profound overview of the physics which are the subject of this thesis. I will describe the interstellar medium with its different constituents, thereby also focussing on magnetic fields as well as on turbulence.

Molecular clouds condense out of the cold neutral medium, a phase of the interstellar medium, and probably proceed to collapse to form a star or stellar cluster. A selection of different mechanisms, which are thought to form molecular clouds is discussed. Once a molecular cloud core is unstable and collapses, the formation of stars is initiated. The different processes at work during the collapse are highlighted and a brief discussion of the distribution of stellar masses is given. All stars inject mass, energy, and momentum into their surrounding medium or their parental core. To which extent is discussed in the last section of this chapter.

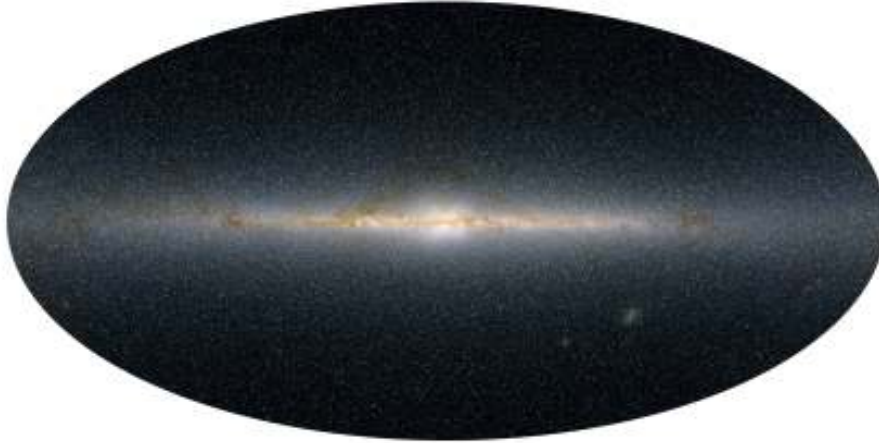


Figure 2.1: Three-colour composite image of the Galactic disc from the 2MASS survey. Shown is the emission at $1.2 \mu\text{m}$, $1.65 \mu\text{m}$, and the $2.2 \mu\text{m}$, respectively. Note the emission from the Small and Large Magellanic Clouds in the lower right. Image taken from http://www.ipac.caltech.edu/2mass/gallery/showcase/allsky_stars/index.html. Image Credit: 2MASS/J.Carpenter, T.H. Jarrett, and R.Hurt.

2.1 The Interstellar Medium

By definition the *interstellar medium* (henceforth ISM) is the medium between the stars. The dynamics and structure of the ISM control the formation of molecular clouds, stars, and the evolution of galaxies.

Figure 2.1 shows a composite image of the infrared emission of the disc of the Milky Way at wavelengths of $\lambda = 1.2 \mu\text{m}$, $\lambda = 1.65 \mu\text{m}$, and $\lambda = 2.2 \mu\text{m}$ taken from the 2MASS survey (Kleimann et al., 1994a,b). The Galactic centre (GC) is located in the middle of this map. The GC reveals a bulge-like shape and one can infer the presence of a Galactic halo of diffuse emission. With increasing distance from the centre, the distribution of matter flattens. Draine (2011) give disc heights of $h \sim 500 \text{ pc}$ at a radial distance of $r \sim 8.5 \text{ kpc}$, i.e. the solar distance. Hence, a major part of the dynamical interactions in the ISM is restricted to a thin disc. The diffuse emission above and below the disc are due to both accretion onto the Galaxy from the intergalactic medium (IGM) and gas expulsion out of the disc due to the feedback from high-mass stars (e.g. Walch et al., 2015). Stellar feedback reveals its presence in $\text{H}\alpha$ emission, that is, the emission resulting from the downward transition of the electron of the H atom from level $n = 3 \rightarrow 2$ with a wave length $\lambda_{3 \rightarrow 2} = 6563 \text{ \AA}$. This is shown in figure 2.2.

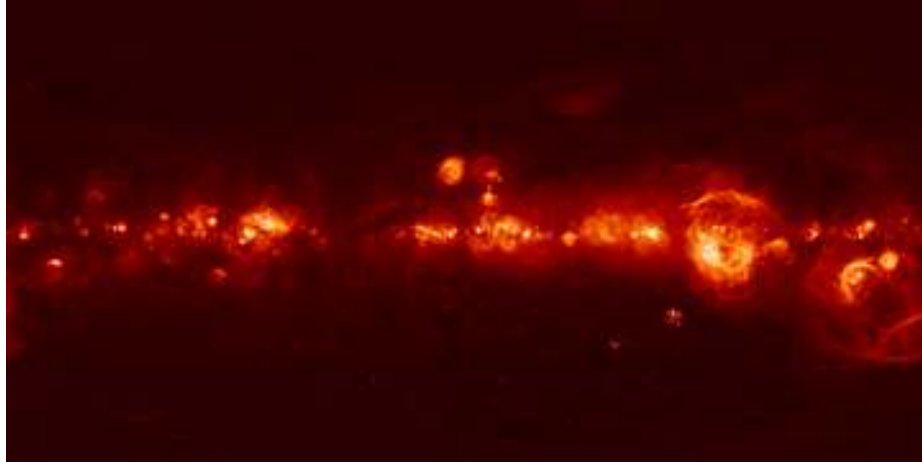


Figure 2.2: H α map from [Finkbeiner \(2003\)](#). The map reveals shells, bubbles, filaments which are associated with regions where high-mass stellar feedback is present. Image credit: <http://www.galaxymap.org>

2.1.1 Composition and Phases

The H α emission mentioned above gives some hint about the composition of the ISM. It is indeed hydrogen, which provides the major part of the gas. About 60 % of hydrogen is in the neutral, atomic form (H I), 23 % in the ionised state (H II), and 17 % in the form of molecular hydrogen (H₂) (see e.g. [Draine, 2011](#)). When the total gas mass within the Galaxy is considered, hydrogen (H I, H II, H₂) provides ~ 70 % of the mass. About 28 % of mass is in the form of helium (He). The left 2 % are in dust and so called *metals* (elements heavier than He) (e.g. [Tielens, 2005](#)).

Dust and metals are most likely to exist deeply embedded in dense regions with column densities $\log N \sim 20$, which provide a significant (self-)shielding against the interstellar radiation. In general, the ISM is organised in different phases, which co-exist in near pressure equilibrium ([McKee and Ostriker, 1977](#)).

Hot Ionised Medium

The hot ionised medium (HIM) originates from the energy injection of high-mass stars. Following [McKee and Ostriker \(1977\)](#) the temperature and density of this phase can be stated to be $T \sim 5 \times 10^5$ K and $n \sim 0.003$ cm⁻³, respectively. This phase is maintained by e.g. supernova explosions. Though, not known precisely, the volume filling factor is $f_V \sim 0.4$ ([Smith, 2004](#)).

Warm Ionised Medium

The warm ionised medium (WIM) consists primarily of H II gas with number densities of $n \sim 0.1 \text{ cm}^{-3}$ and temperatures around $T \sim 8000 \text{ K}$ (Tielens, 2005). To some extent, the hot gas within H II regions around high-mass stars can be attributed to the WIM, although the gas in these regions might also have higher densities. The volume filling factor $f_V \sim 0.1 - 0.25$ and the mass fraction of $f_M \sim 0.16$ are still subject to discussion (Tielens, 2005; Draine, 2011). This component of the ISM is best observed by radio continuum surveys, accounting for the enhanced free-free emission (e.g. Peters et al., 2010; Draine, 2011).

Warm Neutral Medium

Another part of the ISM is the warm neutral medium (WNM). The typical densities range from $n \sim 0.5 \text{ cm}^{-3}$ to $n \sim 2 \text{ cm}^{-3}$ (Stahler and Palla, 2005). However, these values can change dramatically with galactocentric radius (Tielens, 2005). The temperatures of this gas phase range from $T \sim 3500 - 8000 \text{ K}$, and $f_V \sim 0.3 - 0.4$. The mass fraction of this phase is $f_M \sim 0.4 - 0.5$ (Tielens, 2005). Since atomic hydrogen constitutes the major part of the WNM, this phase is best observed in 21 cm emission corresponding to the hyperfine-structure line of the hydrogen atom.

Cold Neutral Medium

Diffuse clouds of HI gas with temperatures of $T \sim 80 - 100 \text{ K}$ define the cold neutral medium (CNM). Due to the near pressure equilibrium conditions, densities are far higher compared to the WIM and WNM, namely around $n \sim 30 - 50 \text{ cm}^{-3}$ (Tielens, 2005). The volume filling fraction of the CNM is rather low, $f_V \sim 0.01$. In contrast, the mass fraction is $f_M \sim 0.36$ (Tielens, 2005). If molecular clouds are taken into account, most of the mass of the ISM is contained in regions with $n \gtrsim 50 \text{ cm}^{-3}$, that is $f_{M,\text{CNM+MC}} \sim 0.6$. Following Draine (2011), the CNM is primarily observed via 21 cm line emission as well as in absorption of optical and UV lines. Notice that the mentioned diffuse HI clouds are pressure-confined entities, rather than being gravitationally bound (e.g. Heiles and Troland, 2005; Crutcher et al., 2009).

The above discussed phases are the basis for the *three-phase model* of the ISM by McKee and Ostriker (1977). As already pointed out for the HIM, this model relies on the major contribu-

tion from high-mass stars. Supernova explosions inject energy and momentum into the ambient medium, which increases the temperatures and pressures. For appropriate supernova rates, sufficiently stable cavities of very hot and tenuous gas appear in which the gas is primarily ionised. The WNM then appears through gas cooling of the HIM. The WNM itself is highly thermally unstable. Small perturbations induce runaway cooling of the gas, which results in the formation of the CNM, which is the third phase. This is in contrast to the original *two-phase* model proposed by Field et al. (1969b,a) in which the CNM coexists with a second warmer phase, the WNM and WIM. However, both models constitute the emergence of *thermally unstable* regimes near $n \sim 1 - 5 \text{ cm}^{-3}$ and $T \sim 1000 - 5000 \text{ K}$, where a decrease in temperature initiates further cooling of the gas (see also Tielens, 2005).

An illustrative overview of the different regimes is given in figure 2.3. Notice that additional regimes are shown that have not been discussed above, but do occur during the lifecycle of stars and the ISM. However, the three-phase model is not appropriate anymore since it assumes the multiple phases to be static and in pressure equilibrium (McKee and Ostriker, 1977). In contrast, the ISM is highly dynamic and not static. Turbulence mixes the different phases and leads to regimes which are not in pressure equilibrium (e.g. Seifried et al., 2011, and references therein).

2.1.2 Energy Densities

Table 2.1 gives a summary of the energy densities in the ISM. Here, typical values for the number density, temperature and magnetic field strength in the solar vicinity are used (see e.g. Vázquez-Semadeni et al., 2007; Crutcher et al., 2009). It is obvious that the different energies are in near equipartition. The equipartition of thermal and turbulent kinetic energy is due to presence of trans- to mildly supersonic motions in the WNM, which originate e.g. from supernova explosions of high-mass stars (see e.g. reviews of Mac Low and Klessen, 2004; Elmegreen and Scalo, 2004; Scalo and Elmegreen, 2004). The equal amounts of energy in the turbulent fluid and the magnetic field is due to collisional coupling of charged particles and neutrals in regions where the ionisation fraction is rather low (e.g. Haverkorn, 2015). In regions of high ionisation fraction, the magnetic field is perfectly frozen-in to the gas, which naturally leads to equipartition. Other possibilities, which lead to equipartition are amplification of the magnetic field by dynamo processes, i.e. the small-scale dynamo (Brandenburg and Subramanian, 2005) or the $\alpha\Omega$ -dynamo due to differential rotation (e.g. Hubbard and Brandenburg, 2012). The cosmic ray energy density is twice as high as the other energy forms, but still of the same order as the aforementioned

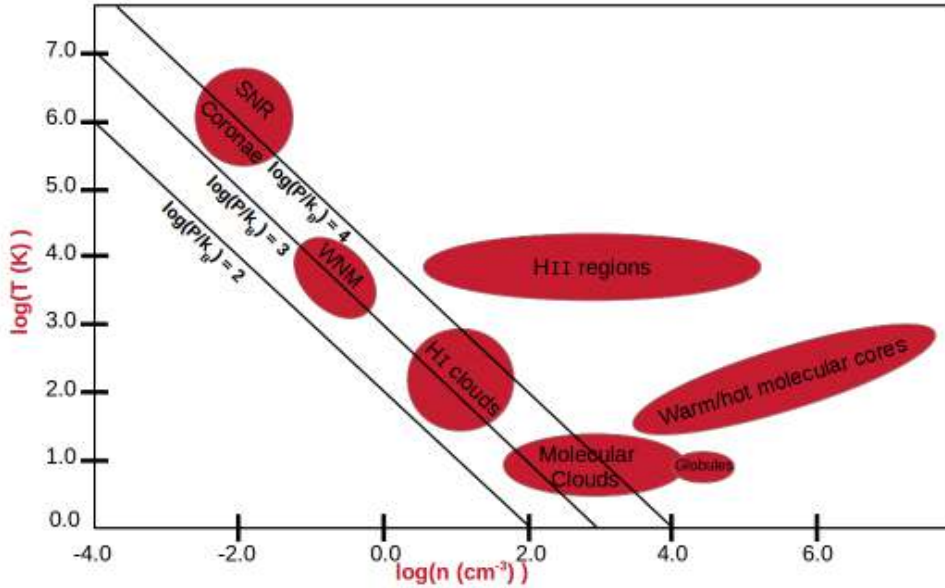


Figure 2.3: Schematic showing the different physical phases of the ISM. Notice the additional phases for illustrative purposes, which have not been mentioned in the text. As indicated, the WNM and cold molecular clouds are in rough pressure equilibrium. Although very tenuous, supernova remnants (SNR) and stellar coronae provide regions, which are significantly over-pressurised. Adapted from Padmanabhan (2001, figure 9.1.) and slightly modified.

energy densities. The reason is that the magnetic field limits the escape fraction of cosmic rays from the Galaxy, resulting in continuous heating of the gas in the ISM (Draine, 2011).

2.1.3 Magnetic Fields

It has early been recognised that the ISM is pervaded by magnetic fields (Hiltner, 1949; Mestel and Spitzer, 1956). This has led to the question, how the magnetic field influences the dynamics of clouds, clumps and cores. A first attempt was the estimate of the magnetic critical mass $M_{\text{crit},B}$ by Mestel and Spitzer (1956, see also section 2.3.3). The critical mass arises from the energy balance of magnetic fields and gravity and is proportional to B^3/n^2 , where B is the magnetic field strength and n is the number density. Hence, stronger magnetic fields increase the critical mass and stabilise the system, while increasing densities will usually imply small masses up to which the system is stable. Since the critical mass is of the order of $10^4 M_{\odot}$ for magnetic field strengths of $1 \mu\text{G}$ and densities of 1 cm^{-3} (see Mestel and Spitzer, 1956), the influence of the magnetic field was thought to explain the observed low star formation efficiencies (e.g. Mouschovias and Spitzer, 1976; Shu,

Table 2.1: Typical energy densities in the ISM.

Energy	Symbol	Value [10^{-12} erg/cm $^{-3}$]	Comment
Thermal	$e_{\text{int}} = \frac{3}{2}nk_B T$	1.04	$n = 1 \text{ cm}^{-3}, T = 5000 \text{ K}$
Turbulent	$e_{\text{turb}} = \frac{1}{2}\rho u^2$	1.06	$n = 1 \text{ cm}^{-3}, u = 10 \text{ km/s}$
Magnetic	$e_B = \frac{B^2}{8\pi}$	0.99	$B = 5 \mu\text{G}$
Cosmic Ray	e_{cr}	2.23	From Draine (2011) ^a

^aNote that [Draine \(2011\)](#) give the energy densities in eV/cm $^{-3}$. The value of 1.39 eV/cm $^{-3}$ in this source is estimated from a hypothetical spectrum which matches the observed high-energy proton flux. See figure 13.5 in [Draine \(2011\)](#).

1977; [Mouschovias and Paleologou, 1980](#)).

In addition to the stability of clumps and cores, the magnetic field can efficiently remove angular momentum from rotating systems by Alfvén waves ([Mouschovias and Paleologou, 1980](#)). On scales of accretion discs this has led to the invention of the *magnetic braking catastrophe* where the build-up of Keplerian discs is suppressed by the magnetic field ([Mouschovias, 1979](#); [Mouschovias and Paleologou, 1980](#); [Basu and Mouschovias, 1994](#)). There since have been many approaches to circumvent this problem, e.g. by non-ideal MHD ([Krasnopolsky et al., 2010, 2011](#)) or turbulence ([Seifried et al., 2012, 2013](#)).

The magnetic critical mass can also be expressed in terms of the *mass-to-magnetic flux ratio* μ/μ_{crit} , where $\mu = M_{\text{gas}}/\Phi$ and

$$\mu_{\text{crit}} \equiv \left(\frac{M_{\text{gas}}}{\Phi} \right)_{\text{crit}} = 0.13/\sqrt{G} \quad (2.1)$$

according to [Mouschovias and Spitzer \(1976\)](#), where the critical value results from the equipartition of gravitational and magnetic energy densities

$$E_{\text{grav}} \equiv \frac{GM\rho}{R} = \frac{B^2}{8\pi} \equiv E_{\text{mag}}. \quad (2.2)$$

Φ is the magnetic flux. A modified version of the critical value was obtained by [Nakano and Nakamura \(1978\)](#) as

$$\mu_{\text{crit}} \equiv \left(\frac{\Sigma}{B} \right)_{\text{crit}} = 0.16/\sqrt{G}. \quad (2.3)$$

Here Σ is the column density and B the magnetic field strength along the line of sight. If $\mu > \mu_{\text{crit}}$, collapse of a region is initiated. In the contrary case, the magnetic field dominates over gravity and perturbed systems will only undergo small oscillations. In the former case, objects are termed *supercritical*, while in the latter they are *subcritical*. For nearly *isolated* ($\dot{M} \sim 0$) systems, the conservation of magnetic flux tended to be a critical issue as in such cases the mass-to-magnetic flux ratio is conserved (Mestel and Spitzer, 1956). But, as the authors pointed out, the relative drift of neutrals and charged particles allows for the slow diffusion of magnetic flux out of the overdense region. With time, this *ambipolar drift* leads to supercritical regions that eventually collapse. This idea was modified to include turbulence by Heitsch et al. (2004). Turbulence is indeed able to speed up the slow process of ambipolar drift, but still fails to explain the fast onset of star formation (Heitsch and Hartmann, 2014). The large timescale of ambipolar drift was also thought to explain the low star formation efficiency of molecular clouds (Mouschovias and Spitzer, 1976). Another possibility suggested already by Mestel and Spitzer (1956) and later put forward by Hartmann et al. (2001, see also Heitsch and Hartmann (2014)) is the accumulation of gas by coherent WNM streams parallel to the magnetic field lines until a certain region becomes supercritical.

To assess the influence of the magnetic field, observations are inevitable, especially with the aim of deriving reliable estimates of the field strength and criticality in the ISM and molecular clouds. To date, there is ongoing discussion about its dynamical importance, which is primarily maintained by these observations (Li et al., 2009; Crutcher et al., 2009; Crutcher, 2012; Li et al., 2014). Thus, in the following, I will briefly discuss methods to observe magnetic fields in the ISM and their basic results.

Dust and Starlight Polarisation

A common technique is measuring polarisation of either starlight by background stars (in the optical) or dust thermal emission (in the far-IR) (see e.g. review by Crutcher, 2012). The polarisation is the result of light being scattered at or re-emitted by elongated, aligned dust grains. The alignment with the local magnetic field is most probably due to radiative torques (Lazarian, 2007; Hoang and Lazarian, 2008). The obtained polarisation vector can then be used to infer the morphology of the magnetic field. In this sense, extinction measurements towards background stars in the optical reveal the morphology of the field in the outer, low- A_V regions, where A_V denotes the visual extinction. The dust emission results are used to infer the field direction in the high- A_V

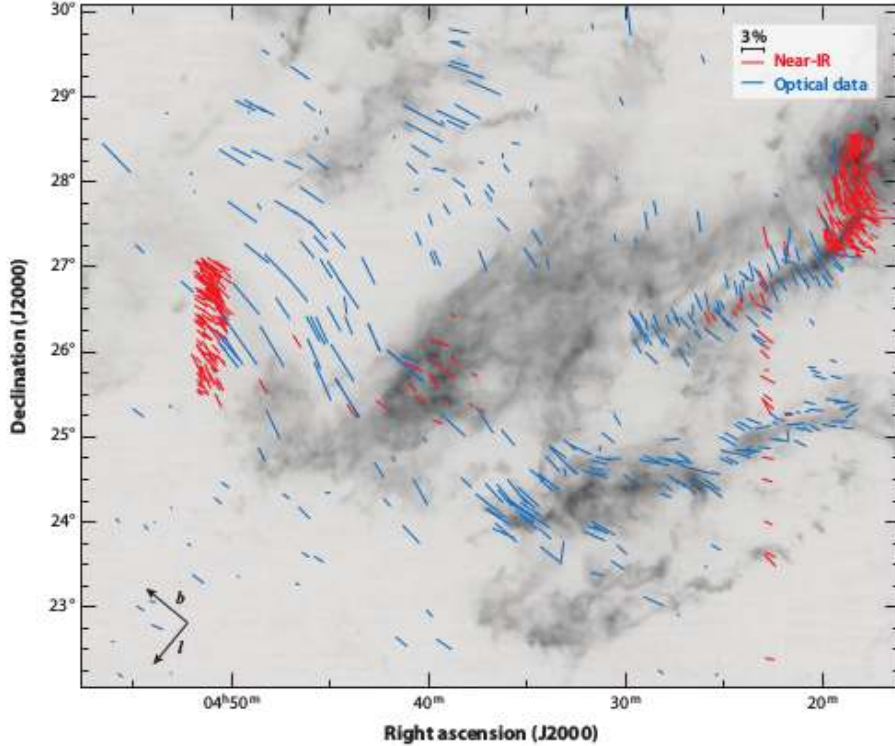


Figure 2.4: Polarisation vectors and ^{13}CO emission map from the Taurus molecular cloud complex. Red vectors denote near-IR data, blue vectors those from optical polarisation. It is evident from the measurements that the magnetic field is primarily perpendicular to the filaments' major axes. However, there are also regions observed, where the field is aligned. In total, the field is able to stabilise the Taurus cloud against gravitational contraction and is interpreted to dominate over turbulence at least on a 2 pc scale. From [Chapman et al. \(2011\)](#).

regions, that is, in the cloud interior ([Crutcher, 2012](#); [Li et al., 2014](#)). Figure 2.4 shows polarisation vectors (rotated by 90° to represent the magnetic field direction) in the optical and near-IR overlaid on a ^{13}CO emission map from [Chapman et al. \(2011\)](#). The data reveal an ordered magnetic field, which is only distorted in some small regions. The field direction is primarily perpendicular to the major axis of the individual filaments. This is consistent with important magnetic fields and gravitational contraction *along the field lines* ([Li et al., 2006a, 2009](#); [Hennebelle, 2013](#)). However, there are also some filaments observed, where the magnetic field morphology is essentially along the main filament axis or disordered ([Planck Collaboration et al., 2014a,b, 2015](#)).

Using dust emission data at $350\ \mu\text{m}$ towards molecular cores in the Orion complex, [Li et al. \(2009\)](#) showed that the magnetic field morphology in the dense cores is preserved with respect to the cloud environment, again strongly indicating dominant magnetic fields. The authors concluded that super-Alfvénic clouds cannot explain this morphology, in contrast to what was found by

Padoan et al. (2004).

The strength of the magnetic field cannot be inferred directly from continuum polarisation data. For this reason, the Chandrasekhar–Fermi (CF) method is often applied (Chandrasekhar and Fermi, 1953). The CF method assumes a displacement of a magnetic field line due to turbulent fluctuations by some angle α (the polarisation angle). The original idea proposed sinusoidal perturbations and determined the magnetic field strength in the plane of sky (POS) as

$$B_{\text{POS}} = \left(\frac{4}{3} \pi \varrho \right)^{1/2} \frac{v}{\alpha}. \quad (2.4)$$

Here v is the velocity dispersion and ϱ the ambient gas density. Estimates with the CF method in the Taurus complex reveal $B_{\text{POS}} \sim 10 - 40 \mu\text{G}$ with the lower value corresponding to lower density regimes (Chapman et al., 2011). However, there is some significant uncertainty in the CF method in inferring the correct reason for tilting and twisting of field lines (Crutcher, 2012).

Zeeman Measurements

A second widely used method is the measurement of the Zeeman effect from which the line of sight (LOS) magnetic field component is achieved (e.g Crutcher et al., 1993). Commonly used interstellar species for this kind of measurements are HI, OH, and CN (Crutcher, 2012). In the normal Zeeman effect, a spectral line is split into three components due to coupling of the magnetic moment of the atom with the ambient magnetic field. The measurements then contain information about all three magnetic field components. However, as Crutcher (2012) state, the strength of the signal is proportional to $(\Delta\nu/\delta\nu) \times B_{\text{LOS}}$ and to $(\Delta\nu/\delta\nu)^2 \times B_{\text{POS}}$. Here $\Delta\nu$ is the frequency shift due to the Zeeman effect and $\delta\nu$ is the width of the spectral line. Since in most observations $\Delta\nu \ll \delta\nu$, information about B_{POS} is lost due to too weak signals.

A compendium of Zeeman measurements towards different sources is given in figure 2.5. Shown is the LOS magnetic field as function of column density. The data points contain diffuse HI clouds, molecular clouds as well as dense cores (Heiles and Troland, 2005; Heiles and Crutcher, 2005; Crutcher, 2012). At low column densities, the LOS magnetic field is almost constant. Since it is the HI clouds which reside there, this constancy agrees well with accumulation of gas along the field lines (Heiles and Troland, 2005; Heiles and Crutcher, 2005). At higher column densities, the magnetic field increases. The dashed line marks the transition from sub- to supercriti-

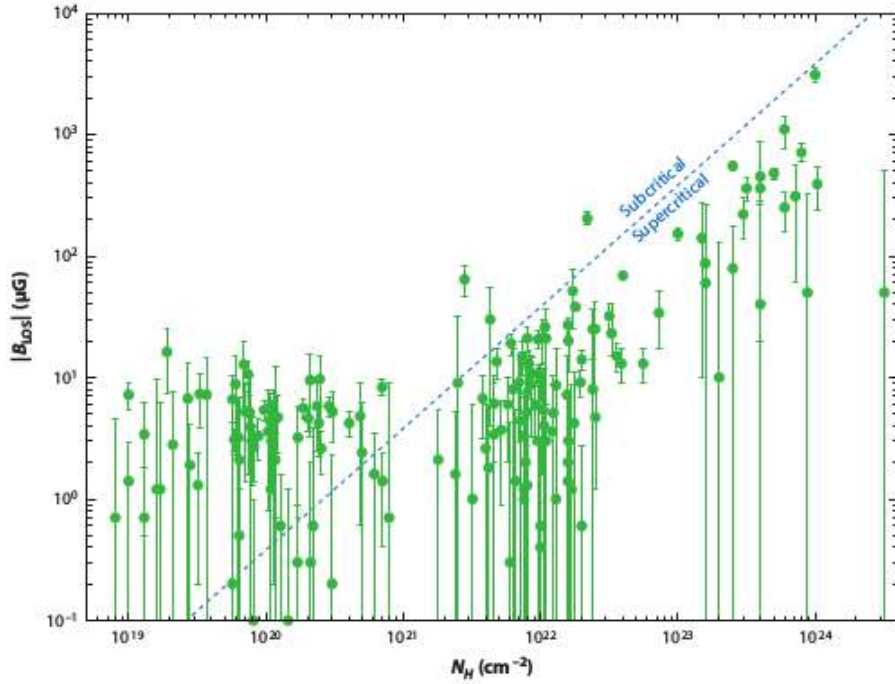


Figure 2.5: Overview of the results from Zeeman measurements. Shown is the LOS magnetic field as function of column density. The dashed line denotes the condition of magnetic criticality, $\mu = \mu_{\text{crit}}$. Almost all measurements of molecular clouds reveal supercriticality. Figure taken from [Crutcher \(2012\)](#).

cal clouds. As [Crutcher \(2012\)](#) highlight, almost all measurements indicate supercritical clouds. However, these observed stages are not consistent with models of ambipolar diffusion mediated star formation ([Crutcher et al., 2009](#)). Studies of the LOS field strength as function of *number* density reveal a scaling $B \propto n^\zeta$ with $\zeta \sim 0.65$ (see also next paragraph). The exponent is more consistent with isotropic contraction, where the magnetic field is not capable of balancing gravity. In contrast, ambipolar diffusion dominated scenarios show exponents $\zeta \sim 0.5$ ([Mouschovias and Ciolek, 1999](#)).

Magnetic Field Strengths and Magnetic Criticality

The field strength estimated from Zeeman measurements indicate $B_{\text{LOS}} \sim 5 - 6 \mu\text{G}$ in the low column density regime, $\log(N [\text{cm}^{-2}]) \lesssim 21$, giving rise to larger values for the *total* field strength. This column density regime is analogous to *volume* densities $n \lesssim 10^4 \text{cm}^{-3}$. From this

density threshold on, the magnetic field scales as (Crutcher et al., 2009; Draine, 2011)

$$B \sim 49 \mu\text{G} \left(\frac{n}{10^4 \text{ cm}^{-3}} \right)^{0.65}, \quad (2.5)$$

indicating typical field strengths in molecular clouds of the order of $B \sim 30 - 50 \mu\text{G}$ (Heiles and Troland, 2005; Crutcher et al., 2009). The supercritical objects with much weaker field strength in figure 2.5 are most likely to have a stronger POS component (Crutcher, 2012). The values for B_{LOS} at higher densities do also agree with the results from polarisation studies (e.g. Li et al., 2009, 2010). However, while Li et al. (2006a, see also Li et al. (2014)) claim the dynamical importance of the magnetic field and its ability to stabilise clouds, the results from Heiles and Troland (2005) and Crutcher et al. (2009) indicate less significant influence. On the one hand, the latter authors report that the mass-to-magnetic flux ratio is supercritical by factors $\sim 2 - 3$ (though with some uncertainty of 50 %). On the other hand, they find $\mathcal{M}_A \sim 1.5 - 2$ (Heiles and Troland, 2005; Heiles and Crutcher, 2005; Crutcher et al., 2009). Although, only slightly *super-Alfvénic* the turbulent energy dominates over magnetic energy, consistent with studies by Padoan et al. (2004). The magnetic field lines should thus be twisted by the turbulent motions, which contradicts the results from Li et al. (2006a) as well as Chapman et al. (2011), who find coherent magnetic fields in molecular clouds as well as in the inter-cloud medium.

The question about the exact dynamical importance of magnetic fields still remains to be evaluated. In addition, it is not fully solved to date *how* molecular clouds achieve the transition from sub- to super-critical states (see e.g. discussion in Banerjee and Körtgen, 2015). Since AD was proven to be inefficient, also in combination with turbulence (Heitsch and Hartmann, 2014), possible solutions are converging flows along field lines (Mestel and Spitzer, 1956; Heitsch and Hartmann, 2014, see also section 2.2.2) or reconnection of magnetic field lines (Lazarian and Vishniac, 1999; Santos-Lima et al., 2011).

2.1.4 Turbulence

The ISM is highly dynamical and turbulent. In the following I will introduce the basic concepts of (magneto-)hydrodynamical, incompressible and compressible turbulence and discuss the historical development of turbulence in the ISM.

Kolmogorov Turbulence

In general, turbulence in a fluid arises when the advection term $\underline{u} \cdot \nabla \underline{u}$ dominates over the viscous term $\nu \Delta \underline{u}$, with \underline{u} (see section 3.1.2) being the velocity and ν being the kinematic viscosity. Due to its non-linearity, the advective term will exponentially amplify small perturbations in the fluid flow (Landau and Lifshitz, 1959). Whether a flow is turbulent or laminar can be estimated by the *Reynolds number*

$$Re \sim \frac{ul}{\nu}. \quad (2.6)$$

Once a fluid is turbulent (i.e. $Re > 1$), vortical motions keep on mixing different regions. Energy, being injected on large scales, cascades down to the small scales in a scale-free process (termed the Richardson cascade). On the smallest scales, the injected energy is finally dissipated into heat. Simple dimensional arguments yield a relation between the spectral energy and the wavenumber, k according to

$$E(k) \propto \varepsilon^{2/3} k^{-5/3}. \quad (2.7)$$

This law holds for incompressible and isotropic turbulence (Kolmogorov, 1941). $E(k)dk$ is the energy in a wavenumber interval $[k, k + dk]$. Using the relation for the kinetic energy per unit mass

$$v_k^2 \sim E(k)dk \sim E(k)k \sim k^{-2/3}, \quad (2.8)$$

it follows that the velocity at a certain spatial scale, l , obeys

$$v_l \propto l^{1/3}. \quad (2.9)$$

The highest velocities are observed on the largest scales.

Burgers Turbulence

Once perturbations in the flow travel at velocities exceeding the local speed of sound, shocks occur. Assuming infinitesimally thin shock fronts, each discontinuity can be represented by a step function (see e.g. Klessen and Glover, 2014). Switching into spectral space by means of a Fourier transform, the energy at a given wavenumber is given by

$$E(k) \propto k^{-2}. \quad (2.10)$$

This form of the spectral energy is the most likely for supersonic turbulence, although the slope of -2 differs only slightly from that of classical Kolmogorov turbulence (Bec et al., 2001; Bec and Khanin, 2007; Klessen and Glover, 2014).

Compressible Turbulence

The above mentioned turbulence models refer to *incompressible* turbulence. However, the ISM is highly compressible (Mac Low and Klessen, 2004; Klessen and Glover, 2014). Hence, there will be modifications in the derivation of the characteristic features of turbulence (e.g. Federrath, 2013). In compressible turbulence, the energy dissipation rate is modified by taking into account the density of the fluid; hence

$$\frac{dE}{dt} \sim \frac{\rho v^2}{t} \sim \frac{\rho v^3}{l} = \text{const.} \quad (2.11)$$

The original dependence of velocity on spatial scale from Kolmogorov turbulence is no longer applicable. Furthermore, the original picture only allows for solenoidal modes in the turbulence. In compressible turbulence, the compressive modes (with $\nabla \times \underline{u}_c = 0$) complicate the behaviour, especially when the fluctuations are supersonic. Near shocks there is a strong coupling between the two modes, revealing itself in transfer of energy from one mode to the other (e.g. Elmegreen and Scalo, 2004). As the ISM is naturally subject to gravitational attraction, strongly compressed regions are able to become gravitationally bound (Mac Low and Klessen, 2004). The compressive modes occurring in the theory of compressible turbulence allow for this coupling of turbulence with gravity. A consistent theory of ISM turbulence has to provide this relationship. This coupling can also be inferred from scaling arguments of the momentum equation. As Vázquez-Semadeni (2015) argue, the advective and pressure gradient terms can equally induce the formation of density variations in an isothermal gas. Hence, using typical scales of the system

$$\frac{u^2}{l} \sim \frac{\Delta \rho c_s^2}{\rho l} \Rightarrow \frac{\Delta \rho}{\rho} \sim \mathcal{M}_s^2. \quad (2.12)$$

The density jump $\Delta \rho / \rho$ scales as the square of the Mach number. For subsonic flows, the gas behaves nearly incompressible. For supersonic flows, strong shocks significantly compress the gas. For typical Mach numbers in the ISM, the density jump can be as high as a factor of 100 (Klessen and Glover, 2014).

The density enhancements are also reflected in the density probability distribution function (henceforth density PDF). As was shown by [Vázquez-Semadeni and García \(e.g. 2001\)](#) the density PDF is *lognormal*, that is $\log(\varrho)$ follows a Gaussian distribution with its variance depending on the Mach number of the gas as (see also review by [Hennebelle and Falgarone, 2012](#); [Federrath and Klessen, 2012](#))

$$\sigma_s^2 = \ln \left(1 + b^2 \mathcal{M}^2 \frac{\beta}{\beta + 1} \right). \quad (2.13)$$

Here $s \equiv \ln(\varrho/\bar{\varrho})$ with $\bar{\varrho}$ being the average density, b being the forcing parameter, β being the ratio of thermal to magnetic pressure and \mathcal{M} being the RMS Mach number, respectively. The forcing parameter is $b = 1/3$ for solenoidal forcing and $b = 1$ for compressive forcing. As the Mach number of the turbulence increases, the width of the density PDF is broadened. This provides larger density jumps. The lognormal distribution is explained by the central limit theorem ([Hennebelle and Falgarone, 2012](#)). Each shock in the gas will increase the density by a certain factor $\varrho_1 \sim \mathcal{M}_1^2 \varrho_0$. If another shock passes the fluid parcel, its density increases by $\varrho_2 \sim \mathcal{M}_2^2 \varrho_1 \sim \mathcal{M}_1^2 \mathcal{M}_2^2 \varrho_0$. For N shocks passing by, the density enhancement is roughly $\varrho_N \sim \mathcal{M}_N^2 \dots \mathcal{M}_1^2 \varrho_0$. Taking the logarithm, the right hand-side becomes a sum, which is, by definition, normally distributed. However, [Federrath et al. \(2008\)](#) caution that the lognormal shape only appears if the compressive modes dominate over the solenoidal modes, thereby complicating the interpretation of density PDFs in compressible turbulence.

Magnetohydrodynamical Turbulence

When a magnetic field is introduced to the dynamics, the picture of turbulence changes and so does the resulting scaling of the energy. In the hydrodynamic case, energy is transferred from the largest down to the smallest vortices within the flow. In the MHD case, this energy transfer is guided by the background magnetic field, which is thought to be the field in the largest vortices (e.g. [Biskamp, 2003](#)). The turbulence is then rather travelling and interacting Alfvén waves. This introduces a new timescale related to the Alfvén speed $v_A = |B|/\sqrt{4\pi\rho}$. The dynamical timescale for the dissipation of kinetic energy is then $N\tau_A$ with N being the number of interactions (in this case collisions between Alfvén waves). Following [Biskamp \(2003\)](#) the hydrodynamic dissipation timescale τ_λ is replaced by a larger timescale τ_λ^2/τ_A . The dissipated energy is then modified to

$$\varepsilon \propto \frac{u^2 \tau_A}{\tau_\lambda^2} \propto \frac{u^4}{\lambda v_A}, \quad (2.14)$$

compared to $\varepsilon \propto u^3/\lambda$ in the hydrodynamic case. The appearance of the Alfvén velocity introduces the complication that the dissipation rate cannot be inferred from dimensional arguments as in the Kolmogorov approach. However, the spectral energy is

$$E(k) \approx (\varepsilon v_A)^{1/2} k^{-3/2}. \quad (2.15)$$

As stated in [Biskamp \(2003\)](#), see also the original work by [Iroshnikov \(1964\)](#), this ansatz for the description of MHD turbulence assumes the turbulence to be isotropic. The anisotropy introduced by the magnetic field was taken into account in later studies by [Sridhar and Goldreich \(e.g. 1994\)](#) as well as [Goldreich and Sridhar \(1995\)](#), see also [Galtier et al. \(2000\)](#) and yields a Kolmogorovian spectrum perpendicular to the field lines and a spectrum with positive scaling exponent for the parallel component.

Turbulence in the Interstellar Medium

Studies of turbulent motions in the ISM go back to [von Weizsäcker \(1951a,b\)](#) who suggested that turbulent motions contribute to the build-up of density enhancements. In the same year, [Chandrasekhar \(1951\)](#) discussed the role of *microturbulence* in a more formal way. In this case, the system scales are much larger than the outer scales of the turbulence (see also [Mac Low and Klessen, 2004](#)). The derivation leads to an effective sound speed, which can be used in the hydrodynamic equations

$$c_{s,\text{eff}}^2 \rightarrow c_s^2 + \frac{1}{3}\sigma^2 \quad (2.16)$$

where σ is the root-mean-square (rms) velocity. However, the turbulent fluctuations were assumed to be only *subsonic* ([Chandrasekhar, 1951](#)).

The idea of turbulent motions entering the momentum and energy budget was supported by [Zuckerman and Evans \(1974\)](#) due to observation of non-thermal broadening of CO lines. Later studies suggested the rms velocity to depend on the wavenumber, k , of the turbulence in order to explain observations of low-mass unstable cores ([Bonazzola et al., 1987](#)). However, as was shown by [Ossenkopf and Mac Low \(2002\)](#), the integral scale of the turbulent motions is comparable to the size of the system (here a molecular cloud) or even larger. Hence, the concept of microturbulence was proven to be inappropriate.

It was in the early 1980's when observations finally revealed the presence of turbulent motions in the ISM ([Larson, 1981](#)). The author primarily used observations of ^{13}CO in order to extract the

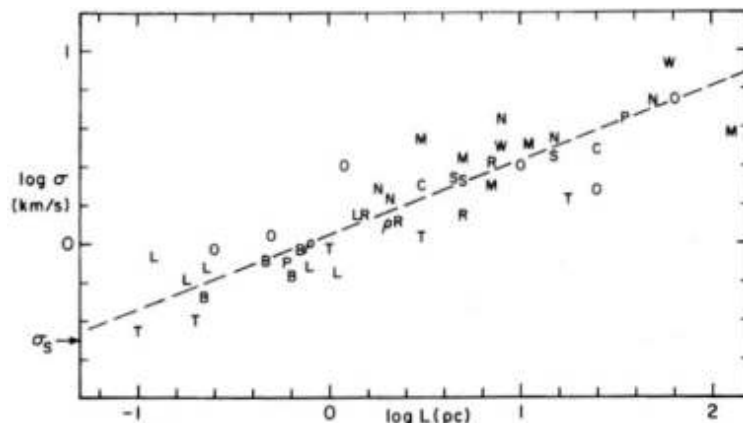


Figure 2.6: Size–linewidth relation from Larson (1981). Actually shown is the three–dimensional velocity dispersion as function of spatial scale for different objects. The dashed line is a fit to the data. Note that Larson stated in his work that the fit was achieved by eye. σ_s is the thermal velocity dispersion. From Larson (1981), Turbulence and star formation in molecular clouds. MNRAS, 194:809–826, figure 1.

apparent scale of the objects as well as to calculate reliable molecular linewidths, δv , from which the three–dimensional velocity dispersion was finally obtained. The resulting data is shown in figure 2.6. The deduced scaling exponent, $\gamma \sim 0.38$, is remarkably close to the one of incompressible (Kolmogorov/hydrodynamic) turbulence, $\gamma = 1/3$. This finding was in almost perfect agreement with previous discussions by Zuckerman and Evans (1974). However, the exact numerical values of the power–law exponent have been questioned by later studies (Solomon et al., 1987; Heyer and Brunt, 2004). Solomon et al. (1987) find $\gamma = 0.5 \pm 0.05$ and Heyer and Brunt (2004) stated that $\gamma = 0.59 \pm 0.07$, both values being higher than the original value found by Larson (1981). It is thus more likely that observed linewidths are a combination of thermal and turbulent motions, rotation as well as MHD waves. Despite these differences, all three studies agree that the rms velocity ~ 1 km/s when $L = 1$ pc, giving rise to a scale L_{therm} , at which the turbulent motions become *subsonic*.

The ISM is also strongly magnetised. Comparison of turbulent to the Alfvén velocity then yields further information on the characteristics of interstellar turbulence. As discussed above, there is no consensus on the magnitude of the magnetic field (Beck, 2001; Crutcher et al., 2009). Using values for the magnetic field from Zeeman observations and the HI velocity dispersion $\sigma \sim 10$ km/s from Tamburro et al. (2009) then reveals that the turbulence in the ISM is *trans–alfvénic* with $M_A \sim 1$ (see also Padoan et al., 1999; Padoan and Nordlund, 1999; Padoan et al., 2011, 2014). Recent studies by Padoan et al. (2015) argue that supernova driven turbulence in the

ISM implies super-alfvénic fluctuations when using observational constraints on the magnetic field strength. As a result, molecular clouds will be super-alfvénic, too, due to continuous energy injection from the supernovae. In contrast, magnetic field measurements reviewed in Beck (2001) and Beck (2015) denote slightly larger values of the magnetic field strength ($B \sim 10 - 15 \mu\text{G}$) and hence the ISM would be *subalfvénic*. This is in agreement with studies by Li et al. (2009) and consistent with the preserved morphology of the field lines.

2.1.5 Heating and Cooling

The individual phases of the ISM reside at different temperatures and densities, which are subject to heating and cooling processes.

Heating

Figure 2.7 shows the radiative heating rate, $\Gamma(n, T)$ as function of number density of the gas from Wolfire et al. (1995). The major heating process over a wide range of densities is the photoelectric effect due to absorption of FUV/EUV photons from the interstellar radiation field by polycyclic aromatic hydrocarbons (PAHs) and by dust grains (see also Tielens, 2005). During the heating process, an electron is released from the dust surface. The kinetic energy of this electron is then converted to thermal energy of the gas via collisions. As the densities decrease and temperatures increase the dust content diminishes. However, it is still the interaction with photons that efficiently heat the gas. In the WNM, heating by cosmic rays and X-rays also plays an important role. The sum of heating by cosmic rays, X-rays and the photoelectric effect approaches a nearly constant rate as function of density.

Cooling

Figure 2.7 also shows the different cooling rates, $n\Lambda(\chi, n, T)$. Cooling is due to radiative decay of collisionally excited atoms. In the WNM, emission of Ly α photons in the optical as well as cooling due to recombination of electrons are the main coolants. In contrast, in the CNM cooling is dominated by metal line cooling, primarily the [C I] and [O I] lines as well as [C II]. The latter line is indeed the major coolant at larger densities. Cosmic rays as well as photoelectrons can excite the fine-structure levels of atoms and yield the resultant cooling (e.g. Tielens, 2005; Draine, 2011).

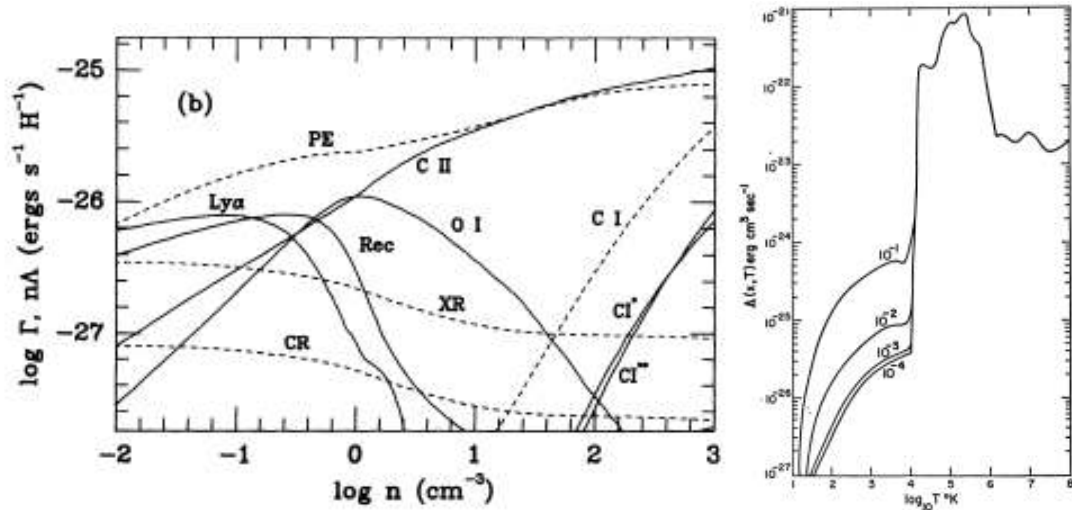


Figure 2.7: *Left:* Heating (dashed) and cooling (solid) processes in the ISM as function of number density, n . The dominant processes are heating by the photoelectric effect as well as line cooling of C^+ at high densities and $Ly\alpha$ cooling at low densities. *Right:* Cooling function as function of temperature. The labels denote different ionisation fractions. Note that cooling is most efficient in a regime corresponding to temperatures at shock fronts. Taken from [Wolfire et al. \(1995, left\)](#), ApJ, 443:152–168 (©AAS. Reproduced with permission.) and [Dalgarno and McCray \(1972, right\)](#).

2.1.6 The Galactic Cycle

The different (thermo–)dynamical and radiative processes operating in the ISM lead to a matter cycle. This *life cycle of the ISM* is depicted in figure 2.8. Commencing on the left, gas and dust *accumulate* in the disc midplane by gravitational settling mediated by the ambient magnetic field, turbulence and heating and cooling. Small perturbations lead to the formation of *condensates*, which can be observed as diffuse H I or dense molecular clouds. For sufficiently high ionisation fractions, the magnetic field will be dragged along with the condensations. Internal turbulence and external pressure fluctuations as well as an inhomogeneous gravitational field induce the *fragmentation* of the clouds. If the fragments become gravitationally unstable, they will undergo collapse and eventually *form stellar clusters or individual stars*. High–mass stars will evacuate their parental core/clump by their feedback processes and finally *disrupt* the entire molecular cloud due to a supernova explosion, thereby producing heavier elements due to the prior nucleosyntheses. The stellar material is injected into the ISM during this explosion. A supernova remnant is left over until it merges with the ISM after a long time. When the enhanced pressure and momentum from the high–mass star’s feedback have vanished, the cycle begins again with accumulation of gas.

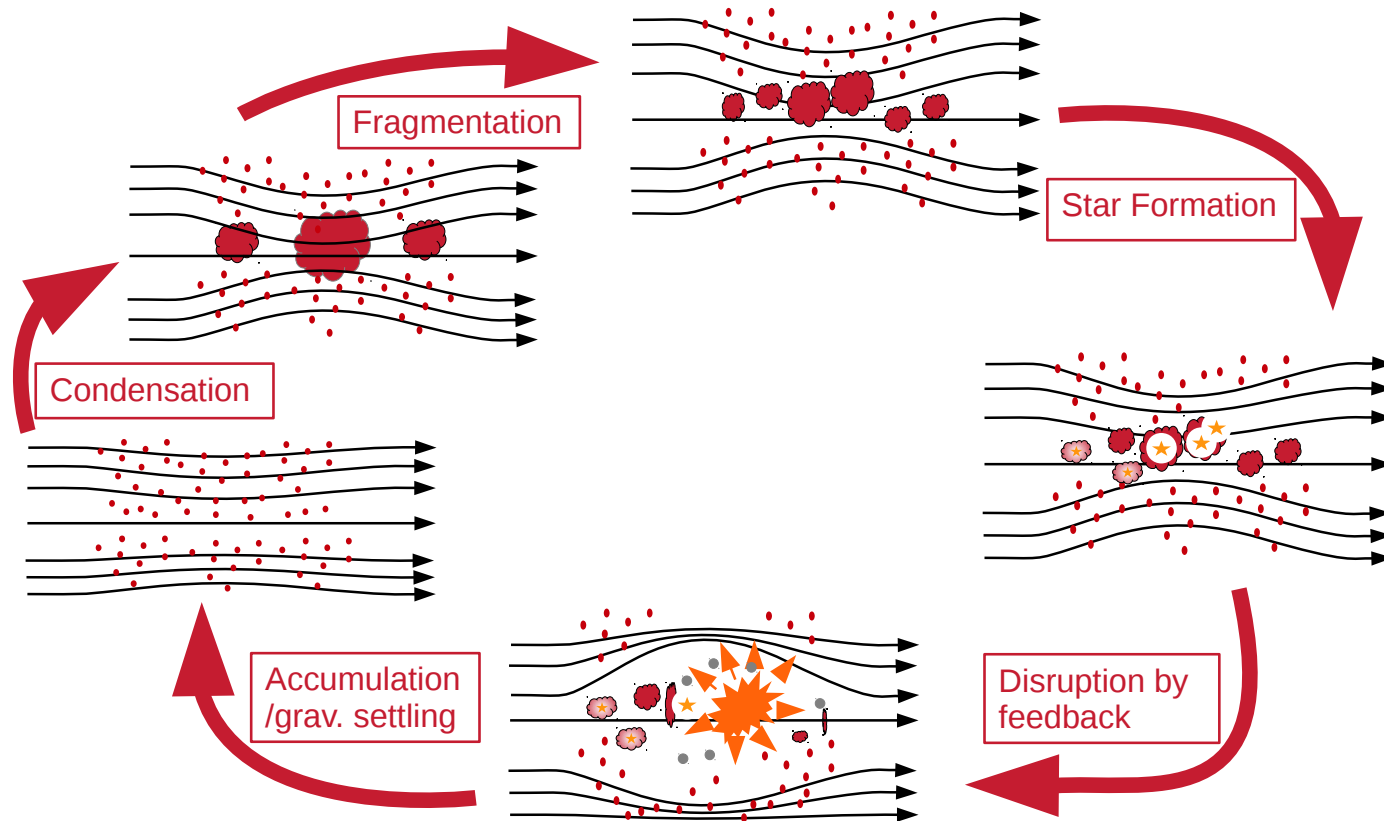


Figure 2.8: Schematically shown is the Galactic matter cycle. Starting in the lower left corner, matter is being accumulated on large scales due to global gravitational attraction, compression by spiral density waves, etc. Once, sufficiently stable potential wells have emerged, the gas condenses into the CNM phase and becomes even cooler when forming molecular clouds. These clouds then fragment to form even smaller objects. If the mass of those objects exceeds their Jeans mass, collapse initiates the formation of stars. Some of them only influence their natal regions in a non significant manner, that is, they are low-mass stars. The high-mass stars are able to disperse their parental clumps/clouds and finally end their lives as a supernova, leaving behind a neutron star. When the hot bubble has cooled to temperatures of the WNM, the cycle starts again.

2.2 Molecular Clouds

Molecular clouds are the nurseries of stars and stellar clusters. The formation of stars is certainly linked to the dynamics of the dense and cold gas as well as to the cloud's chemical composition. Turbulence within the clouds is primarily linked to the star formation rate and efficiency of the clouds since it actually is the stellar component, which shapes the structure and dynamics of the ISM in the cloud's environment.

In this chapter I will focus on molecular clouds, their basic properties, what is known from observations, and how they possibly form and disperse.

2.2.1 Properties of Molecular Clouds

In general, molecular clouds are the coldest and densest parts of the ISM. At the same time, they occupy only a small volume in space (e.g. [Blitz, 1993](#); [Dobbs et al., 2014](#)). The size spectrum of molecular clouds ranges from 10 pc to ~ 100 pc ([Stahler and Palla, 2005](#)). Their densities range from $\sim 100 \text{ cm}^{-3}$ to $\sim 10^4 \text{ cm}^{-3}$ depending on the size, with an average density of $\sim 400 \text{ cm}^{-3}$ ([Solomon et al., 1987](#), see also table 2.2). Regions of enhanced density usually will arrange in a filamentary network (e.g. [Banerjee et al., 2009](#); [André et al., 2014b](#)). The high densities are most probably the result of self-shielding processes of e.g. H_2 and CO ([Dobbs et al., 2014](#)). This shielding will generate regions of cold gas due to the lack of heating sources as well as the presence of efficient coolants like CO, HCN, NH_3 , CS, and C^+ (e.g. [Glover and Clark, 2012](#); [Glover et al., 2015](#)). With increasing distance to the densest and coldest parts, the material of the cloud heats up and becomes more tenuous. Hence, the cloud is surrounded by a halo of diffuse HI gas ([Hennebelle and Falgarone, 2012](#)). Their masses lie between a few ten solar masses for small clouds and $\sim 10^5 M_\odot$ for giant molecular clouds (GMCs). However, the total mass of gas in clouds throughout the Milky Way is $\sim 10^9 M_\odot$ (e.g. [Stahler and Palla, 2005](#); [Draine, 2011](#)). The large spread in masses is often attributed to either their star formation rate (SFR) or their formation process ([Stahler and Palla, 2005](#); [Hennebelle and Falgarone, 2012](#)). Observations reveal a similar spread in the clouds' surface densities. These range from $10 M_\odot/\text{pc}^2$ for diffuse HI clouds to $150 M_\odot/\text{pc}^2$ for GMCs (e.g. [McKee and Ostriker, 2007](#); [Roman-Duval et al., 2010](#)).

Table 2.2 also lists the linewidth of CO. At typical cloud densities, CO is usually being traced by observing its isotopologue $^{12}\text{C}^{18}\text{O}$ since it is optically thin in this regime (e.g. [Carlhoff et al., 2013](#)). Notice, however, that at even higher densities $n \geq 10^5 \text{ cm}^{-3}$ this molecular tracer also becomes optically thick or freezes out on dust grains, which leads to a CO depletion ([Bodenheimer,](#)

Table 2.2: List of typical cloud properties. Taken from [Blitz \(1993\)](#), [Stahler and Palla \(2005\)](#), and [Bodenheimer \(2011\)](#).

Type	Average Density [cm ⁻³]	Mean Radius [pc]	Mass [M _⊙]	Temperature [K]	Linewidth ^a [km s ⁻¹]
Giant Molecular Cloud	100	20–50	10 ⁵	15	7
Molecular Cloud	300	5–10	10 ⁴	10	4
Diffuse Cloud ^b	500	3	50	50	2–4
Dark Cloud	10 ³	2	30	10	—
Dense Core	10 ⁴ –10 ⁵	0.1	10	10	0.3

^aAs traced by CO.

^b[Stahler and Palla \(2005\)](#) define a diffuse cloud according to their low extinction $A_V \lesssim 1$ and not by their density.

[2011](#); [Carlhoff et al., 2013](#)). The linewidth of the thermally broadened line is given by ([Stahler and Palla, 2005](#), $\mu = 1.27$)

$$\Delta v_{\text{FWHM,therm}} = \sqrt{\frac{8\ln(2)k_B T}{\mu m_H}} \approx 0.19 \times \left(\frac{T}{1 \text{ K}}\right)^{1/2} \text{ km/s.} \quad (2.17)$$

Comparison with the values from table 2.2 reveal that the observed linewidths greatly exceed the thermal linewidth. This indicates that molecular clouds are turbulent and that the broadening is to a major extent due to non-thermal processes. [Blitz \(1993\)](#) name turbulent motions as one reason, but also MHD waves can induce the broadening ([Stahler and Palla, 2005](#)). The only outlier in this comparison is the linewidth for dense cores with velocities of less than 1 km s⁻¹, but this can be explained by the transition to subsonic motions at ~ 0.1 pc ([Larson, 1981](#); [André et al., 2014a,b](#), see also section 2.1.4 on turbulence).

2.2.2 Formation of Molecular Clouds

As stated before, the mass spectrum of molecular clouds covers a rather wide range of masses. In addition to intrinsic effects like turbulence (which may disperse the gas), the range of masses is a natural consequence of the different formation mechanisms. Some clouds do form by processes, which act on Galactic scales. Other clouds may form due to more localised events. Below, I will introduce possible formation mechanisms, which seem to form molecular clouds on a frequent level and which are intrinsically coupled to the dynamics of the ISM.

Parker Instability

Horizontally aligned magnetic field lines, if slightly perturbed, can undergo buoyant oscillations, thereby building magnetic ridges and valleys (Parker, 1966). A gaseous disc in initial magneto–hydrostatic equilibrium with a vertically oriented gravitational field will always be unstable to this kind of instability (Shu, 1992). Gas settles in the disc midplane due to the influence of the vertically oriented gravitational field (here due to stars). The gas will then move along the magnetic field lines, preferentially towards magnetic valleys, that is, towards the lowest point of a field line. The accumulation of gas in such valleys will in turn drag the field along towards the central parts of the disc, which amplifies the buoyancy of the field. As Dobbs et al. (2014) point out, the most unstable mode of this instability is proportional to $2\pi H$, where H is the scale height and the growth rate is $\sim v_A/H$ (McKee and Ostriker, 2007). However, perturbations with longer wavelengths will grow slower, but the collapse of the gas along the field lines will be nearly at free–fall (see Shu, 1992). Since $H \sim 100 - 200$ pc, it is in general possible to accumulate enough mass within the valleys such that clouds with masses $M_{\text{cloud}} \sim 10^5 - 10^6 M_\odot$ form. This is indeed confirmed by numerical simulations with an external stellar potential only (see e.g. Mouschovias et al., 2009). In addition, the authors report cloud separations of $dC \sim 500$ pc and magnetic field strengths in the midplane of $B \sim 4.3 \mu\text{G}$ with a slightly larger rms component, but in agreement with observations.

Figure 2.9 shows the resulting Parker instability from simulations by Mouschovias et al. (2009). The left subfigure indicates the stage of linear growth, whereas the other subfigures depict the phase where the instability grows non–linearly. The authors point out that it takes roughly 18 Myr to reach the non–linear stage. Simulations including effects like turbulent fluctuations or Galactic rotation observe only a slight increase in gas density at the midplane of the disc (Kim et al., 1998, 2001, 2002). It was concluded that the Parker instability might be too inefficient to form GMCs but may trigger or amplify other instabilities (McKee and Ostriker, 2007). On the other hand, more recent simulations by Lee and Hong (2011) suggest that the Parker instability may indeed form GMCs, but only in combination with the Jeans instability due to self–gravity, because the latter is able to suppress the convective instability, which naturally arises from the buoyancy of the field lines in the classical Parker instability.

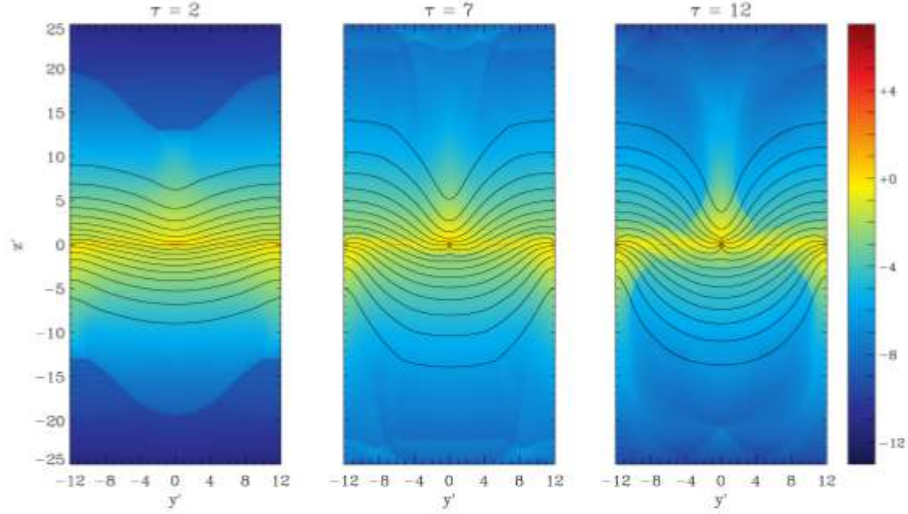


Figure 2.9: Numerical simulation of the Parker instability. Colour coded is the density. Black solid lines denote the magnetic field lines. The field lines first become only slightly perturbed during the linear growth stage, but then greatly deform at later stages. From Mouschovias et al. (2009), Formation of interstellar clouds: Parker instability with phase transitions. MNRAS, 397:14–23, figure 3.

Cloud–Cloud Collisions

Frequent observations of diffuse HI clouds in the ISM have led to the suggestion that (giant) molecular clouds form due to collisions of two or more low-mass clouds (Field and Saslaw, 1965; Kwan, 1979). However, the latter authors found the time to build up clouds with masses $> 10^5 M_{\odot}$ is $\gtrsim 10^4$ Myr (see also Blitz and Shu, 1980; Elmegreen, 1990) and it was hence concluded to be a negligible formation process. But, as clouds are formed within spiral-arms or in the interarm regions they can undergo frequent collisions during one spiral arm revolution (e.g. Tasker and Tan, 2009; Tan et al., 2013; Dobbs et al., 2015). Values range from one collision every $1/4$ orbit (Tasker and Tan, 2009) to a collision every $1/40$ th of an orbit (Fujimoto et al., 2014, see also Dobbs et al. (2015)). The latter authors included more sophisticated physics compared to the former. However, both studies highlight a revival of cloud–cloud collisions as a possible mechanism to form high-mass clouds.

The collisions of clouds naturally lead to either the formation of more massive clouds or to the disruption of the projectile clouds (e.g. Tasker and Tan, 2009; Tasker, 2011; Dobbs et al., 2014). This depends to a large fraction on the Mach numbers of the colliders (McLeod et al., 2011; Wu et al., 2015) as well as the impact parameter between the clouds (Wu et al., 2015). The possible success of this model is its ability to account for the observed cloud–mass spectrum since a large

variety of projectile masses as the basis can form either lower-mass clouds due to destruction or subsequently fill up the high-mass tail of the spectrum (Dobbs et al., 2014). In addition, as stated in Dobbs et al. (2014), the observed quasi-periodic spacing of GMCs can be explained by Galactic scale simulations and the influence of the epicyclic frequency (see also Dobbs et al., 2011). Once, the collision was successful in the respect of forming a GMC, formation of high-mass stars might be triggered due to the large reservoir of gas (Wu et al., 2015; Balfour et al., 2015).

Colliding Warm Neutral Medium Streams

Ballesteros-Paredes et al. (1999) suggested that molecular clouds can form in the collision plane of two converging streams of warm H I. Their intention was to bring up a solution to the small spread in stellar ages of only 1–3 Myr observed in the Taurus–Auriga complex.

In this scenario, to oppositely directed WNM streams form a shock-compressed layer in between (see figure 3.3 for a schematic). The density and temperature are increased, which is sufficient to induce runaway cooling due to thermal instability (e.g. Field, 1965; Vázquez-Semadeni et al., 2007). In addition, the WNM streams are turbulent. The turbulent fluctuations yield regions within the shocked slab between the flows where the thermal pressure of the slab is not opposite to the external ram-pressure of the flows. Instead, the thermal pressure gradient within the slab will induce motions perpendicular to the flows, thereby increasing the pressure support in nearby regions. As a result, other regions in the slab will break up due to the lack of support and become unstable. Beside this non-linear thin-shell instability (NTSI, Vishniac, 1994; Heitsch et al., 2007) the slab is prone to Kelvin–Helmholtz instabilities because of the strong shearing motions (see Heitsch et al., 2008b,a). The combined action of turbulence and thermal and dynamical instabilities then leads to the formation of a filamentary network. These filaments are cold density enhancements that are immersed in a warm, diffuse medium (Hennebelle et al., 2008; Banerjee et al., 2009; Vázquez-Semadeni et al., 2011; André et al., 2014a,b).

The ISM is also magnetised (Beck, 2001; Crutcher et al., 2009). Hence, the flows might be aligned with the ambient background magnetic field. In the contrary case of motion perpendicular to the magnetic field, magnetic pressure and magnetic tension are able to either delay or completely suppress the formation of *molecular* clouds (Heitsch et al., 2009). Inoue and Inutsuka (2009) argue that an inclination between the flow velocity and the magnetic field, which is too large, will only result in H I clouds without any further evolution towards molecular states. This has also been inferred from one-dimensional simulations of Hennebelle and Pérault (1999).

The advantage of this kind of formation model is its ability to explain e.g. the observed sheet-like morphologies of nearby clouds (Dobbs et al., 2014) as well as the small stellar age-spread (Ballesteros-Paredes et al., 1999). The former is due to gas motion along magnetic field lines and the confinement of the resulting cloud by the external ram pressure (e.g. Vázquez-Semadeni et al., 2009). The latter can be explained by the following:

Gravitational energy has to exceed (in absolute values) the opposing thermal (and magnetic) energy. The lower limit is then given by an equilibrium of energies. The necessary column density for the gas to afford gravitational collapse is then (Franco and Cox, 1986; Hartmann et al., 2001)

$$N_{\text{grav}} \sim 1.07 \times 10^{20} \left(\frac{T}{10 \text{ K}} \right)^{1/2} \left(\frac{n}{1 \text{ cm}^{-3}} \right)^{1/2} \text{ cm}^{-2}. \quad (2.18)$$

If a magnetic field is taken into account, the above equation is modified by including a term $\propto \sqrt{\beta}$. In a magnetised fluid, the gas also has to be *supercritical*. From $\mu = \mu_{\text{crit}}$ follows (e.g. Hartmann et al., 2001; Vázquez-Semadeni et al., 2011)

$$N_{\text{crit}} \sim 2.92 \times 10^{20} \left(\frac{B}{1 \mu\text{G}} \right) \text{ cm}^{-2}, \quad (2.19)$$

where the critical mass-to-magnetic flux ratio $\mu_{\text{crit}} = 0.16/\sqrt{G}$ from Nakano and Nakamura (1978) was utilised. Furthermore, the gas becomes *molecular* at

$$N_{\text{mol}} \sim (1 - 2) \times 10^{21} \text{ cm}^{-2}, \quad (2.20)$$

as was shown by Franco and Cox (1986) and van Dishoeck and Black (1988). Hence, the gas in the ISM becomes gravitationally unstable, magnetically supercritical, and molecular at the same time, which then implies rapid onset of star formation in a globally collapsing molecular cloud (Ballesteros-Paredes et al., 1999; Elmegreen, 2007; Vázquez-Semadeni et al., 2011).

It should be noted that converging streams do not have a unique origin. In fact, large scale gravitational instabilities or the above mentioned Parker instability induce converging gas motions (Hennebelle and Falgarone, 2012). On the other hand, expanding supernova shells may collide and form a molecular cloud (Inoue and Inutsuka, 2008, 2009, 2012; Ntormousi et al., 2011, 2014). The latter was actually observed most recently by Dawson et al. (2015). In addition, as Hennebelle and Falgarone (2012) point out, converging gas motions are also observed at the junctions of filaments within molecular clouds (see also Hacar and Tafalla, 2011).

One constraint of this approach, however, is the inability to form GMCs with masses $M_{\text{GMC}} \geq 10^5 M_{\odot}$ (Dobbs et al., 2014). The typical masses of clouds formed by converging WNM flows are of the order of $10^4 M_{\odot}$ (e.g. Vázquez-Semadeni et al., 2007; Banerjee et al., 2009; Vázquez-Semadeni et al., 2011; Hennebelle and Falgarone, 2012; Körtgen and Banerjee, 2015). This mass limit is linked to the spatial extent of the WNM streams. Thus, the larger the coherent flows the greater the final mass of the cloud. However, the coherence of the flows might be destroyed by turbulence in the ISM (Carroll-Nellenback et al., 2014). Furthermore, accumulation of gas in the ISM is primarily guided by the magnetic field. As McKee and Ostriker (2007) point out this implies a form of accretion that is very inefficient since it is along one dimension only. But, as stated in Vázquez-Semadeni et al. (2011) the accretion becomes three dimensional and much more efficient as soon as the gas has become dense, cold and gravitationally unstable.

2.2.3 Scaling Relations of Molecular Clouds

Observations provide a wealth of data about molecular clouds. Similar to the distribution of stellar masses (e.g. Salpeter, 1955; Kroupa, 2001), molecular cloud masses follow a power-law distribution $dN \propto M^{-\delta} dM$ as well with an exponent $\delta < 2$ (Dobbs et al., 2014, and references therein). The value of δ indicates that a major part of the mass is in the most massive clouds since $N(M) \propto M^{-\delta+1}$. Observations of molecular clouds in the Milky Way found $\delta \in [1.5, 1.8]$ (Solomon et al., 1987; Heyer et al., 2001; Roman-Duval et al., 2010). For comparison, in other galaxies the range for δ is a slightly larger (from 1.6 to 2.3, Fukui et al., 2008; Rosolowsky and Blitz, 2005; Gratier et al., 2012). However, all authors caution that the large spread may be a result from greatly biased CO-to-H₂ conversion factors.

In addition to the mass of the clouds and the surface densities mentioned above, certain dynamical properties of molecular clouds can be inferred. The pioneering work by Larson (1981) revealed the following scaling relations

$$\begin{aligned} \sigma \text{ (km/s)} &\propto M \text{ (M}_{\odot}\text{)}^{0.2} \\ \sigma \text{ (km/s)} &\propto L \text{ (pc)}^{0.38} \\ n \text{ (H}_2\text{)} \text{ (cm}^{-3}\text{)} &\propto L \text{ (pc)}^{-1.1} \end{aligned} \tag{2.21}$$

Here σ , n , L , and M are the velocity dispersion, number density of H₂, cloud size and cloud mass, respectively. The first relation shows a rather weak scaling of internal cloud velocity dispersion and cloud mass. The second one has been attributed to the presence of turbulence since

it is remarkably close to the power-law index of $1/3$ found in incompressible hydrodynamic turbulence. Although the exact values of the exponents have been discussed in recent years, they nevertheless indicate an intimate connection of the clouds and the surrounding ISM (Solomon et al., 1987; Heyer et al., 2009; Ballesteros-Paredes et al., 2011a). Recent observations by Heyer et al. (2009), however, suggest an extended scaling of velocity dispersion according to

$$\sigma \text{ (km/s)} = 0.7 \left(\frac{\Sigma_{\text{GMC}}}{100 \text{ M}_{\odot} \text{ pc}^{-2}} \right)^{1/2} \left(\frac{L}{1 \text{ pc}} \right)^{1/2}. \quad (2.22)$$

Here Σ_{GMC} is the cloud's surface density and the clouds are assumed to be virialised with $\alpha_{\text{vir}} \sim 1$. The observational data is shown in figure 2.10. This more generalised scaling relation has been confirmed by follow-up observations also of extra-galactic clouds (see e.g. Roman-Duval et al., 2010). The presence of scaling with surface density urges the question whether turbulence is as important in generating this relation as is gravity (Heyer et al., 2009; Ballesteros-Paredes et al., 2011a,b).

Another relation found by Larson (1981) is the mean-density scaling relation, which follows directly from dimensional constraints of the involved variables and may change when the exponent of one of the other scaling relations is changed. However, recent analysis by Stanchev et al. (2015, see figure 2.10, right) of the Perseus molecular cloud revealed a power-law exponent very close to the original one from Larson (1981). The analysis was also dedicated to the study of regions of diffuse gas surrounding the Perseus cloud. Here, the exponent was found to be shallower, more consistent with a regime dominated by supersonic turbulence. In contrast to previous studies (Heyer et al., 2009; Roman-Duval et al., 2010), the authors used the definition of effective sizes/abstract scales determined from the width of lognormal distributions fitted to different parts of the column density PDF, rather than determining the apparent size in the plane of the sky. In this respect, every lognormal distribution of a given regime of the column density PDF refers to a certain spatial scale of the molecular cloud. The findings are consistent with turbulence dominated ISM dynamics (see also Kritsuk et al., 2007, 2013).

2.2.4 Molecular Cloud Lifetimes

The lifetime of a molecular cloud is linked to its dynamics and the rate at which it forms stars (Tan, 2000, 2005, and references therein). The dynamical timescale is defined as $\tau_{\text{dyn}} = R/\sigma$ with R being the cloud size and σ being the internal velocity dispersion. From the virial theorem

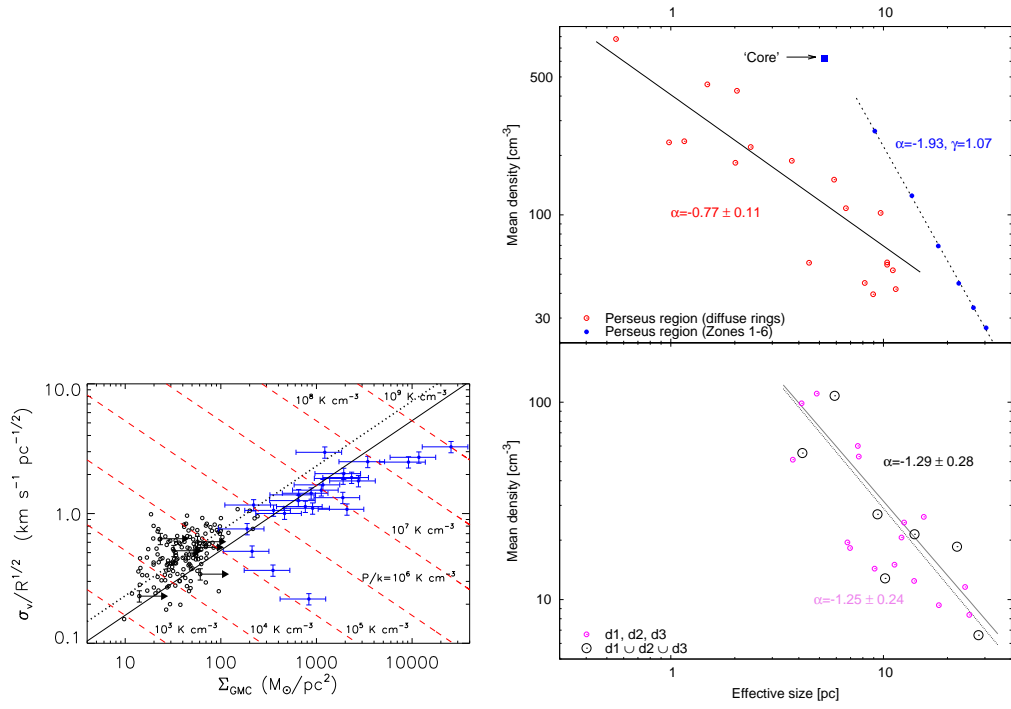


Figure 2.10: *Left:* Velocity dispersion weighted by \sqrt{L} as function of cloud surface density from Heyer et al. (2009). The origin of this scaling relation is still subject to debate, that is, whether it arises by turbulent fluctuations shaping the cloud or by gravitational contraction inducing these fluctuations. Provision of this figure by Clare Dobbs is greatly acknowledged. *Right:* Mean density scaling relation from Stanchev et al. (2015) showing great agreement with the original Larson relation. The relevant exponent is α in the subfigures. For the Perseus MC the slope is steeper, indicating gravity as the relevant source. In the diffuse rings surrounding the cloud the exponent is between the one from Larson (1981) and Solomon et al. (1987). The diffuse zones outside Perseus (denoted as d1,d2,d3) show a rather good scaling with turbulence in the ISM. Right figure from Stanchev et al. (2015), Tracing the general structure of Galactic molecular clouds using Planck data - I. The Perseus region as a test case. MNRAS, 451:1056–1069, figure 5.

$$2E_{\text{kin,turb}} + E_{\text{grav}} = 0 \quad (2.23)$$

and the assumption of a spherical cloud follows the relation between cloud mass and 1D velocity dispersion

$$\sigma = \sqrt{\frac{GM}{5R}} = \sqrt{\frac{4\pi G \rho}{15}} R. \quad (2.24)$$

Using this expression, the dynamical timescale reads

$$\tau_{\text{dyn}} = \frac{R}{\sigma} = \sqrt{\frac{15}{4\pi G \rho}} \sim 2\tau_{\text{ff}}. \quad (2.25)$$

Here, $\tau_{\text{ff}} = \sqrt{3\pi/32G\rho}$ is the free-fall timescale (see section 2.3.2). For typical densities of molecular clouds of $n \sim 100 \text{ cm}^{-3}$ the free-fall and dynamical timescale are 4 Myr and 8 Myr, respectively. Estimates of cloud lifetimes by [Koda et al. \(2009\)](#) in contrast give values of $\tau_{\text{cloud}} \sim 100 \text{ Myr}$, which is up to two orders of magnitude longer. However, the estimates were based on the lifetime of an H_2 molecule passing a spiral-arm region. As stated in [Dobbs et al. \(2014\)](#) this formalism does not apply for H_2 poor galaxies. A recent study by [Kawamura et al. \(2009\)](#) arranged observed molecular clouds into three distinct classes based on their star formation activity. Determining the ages of stellar clusters within the different classes allowed them to give timescales $\sim 25 \text{ Myr}$ for the lifetime of a cloud. Further studies by [Elmegreen \(2000\)](#) and [Ballesteros-Paredes and Hartmann \(2007\)](#) analysed lifetimes based on the observed star's position in the Hertzsprung–Russell diagram. Their conclusion was that $\tau_{\text{cloud}} \sim 10 \text{ Myr}$, far lower than those from [Koda et al. \(2009\)](#) and more consistent with recent numerical simulations ([Colin et al., 2013](#)).

Other approaches define the lifetime of the cloud by their ability to form stars and thus its depletion due to stellar feedback; hence

$$\tau_{\text{cloud}} \sim \frac{M_{\text{cloud}}}{\dot{M}} \quad (2.26)$$

where \dot{M} is the star formation rate. As [Krumholz et al. \(2014\)](#) point out, the depletion timescale is $\tau_{\text{cloud}} \sim (1 - 3) \tau_{\text{ff}}$. This also indicates that the internal velocity dispersion is linked to the feedback from stars. Depending on the star formation activity, this timescale is comparable to observed values.

2.2.5 Star Formation Rate and Efficiency

The lifetime of a molecular cloud is strongly correlated with its ability to convert dense gas into stars. This ability is quantified by the star formation rate (SFR, in M_{\odot}/yr) and star formation efficiency (SFE). The instantaneous SFE evaluates, which fraction of gas is in stars at a certain time (e.g. [Vázquez-Semadeni et al., 2011](#); [Dobbs et al., 2014](#), and references therein)

$$\text{SFE}(t) = \frac{M_*(t)}{M_*(t) + M_{\text{gas}}(t)} \quad (2.27)$$

with M_* being the mass in stars and M_{gas} being the mass of the cloud. The spread in the SFE is large, ranging from $\text{SFE} \sim 0.03$ in large complexes to $\text{SFE} \sim 0.5$ in individual star forming clouds (Evans et al., 2009). On average, however, the SFE is only a few percent (Evans et al., 2009; Dobbs et al., 2014) and hence the conversion of gas to stars is very inefficient. The instantaneous SFE can also decrease due to accretion of the cloud. Krumholz and McKee (2005, see also Krumholz and Tan (2007)) thus suggested to use the star formation efficiency per free-fall time

$$\text{SFE}_{\text{ff}} = \frac{\dot{M}}{M_{\text{gas}}/\tau_{\text{ff}}}. \quad (2.28)$$

Estimates yield $\text{SFE}_{\text{ff}} \sim 0.01 - 0.06$ regardless of the mass in cloud gas (which is biased by the threshold density from which on the mass is estimated) (e.g. Dobbs et al., 2014).

Discussions on the SFR go back to Zuckerman and Palmer (1974). The authors argue that the SFR should be as high as $200 M_{\odot}/\text{yr}$ if all gas within the Milky Way were at free-fall. However, observations yield $\text{SFR} \sim 3 - 4 M_{\odot}/\text{yr}$ (see e.g. Diehl et al., 2006). Robitaille and Whitney (2010) find even lower values of $\text{SFR} \sim 0.7 - 1.5 M_{\odot}/\text{yr}$. These values are consistent with low values of the SFE and are interpreted to be a result of magnetic fields, turbulence and stellar feedback preventing gas from being converted into stars too quickly.

2.3 Formation of Stars

Most stars form in stellar clusters (Lada and Lada, 2003). However, a molecular clump or cloud core needs to break up into multiple fragments in order to form a cluster of stars. In the following I will explain the basic concepts for the formation of low-mass stars from such collapsing fragments. The formation of high-mass stars essentially follows the same rules, but approaches some issues when dealing with the competition of accretion and evaporation by stellar radiation.

2.3.1 Jeans Analysis

Collapse of an overdense region is being initiated when

$$E_G > E_T + E_K + E_B + E_R, \quad (2.29)$$

where

$$\text{Gravitational Energy} \quad E_G = C_g \frac{GM^2}{R} \quad (2.30)$$

$$\text{Thermal Energy} \quad E_T = \frac{3}{2} \int P dV \quad (2.31)$$

$$\text{Turbulent Energy} \quad E_K = \frac{1}{2} \int \rho \sigma_t^2 dV \quad (2.32)$$

$$\text{Magnetic Energy} \quad E_B = \frac{1}{8\pi} \int B^2 dV \quad (2.33)$$

$$\text{Rotational Energy} \quad E_R = \frac{1}{2} \int \rho \Omega^2 r^2 dV. \quad (2.34)$$

Here C_g is a geometrical constant. Now assuming zero rotation ($E_R = 0$) and all other quantities to be constant throughout the volume, the minimum mass for gravitational collapse to occur is

$$M_J = \sqrt{\frac{3}{32\pi C_g^3 G^3 \rho}} (3c_s^2 + v_a^2 + \sigma_t^2)^{3/2}, \quad (2.35)$$

which is the *Jeans mass* of a system. The numerical constants appearing in the paranthesis in front of the different velocities as well as the constants in the leading prefactor depend on the way this mass is being derived. Using perturbation analysis of the (magneto-)hydrodynamic equations,

the correct expression of the Jeans mass reads

$$M_J = \frac{\pi^{5/2}}{6} \frac{1}{(G^3 \rho)^{1/2}} (c_s^2 + v_a^2 + \sigma_t^2)^{3/2}. \quad (2.36)$$

Although the derivation from equipartition of energies is quite informal, the result reveals the correct relations between the Jeans mass and the variables describing the system. For a non-magnetised and non-turbulent fluid ($v_a = \sigma_t = 0$), the thermal Jeans mass shows $M_J \propto \rho^{-1/2}$ and $M_J \propto T^{3/2}$. The denser/colder the system, the smaller its critical mass for gravitational collapse. In contrast, internal thermal energy injection will raise the Jeans mass.

Writing equation 2.36 in terms of a length scale, one obtains the *Jeans length* which obeys the following:

$$\lambda_J = \sqrt{\frac{\pi c_s^2}{G \rho}} = 12.3 \left(\frac{T}{1 \text{ K}} \right)^{1/2} \left(\frac{n}{1 \text{ cm}^{-3}} \right)^{-1/2} \text{ pc}. \quad (2.37)$$

Once the wave length of a perturbation exceeds λ_J or the mass exceeds M_J , the perturbations enforce instability of the whole system and it will collapse.

2.3.2 Free-Fall Timescale

In an unstable system, where the Jeans mass is effectively $M_J = 0$, gravitational collapse is assumed to be in pressureless free-fall. In this sense, the same argument is stated to be $M_{\text{system}}/M_J \rightarrow \infty$. The *free-fall* timescale

$$t_{\text{ff}} = \sqrt{\frac{3\pi}{32G\rho_0}} \quad (2.38)$$

is the time for a shell of a sphere to reach the centre. This time depends solely on the ambient density. Its relation to the Jeans length is given by

$$\lambda_J \approx c_s t_{\text{ff}} \quad (2.39)$$

under homogeneous and isothermal conditions. That is, pressure disturbances travel roughly one Jeans length within a free-fall time. Table 2.3 summarises the different timescales for entities in the ISM of different densities.

Table 2.3: Overview of the free-fall timescale, Jeans length and mass of different objects in the ISM assuming a mean molecular weight $\mu = 1.27$.

Object	Density (cm^{-3})	Free-Fall Timescale (Myr)	Jeans length (pc)	Jeans mass (M_{\odot})	Comment
WNM	1	45.7	870.0	1.1×10^7	$T=5000$ K
Molecular Cloud	100	4.5	4.76	177.76	$T=15$ K
Molecular Clump	10^4	0.45	0.39	9.68	$T=10$ K

2.3.3 Magnetic Fields and Star Formation

It has early been recognised by [Mestel and Spitzer \(1956\)](#) that magnetic fields provide an additional pressure, which counteracts gravity. For an equilibrium situation with vanishing thermal energy they found a minimum mass

$$M \approx 2.31 \times 10^4 \left(\frac{B}{1\mu\text{G}} \right)^3 \left(\frac{n}{1\text{cm}^{-3}} \right)^{-2} M_{\odot}, \quad (2.40)$$

up to which a system is stable. Sometimes, it is more convenient to write the energy balance in terms of the *mass-to-magnetic flux ratio* μ (see also section 2.1.3). By definition, the magnetic flux

$$\Phi = \int \underline{B} \cdot \underline{n} dS \quad (2.41)$$

is a conserved quantity in a comoving fluid element in the limit of *ideal* MHD (for an extensive description of MHD, see chapter 3.1). Here, S is the surface through which the magnetic flux is evaluated and \underline{n} is the surface normal vector. As a reminder, this conservation emphasises the problem that isolated systems with negligible mass accretion have a fixed value of μ/μ_{crit} . It follows that subcritical regions stay subcritical for all time. Hence, there must be some way to overcome magnetic pressure.

As suggested by [Mestel and Spitzer \(1956\)](#), and phenomenologically discussed in section 2.1.3), the process of *ambipolar diffusion* (AD) allows for the formation of stars even in the presence of strong magnetic fields. This idea was put forward by [Mouschovias and Spitzer \(1976\)](#) as well as [Shu \(1983\)](#) and [Shu et al. \(1987\)](#) and will be introduced below.

Ambipolar Diffusion

The magnetic field is only coupled to the charged particles in the gas. Molecular clouds, however, are only slightly ionised (ionisation fraction of $f_i \approx 10^{-8} - 10^{-6}$, Mouschovias and Spitzer, 1976, see also figure 2.11). The magnetic field is hence only passively felt by the neutral species due to collisional coupling with the charged particles. These collisions give rise to a drift motion of the neutrals past the ions and electrons, which can also be understood as a loss of magnetic flux. In a static situation the forces exerted on the ions – which are dominated by the Lorentz force and the drag/collisional term – have to outweigh each other. That is

$$\gamma \varrho_i \varrho_n (\underline{u}_i - \underline{u}_n) = \frac{1}{4\pi} (\nabla \times \underline{B}) \times \underline{B}. \quad (2.42)$$

Here, the different densities of ions and neutrals occur as well as the collisional coupling constant, γ , in units of $\text{cm}^3 \text{g}^{-1} \text{s}^{-1}$. The contribution from the electrons has been neglected since it is the ion species, which carries the major part of the momentum (Shu, 1992).

Now assuming the magnetic field as well as the relative drift velocity, $|\underline{v}_{\text{rel}}| = |\underline{u}_i - \underline{u}_n|$, to vary over a typical spatial scale L , the *ambipolar diffusion timescale* can be estimated according to

$$\tau_{\text{AD}} = \frac{L}{|\underline{u}_i - \underline{u}_n|} = \frac{4\pi\gamma\varrho_i\varrho_n L^2}{B^2}, \quad (2.43)$$

where ∇ is approximated by $1/L$ (Shu, 1992). Using the common relation between the neutral and charged particle densities, $\varrho_i = C\varrho_n^{1/2}$, (Shu, 1992, see also Elmegreen (1979)) the ambipolar diffusion timescale can be rewritten as

$$\tau_{\text{AD}} \approx 0.122 \left(\frac{n}{1 \text{ cm}^{-3}} \right)^{3/2} \left(\frac{B}{1 \mu\text{G}} \right)^{-2} \left(\frac{L}{1 \text{ pc}} \right)^2 \text{ Myr}. \quad (2.44)$$

Notice that the ionisation fraction $f_i = n_i/n_n$ enters equation 2.44 when the relation from Shu (1992, see also Elmegreen (1979)) is *not* being used. In figure 2.11 the ambipolar diffusion timescale τ_{AD} is compared with the free-fall timescale. For the calculation of $\tau_{\text{AD}}(n)$, the empirical relation $B(n) = 49 \mu\text{G} \times (n/10^4 \text{ cm}^{-3})^{0.65}$ from Crutcher et al. (2010, see also Crutcher (2012)) as well as $L = 1.23 (n/10^4 \text{ cm}^{-3})^{-0.81}$ from the Larson relations (see e.g. Draine, 2011) have been used. Above a density of $n \approx 2 \times 10^6 \text{ cm}^{-3}$, ambipolar diffusion proceeds faster than gravitational free-fall, indicating that cores are formed at first via diffusive processes.

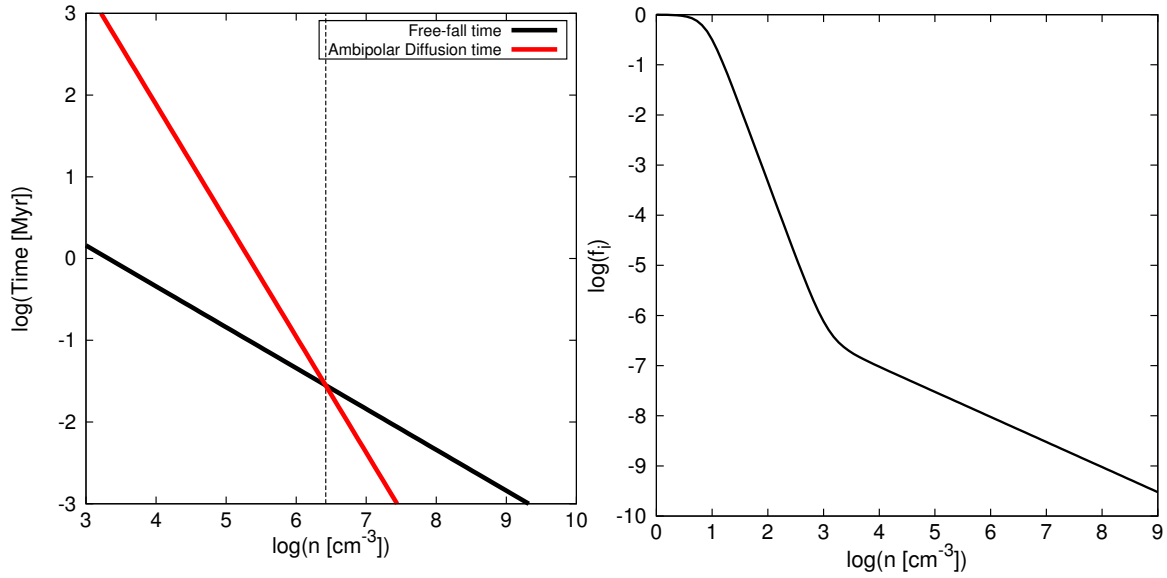


Figure 2.11: *Left:* Comparison of the free-fall timescale (black solid) with the ambipolar diffusion timescale (red solid) as function of number density. The vertical dashed line marks the density where both timescales are equal ($n \approx 2.6 \times 10^6 \text{ cm}^{-3}$). *Right:* Ionisation fraction as function of neutral gas density following the prescription in Fiedler and Mouschovias (1993). For further information, please see text.

The principal behind the idea of ambipolar diffusion is depicted in figure 2.12. In a static system, the neutral species slowly drift at a speed with amplitude $|\underline{v}_{\text{rel}}|$ towards the gravitational potential well past the ions and electrons. On the other hand, the magnetic field lines are frozen-in to the outward drifting charged particle species and hence diffuse out of the core region (when the neutral gas is thought to be at rest). The result is a loss of magnetic flux.

As indicated above, the direction of the drift speed is equal to that of the Lorentz-force. Particles can move along the curved magnetic field lines towards the *valley* created by gravitational attraction. In the very centre of this valley, the particles then undergo the drift motion perpendicular to the field lines.

2.3.4 Collapse of Individual Cloud Cores

At some point a *supercritical* core has formed and the magnetic field is expected to be not important for the further evolution. The core is subject to collapse with thermal pressure being the primary agent counterbalancing gravitational attraction. Initially, the core is in hydrostatic equilibrium, but can easily be rendered unstable due to e.g. gas cooling or increase of external pressure (Bodenheimer, 2011). Under isothermal conditions – which is a fairly good assumption because

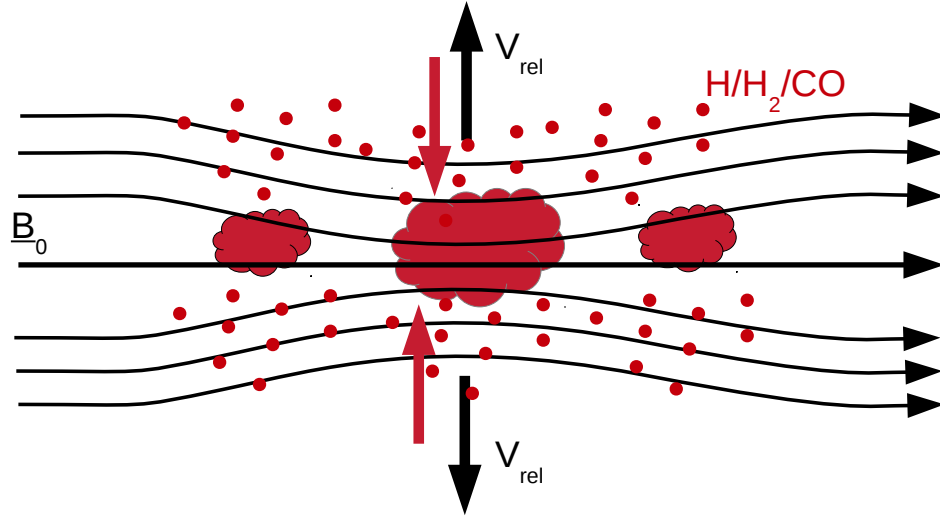


Figure 2.12: Schematic of the ambipolar diffusion process. This process can be viewed in two ways. 1) The magnetic field lines (solid black arrows), which thread a certain region diffuse out of that region at a speed v_{rel} (vertically oriented black arrows). 2) Neutral particles (exemplarily H, H_2, CO shown as red dots) drift towards the centre of the gravitational potential well at a speed v_{rel} (red arrows) and the magnetic field lines are assumed to be static.

the collapsing gas is optically thin for the infrared radiation from heated dust grains – the solution to the hydrostatic equation gives the *isothermal Lane–Emden equation* (e.g. Chandrasekhar, 1967)

$$\frac{1}{\zeta^2} \frac{d}{d\zeta} \left(\zeta^2 \frac{d\Psi}{d\zeta} \right) = \exp(-\Psi), \quad (2.45)$$

which is a non-linear ordinary differential equation for the dimensionless variable $\Psi = \Phi/c_s^2$ as function of (dimensionless) length

$$\zeta = \left(\frac{4\pi G \rho_c}{c_s^2} \right)^{1/2} r.$$

Knowledge of Ψ and ζ then fully characterises the isothermal sphere. Figure 2.13 shows the density contrast (ratio of central to envelope density) as function of dimensionless radius from Shu (1977). The density profiles reveal a flat inner part and a power-law behaviour for increasing radii. The different curves correspond to different initial core-to-envelope density ratios, representing the self-similar behaviour of the solutions to the Lane–Emden equation. Some solutions

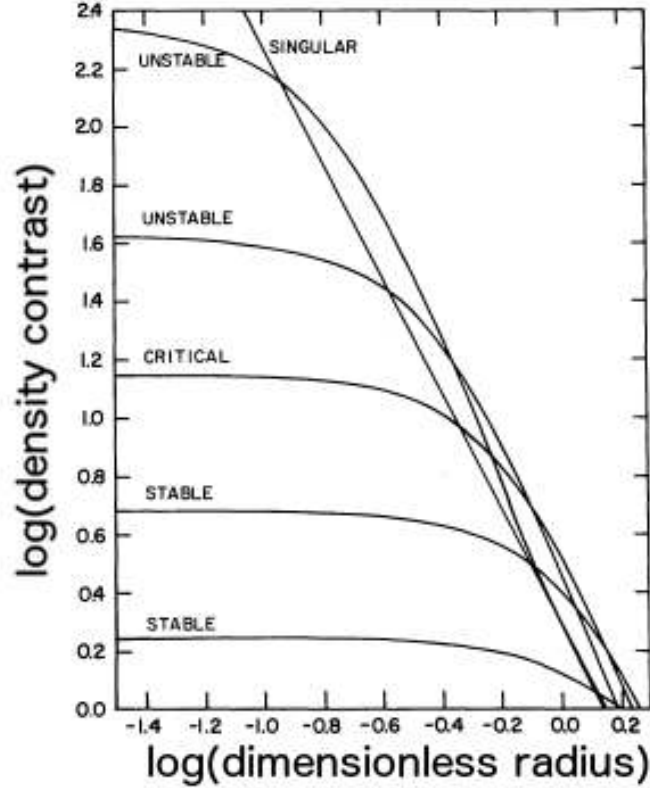


Figure 2.13: Profile of the normalised density as function of non-dimensional radius for the isothermal sphere. The different curves indicate different ratios of the core density to the envelope density. This ratio determines the external pressure that acts onto the sphere as well as the mass embedded within it. The labels *stable*, *critical*, *unstable* correspond to whether the mass included in the sphere is smaller, equal to, or larger than the critical mass. For large radii and infinite core density the density profile approaches that of a *singular isothermal sphere*. From [Shu \(1977\)](#).

observe stability, that is, the isothermal spheres re-expand to the initial state if being compressed. The unstable profiles result in a collapse of the sphere as soon as a small perturbation disturbs the system. The critical regime corresponds to the case, where the mass within the sphere is equal to the threshold mass for gravitational collapse, which is the Bonnor–Ebert mass ([Ebert, 1955](#); [Bonnor, 1956](#))

$$M_{\text{BE}} = m \frac{c_s^4}{P^{1/2} G^{3/2}}. \quad (2.46)$$

Calculations provide $m = 1.18$ ([Stahler and Palla, 2005](#)). It is interesting to observe that the density profile shows a power-law tail at large radii, corresponding to $\rho(r) \propto r^{-2}$. The exact

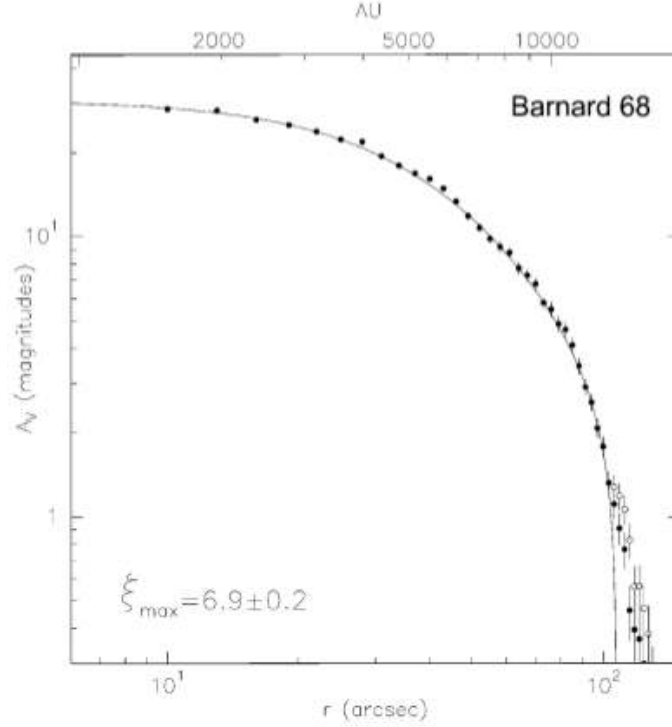


Figure 2.14: Shown is the extinction profile of Barnard 68 taken from [Alves et al. \(2001\)](#). The value of the measured extinction falls off with radial distance and can be fitted by a Bonnor–Ebert density profile with the non-dimensional maximum radius $\zeta_{\max} = 6.9 \pm 0.2$. This radius is slightly higher than the critical radius for collapse, $\zeta_{\text{crit}} = 6.5$.

functional form of the gas density is

$$\rho(r) = \frac{c_s^2}{2\pi G r^2}. \quad (2.47)$$

This is the result of the fact that the density ratio converges to a constant value for large radii. However, the corresponding potential Ψ *does not* satisfy the boundary conditions of the Lane–Emden equation at $\zeta = 0$ (which is the boundary condition at $r = 0$) and the above mentioned density profile refers to a *singular isothermal sphere* ([Shu, 1977, 1992](#)). Figure 2.14 shows observational evidence for Bonnor–Ebert spheres from [Alves et al. \(2001\)](#), namely the extinction profile of the isolated cloud Barnard 68. The profile can be fitted with a maximum radius of $\zeta_{\max} = 6.9 \pm 0.2$, which is only marginally higher than the critical radius for collapse of such a sphere, $\zeta_{\text{crit}} = 6.5$. The authors conclude that Barnard 68 is in the critical range of stability and might be on its way into gravitational collapse.

Indications for a Paradigm Shift

Although there is observational evidence for the theoretical description of isothermal spheres in hydrostatic equilibrium, there is also much argumentation that such a description cannot be a generalised theory of (low-mass) star formation (e.g. [Andre et al., 2000](#); [Mac Low and Klessen, 2004](#); [Crutcher et al., 2009, 2010](#)).

As [Shu \(1977\)](#) already pointed out, the model lacks a magnetic field during the collapse of the sphere as it is assumed to be negligible during these stages. The cores start out as subcritical objects, which become supercritical with time due to ambipolar diffusion. But, this would indicate an increasing mass-to-magnetic flux ratio with decreasing distance to the centre of the core, but, as was shown by [Crutcher et al. \(2009\)](#) using Zeeman measurements, this is not the case. The authors measured the magnetic field strength and mass of the core and envelope and estimated the ratio of the core mass-to-flux ratio to the envelope mass-to-flux ratio, \mathcal{R} . The ratio was $\mathcal{R} < 1$ for all measurements, which is not consistent with the theoretical predictions of ambipolar diffusion mediated star formation.

Detailed inspection of figure 2.11 reveals that the free-fall timescale at typical core densities is at least a factor of ten smaller than the AD timescale. Cores of such high densities thus must have formed by other processes than ambipolar drift. Furthermore, studies by [Ballesteros-Paredes et al. \(1999\)](#), [Elmegreen \(2000\)](#), and [Hartmann et al. \(2001\)](#) reveal that the observed stellar age spread is remarkably small. This again points at $\tau_{\text{ff}} < \tau_{\text{AD}}$.

The accretion rate predicted by the model of [Shu \(1977\)](#) is

$$\dot{M} \approx \beta \frac{c_s^3}{G} \approx 3.6 \times 10^{-6} \left(\frac{c_s}{0.25 \text{ km s}^{-1}} \right)^3 M_{\odot} \text{ yr}^{-1}, \quad (2.48)$$

with β being a constant, which depends on the initial mass of the system (e.g. [Shu, 1977](#); [Girichidis et al., 2011](#)). The intriguing fact is that the predicted accretion rate is constant, and it takes around 1 Myr to accrete 1 M_{\odot} . In contrast, [Andre et al. \(2000\)](#) argue that observed accretion rates are highly variable by factors of 5–10, in strong contradiction to $\dot{M} = \text{const}$. The authors also mention that the high fraction of binaries/multiples cannot be understood in terms of the this model (see also [Lada, 2006](#), and references therein).

2.3.5 Star Formation in Filaments

Latest results from the *Herschel* space observatory have re-emphasised the importance of filaments in star formation theory (e.g. André et al., 2010, 2014b). These interstellar filaments are identified independent of the parental cloud's location or its interaction with stellar clusters or the turbulent ISM (e.g. Hatchell et al., 2005; McClure-Griffiths et al., 2006; Stanchev et al., 2015). A filament is defined to be an elongated, overdense structure with an estimated aspect ratio greater 5–10 (André et al., 2014b). It is found that filaments show a rather universal radial density profile consistent with a Plummer-type profile (Arzoumanian et al., 2011)

$$\varrho(r) = \frac{\varrho_c}{\{1 + (r/R)^2\}^{p/2}}. \quad (2.49)$$

Here ϱ_c is the density in the central parts of the filament, R is the radius of the inner region where the density profile is flat, and p is some power-law exponent for large radii with $p \sim 2$ (Arzoumanian et al., 2011). Figure 2.15 shows results of a *Herschel* survey towards the IC 5146 molecular cloud. The main filament density profile is well fitted by a Plummer-type function. Also shown are the derived widths as function of column density for the filaments in IC 5146, Aquila and Polaris (Arzoumanian et al., 2011). It is seen that the filament widths scatter around an average value of 0.1 pc. The width is defined to be the diameter of the flat inner part of the density profile. The authors find a similar width for all their observed targets and they claim this width to be universal. The magnetic field in these filaments is to a major extent perpendicular to the major axis (Chapman et al., 2011; Li et al., 2014). The compression of the gas is due to supersonic motions in the ISM and mainly along the field lines (Hennebelle, 2013; André et al., 2014b). The width may then be explained by shocks in which the turbulent energy is dissipated and transformed into compressive work on the gas (Padoan et al., 2001). This is supported by the fact that turbulence makes a transition from super- to subsonic at scales of ~ 0.1 pc (Goodman et al., 1998; Falgarone et al., 2009). Another possibility suggests dissipation of MHD waves in regions of primarily neutral gas where they cannot propagate (see discussion in Hennebelle, 2013). However, as stated by André et al. (2014b) the mechanism for producing this width is still not fully understood and there is at least numerical evidence for filaments having smaller width (e.g. Seifried and Walch, 2015, and references therein).

Star formation proceeds in the densest parts of those filaments where individual regions collapse to dense cores (André et al., 2014b). The collapse process may also be enhanced in *hub filaments*,

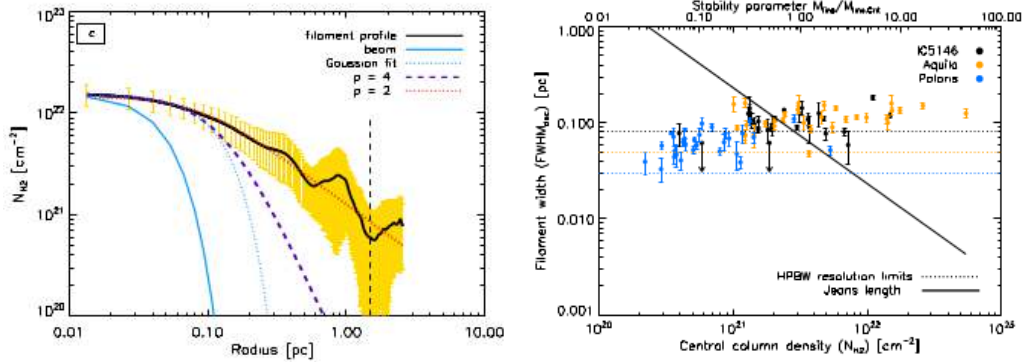


Figure 2.15: *Left:* Density profile for the main filament in the IC 5146 molecular cloud. The radial density profile is clearly fitted by a Plummer-like function with a power-law exponent of $p \sim 2$. The yellow shading indicates the dispersion along the filament. *Right:* Overview of filament widths as function of column density. All filaments tend to have widths around 0.1 pc. From [Arzoumanian et al. \(2011\)](#).

that is, in filaments possessing radially outward directed lower column density filaments with slightly converging motions directed towards the hub filament ([Myers, 2009](#)).

2.3.6 Gravoturbulent Star Formation

Irrespective of the size, morphology or mass of molecular clouds, filaments and cores, their lifetimes are intimately linked to the process of star formation. As discussed above, there are models which suggest short lifetimes of molecular clouds due to the fast onset of star formation ([Elmegreen, 2000](#); [Ballesteros-Paredes et al., 2011b](#)). Ambipolar diffusion regulated star formation proceeds too slow, but there emerged a theory of star formation controlled by supersonic turbulence ([Mac Low and Klessen, 2004](#); [Elmegreen and Scalo, 2004](#); [Scalo and Elmegreen, 2004](#)). Energy is injected on large scales, comparable to or even larger than the sizes of molecular clouds ([Ossenkopf and Mac Low, 2002](#)). The turbulence is mildly subsonic to transsonic with respect to the WNM, but highly supersonic in the CNM. This leads to the formation of strong shocks in which the turbulent energy can be dissipated ([Padoan et al., 2001](#)). The shock-compressed layers then can undergo thermal instability to form clouds, filaments, and cores. The beauty of this model is that it explains support of molecular clouds against gravity on global scales and the observation of hierarchical fragmentation on smaller scales ([Mac Low and Klessen, 2004](#); [Vázquez-Semadeni et al., 2007](#)). The model also assumes weak magnetic fields, that is, magnetic energy is at most comparable to the turbulent energy ([Klessen et al., 2000](#)). Observations reveal that clouds and cores might be slightly super-alfvénic with $\mathcal{M}_a \sim 1.5$ ([Crutcher et al., 2009](#);

Crutcher, 2012). Super–alfvénic motions are thought to be the natural outcome in a supernova driven ISM (e.g. Padoan et al., 2015). Supernovae as the driving source provide the necessary long wavelength modes at which turbulence is typically injected as well as strong enough compression of the gas. The latter will then induce a sufficiently small collapse time compared to the dynamical time of shocks passing by since $\tau_{\text{ff}} \propto 1/\sqrt{\rho}$.

2.3.7 Formation of a Protostar

Once collapse of an unstable core commences, the gas falls towards the centre of the gravitational potential well. Larson (1969) and Penston (1969) reported on the first numerical calculations of this type of collapse. The release of gravitational energy is used up as thermal energy. Since the gas is optically thin to the far–IR emission from heated dust grains, thermal energy is efficiently radiated away and the gas stays nearly isothermal at $T \sim 10$ K. Further evolution leads to optically thick conditions under which the radiation will heat up the collapsing gas. The increasing thermal pressure will counterbalance gravitational contraction and a hydrostatic object forms. The infalling material will further heat this core due to dissipative processes at the shock front. Once, the temperature within the core reaches $T \sim 2000$ K, H_2 will be dissociated. The dissociation is endothermic and hence thermal energy is used for this process. As a result, the core loses its thermal pressure support and a second phase of collapse begins with the final object being the protostar (e.g. Larson, 1969).

The further evolution of the protostar is governed by the interplay of gravitational contraction and radiation. The change of gravitational potential energy over time is the origin of the prestellar object’s luminosity

$$L \sim -\frac{dE_G}{dt} \sim \frac{GM^2}{R^2} \frac{dR}{dt}. \quad (2.50)$$

The resulting *Kelvin–Helmholtz* timescale

$$t_{\text{KH}} \sim \frac{GM^2}{RL} \sim 18.75 \left(\frac{M}{1 M_\odot} \right)^2 \left(\frac{R}{1 R_\odot} \right)^{-1} \left(\frac{L}{1 L_\odot} \right)^{-1} \text{ Myr}, \quad (2.51)$$

describes the time for a prestellar object to contract to its final main–sequence values of L , R , and M , when it starts burning hydrogen. However, high–mass stars reveal very short Kelvin–Helmholtz timescales that can be even shorter than the typical timescales of the accretion of material from the surrounding core (Beuther et al., 2007). Hence, high–mass stars are more likely to start burning hydrogen while still accreting material. In contrast, low–mass stars have already

gathered their final mass when entering the main–sequence.

2.3.8 Models of High–Mass Star Formation

The above discussion was dedicated to the formation of low–mass stellar objects. Although there is evidence that the formation of high–mass stars is very similar, there still occur some issues, some of which are related to the strong activity of the protostellar objects (see e.g. review in [Beuther et al., 2007](#)). On the other hand, high–mass star formation is difficult to observe ([Tan et al., 2014](#)). The Kelvin–Helmholtz timescale is about $t_{\text{KH}} = 10^4$ yr ([Kahn, 1974](#); [Tan et al., 2014](#)). Hence, this timescale can be much shorter than the typical timescale for accretion. In this case, the high–mass stars still accrete gas while already being on the main–sequence. Most of the models introduced below do agree to some degree with what is known from observations.

Stellar Collisions

The radiation feedback of high–mass protostellar objects leads to a strong decrease in the gas reservoir that can be accreted onto the prestellar object. This, in turn, will limit the maximum mass of the future star. A first attempt to circumvent this problem was introduced by [Bonnell et al. \(1998\)](#). This model assumes frequent collisions of high–mass protostellar objects. The high optical depth of these regions ensures that radiation pressure is not important. The advantage of this model is that it makes use of the fact that most stars form in stellar clusters ([Lada and Lada, 2003](#)). In this sense it is comparable with observations. However, as [Moeckel and Clarke \(2011\)](#) point out, the stellar density has to be enormously high ($\geq 10^8$ pc^{−3}) for this model to work. But, such densities are not observed (see also [Tan et al., 2014](#)). In addition, mutual stellar collisions would form only a few high–mass stars, rather than forming a wealth of intermediate to high–mass stars in accordance with observed stellar mass distributions ([Moeckel and Clarke, 2011](#)).

Competitive Accretion

In another model, [Bonnell et al. \(2001\)](#) proposed the formation of high–mass stars via competitive accretion (CA). In a CA scenario the location of a protostar within the parental core is one of the major agents. Two cases can be considered: *Case 1*) A protostellar object is located in the centre of the core. The very central location is then analogous to the location of the centre of the potential well (for typical mass density profiles $\rho \propto r^{-a}$, $a > 0$). This allows for channeled mass

accretion along filamentary structures as the gas within the core will naturally settle down to the centre. Hence, high-mass stars will be observed in the central regions of a stellar cluster. *Case 2)* A protostellar object is located near the core boundaries. In this case, the protostellar object will evolve to a low-mass star since the accretion onto the stellar object will be less efficient. On the one hand, the location near the boundaries implies a low-density environment. On the other hand, the gas near this location is also subject to tidal interactions with the more central parts of the core.

The second major point for CA is the fact that high-mass protostellar objects will have higher accretion rates due to their increased mass and vice versa. In combination with a location near the centre of the gravitational potential this will be the most favourable case for high-mass stars. As was already pointed out by [Bonnell et al. \(2001\)](#) this mechanism leads to a more consistent stellar mass spectrum. However, this model was put into question by [Krumholz et al. \(2005\)](#) due to the relatively unrealistic initial conditions. [Bonnell et al. \(2001\)](#) started from $\alpha_{\text{vir}} = E_{\text{turb}}/E_{\text{grav}} \ll 1$, but observations reveal $\alpha_{\text{vir}} \approx 1$ as argued by [Krumholz et al. \(2005\)](#). But, since turbulent fluctuations increase with spatial scale, even less bound or unbound initial conditions will lead to high-mass star formation ([Bonnell and Bate, 2005](#)). The turbulence on the small scales and the weak correlation with larger spatial scales will not affect the accretion of the high-mass objects in the core centre (see also [Zinnecker and Yorke, 2007](#)).

The Core Accretion or Monolithic Collapse Model

The core accretion model was proposed and later refined by [McKee and Tan \(2002, 2003\)](#), (see also [Yorke and Sonnhalter \(2002\)](#) for earlier numerical studies.). The basis for this model is a clump containing a few thousand solar masses. The clump is assumed to be in virial equilibrium with turbulence being the major support against gravity. These turbulent fluctuations rarefy the gas on the one hand. On the other hand, they provide the seeds for gravitationally bound regions due to compression ([Klessen et al., 2000](#); [Heitsch et al., 2001](#)). The bound cores will then collapse as soon as they become Jeans unstable. They can be assumed as isolated systems, i.e. interactions with other cores are not frequent enough or the timescale of their interaction is larger than the dynamical timescale of the collapse.

A key feature of this approach is the direct correlation with the stellar mass spectrum. The final mass of the star is primarily controlled by the mass of the collapsing core and $m_{\text{star}} \sim \varepsilon M_{\text{core}}$ with a conversion factor $\varepsilon \sim 0.5$ accounting for protostellar feedback ([Matzner and McKee,](#)

2000). Once, feedback by protostars has begun, the accreting core material should be dispersed by the build up of large H II regions. However, the core accretion model takes care of this fact by starting from nearly isolated, high-mass cores. Firstly, there is a large enough supply of gas that can be accreted onto the stellar object. Secondly, accretion discs are optically thick to the radiation, because they are naturally of the order of 30 % of the stellar mass (Tan et al., 2014). Hence, when the protostar commences dispersing the gas, accretion will still be able from the disc. Furthermore, the optically thick disc will funnel the hot and ionised gas in such way that collimated outflows are created rather than spherical ones.

Fragmentation-Induced Starvation

Once, high-mass stars generate large H II regions, the surrounding gas should be dispersed rather than accreted. However, some portions of the surrounding gas survive the impact of the stellar radiation (either due to self-shielding or due to mixing via shell instabilities). This gas reservoir can be accreted. On the other hand, the permeating stellar radiation will lead to fragmentation of the collapsing, dense gas. These fragments are then seen to collapse themselves and form individual low-mass objects. This process is hence called *fragmentation-induced starvation* (Peters et al., 2010). The final mass of the star is reduced due to its own feedback processes. In contrast to this negative impact, the heat exerted onto the gas will increase the local thermal Jeans mass of the fragments. Thus a larger mass has to be accumulated in order to render these fragments unstable. A natural outcome is the formation of further high-mass stars in case of collapse (see also Girichidis et al., 2012).

2.4 Stellar Initial Mass Function

Once stars have formed they represent a certain mass spectrum, also known as the *initial mass function* (IMF). The question, whether the IMF is universal or not is subject to ongoing discussion (see e.g. review by Offner et al., 2014). First attempts to describe the distribution of stars go back to studies of Salpeter (1955). From such studies it is evident that high-mass stars represent a minority in number counts.

Salpeter (1955) stated that the number of stars in a given mass interval follows

$$N(m) \propto m^{-\alpha}, \alpha = 2.35. \quad (2.52)$$

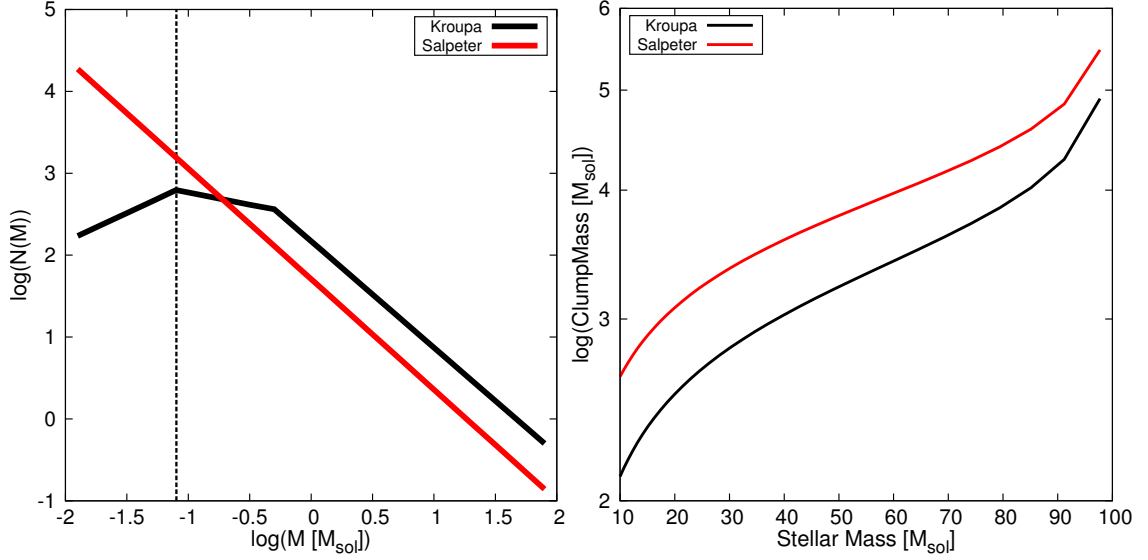


Figure 2.16: *Left:* Salpeter and Kroupa IMF for a total clump mass of $M_{\text{clump}} = 1500 M_{\odot}$. The vertical dashed line represents the peak of the Kroupa IMF at $0.08 M_{\odot}$. *Right:* Minimum clump mass to form one high-mass star of the given mass.

This IMF is shown in figure 2.16, where it is also compared to the Kroupa–IMF (Kroupa, 2001, see below). However, the observational data lacked the detection of low-mass objects and follow-up studies have shown that the IMF peaks at around $M_{\text{peak}} \sim 0.08 M_{\odot}$ and falls off towards smaller masses (e.g. Alves et al., 2007). A different model for the IMF, assuming a broken power-law was suggested by Kroupa (2001, see also figure 2.16). This form of the IMF reads

$$N(m) \propto m^{-\alpha}, \begin{cases} \alpha = 0.3, & 0.01 M_{\odot} \leq m \leq 0.08 M_{\odot} \\ \alpha = 1.3, & 0.08 \leq m \leq 0.5 M_{\odot} \\ \alpha = 2.3, & 0.5 M_{\odot} \leq m \end{cases} \quad (2.53)$$

and is more consistent with observational star counts. Another commonly used representation of the IMF is given by a log-normal distribution for the masses below $1 M_{\odot}$ (Miller and Scalo, 1979)

$$N(m) \propto \exp\left(-\log\left(\frac{m}{m_c}\right)^2 / 2\sigma^2\right) \quad (2.54)$$

with $m_c \sim 0.2 M_{\odot}$ and $\sigma = 0.55$ (e.g. Chabrier, 2005).

2.5 Protostellar and Stellar Feedback

Once a (proto-)star has been formed it injects mass, energy and momentum into the parental core surrounding it. These injection events are primarily due to bipolar jets and outflows in the early phases, when the protostellar object is still accreting material from the accretion disc surrounding it. In the later stages, the stars feedback onto the surrounding medium by ejecting stellar winds. These winds are to a major part thermally driven, but high-mass stars can also produce line-driven winds due to their large UV-photon emission. The latter wind produces a strong radiation pressure, which is exerted onto the environment. Beside those winds, high-mass stars create large regions of heavily ionised material, known as H II regions – an effect that is not seen for low-mass stars. In the end, the high-mass stars end their short lives in a powerful supernova explosion, ejecting most of their mass into the ambient medium and leaving behind a neutron star or black hole.

These different feedback mechanisms are going to be discussed briefly on the following pages.

2.5.1 Protostellar Jets

The first feedback process to discuss is stellar jets. This feedback mechanism arises during the protostellar or class 0 stages of stellar birth (Stahler and Palla, 2005).

The presence of jets has been recognised for the first time by Herbig (1950) and Haro (1952) due to observations of regions of enhanced emission in $H\alpha$ near NGC1999. G. Haro ruled out faint stellar objects since there has been no emission measured in the infrared. H II regions were also excluded since the observed spectra revealed singly ionised as well as neutral species, which is in contradiction to highly ionised gas around high-mass stars. Follow-up observations, also revealing regions of faint emission, traced these objects back to a single source, which was then evident to be a (proto-)star (see Reipurth and Bally, 2001, and references therein). The spectra of those *Herbig-Haro objects* (HH objects) were observed to also reveal strong emission in [S II] at 6717 Å and 6731 Å. The ratio of the $H\alpha$ intensity to this in the [S II] lines then yields information about the strength of shocks in those regions. However, since the estimated shock propagation speeds were far lower than the proper motion of the observed HH objects, many models have been suggested for their formation and origin (see e.g. review of Reipurth and Bally, 2001), two of which are named below.

The first is related to the common process of emanating winds. In this model, the nearly spherical wind is being collimated into jet-like streams due to enhanced ram pressure of the environment

and the accreting material. The external ram pressure then acts similar to a nozzle and the material is also accelerated, giving rise to fast outflows (e.g. Frank and Mellema, 1996; Mellema and Frank, 1997; Königl, 1999). This process of hydrodynamic collimation has been put into question since the ram pressure of the stellar wind should blow away the infalling envelope and hence the collimating agent (Reipurth and Bally, 2001).

The second model incorporates the magnetic fields of either the star or the accretion disc (e.g. Blandford and Payne, 1982; Shu et al., 1995). The presence of the field naturally leads to weaker ram pressure from the external medium. In general, the field is parallel to the rotation axis of the stellar object, but is being twisted due to it being frozen-in to the gas. Gas motion along the magnetic field lines then allows for outflows from the poles of the system. The rotation results in the generation of toroidal field components which collimate the outflow in a self-consistent way (Pelletier and Pudritz, 1992). How the magnetic field is being generated in these models as well as in reality is subject to discussion (see e.g. Bodenheimer, 2011). However, numerical analyses indicate mass loss rates due to the outflows comparable to observational results. The latter reveal $\dot{M} \propto 10^{-7} M_{\odot} \text{ yr}^{-1}$. For younger objects the emission becomes more intense in the infrared in the [O I] line. Here observations reveal $\dot{M} \propto 10^{-6} M_{\odot} \text{ yr}^{-1}$ (Stahler and Palla, 2005). Figure 2.17 shows the momentum-transfer rate, $\dot{M}v$, as function of bolometric luminosity, L_{bol} , from Wu et al. (2004). These observations reveal a trend towards increasing outflow rates with increasing luminosity. In turn, this indicates that the mass outflow rate decreases with increasing age (e.g. Reipurth and Bally, 2001). That is, because the luminosity for the objects in figure 2.17 is due to accretion of infalling material and is given by

$$L_{\text{accr}} \propto \frac{GM}{R} \dot{M}. \quad (2.55)$$

In addition, the figure reveals the outflow rate due to radiation $F = L_{\text{bol}}/c$. This rate is up to two orders of magnitude lower than the measurements. Wu et al. (2004) interpret this as radiation not being capable of driving such jets alone.

2.5.2 Stellar Winds

As already mentioned earlier, stars act onto their environment by expelling matter. The continuous driving of such flows is referred to as stellar winds. The driving mechanism of these winds depends on the star's mass as well as on its internal dynamics. Some driving mechanisms are discussed in the following.

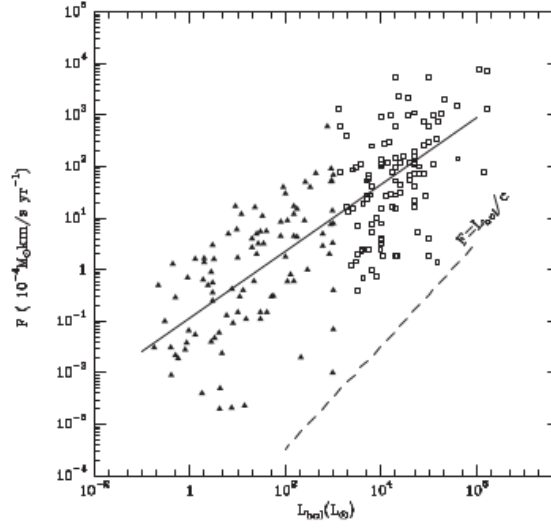


Figure 2.17: Shown is the rate of transfer of momentum ($\dot{M}v$) as function of bolometric luminosity of the driving source. Open symbols denote high-mass objects, filled symbols low-mass sources. The solid line is a least square fit to the observational data, the dashed line denotes the momentum transfer delivered from radiation. From [Wu et al. \(2004\)](#).

Thermally Driven Winds

The newly formed star can drive powerful winds that inject energy, momentum and mass into the ambient medium. One mechanism to drive such winds is due to the thermal pressure from the star's outer atmosphere, the *corona*. The large pressure gradient between the stellar surface and the ambient medium originates in the temperature of the star itself. The resulting wind velocities range from 300 km/s for slow winds to a few $\times 10^3$ km/s for fast winds (e.g [Stahler and Palla, 2005](#)). However, thermal pressure gradients can only drive slow winds. A solution for thermally driven stellar winds was firstly proposed by [Parker \(1958\)](#). In the *isothermal* and stationary limit the governing equation for the wind velocity, v_w , reads

$$(v_w^2 - c_s^2) \frac{dv_w}{dR} = v_w \left(\frac{2P}{\rho R} - \frac{GM_{\text{star}}}{R^2} \right). \quad (2.56)$$

Depending on the speed of sound (or equivalently the temperature of the star) and the mass, there is a unique and physically valid solution for the above differential equation. As [Stahler and Palla \(2005\)](#) point out, the wind velocity has to equal the sound speed at the critical distance

$$R_c = \frac{GM_{\text{star}}}{2c_s^2} = 7R_\odot \left(\frac{M_{\text{star}}}{M_\odot} \right) \left(\frac{T}{10^6 \text{ K}} \right)^{-1}, \quad (2.57)$$

which is hence often referred to as the *sonic point*. From this distance on the wind travels supersonically. However, the initial velocities of escaping material are in most cases lower than the star's escape velocity. Hence, the matter travels slowly away from the stellar surface into the corona. This increases the pressure gradient with respect to regions in the inside. These regions will then tend to expand due to the occurring pressure gradient and a steady wind is formed, which emanates from the stellar surface and coronal base. The question, how the wind is powered internally, that is, how thermal energy is provided to the outer layers is not fully understood to date. [Stahler and Palla \(2005\)](#), and references therein) review that the best candidates are turbulence as well as energy injection from Alfvén waves. As the authors also argue, the latter is indeed able to provide the necessary energy. However, the Alfvén waves need to be damped since their energy input is far too efficient.

Magneto–Centrifugally–Driven Winds

If the stars possess a magnetic field, this gives rise to another form of winds. These winds are a combination of magnetic interactions and rotation, where the latter implies centrifugal forces acting on the emanating gas (e.g. [Mestel, 1968](#)). This type of stellar wind is also present when thermally driven winds are absent due to too low temperatures. As [Mestel \(1968\)](#) argue, the magnetic winds depend on the ratio of magnetic and (wind–)kinetic energy. If magnetic energy dominates, the escaping material will follow the rotating field lines, while slowly moving outward. In the contrary case, the emanating gas will drag the field lines away from the star. The gas will then gain translational energy from the magnetic field over the course of its expansion and is hence accelerated very efficiently ([Lamers and Cassinelli, 1999](#)). Note that this concept is very similar to the disc–wind theory developed by [Blandford and Payne \(1982\)](#), see also [Pudritz and Norman \(1983\)](#) and [Pudritz and Norman \(1986\)](#)), where rotating magnetic field lines, which are anchored to the protostellar disc, fling material out of the plane. The material can then be collimated into a jet by strong toroidal magnetic field components (see also paragraph on jets).

Line–Driven Winds

High–mass stars with $M_{\text{star}} \geq 8 M_{\odot}$ reveal wind velocities far greater than these for low–mass stars. The reason is an additional force, which arises due to the high photon flux in the UV–range. Following [Draine \(2011\)](#) the emitted photons impart momentum to the surrounding gas by being absorbed and thus inducing the transition of an electron towards another energy level. The mo-

momentum gained by the gas particle is then shared with further gas particles by mutual two-body collisions. The excited atoms will emit a photon themselves when they get deexcited. The emitted photon may then interact with another atom in the gas. Effectively, the whole process can be thought of being a scattering process (Stahler and Palla, 2005). Due to the discrete transitions of the electrons, only certain spectral lines are able to sufficiently excite the emanating particles. The outflowing material is thought to be *line-driven*. The energy flux per unit frequency can be assumed to exponentially decrease

$$F_\nu(r) = F_0(r) \exp[-\tau_\nu(r)]. \quad (2.58)$$

Here, τ_ν is the optical depth at frequency ν and F_0 is the unattenuated energy flux. Since the emerging particles may interact with photons of different frequencies (or energies), the total force per unit mass is

$$f_{\text{rad}} = \frac{1}{c} \int_0^\infty \kappa_\nu F_\nu(r) d\nu, \quad (2.59)$$

where c is the speed of light and κ_ν is the line opacity. The quantity f_{rad} can be added to the momentum equation in order to represent the acceleration of the wind by radiation.

2.5.3 H II Regions

The photon flux of high-mass stars contains far-UV radiation with energies $6 \leq h\nu \leq 13.6 \text{ eV}$. The major part, however, consists of Lyman continuum photons with $E_{\text{LyC}} \geq 13.6 \text{ eV}$. This energy is enough to either ionise H I or to dissociate H₂ molecules.

In a stationary state, the ionisation by the stellar radiation must equal the recombination of free electrons and protons in the surrounding medium. With the assumption of neutrality, the volumetric recombination rate is

$$\mathcal{R} = \alpha_{\text{rec}}(T) n_{\text{H}}^2, \quad (2.60)$$

where n_{H} is the hydrogen number density and α_{rec} is the temperature dependent recombination coefficient in units of $\text{cm}^3 \text{ s}^{-1}$. For a spherical volume the required equality yields

$$\frac{4\pi}{3} \alpha_{\text{rec}}(T) n_{\text{H}}^2 R_{\text{S}}^3 = \mathcal{Q}_\nu \implies R_{\text{S}} = \left(\frac{3\mathcal{Q}}{4\pi \alpha_{\text{rec}} n_{\text{H}}^2} \right)^{1/3} \quad (2.61)$$

Table 2.4: Tabulated radii of the Strömgren–sphere for high–mass stars of different spectral type. The density of hydrogen is assumed to be $n_{\text{H}} = 10^3 \text{ cm}^{-3}$ and $\alpha_{\text{rec}}(T = 10^4 \text{ K}) = 2.6 \times 10^{-13} \text{ cm}^3 \text{ s}^{-1}$. Values for α_{rec} , n as well as the masses and emission rates are taken from [Stahler and Palla \(2005\)](#).

Spectral Type	Mass M_{\odot}	$\log Q$ 1/s	Strömgren radius (pc)
O4	70	49.9	1.35
O5	60	49.4	0.92
O6	40	48.8	0.58
O7	30	48.5	0.46
B0	18	47.1	0.16
B1	13	45.4	0.04
B2	10	44.8	0.03

The quantity R_{S} is called the Strömgren–radius (see also [Strömgren, 1939](#)) and Q is the photon emission rate. Radii of the Strömgren–sphere for typical high–mass stars are listed in table 2.4.

Usually, obtaining a region with a radius equal to R_{S} takes a long time since the ionised hydrogen atoms keep on recombining with free electrons on the one hand and are scattered through the volume on the other hand. As [Draine \(2011\)](#) point out, temperatures within the *Strömgren–sphere* are of the order of $T \geq 10^4 \text{ K}$, much hotter than the cold, molecular environment with $T \approx 10 - 100 \text{ K}$. The H II regions are thus over–pressurised cavities in the vicinity of the high–mass star and hence induce the emergence of a shock front, which travels supersonically into the ambient cold medium. The shock front is followed by the so called *ionisation front*. The latter arises due to the fact that there are still photons that do neither ionise nor dissociate the gas surrounding the star. Instead, they reach and ionise the gas surrounding the Strömgren–sphere. Usually, the dense gas around the star is not able to react to the ionising photons in a sufficiently short period of time. This gives rise to regions of further ionised gas. With time the region thus expands according to [Spitzer \(1978, see also Dale \(2015\)\)](#) as

$$R(t) = R_{\text{S}} \left(1 + \frac{7 c_{\text{II}} t}{4 R_{\text{S}}} \right)^{4/7}, \quad (2.62)$$

with c_{II} being the sound speed within the H II gas.

Observations of H II regions are primarily in the (far) infrared due to emission of heated dust grains as well as radio continuum observations of free–free emission ([Peters et al., 2010](#)). Another possibility is observation of recombination lines in $\text{H}\alpha$ ([Stahler and Palla, 2005](#)). Irrespec-

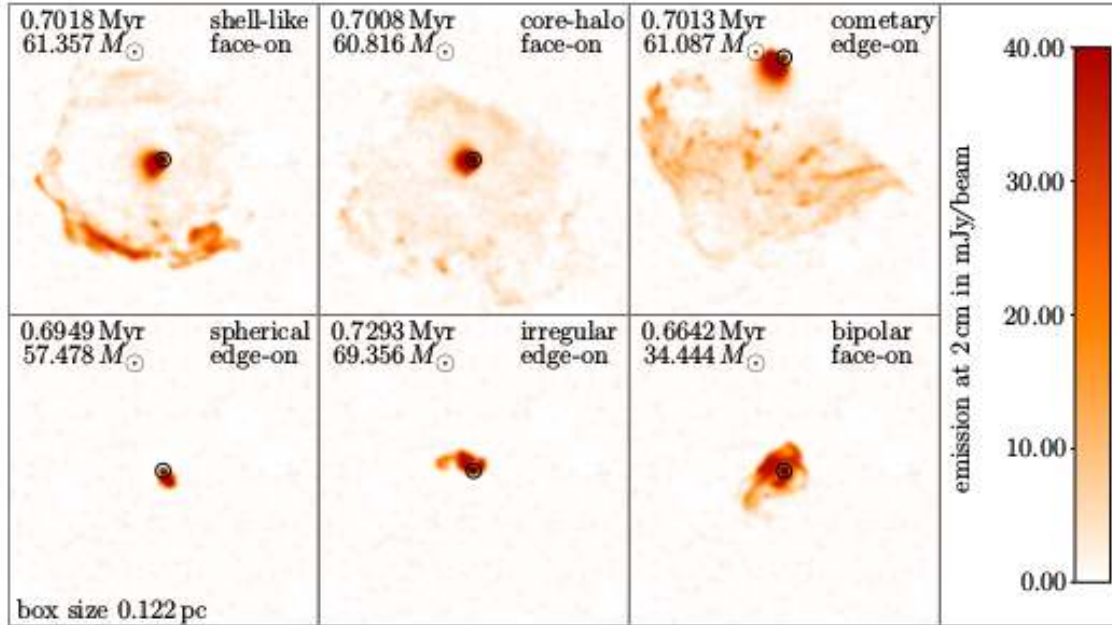


Figure 2.18: Synthetic observations in the radio regime at wavelength $\lambda = 2$ cm resulting from free-free emission showing the different H II region morphologies. Taken from [Peters et al. \(2010\)](#).

tive of the observational technique, H II regions can be classified according to their (observed) morphology (see figure 2.18). The classification is mostly based on the size and regularity of these regions:

- *Shell-like regions:* Observations indicate a dense shell of compressed, emitting material.
- *Core-halo morphology:* Observations reveal an emission peak surrounded by a lower intensity halo.
- *Cometary:* Inhomogeneities in the surrounding gas produce a dense shell on one side of the region, whereas the other side indicates tail like features.
- *Irregular:* No evident structure is observed.
- *Spherical:* The H II region is observed to expand spherically symmetric.
- *Bipolar:* Surrounding material forces the hot gas to expand anisotropically.

2.5.4 Supernovae

At the end of their short lives, high-mass stars inject a huge amount of energy (and momentum) into the ambient medium in one single event, called a *supernova*. During a supernova, the luminosity of the star can be as high as $10^{10} L_{\odot}$, comparable to that of the entire host-galaxy (Weigert et al., 2009).

Types of supernovae

Supernovae are grouped into distinct categories depending on their (observed) spectrum. An illustrative picture is shown in figure 2.19. If the spectrum reveals strong hydrogen lines, the supernova is referred to as being of type II, that is, a core-collapse supernova. High-mass stars fall into this category. If, in contrast, the spectrum shows no hydrogen lines, it is obvious that it must be an evolved star. These cases are called type I (Weigert et al., 2009). However, it is not obvious, what kind of star exploded and hence a further, more detailed, classification is required. This is usually achieved by the proof of silicon lines in the spectra. If those lines are present, it is a type Ia supernova. In this category, a white dwarf has passed the Chandrasekhar-mass limit by accretion, which ultimately leads to a supernova. In the contrary case of either very weak or completely missing silicon lines, the supernova is called type Ib/Ic, where the latter differentiation is according to the presence/absence of helium lines in the spectrum. The latter two types indicate again that a high-mass star exploded. In these cases, contrary to type II SN, the high-mass stars have undergone a Wolf-Rayet phase of enhanced mass-loss, during which the outer (hydrogen) shells have been expelled (LeBlanc, 2010).

Mechanism of a core-collapse supernova

Type Ia supernovae are due to runaway thermonuclear fusion processes, because the white dwarf crossed the Chandrasekhar mass. Type II, Ib, and Ic supernovae, respectively, are due to the collapse of a high-mass star's core. The velocity at which the stellar material is ejected can reach $v_{ej} = 10^4$ km/s. The processes leading to such high velocities will briefly be presented below.

During the main-sequence lifetime, the hydrogen burning creates a helium core. However, since high-mass stars are also very hot, the helium core will burn and produce a carbon-oxygen core (LeBlanc, 2010). At this stage, the high-mass star has already left the main-sequence and entered the red supergiant phase. The carbon in the carbon-oxygen core will continue to burn and a

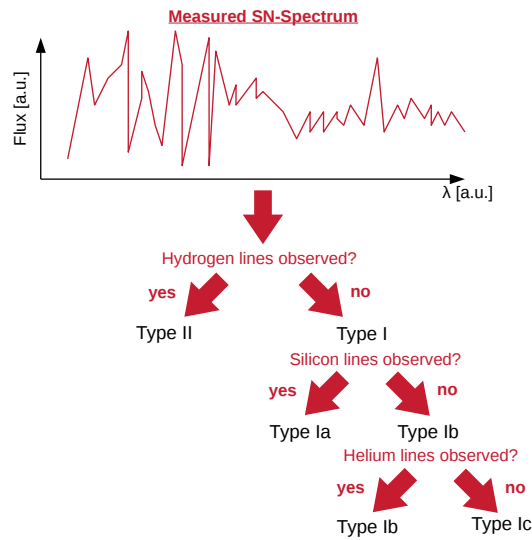


Figure 2.19: The different types of supernovae refer to the presence or absence of hydrogen lines in the spectra. Further, more detailed, classification is achieved by looking at silicon and helium lines. In most cases it is a high-mass star that went supernova (type II, Ib, Ic). To a lesser extent, white dwarfs accreted enough material to pass the critical threshold mass which makes them explode.

oxygen–neon core evolves. The burning of this latter phase creates a shell of silicon, which then produces an iron–core since the temperatures of $T \approx 10^9$ K are high enough for this reaction. From this stage on no further burning is achieved since reactions leading to heavier elements than iron are endothermic (LeBlanc, 2010).

The high temperatures in the innermost iron–core lead to photodisintegration, a process during which heavy nuclei are destroyed by interactions with photons. The photodisintegration will lead to free protons and electrons, which then react to form a neutron. With ongoing neutron formation, the additional pressure due to electron degeneracy vanishes. As a result, the inner core collapses. The outer shells are nearly unaffected, because the disturbance travels at the sound speed. The collapse of the inner core compresses the inner regions to densities at which the material is also opaque to neutrinos. At the same time, the core becomes stiff and the infalling material is being reflected. Since the latter is nearly at free–fall at this time, the reflection velocities can be as high as 10^4 km/s, hence being supersonic and thus creating an outward moving shock–front. The region downstream the shock is heated and the enormous pressure drives the material further outwards. In the end, the shock reaches the outer shells and pushes them out into the ambient medium. The temperatures are high enough to ensure that cooling is negligible and the material is in a state of free expansion.

The evolutionary stages of a supernova remnant

A supernova injects $E_{\text{SN}} = 10^{51}$ erg into the ambient medium. The subsequent evolution of the supernova remnant (henceforth SNR) can be divided into four distinct stages (Shu, 1992; Draine, 2011):

The free-expansion phase

During the first time after the supernova, the ejected material moves outwards on ballistic trajectories. The temperatures are high enough and the densities low enough that radiative cooling is not relevant. The evolution of the remnant obeys

$$R_{\text{SNR}} = v_{\text{SNR}} t.$$

Since a great volume surrounding the high-mass star has been evacuated by the star's ionising radiation, the SNR can travel almost unaffected for several hundred years.

The energy-conserving or Sedov-Taylor phase

Albeit the density of the surrounding medium is very low, the propagating shock front will sweep up enough material over time, so that the mass of this swept-up shell becomes comparable to the total mass of the ejecta. This induces the formation of a reverse shock, which propagates towards the centre of the SNR. As a result the interior to the outward moving shock gets thermalised. Up to this point, the evolution of the SNR was subject to adiabatic cooling. This stage is energy-conserving. The injected energy constitutes of 35 % kinetic energy and 65 % thermal energy. A detailed description of this stage was given by Sedov (1959) by assuming the explosion of a point-mass source. The variations in the density surrounding the expanding SNR can be neglected (due to the influence of the radiation) and the pressure is small compared to the pressure within the SNR. The evolution follows from dimensional arguments and is given by

$$R_{\text{Sedov}} = \zeta \left(\frac{Et^2}{\rho} \right)^{1/5},$$

where ζ is a constant of order unity, as well as

$$u_{\text{Sedov}} = \frac{dR_{\text{Sedov}}}{dt} = \frac{2}{5} \frac{R_{\text{Sedov}}}{t}.$$

The pressure-driven snowplow phase

When the cooling timescale becomes comparable to the dynamical timescale of the remnant, thermal energy is lost primarily due to metal line cooling. This cooling is especially important at the outer radius of the SNR. The material cools so efficient that the region thickens and a dense shell forms. From this stage on the SNR evolution is momentum-conserving and driven by the greatly increased pressure in the interior (see e.g. Cox, 1972). The governing equation is

$$\frac{d}{dt} (Mu_{\text{Sedov}}) = 4\pi R^2 P_{\text{int}}. \quad (2.63)$$

Assuming the SNR to be spherical and $R(t) = Dt^\eta$ one finds

$$\begin{aligned} R_{\text{pdsp}} &= \left(\frac{105 E_{\text{int},0} R_0^2}{4\pi \varrho_0} \right)^{1/7} t^{2/7} \\ u_{\text{pdsp}} &= \frac{2}{7} \frac{R_{\text{pdsp}}}{t}. \end{aligned} \quad (2.64)$$

Here $E_{\text{int},0}$, R_0 , ϱ_0 are the internal energy, radius and density at the time when cooling becomes important.

The momentum-driven snowplow phase

Once the interior of the SNR has sufficiently cooled, the internal pressure is not able to drive the evolution anymore. At this time, the SNR is driven by the momentum of the gas. The evolution of the SNR radius as function of time can again be constructed via dimensional arguments. Let

$$R = \chi p^\alpha \varrho^\beta t^\gamma, \quad (2.65)$$

with p being the momentum and χ a constant. By comparing dimensions, this yields

$$L^1 = \chi M^\alpha L^\alpha T^{-\alpha} M^\beta L^{-3\beta} T^\gamma. \quad (2.66)$$

Here M , L , T are mass, length and time dimensions. Further analysis gives an algebraic

system

$$\begin{aligned}
 0 &= \alpha + \beta \\
 1 &= \alpha - 3\beta \\
 0 &= -\alpha + \gamma
 \end{aligned}
 \tag{2.67}$$

from which $\alpha = 1/4$, $\beta = -1/4$, and $\gamma = 1/4$ follows. The resulting radius and velocity in the momentum-driven snowplow phase are

$$\begin{aligned}
 R_{\text{mdsp}} &= \chi \left(\frac{pt}{\rho} \right)^{1/4} \\
 u_{\text{mdsp}} &= \frac{1}{4} \frac{R_{\text{mdsp}}}{t}.
 \end{aligned}
 \tag{2.68}$$

The evolution of a SNR from the initial phase right after the supernova to the moment when it fades away into the ISM can be summarised as follows

Free expansion phase	$R(t) \propto t$
Sedov-Taylor phase	$R(t) \propto t^{2/5}$
Pressure-driven Snowplow phase	$R(t) \propto t^{2/7}$
Momentum-driven Snowplow phase	$R(t) \propto t^{1/4}$

(2.69)

3

Theory and Numerical Method

3.1 Magnetohydrodynamics

The ISM is usually modelled as a fluid, either using pure hydrodynamics or with magnetic fields included. The inclusion of the magnetic field depends on the specific energy budget and the resulting importance of the field for the overall dynamics. Since the ISM is strongly magnetised, the basic equations are these of the magnetohydrodynamic theory. In the following, the evolution equations for the macroscopic quantities will be derived. A basic result will be the appearance of a *closure problem*, which states that each evolution equation depends on a quantity (the respective flux) that needs to be evolved in time as well. However, the closure problem is solved by introducing an equation of state. In addition, I will briefly discuss the limits of the MHD approach.

3.1.1 The Vlasov–Maxwell–Poisson–System

In general, a gas consists of individual particles, which can be represented by an ensemble averaged phase space density $f_s(\underline{x}, \underline{v}, t)$ in order to circumvent the problem of determining the

evolution of each individual particle. Here, the index s denotes the particle species s . This function describes the macroscopic variables of the gas and assumes that the particles are statistically correlated in space, velocity and time. The problem reduces from N equations for the individual particle trajectories to one equation for the evolution of the ensemble averaged distribution function (Baumjohann and Treumann, 1996). The temporal change can be written as

$$\frac{d}{dt} f_s(\underline{x}, \underline{v}, t) = \frac{\partial f_s}{\partial t} + \frac{\partial f_s}{\partial \underline{x}} \frac{d\underline{x}}{dt} + \frac{\partial f_s}{\partial \underline{v}} \frac{d\underline{v}}{dt} = 0, \quad (3.1)$$

where the gas is assumed to be collisionless and the phase space density to be conserved. This equation is referred to as *Vlasov-equation*¹. The second term in equation 3.1 can be rewritten as

$$\frac{\partial f_s}{\partial t} + \frac{\partial f_s}{\partial \underline{x}} \frac{d\underline{x}}{dt} + \frac{\partial f_s}{\partial \underline{v}} \frac{d\underline{v}}{dt} = \frac{\partial f_s}{\partial t} + \underline{v} \cdot \nabla_{\underline{x}} f_s + \frac{\underline{F}}{m} \cdot \nabla_{\underline{v}} f_s = 0. \quad (3.2)$$

Here, a gradient with respect to the location occurs as well as with respect to the velocity. The equation reveals that the evolution is governed by the forces acting on the particles. In the ISM these forces are primarily due to (self-)gravity as well as the Lorentz force. The Vlasov-equation is a first order partial differential equation in all three variables. Although the equation itself is linear, the coupling to the Maxwell-equations makes it highly non-linear, since the occurring electromagnetic fields depend on quantities, which are derived from the distribution function. The macroscopic variables describing the gas only depend on space and time. So one can integrate the distribution function over velocity-space to create its moments. The first three moments are defined as

$$n_s = \int f_s(\underline{x}, \underline{v}, t) d^3v \quad (3.3)$$

$$\underline{v}_{b,s} = \frac{1}{n_s} \int \underline{v} f_s(\underline{x}, \underline{v}, t) d^3v \quad (3.4)$$

$$\underline{\underline{P}}_s = m_s \int (\underline{v} - \underline{v}_{b,s}) \otimes (\underline{v} - \underline{v}_{b,s}) f_s(\underline{x}, \underline{v}, t) d^3v \quad (3.5)$$

Here, n_s is the number density, $\underline{v}_{b,s}$ is the bulk flow velocity, and $\underline{\underline{P}}_s$ is the pressure tensor, respectively. The latter is thus defined as the contributions from the fluctuations of the velocities with respect to the average velocity, $\underline{v}_{b,s}$. The symbol \otimes denotes the dyadic product. For isotropic

¹In the literature it is also termed *collisionless Boltzmann-equation*, since it is derived from the Boltzmann-equation of statistical physics.

systems, the pressure tensor is diagonal and one can define the scalar pressure

$$p_s = \frac{m_s}{3} \int (\underline{v} - \underline{v}_{b,s})^2 f_s(\underline{x}, \underline{v}, t) d^3v. \quad (3.6)$$

The evolution equations for number density, fluid velocity, and pressure (or analogous energy) are then generated by creating the moments of the Vlasov–equation 3.2. The zeroth moment is the continuity equation.

The Continuity Equation

Integration of equation 3.2 over velocity space yields

$$\frac{\partial}{\partial t} n_s + \nabla \cdot (n_s \underline{v}_{b,s}) = 0 \quad (3.7)$$

The continuity equation is the governing equation for the time evolution of the fluid density. In the above form it states that the density² within any given volume only changes due to a mass–/particle–flux through the surface of the volume. The density is a conserved quantity. In the case of e.g. chemical reactions, the right hand side is not zero. Instead there are source terms for which further equations are needed.

Equation 3.7 contains the flux term, which is proportional to the bulk flow velocity, $\underline{v}_{b,s}$. This is the first–order moment of the phase space density $f_s(\underline{x}, \underline{v}, t)$. Hence, a second equation is needed in order to find the evolution equation for the flux.

The Momentum Equation

The bulk flow velocity is the first–order moment of the phase space density. By multiplying equation 3.2 dyadically by \underline{v} and integrating over velocity space one obtains (following the explanation given in [Baumjohann and Treumann, 1996](#))

$$\int \underline{v} \otimes \left(\frac{\partial f_s}{\partial t} + \underline{v} \cdot \nabla_x f_s + \frac{F}{m} \cdot \nabla_v f_s \right) d^3v = \text{const.} \quad (3.8)$$

²The current notation is for the number density. However, if the particle mass is constant it is analogous for the mass density after multiplication by mass.

The particle velocity \underline{v} and the velocity space volume element are independent variables. Thus, in the first term the differentiation with respect to time can be taken out of the integrand. The result is the time evolution of the flux density, $n_s \underline{v}_{b,s}$. The second term reads

$$\int \underline{v} \otimes (\underline{v} \cdot \nabla_x) f_s(\underline{x}, \underline{v}, t) d^3v = \nabla_x \cdot \int (\underline{v} \otimes \underline{v}) f_s(\underline{x}, \underline{v}, t) d^3v.$$

Rearrangement of the dyadic product yields

$$\nabla_x \cdot \int (\underline{v} \otimes \underline{v}) f_s(\underline{x}, \underline{v}, t) d^3v = \frac{1}{m} \nabla \cdot \underline{\underline{P}}_s + \nabla \cdot (n_s \underline{v}_{b,s} \otimes \underline{v}_{b,s}).$$

The third term contains all occurring forces (gravity, electromagnetic forces, viscous forces). Integration over velocity space then gives

$$\int \underline{v} \otimes \left(\frac{\underline{F}}{m} \cdot \nabla_v f_s \right) d^3v = -\frac{en_s}{m_s} \left(\underline{E} + \frac{1}{c} \underline{v}_{b,s} \times \underline{B} \right) + n_s \nabla \Phi,$$

where only the electromagnetic and gravitational forces have been included. Rewriting the integrated first-order moment equation then yields

$$\frac{\partial}{\partial t} (n_s \underline{v}_{b,s}) + \nabla \cdot (n_s \underline{v}_{b,s} \otimes \underline{v}_{b,s}) = -\frac{1}{m_s} \nabla \cdot \underline{\underline{P}}_s + \frac{en_s}{m_s} \left(\underline{E} + \frac{1}{c} \underline{v}_{b,s} \times \underline{B} \right) - n_s \nabla \Phi \quad (3.9)$$

which is the conservation equation for the fluid momentum. Note that the index x of the ∇ -operator has been dropped because all variables only depend on the spatial coordinates.

The Energy Equation

The momentum equation contains the pressure tensor $\underline{\underline{P}}$. Thus, an additional conservation equation is needed. For isotropic pressures, one can determine a scalar equation for the scalar pressure $p = \frac{1}{3} \text{tr}(\underline{\underline{P}})$, where $\text{tr}(\underline{\underline{P}})$ is the trace of $\underline{\underline{P}}$. Multiplying the Vlasov-equation by the energy $\frac{1}{2} m_s |\underline{v}_b|^2$ and integrating over velocity space yields the resulting equation

$$\begin{aligned} \frac{\partial}{\partial t} \left(\frac{3}{2} p_s + \frac{1}{2} n_s m_s |\underline{v}_{b,s}|^2 \right) + \nabla \cdot \left\{ \left(\frac{3}{2} p_s + \frac{1}{2} n_s m_s |\underline{v}_{b,s}|^2 \right) \underline{v}_{b,s} + \underline{\underline{P}} \cdot \underline{v}_{b,s} + \underline{q} \right\} \\ = en_s \underline{E} \cdot \underline{v}_{b,s} - n_s m_s \nabla \Phi \cdot \underline{v}_{b,s} \end{aligned} \quad (3.10)$$

The energy equation is the conservation equation for the total energy. The flux term additionally contains the heat flux vector \underline{q} as well as the *external* pressure $\underline{\underline{P}}$, which includes the work done on the volume element by the surrounding medium. The right hand side of equation 3.10 contains source terms. The first one is the electromagnetic term, the second one incorporates the generation of (internal) energy due to gravitational forces.

3.1.2 The Magnetohydrodynamic (MHD) Equations

In the previous sections the basic equations for the evolution of the macroscopic quantities of a gas from the Vlasov–equation were derived. A gas, however, consists of different particle species. In the simplest case, the particles are negatively charged electrons as well as singly–charged ions. Since the above derived equations are valid for each individual particle species at the same time, they have to be valid for the *total quantities* as well. Therefore, the following macroscopic variables, which describe *the whole fluid at once* are introduced (with the indices i and e representing ions and electrons, respectively)

$$m = m_i + m_e \quad (3.11)$$

$$n = \frac{m_i n_i + m_e n_e}{m_i + m_e} = \frac{1}{m} \sum_{s=i,e} m_s \int f_s(\underline{x}, \underline{v}, t) d^3v \quad (3.12)$$

$$\underline{u} = \frac{n_i \underline{v}_{b,i} + n_e \underline{v}_{b,e}}{n_i + n_e} = \frac{1}{n} \sum_{s=i,e} \int \underline{v} f_s(\underline{x}, \underline{v}, t) d^3v \quad (3.13)$$

$$p = p_i + p_e = \sum_{s=i,e} \frac{m_s}{3} \int (\underline{v} - \underline{v}_{b,s})^2 f_s(\underline{x}, \underline{v}, t) d^3v \quad (3.14)$$

With these definitions, the basic MHD equations become (Stahler and Palla, 2005)

$$\boxed{\frac{\partial}{\partial t} \rho + \nabla \cdot (\rho \underline{u}) = 0} \quad (3.15)$$

$$\boxed{\frac{\partial}{\partial t} (\rho \underline{u}) + \nabla \cdot (\rho \underline{u} \otimes \underline{u}) = -\nabla p + \frac{1}{c} \underline{j} \times \underline{B} - \rho \nabla \Phi} \quad (3.16)$$

$$\boxed{\frac{\partial}{\partial t} \left(\frac{3}{2}p + \frac{1}{2}\rho |\underline{u}|^2 \right) + \nabla \cdot \left\{ \left(\frac{3}{2}p + \frac{1}{2}\rho |\underline{u}|^2 \right) \underline{u} + \underline{\mathcal{P}} \cdot \underline{u} \right\}} \quad (3.17)$$

$$= \underline{j} \cdot \underline{E} - \rho \nabla \Phi \cdot \underline{u}$$

where I have used the facts that the gas is quasi-neutral (i.e. $\sum_i n_i \approx n_e$) and that $m_i \gg m_e$. In the momentum and energy equations new terms $\underline{j} \times \underline{B}$ and $\underline{j} \cdot \underline{E}$ occur, with the current density, \underline{j} , defined as $\underline{j} = en(\underline{v}_{b,i} - \underline{v}_{b,e})$. From the Maxwell equations, the current density can be related to the magnetic field according to Ampère's law, $\frac{4\pi}{c}\underline{j} = \nabla \times \underline{B}$. Hence, the Lorentz term in the momentum equation becomes

$$\frac{1}{c}\underline{j} \times \underline{B} = \frac{1}{4\pi}(\nabla \times \underline{B}) \times \underline{B} = -\frac{1}{8\pi}\nabla |\underline{B}|^2 + \frac{1}{4\pi}(\underline{B} \cdot \nabla)\underline{B},$$

with the first term in the rightmost equation being *magnetic pressure* and the second one being *magnetic tension*.

In the energy equation, respectively, the product $\underline{j} \cdot \underline{E}$ is observed. This is usually called *Joule heating* term as it represents the generation of internal energy from the electric field and current density. Instead of replacing the current density, it is convenient to transform the electric field. This can be achieved by using *the generalised Ohm's law* (Baumjohann and Treumann, 1996)

$$\underline{E} + \frac{1}{c}\underline{u} \times \underline{B} = \eta \underline{j} + \frac{1}{ne}\underline{j} \times \underline{B} - \frac{1}{ne}\nabla p + \frac{m_e}{ne^2}\frac{\partial}{\partial t}\underline{j}. \quad (3.18)$$

Equation 3.18 represents the most general form of Ohm's law in a conducting fluid. On the left hand side, there is the convective electric field $\frac{1}{c}\underline{u} \times \underline{B}$. The right hand side consists of the Ohmic term $\eta \underline{j}$, the Hall-term $\propto \underline{j} \times \underline{B}$, the pressure gradient term as well as the temporal variation of the current density. The latter can be thought of electron inertia (Baumjohann and Treumann, 1996). Note that in the absence of a magnetic field all terms except the gradient term vanish. This term can account for charge separation and may generate magnetic fields (also known as Biermann battery). In the simplest form of *ideal* MHD the above relation turns into the well-known *frozen-in* or *flux-freezing* condition

$$\underline{E} = -\frac{1}{c}\underline{u} \times \underline{B}. \quad (3.19)$$

The magnetic field is frozen-in to the (electron) fluid. The Joule heating term in the energy equation then becomes

$$\underline{j} \cdot \underline{E} = \underline{j} \cdot \left(-\frac{1}{c} \underline{u} \times \underline{B} \right) = \frac{1}{c} \underline{u} \cdot (\underline{j} \times \underline{B}),$$

thereby indicating that magnetic pressure and magnetic tension also provide a source of energy.

3.1.3 Validity of the MHD Approach

The (magneto-)fluid-dynamical description can be applied to the ISM, if the following two conditions are fulfilled by the system of interest:

- a) The typical scale of the system, L_{sys} , has to be large compared to the ion gyroradius. That is

$$L_{\text{sys}} > r_{g,i} = \frac{m_i c v_{\perp}}{e B} = 3.36 \times 10^{-12} \left(\frac{v_{\perp}}{\text{km/s}} \right) \left(\frac{B}{\mu\text{G}} \right)^{-1} \text{ pc.} \quad (3.20)$$

- b) The timescales that determine the dynamics of the system have to be long compared to the ion gyration time

$$\tau_{\text{sys}} > \tau_{c,i} = \frac{2\pi m_i c}{e B} = 2.07 \times 10^{-11} \left(\frac{B}{\mu\text{G}} \right)^{-1} \text{ Myr.} \quad (3.21)$$

Here, c is the speed of light, m_i the mass of a singly-charged ion. e is the elementary charge, B the magnetic field strength and v_{\perp} is the velocity perpendicular to the magnetic field lines. Since the typical sizes of molecular clouds are of the order of a few to a few tens of pc and the timescale for the formation of clouds and stars is of the order of Kyr to Myr, both conditions are fulfilled and the fluid approach is justified.

A counterexample is the interaction of Saturn's largest moon, Titan, with the plasma in Saturn's magnetosphere. The gyroradius of ambient O^+ and N^+ ions is comparable to, or even larger, than the moon itself (e.g. [Simon et al., 2007](#)). The cycloidal arcs defining the motion of the ions in the electromagnetic field then induce a significant asymmetry in the plasma flow past the moon which is not seen in simulations treating all species as a single fluid ([Müller et al., 2010](#)).

3.1.4 Heating and Cooling Source Terms

The ISM is subject to various heating and cooling processes. In this sense, the energy equation 3.10 needs to include two source terms for heating and cooling of the gas. However, the Vlasov–Maxwell–Poisson system assumes a *collisionless* gas and thus heating and cooling by collisions is neglected. Including these processes then yields

$$\begin{aligned} \frac{\partial}{\partial t} \left(\frac{3}{2}p + \frac{1}{2}\rho |\underline{u}|^2 \right) + \nabla \cdot \left\{ \left(\frac{3}{2}p + \frac{1}{2}\rho |\underline{u}|^2 \right) \underline{u} + \underline{\mathcal{P}} \cdot \underline{u} \right\} \\ = \underline{j} \cdot \underline{E} - \rho \nabla \Phi \cdot \underline{u} + n\Gamma(\chi, T) - n^2\Lambda(\chi, T), \end{aligned} \quad (3.22)$$

where the source terms are highlighted. Because heating is primarily due to cosmic rays, there is a linear dependence on density. Cooling involves two–body interactions (cooling of species 1 due to collision with species 2 and vice versa) and is thus proportional to n^2 . The variable χ in the cooling and heating functions denotes the electron fraction of the gas (see e.g., [Dalgarno and McCray, 1972](#), for the effects of varying χ).

3.1.5 The Maxwell Equations

Since electromagnetic fields occur in the MHD equations, the Maxwell equations have to be taken into account in order to evolve those fields in time. These are:

The induction equation

$$\frac{\partial}{\partial t} \underline{B} = -c \nabla \times \underline{E}, \quad (3.23)$$

which relates the temporal evolution of the magnetic field to the curl of the ambient electric field. Time–varying magnetic fields induce vortical electric fields. With the notion of the convective electric field from above, the induction equations becomes

$$\frac{\partial}{\partial t} \underline{B} = \nabla \times (\underline{u} \times \underline{B}). \quad (3.24)$$

Using this description of the induction equation shows that it has become a transport equation for magnetic flux.

Ampère's law

$$\nabla \times \underline{B} = \frac{4\pi}{c} \underline{j} + \frac{1}{c} \frac{\partial}{\partial t} \underline{E}. \quad (3.25)$$

Time-varying electric fields as well as electric currents induce magnetic fields. The temporal variations of the electric field are small compared to the speed of light and Ampère's law can be modified to

$$\nabla \times \underline{B} = \frac{4\pi}{c} \underline{j}, \quad (3.26)$$

which has already been used for the derivation of the magnetic pressure and the magnetic tension.

The solenoidal constraints

$$\begin{aligned} \nabla \cdot \underline{E} &= 4\pi \varrho = 0 \\ \nabla \cdot \underline{B} &= 0. \end{aligned} \quad (3.27)$$

There are no magnetic and electric sources and sinks. Hence, the electric and magnetic field lines in an ionised gas are always closed. However, small deviations from quasi-neutrality will lead to electric sources and sinks, which are given by the charges.

3.1.6 The Poisson Equation

The momentum and energy equation include the gravitational potential, Φ . Therefore, the whole system of equations needs to be extended to include an equation for the gravitational potential. This equation is known as the *Poisson equation*

$$\nabla^2 \Phi(\underline{x}) = 4\pi G \varrho(\underline{x}). \quad (3.28)$$

This equation relates the gravitational potential to the mass-density of the gas, indicating that the gas itself is the source of gravitational attraction. In general, equation 3.28 only accounts for the *self-gravity* of the gas. Here, G is Newton's gravitational constant. Further contributions to the *total* gravitational potential, i.e. due to the gravitational potential of stars themselves, may directly be included in the Poisson equation since it is linear in Φ and in $\varrho(\underline{x})$ (see e.g. [Walch et al., 2014](#), and references therein).

3.1.7 Non-Ideal Effects

If the gas gets denser due to gravitational contraction or external compression, it may be subject to collisions between individual particles. One essential assumption of the ideal MHD limit is infinite conductivity. This assumption is violated if collisions become frequent. Then, the conductivity will be finite and is usually treated as a second-rank tensor, $\sigma_{ij} < \infty$ for $i, j \in \{1, 3\}$. The matrix notation of $\underline{\underline{\sigma}}$ takes into account anisotropic conductivities (parallel to and perpendicular to the magnetic field).

Ohmic Diffusion

A finite conductivity implies non-vanishing magnetic resistivity, η . As a result, there will be a resistive term in the induction equation

$$\frac{\partial}{\partial t} \underline{B} = \nabla \times (\underline{u} \times \underline{B}) - \nabla \times \left(\underline{\underline{\eta}} \nabla \times \underline{B} \right) \quad (3.29)$$

with $\underline{\underline{\eta}} = \frac{c^2}{4\pi \underline{\underline{\sigma}}}^{-1}$. For isotropic and spatially constant conductivity/resistivity, the induction equation will become a diffusion equation

$$\frac{\partial}{\partial t} \underline{B} = \nabla \times (\underline{u} \times \underline{B}) - \eta \nabla^2 \underline{B}. \quad (3.30)$$

Hence, in case of zero fluid motion, the magnetic field evolution is controlled by the diffusion of field lines.

Ambipolar Diffusion

Ambipolar diffusion has already been discussed in section 2.3.3 on a rather phenomenological basis. In a static system the momentum equation reads

$$\underline{0} = \underline{j} \times \underline{B} - \xi (\underline{u} - \underline{v}_n), \quad (3.31)$$

where gravitational and pressure gradient terms have been neglected. The constant ξ contains the collisional coupling constant as well as the densities of the interacting species. The apparent scattering process results in a drift perpendicular to the magnetic field lines. Solving for the velocity

of the charged particles yields

$$\underline{u} = \frac{1}{\xi} \underline{j} \times \underline{B} + \underline{v}_n. \quad (3.32)$$

The collisional coupling between the charged and neutral particles results in a momentum transfer between both species, but also influences the induction equation. The modified induction equation

$$\frac{\partial}{\partial t} \underline{B} = \nabla \times (\underline{v}_n \times \underline{B}) + \nabla \times \left[\left(\frac{1}{\xi} \underline{j} \times \underline{B} \right) \times \underline{B} \right] \quad (3.33)$$

contains a coupling term to the neutral species as well as a term proportional to the Lorentz force. If the latter was zero, i.e. $\frac{1}{\xi} = 0$, the magnetic field would be frozen-in to the neutral particles and no diffusion of the field would occur at all (Shu, 1992). In contrast, if $\frac{1}{\xi} \neq 0$, the second term in the above equation can be rewritten as follows:

$$\nabla \times \left[\left(\frac{1}{\xi} \underline{j} \times \underline{B} \right) \times \underline{B} \right] = -\nabla \times \frac{1}{\xi} (j |\underline{B}|^2) = \frac{c}{4\pi\xi} [(\nabla \times \underline{B}) \times \nabla |\underline{B}|^2 - |\underline{B}|^2 \nabla^2 \underline{B}]. \quad (3.34)$$

Here $\xi = 4\pi\gamma_c\varrho_n\varrho_i = \text{const}$. The induction equation now contains additional terms, which are of diffusive nature. A numerical realisation has been studied by Duffin and Pudritz (2008) and Vázquez-Semadeni et al. (2011). Note that the above discussed derivation is a *strong-coupling approach*. A *multi-fluid* approach in the limit of ideal MHD has been discussed by Pinto et al. (2008). The latter essentially makes use of the different conductivities arising through collisional coupling.

3.1.8 Wave Modes in MHD

Perturbations of the fluid flow generate waves that transport the information to other locations in the volume. In classical hydrodynamics, only one wave mode exists, namely the ordinary sound wave

$$c_s^2 = \frac{\partial P}{\partial \varrho} = \gamma \frac{k_B T}{\mu m}. \quad (3.35)$$

In MHD, the ambient magnetic field introduces three additional waves, which are the

Alfvén wave

$$|\underline{v}_A| = \frac{|\underline{B}|}{\sqrt{4\pi\varrho}} \quad (3.36)$$

as well as the fast and slow *magnetosonic* waves

$$|v_{f,s}| = \frac{|\underline{v}_A|^2 + c_s^2}{2} \pm \sqrt{\frac{1}{4} (|\underline{v}_A|^2 + c_s^2) + |\underline{v}_A|^2 c_s^2 \cos^2(\theta)}. \quad (3.37)$$

The angle θ is the angle between the wave vector and the magnetic field. As the Alfvén wave travels only along the magnetic field lines with perpendicular perturbations, it is a transversal wave. Due to these facts, the emergence of Alfvén waves is purely anisotropic and energy can be transported over large distances without being dissipated significantly (Baumjohann and Treumann, 1996). This reflects in the wave’s property of not being dispersive (i.e. $\partial\omega/\partial k = \text{const}$). The magnetosonic waves, in contrast, can travel perpendicular to the magnetic field. Due to their additional dependence on the sound speed, these waves are thought of being compressive waves. However, if the medium is shocked, it is the fast magnetosonic wave, which is responsible.

3.1.9 MHD Summary

A gas consists of individual particles, which interact with each other or with some fields. Following their temporal evolution is too complicated. Rather than looking at each individual particle within the gas, one can represent them by a distribution function, which gives the number of particles (or the particle density) in six-dimensional phase space. The evolutionary path of the distribution function is described by the *Vlasov-equation* if collisions between particles are neglected. The Vlasov-equation is thus a conservation equation for the distribution function. Taking the moments of the distribution function at each time t yields the macroscopic quantities which describe the fluid. The moments of the conservation equation then give the conservation equations for the individual moments. Together with Maxwell’s equations and an equation of state, the MHD equations provide a closed system of equations, which can be used to describe the average macroscopic quantities of the fluid.

Listed below are the basic equations of (ideal) MHD in an isotropic system.

$$\begin{aligned}
\frac{\partial}{\partial t} \rho + \nabla \cdot (\rho \underline{u}) &= 0 \\
\frac{\partial}{\partial t} \rho \underline{u} + \nabla \cdot (\rho \underline{u} \otimes \underline{u}) &= -\nabla p + \underline{j} \times \underline{B} - \rho \nabla \Phi \\
\frac{\partial}{\partial t} \left(\frac{3}{2} p + \frac{1}{2} \rho |\underline{u}|^2 \right) + \\
\nabla \cdot \left\{ \left(\frac{3}{2} p + \frac{1}{2} \rho |\underline{u}|^2 \right) \underline{u} + P \underline{u} \right\} &= n \Gamma(\chi, T) - n^2 \Lambda(\chi, T) + \underline{u} \cdot (\underline{j} \times \underline{B}) - \rho \nabla \Phi \cdot \underline{u} \\
\frac{\partial}{\partial t} \underline{B} + \nabla \times (\underline{B} \times \underline{u}) &= 0 \\
\nabla \cdot \underline{B} &= 0 \\
\underline{E} &= -\frac{1}{c} \underline{u} \times \underline{B} \\
\nabla \times \underline{B} &= \frac{4\pi}{c} \underline{j} \\
\nabla^2 \Phi &= 4\pi G \rho \\
p &= (\gamma - 1) \rho \varepsilon
\end{aligned}
\tag{3.38}$$

The heat flux vector \underline{q} was neglected due to its negligible influence on the systems of interest. The equation of state relates the pressure and internal energy density, with γ being the ratio of specific heats, $\gamma = c_p/c_v$. During the course of this study, $\gamma = 5/3$ for monatomic gases. Non-ideal MHD effects like Ohmic or ambipolar diffusion introduce further terms in the momentum, energy and induction equation.

3.2 The FLASH Code

The evolution of molecular clouds can usually not be analysed by analytical approaches, because the physics is highly non-linear and too involved. In this case, numerical tools are the best way and are used extensively in order to study the temporal evolution of such complex systems. In the following chapter the FLASH³ code will be introduced and some characteristic attributes are described. A major review can be found in Fryxell et al. (2000) as well as in Dubey et al. (2008).

³<http://www.flash.uchicago.edu/site/flashcode/>

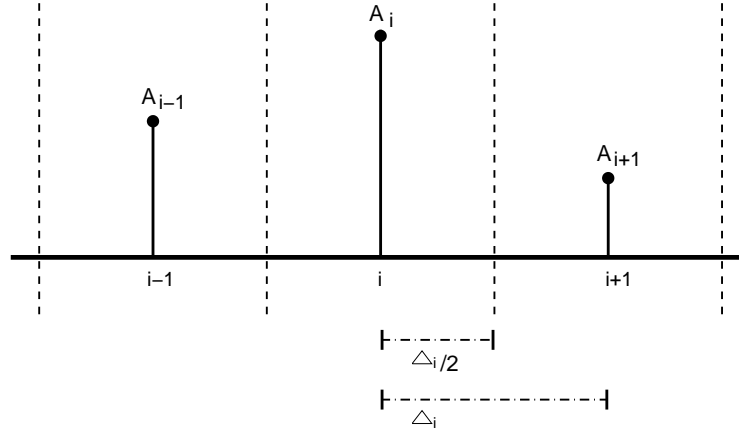


Figure 3.1: Shown is a schematic of a numerical grid in one dimension. The individual grid points are denoted by $i, i - 1$, and $i + 1$, respectively. At each grid point, the solution variable A_i has a certain value, indicated by the height of the vertical arrow. The dashed lines are the cell interfaces. The grid points are separated by Δ_i , the cell interface from the cell centre by $\Delta_i/2$.

3.2.1 Basics

The FLASH code is a multi-purpose adaptive mesh refinement (AMR, see below), Eulerian (fixed spatial coordinates) grid code (Berger and Colella, 1989). It is able to handle different physical problems by solving the respective equations (e.g. HD/MHD, relativistic HD/MHD, etc.). Since the ISM dynamics are described by the ideal MHD equations, the problem at hand is thus solving these equations in time on a numerical grid. The basic method is a *finite volume* approach, that is, a solution variable $A(x, y, z)$ is defined on the grid as

$$A(x_i, y_j, z_k) = A_{ijk} = \frac{1}{V_{ijk}} \int_{z_k - \Delta_k/2}^{z_k + \Delta_k/2} \int_{y_j - \Delta_j/2}^{y_j + \Delta_j/2} \int_{x_i - \Delta_i/2}^{x_i + \Delta_i/2} A_{ijk} dx_i dy_j dz_k. \quad (3.39)$$

Here $\Delta_{i,j,k}$ is the distance to the neighbouring data points and half the grid spacing denotes the location of the cell interfaces. Figure 3.1 depicts the numerical grid and notation for a problem in one dimension. The individual values A_i in adjacent cells represent discontinuities, where the discontinuity is located at the cell interfaces (see e.g. Toro, 2009). Thus, one can solve a Riemann problem where the solution is the flux across the cell boundaries. Here, the flux is the divergence term of a general conservation equation for some property A .

Numerical Solvers

The FLASH code is able to solve the Riemann–problem at the cell–interfaces with different methods. For the underlying studies, a robust multi–wave solver is used (Bouchut et al., 2007). This robust solver ensures positive values of density and internal energy by definition and has been implemented into FLASH by Waagan et al. (2011). The inclusion of self–gravity highlights the need for an efficient and fast Poisson–solver. FLASH provides a multigrid solver as the standard tool, but there is also a faster tree–solver implemented by R.Wünsch⁴, based on a Barnes–Hut tree.

3.2.2 Sink Particles

The momentum equation 3.9 includes the gravitational potential, Φ , which accounts for the self–gravity of the gas. If individual parcels within the simulation volume are in a state of gravitational collapse, the density continuously increases. In this case, the computation of the gravitational potential becomes very time–consuming, since the dominant physical timescale is then the free–fall timescale, t_{ff} . Resolving every single collapsing region is not possible. In addition, the numerical timestep is restricted by the Courant–Friedrichs–Levy (CFL) criterion with $\Delta t_{\text{num}} \propto \Delta x$. The smaller the grid spacing (e.g. due to refinement) the smaller the timestep.

To pass this critical issue, Bate et al. (1995) incorporated *sink particles* into their smoothed particle hydrodynamics (SPH) code to follow the collapse of individual regions for a few free–fall times without any restrictions on the timestep. In FLASH, the sink particles are modelled as Lagrangian particles, which are evolved using a Leapfrog–scheme, which is second–order accurate in time. The basic criteria which a volume of gas has to fulfill in order to be replaced by a sink particle, are as follows (a detailed description can be found in Federrath et al. (2010)):

- a) The cells within the control volume (CV) are on the highest level of refinement.
- b) The gas flow within the CV is converging (i.e. $\nabla \cdot \underline{u} < 0$). Here it is also taken care of converging motions along the three principal axes, since – as Federrath et al. (2010) caution – multiple shocks can generate $\nabla \cdot \underline{u} < 0$.
- c) The CV consists of a gravitational potential minimum.
- d) The total mass of the CV should be larger than its Jeans mass.

⁴Sadly, there is no publication on this tree–solver.

- e) The gas within the CV should be bound.
- f) The CV is not within the accretion radius of a nearby sink particle.

Sink Particles and Magnetic Flux

In ideal MHD, magnetic flux is a conserved quantity. However, as gas collapses, the magnetic field strength should increase and should stabilise that region again. Numerical simulations are subject to artificial diffusion, since they are only approximations to the exact differential equation. This numerical diffusion implies a diffusion of the magnetic field, which reduces the magnetic flux or keeps it constant at the highest level of refinement. Thus, the gas can converge to sufficiently high densities without dragging the magnetic field along.

3.2.3 Grid Refinement

The numerical grid is not being refined arbitrarily. Instead, the FLASH code uses a refinement criterion, which is based on the second spatial derivative of a variable. The second derivative is then normalised to its numerical representation, that is

$$\varepsilon \approx \left| \frac{\partial^2 f}{\partial x^2} / \left(\frac{\Delta f}{\Delta x} \right)^2 \right|. \quad (3.40)$$

If ε is smaller/larger than a given numerical value – which is chosen by the user – the grid at the given position is derefined/refined. This provides a good numerical resolution on the one hand and on the other hand this estimate is able to sufficiently capture discontinuities in the variables. Since it is dimensionless, any physical variable used by the code can be chosen as the refinement–quantity.

If a certain region is marked for refinement/derefinement, the whole cubic block of 8^3 cells is refined – in contrast to refinement of individual cells. Figure 3.2 illustrates the basic concept of the AMR technique.

The Truelove Criterion

Besides the usual refinement criteria implemented in FLASH, there is one criterion being more related to the collapse of dense cores – the Truelove–criterion (Truelove et al., 1997). The local Jeans length of a gas volume has to be resolved with at least four grid cells, $L_J = 4\Delta$, in order to

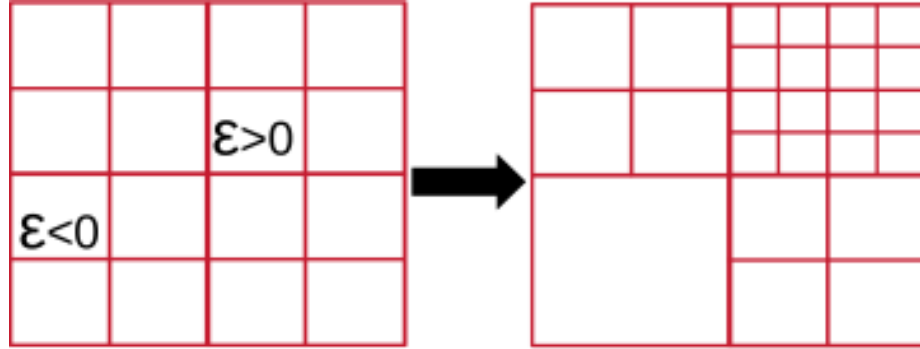


Figure 3.2: Schematic of the AMR technique. The initial grid contains two regions that are marked for refinement and derefinement. A cell is split into two smaller ones during refinement and two cells are merged when being derefined.

prevent artificial fragmentation of the gas. The latter is a result of growing numerical errors that behave like physical perturbations at insufficient numerical resolution.

3.3 Initial Conditions

This study makes extensively use of the *colliding flow approach* (Ballesteros-Paredes et al., 1999; Vázquez-Semadeni et al., 2007; Banerjee et al., 2009). The numerical realisation of this ansatz and the chosen physical parameters are discussed in the following.

The simulation volume is initially filled with WNM gas of uniform density $n = 1 \text{ cm}^{-3}$ and temperature $T = 5000 \text{ K}$. This is the corresponding thermal equilibrium temperature and the density is in the thermally unstable range (e.g. Vázquez-Semadeni et al., 2007). Since the ISM is magnetised, a homogeneous magnetic field is added, with $B_0 = 3 \mu\text{G}$ along the x -axis. Note that also higher values of the background field are taken into account. However, $B_0 = 3 \mu\text{G}$ represents the fiducial value.

The cloud forms in between two converging WNM streams, which have a cylindrical form with length $l = 112 \text{ pc}$ and radius $r = 64 \text{ pc}$ and are either aligned in a parallel or anti-parallel way to the initial magnetic field. The flows have – in most simulations – a bulk velocity of $v_0 = 11.4 \text{ km/s}$ that corresponds to an isothermal Mach number $\mathcal{M}_f = 2$. Additionally, turbulent fluctuations are overlayed with an energy spectrum $E(k) \propto k^{-2}$ representing shock-dominated turbulence (Elmegreen and Scalo, 2004; Mac Low and Klessen, 2004). The initial conditions are shown schematically in figure 3.3 and summarised in table 3.1.

Table 3.1: Summary of the parameters for the performed simulations of head-on colliding flows. When a range is given, the values denote the minimum and maximum values, but do not necessarily correspond to the minimum/maximum of other parameters.

Variable Name	Abbreviation	Unit	Value(–range)
Number Density	n	cm^{-3}	1
Mean Molecular Weight	μ_{mol}	–	1.27
Temperature	T	K	5000
Isothermal Sound Speed	c_s	km/s	5.7
Adiabatic Sound Speed	$c_{s,a}$	km/s	7.4
Magnetic Field Strength	B_0	μG	3–5
Flow Length	l	pc	112
Flow Radius	r	pc	64
Flow Mass ^a	M_{flow}	M_{\odot}	45213
Isothermal Flow Mach Number	\mathcal{M}_f	–	2–5
Isothermal RMS Mach Number	\mathcal{M}_{rms}	–	0.4–1.5
Alfvén Mach Number	\mathcal{M}_A	–	0.39–2
Plasma–Beta	$\beta = P_T/P_B$	–	0.69–1.93
Normalised Mass–To–Magnetic Flux Ratio NN ^b	$\mu/\mu_{\text{crit,NN}}$	–	0.47–0.79
Normalised Mass–To–Magnetic Flux Ratio MS ^c	$\mu/\mu_{\text{crit,MS}}$	–	0.58–0.97

Remarks:

^aThis mass refers to a single flow. The total mass of the flows is thus twice this value.

^bNormalised to the critical value calculated by [Nakano and Nakamura \(1978\)](#).

^cNormalised to the critical value estimated by [Mestel and Spitzer \(1956\)](#).

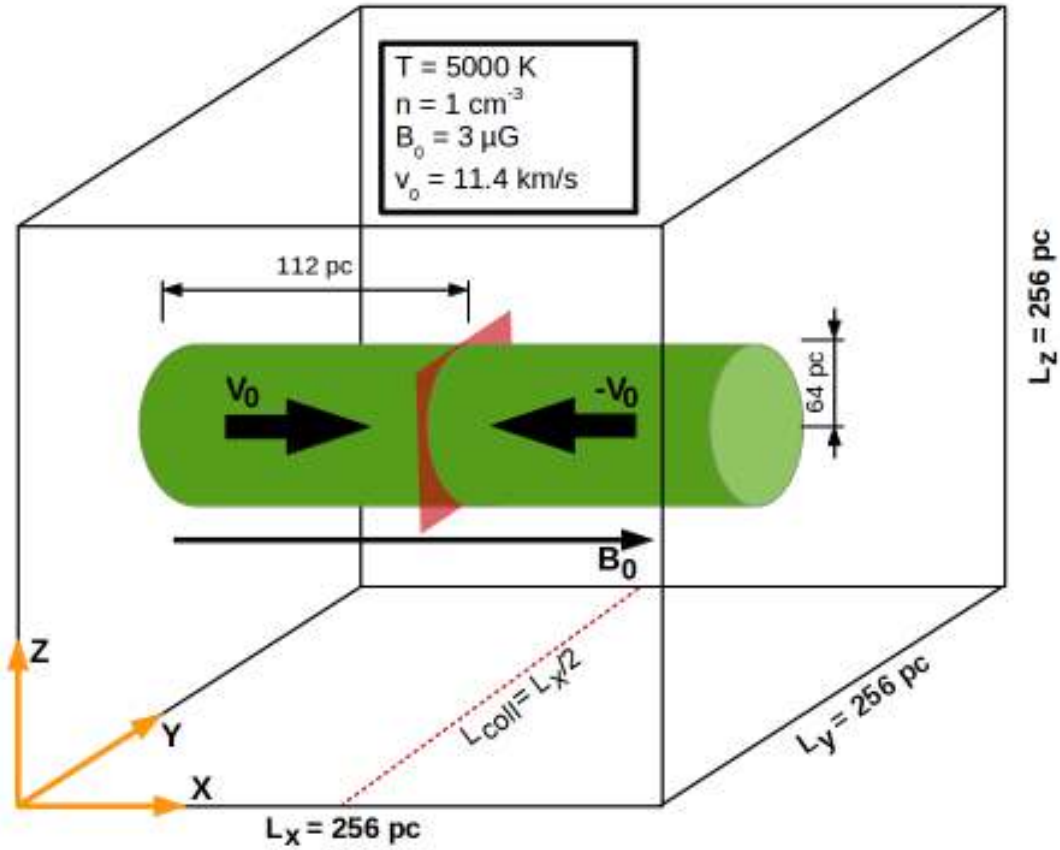


Figure 3.3: Schematic of the initial conditions for the performed colliding flow simulations. The red plane depicts the plane where the flows collide. The projection is shown as the red dashed line. For further explanation, see text.

3.4 The Supernova–Model

Feedback from high–mass stars is an essential ingredient of the lifecycle of molecular clouds, the ISM and the Galaxy as a whole. It is thus necessary to perform studies investigating the role of the different feedback mechanisms for the evolution of molecular clouds. Here, the focus is on the impact of supernova explosions and their relevance for the evolution and dynamics of molecular clouds. To get a better understanding of the feedback, the recipe how it is implemented is being discussed.

The feedback model is coupled to the sink particles. As shown in [Körtgen et al. \(2015, submitted to MNRAS, see also appendix A.2\)](#), the *total mass in sink particles* is independent of the numeri-

cal resolution. This enables a description that includes all particles formed during the runtime of the simulation. By using a [Kroupa \(2001\)](#)–IMF the number of high–mass stars in a certain mass interval can be estimated. The mass interval is somewhat arbitrary, but it is chosen in such a way that the supernova goes off in a reasonable short period of time after the sink particle has formed. Otherwise, the large scale dynamics are biased by the lack of feedback mechanisms prior to the supernova. With a minimum mass $M_{\min} = 0.01 M_{\odot}$ and a maximum mass $M_{\max} = 100 M_{\odot}$, the evaluation of the IMF reveals a total mass within the cluster or cloud of $M_c = 160 M_{\odot}$ in order to form at least one high–mass star with $M_{\text{massive}} \in [10, 30] M_{\odot}$ (see also section 2.4 on the IMF). From the mass–luminosity relation a stellar lifetime can be estimated, which yields $t_{30} \sim 2 \text{ Myr}$ for a star with $M = 30 M_{\odot}$ (see e.g. [Weigert et al., 2009](#)). The procedure can be summarised as follows:

- Check every timestep, whether the total sink particle mass exceeds M_c
- In case of $M_{\text{tot,sinks}} > M_c$ find the most massive sink particle.
- Ensure that the most massive sink particle fulfills:
 - a) $M_{\text{sink}} \geq 30 M_{\odot}$ and
 - b) $t_{\text{sink}} \geq 2 \text{ Myr}$.
- If the above criteria are matched, then inject $E_{\text{SN}} = 10^{51} \text{ erg}$ of energy with 65 % as thermal and 35 % as kinetic energy in the control volume.
- Deactivate the sink particle, that is, stop accretion and further feedback (in case the particle still has $M_{\text{sink}} \geq 30 M_{\odot}$).

A brief note on numerical issues with radiative cooling

The gas is still subject to radiative cooling. Thus, the choice of the of the control volume, wherein energy is injected is not arbitrary or the size should at least be chosen carefully. If, however, the sound crossing time within the volume is larger than the cooling time, one can switch off the cooling (e.g. [Colín et al., 2010](#)). This ensures that the shock wave can travel unimpeded within

the control volume. For the course of this study, radiative cooling is never turned off since the cooling time is $\tau_{\text{cool}} \approx 6\tau_{\text{dyn}}$ and the overall timestep right after the supernova is small enough (a few tens of years) to ensure a sufficient temporal resolution.

3.5 Chapter Summary

The finite volume, AMR code FLASH is used for numerical simulation of the evolution of molecular clouds by convergence of two streams of the WNM. The flows are moderately supersonic, magnetically sub- to supercritical as well as mildly or moderately turbulent. The turbulent fluctuations are injected according to a Burgers type energy spectrum. The initial magnetic field strength is varied in order to represent different ISM conditions. The forming sink particles are free to accrete gas from the molecular cloud. Once a sink particle is massive enough it can go off as a supernova. Supernova feedback is implemented according to a Sedov–Taylor solution.

4

Impact of Magnetic Fields on the Formation and Evolution of Molecular Clouds

Magnetic fields are an important ingredient in the ISM. Their importance for the formation of clouds and stars is still strongly debated (e.g. [Padoan et al., 1999](#); [Mac Low and Klessen, 2004](#); [Li et al., 2014](#)). In the following chapter, I will discuss the impact of different magnetic field strengths in the ISM on the formation of molecular clouds by the convergence of two WNM streams. The results and critical discussion presented in this chapter were published in parts in [Körtgen and Banerjee \(2015\)](#), *MNRAS*, 451, 3340.

My Contribution

The publication is a multi-authored work. I will give a brief statement on my contribution to this work. I am the first author. I have performed all simulations and generated the setup for the inclined WNM flows. I did the post-processing analysis of the data as well as their interpretation. I wrote the text for the publication. However, discussions with and new thoughts by my

co–author have increased the quality of the paper and lead to new figures in the paper, which supported the interpretation very well.

4.1 Introduction

Stars and stellar systems form within the densest regions of molecular clouds, in gravitationally unstable cores which reside at the junctions of filaments (e.g. André et al., 2014a,b, but see also section 2.3.5). Prior to gravitational collapse the build–up of filaments and the respective sub-structures is primarily controlled by magnetic fields and supersonic turbulence (e.g., Shu et al., 1987; Mac Low and Klessen, 2004; Crutcher et al., 2010). But, the importance of magnetic fields for star formation is still debated (see e.g., Li et al., 2014; Padoan et al., 2014, see e.g section 2.1.3). On the one hand, the idea of supersonic turbulence controlling the star formation process assumes less important magnetic fields and thus primarily supercritical states. In such a scenario, the magnetic field lines are dragged along with the flow and density enhancements will collapse as soon as they become Jeans unstable. Furthermore, the turbulence is then not only supersonic but also *superalfvénic* (e.g., Padoan et al., 1999; Padoan and Nordlund, 1999). This leads to highly twisted field lines and the resulting molecular clouds and clumps will not be coherent entities. The morphology instead will be influenced by the statistics/nature of the turbulence.

To remind the reader, Mestel and Spitzer (1956) first quantified the influence of magnetic fields on star formation by introducing the mass–to–magnetic flux ratio $\mu \equiv M/\Phi$. Usually, this quantity is normalised to its critical value $\mu_c \simeq 0.13/\sqrt{G}$ (or $\mu_c \simeq 0.16/\sqrt{G}$ for more sheet–like clouds (Nakano and Nakamura, 1978)). If the magnetic field is strong enough, accretion onto the cloud complex is mediated by the Lorentz force and mainly parallel to the field lines (e.g. Kudoh et al., 2007; Inoue and Inutsuka, 2008; Kudoh and Basu, 2011; Hennebelle, 2013). In the cloud interior, strong fields stabilise the filaments and clumps against gravity. This also results in a reduced fragmentation efficiency.

Observationally, it has been shown in recent years that the magnetic field is indeed crucial for the star formation process (e.g., Beck, 2001; Crutcher et al., 2010; Li et al., 2010; Crutcher, 2012; Li et al., 2014; Pillai et al., 2015, but see also discussion in section 2.1.3). Li et al. (2010) used sub–mm polarisation measurements to retrieve the morphology of the magnetic field in molecular clouds and Galactic spiral arms. The authors have shown that the overall morphology of the field does not change significantly from the large scales down to the inner parts of molecular clouds. Nearby molecular clouds and cloud cores can be separated into two regimes according to their column

density and magnetic field strength. The low column density regime coincides with magnetically subcritical HI clouds. As was pointed out by Crutcher (2012, and references therein), these data are primarily diffuse HI clouds that are *not self-gravitating*, but are rather in pressure equilibrium with their surroundings.

At higher column densities the field strength increases close to linear with increasing column density. At this stage, almost all measurements indicate (super-)criticality by a factor of $\sim 2 - 3$ (e.g. Crutcher, 2012).

Numerically, the issue of magnetic fields and their relevance for molecular cloud formation has been investigated by many authors (e.g., Inoue and Inutsuka, 2008; Price and Bate, 2008, 2009; Kudoh and Basu, 2011; Vázquez-Semadeni et al., 2011; Inoue and Inutsuka, 2012; Chen and Ostriker, 2014). Most of them concentrated on the initial stages of the formation process. Already at this early temporal stage, the magnetic field was shown to be crucial. Price and Bate (2008) conducted smoothed particle hydrodynamics simulations of a $50 M_{\odot}$ molecular cloud of radius $R = 0.375$ pc including magnetic fields of different strength (parameterised by critical mass-to-flux ratios of ∞ , 20, 10, 5, and 3). They found that strong fields tend to suppress fragmentation on the one hand and the formation of stars on the other hand. However, as they point out, strong fields generate voids within the molecular cloud, which are magnetically supported with plasma- $\beta > 1$. In addition, on very small scales, magnetic tension is able to prevent multiple fragments from merging, thus *promoting* fragmentation.

More consistent with the results presented in this chapter is the work by Heitsch et al. (2009). They have used MHD simulations of converging flows to analyse the impact of magnetic field strength and orientation on the formation of (molecular) clouds. Specifically, they looked at the extreme cases of the magnetic field being either aligned with or perpendicular to the flow direction. The flows were driven continuously due to the choice of inflow boundary conditions. Hence, the mass-to-flux ratio in their study would approach infinity in the limit of infinite timescales. Note that the authors have not included self-gravity in their simulations. Thus, every overdense substructure is pressure confined. However, they identify filaments and clumps that form due to turbulent compression, with clouds becoming more filamentary if magnetic fields are included. But, it is the alignment of the magnetic and (initial) velocity field that controls the formation of dense structures. As the authors point out, clouds are able to condense out of the WNM, if the fields are aligned. In case the magnetic field is perpendicular to the inflows, magnetic pressure suppresses the formation of dense structures, which could be termed molecular. However, there exist regions, which merge to form a filamentary network of *diffuse* gas.

Inoue and Inutsuka (2009) studied the evolution of the shocked slab between two converging flows in the ISM by means of two-fluid MHD simulations in a $30 \text{ pc} \times 10 \text{ pc}$ box. The authors varied the angle between the mean magnetic field and the flows. From analytical estimates they found a critical velocity, which depends on the magnetic field strength and the mentioned angle. If the flow velocity is larger than the critical velocity only HI clouds are able to form because of dominating magnetic pressure. If it is less than the critical velocity, dense molecular clouds condense out of the WNM within the shocked slab. As the authors also point out, the dependence on the angle is crucial for the evolution of the gas within the slab, since the critical velocity goes to zero for angles approaching 90° .

Most recently, Chen and Ostriker (2014) studied the formation of prestellar cores due to the convergence of gas flows within molecular clouds. In detail, their simulation box was about 1 pc , representing a collapsing molecular clump. In order to analyse the core formation process, they used ideal MHD as well as non-ideal MHD via ambipolar diffusion (AD). In all of their models core formation was initiated by the collision of gas streams along the background magnetic field. With AD only the later stages were seen to differ from the ideal MHD models, since the density regimes where AD is becoming efficient are build up via accumulation of gas by colliding flows. The mass-to-flux ratio of the cores formed in their simulations is in the range $\mu/\mu_c \sim 0.5 - 7.5$ with a median value of $\mu/\mu_c \approx 3$. Thus, most of the cores are supercritical¹.

However, it is important to conduct large scale simulations in order to take into account the whole evolutionary track of the gas from the diffuse ISM to the dense cores. This was achieved by Vázquez-Semadeni et al. (2011), who analysed molecular cloud formation subject to magnetic fields of different initial strength. It has been shown that stronger fields tend to delay the onset of star formation. As indicated in section 2.2.2 (see also Hartmann et al., 2001; Vázquez-Semadeni et al., 2006, 2007) the diffuse gas becomes molecular, self-gravitating *and* magnetically supercritical *at the same time*. This can explain the subcriticality of the diffuse HI clouds shown in Crutcher et al. (2010); Crutcher (2012). Heitsch and Hartmann (2014) mention that the supercritical state can be reached via gas accretion along the magnetic field lines. But as was stated by Hartmann et al. (2001), the accumulation length to become magnetically supercritical is

$$L_c \approx 470 \left(\frac{B_0}{5 \mu\text{G}} \right) \left(\frac{n}{1 \text{ cm}^{-3}} \right)^{-1} \text{ pc}. \quad (4.1)$$

¹Note that the authors use inflow boundary conditions for the two converging flows. Hence, the mass-to-flux ratio of the simulation domain will grow with time and so it will for the cores as they accrete mass from an practically infinite mass reservoir.

Vázquez-Semadeni et al. (2011) argue that, since the magnetic field lines in the Galactic plane describe closed circles, this length scale is easily overcome. This also indicates that the mass-to-flux ratios are lower limits and the data points shown in Crutcher et al. (2010) are only a temporal stage of subcriticality. But, as Carroll-Nellenback et al. (2014) point out, flow lengths of $L > 500$ pc are too large in order to sustain a large scale coherent flow. Bulk motions of this order of magnitude should rather fragment due to supersonic turbulence and thus diminish. Hence, the build-up of supercritical clouds would be delayed or even suppressed completely. The process, how molecular clouds achieve the transition from sub- to supercritical states is thus still an open question. In this chapter we tie in with the work of Vázquez-Semadeni et al. (2011) by determining molecular cloud formation under different initial conditions. The numerical model and the initial conditions have already been introduced in section 3.3. Section 4.2 deals with the formation and evolution of clouds formed by head-on converging WNM streams under varying initial conditions. The following section 4.3 then introduces the tilt of one flow with respect to the magnetic field and discusses in detail the evolution of the clouds and their subsequent star formation activity. This chapter is closed with a brief summary in section 4.4, where we also discuss the role of ambipolar diffusion.

4.2 Molecular Cloud Formation by Head-On Colliding Flows

Colliding streams of gas are ubiquitous in the ISM (e.g. due colliding supernovae shells, Inoue and Inutsuka, 2008) as well as in the interior of molecular clouds (e.g. in filaments or the junctions of filaments, Hennebelle et al., 2008; Chen and Ostriker, 2014). Therefore the dynamics and the structure can vary significantly, depending on the galactic or local environment or the respective driving mechanism (e.g. Inoue and Inutsuka, 2008, 2012). In this section we summarise the evolution of molecular clouds, which are being formed by head-on colliding flows. For more thorough analyses, we refer the reader to section 2.2.2 and to the studies of e.g. Banerjee et al. (2009); Vázquez-Semadeni et al. (2006); Vázquez-Semadeni et al. (2011); Hennebelle and Pérault (1999); Hennebelle et al. (2008); Heitsch et al. (2008a). An overview of the main initial physical parameters of the respective simulations is given in table 4.1.

4.2.1 Varying the Turbulent Velocity

The dynamics of molecular clouds which formed in the compression zone of two colliding streams strongly depend on the initial kinematics of the individual flows. On the one hand, the

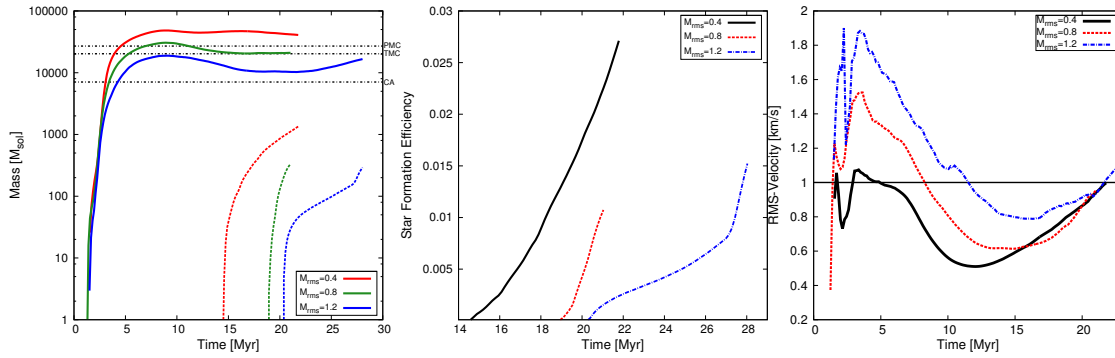


Figure 4.1: *Left:* Evolution of cloud (solid) and sink particle (dashed) masses for three turbulent velocity fields. The onset of star formation is clearly seen to be delayed due to the action of turbulent motions that keep dissolving dense structures. The horizontal dash-dotted, black lines denote the masses of observed molecular clouds, like the Perseus MC (PMC, Lombardi et al., 2010), the Taurus MC (TMC, Lombardi et al., 2010), and the Corona Australis complex (CA, Alves et al., 2014). *Middle:* Star formation efficiency for B3M . . . I . . . runs (see table 4.1). *Right:* Corresponding root mean square velocity of the dense gas. The RMS-velocities converge after turbulence has decayed and global collapse of the cloud has begun. Before this point, the amplitude of the resulting turbulent velocities is determined by the initial conditions.

flows are supersonic with respect to the WNM and thus generate strong shocks and compressions (Vázquez-Semadeni et al., 2007; Banerjee et al., 2009). On the other hand, large scale instabilities as well as stellar feedback inject energy into the ambient ISM. This energy, if not already in the form of kinetic energy, can be converted to kinetic energy and thus a turbulent regime is produced, where the turbulence cascades down until it is dissipated on atomic/molecular scales. This turbulence is primarily supersonic (e.g., Mac Low and Klessen, 2004). These random motions generate a certain level of anisotropy within the bulk flows and the respective contribution to the process of molecular cloud formation is two-folded. Firstly, turbulence contributes an effective ram pressure, which can help to stronger compress fluid elements. Secondly, the inhomogeneous velocity field distorts the overall bulk flow and reduces the mass flux, which then directly translates to the build up of less massive clouds (see figure 4.1).

If the collision of the WNM streams is along the magnetic field lines, the early stages ($t \leq 3$ Myr) of cloud formation can be understood as being nearly independent of the magnetic field. The first phases during the collision are thus controlled by the bulk and turbulent velocity (see table 4.1). Figure 4.1 shows the evolution of the dense gas ($n \geq 100 \text{ cm}^{-3}$) for different initial turbulent Mach numbers. The compression by the flows induces the formation of a molecular cloud by the combined action of dynamical and thermal instability (e.g., Vázquez-Semadeni et al., 2007; Heitsch et al., 2008a; Banerjee et al., 2009). Due to the onset of runaway cooling of thermally unstable gas, the cloud becomes more massive with time. At the same time it assembles mass by

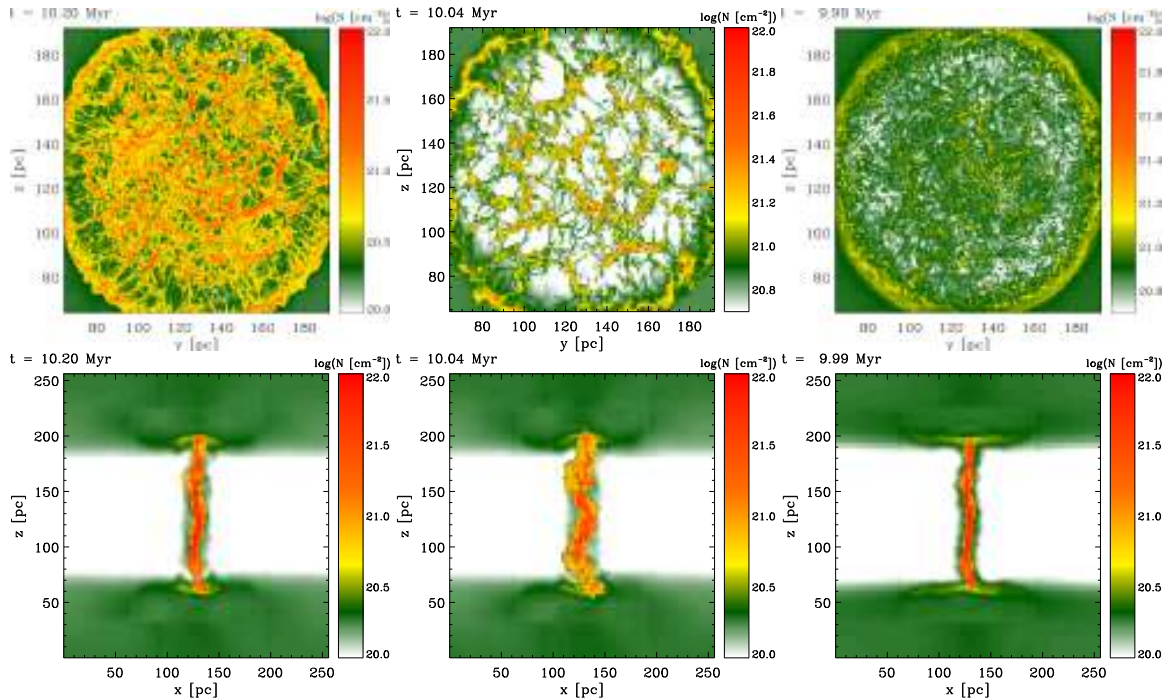


Figure 4.2: *Top:* Column density along the direction of the background magnetic field (x -direction) at a time $t \approx 10$ Myr. In this case, the flows have collided head-on. *Bottom:* Column density in the plane perpendicular to the background magnetic field. *Left to right:* Runs B3M0.410, B3M0.810, and B5M0.510. The effect of turbulence in shaping the molecular cloud is evident. Stronger magnetic fields tend to smoothen the density field and clearly defined filaments are hardly seen.

accretion of gas along the field lines. Independent of the degree of turbulence, the onset of dense gas formation starts at the same time indicating the dominance of the ram pressure by the bulk flows. Only at slightly later times around $t \approx 2 - 3$ Myr the effects of different turbulent Mach numbers are seen. Flows of higher turbulent Mach numbers reduce the mass flux and hence reduce the final mass of the cloud. This is seen in figure 4.2. The stronger the turbulence, the less compact is the resulting cloud. The mass concentrates in pressure confined filaments, which are further immersed in a diffuse, warm medium, with a steep density and temperature gradient between the WNM and CNM that can be interpreted as a phase-transition front rather than a contact discontinuity due to the ambient mass flux across the transition layer (Banerjee et al., 2009).

At later stages, the initial turbulence has decayed and the presence of turbulent motions is due to self-gravity (see e.g. Ballesteros-Paredes et al., 2007). Once self-gravity dominates, certain regions then proceed to collapse to form a star. The onset of star formation is clearly delayed by the presence of stronger initial turbulence (see figure 4.1).

4.2.2 Dependence on the Magnetic Field Strength

In the previous section we have neglected the possible influence of the magnetic field. However, the magnetic field affects the overall evolution of molecular clouds in the ISM as well as their preceding condensation out of the latter (e.g., [Hennebelle and Pérault, 1999](#); [Hennebelle, 2013](#)). As a reminder, as was shown by [Crutcher et al. \(2010\)](#) using Zeeman measurements, the *line-of-sight* component of the interstellar magnetic field can be approximated by an interval of nearly constant magnitude followed by a regime that consists of a linear increase of the field strength as function of (column-)density. Since Zeeman splitting provides information of one component only, the total magnetic field strength will be larger. It is thus reasonable to investigate the influence of varying magnetic field strength on the molecular cloud formation process. This has recently been done by [Vázquez-Semadeni et al. \(2011\)](#) for initial magnetic field strengths of $|\underline{B}| = \{2, 3, 4\} \mu\text{G}$ (corresponding to $\mu = \{1.18, 0.79, 0.59\}^2$) and the action of ambipolar diffusion. Our study covers the upper range of their values, namely the range of $|\underline{B}| = \{3, 4, 5\} \mu\text{G}$. The choice of these field strengths gives thermally dominated ($|\underline{B}| = 3 \mu\text{G}$) environments, regimes with an equipartition of thermal and magnetic energies ($|\underline{B}| = 4 \mu\text{G}$), and completely magnetically dominated regions ($|\underline{B}| = 5 \mu\text{G}$). The evolution of the cloud and sink particle mass for different initial field strengths is shown in figure 4.3. Here, the final cloud masses do not differ too much from each other, showing that the initial turbulent motions are more efficient in controlling the early phases of gas accumulation. But differences are seen in the early mass accretion. The cloud, which is embedded in a strong magnetic field is seen to be build up at a slightly earlier time after the start of the simulation. Furthermore the accretion of matter from the diffuse halo surrounding the cloud at early times differs for the strongest initial magnetic field. This fact can be explained by momentum and energy conservation. Since the flows collide head-on, the gas is compressed in the collision layer. The external ram pressure by the flows forces the gas to move perpendicular to the magnetic field lines in order to ensure conservation of linear momentum. At the same time gas compression enhances the magnetic field strength. Magnetic tension then acts as a restoring force and since the plasma- β is less than unity, the dominant magnetic field is too stiff to be bend efficiently. This results in a less efficient gas motion perpendicular to the original bulk flow motion and an earlier compression of the gas. Thus, efficient accretion happens only along the field lines. The rightmost plot in figure 4.2 shows the column density after $t \approx 10 \text{ Myr}$

²Note, the values for the mass-to-flux ratio in [Vázquez-Semadeni et al. \(2011\)](#) refer to the box length of 256 pc, instead of the flow length of 112 pc, which we here take care of.

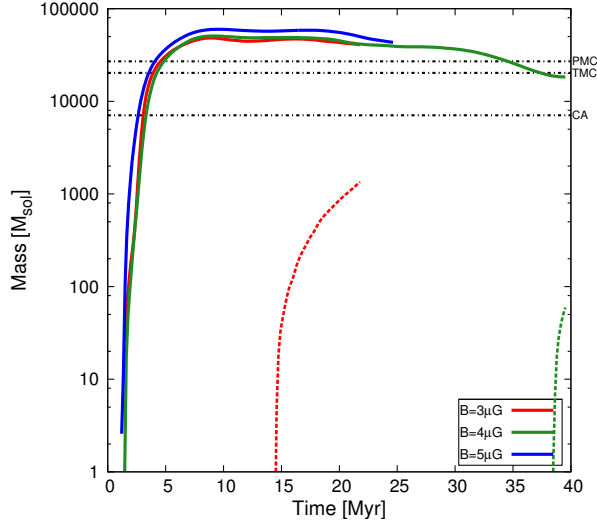


Figure 4.3: Evolution of cloud (solid) and sink particle (dashed) masses for three magnetic field strengths. The clouds assemble similar final masses, but some slight differences in the accretion phase are seen. More prominent is the lack/delay of star formation for simulations with $|B| > 3 \mu\text{G}$. The horizontal dash-dotted, black lines denote the masses of observed molecular clouds, like the Perseus MC (PMC, Lombardi et al., 2010), the Taurus MC (TMC, Lombardi et al., 2010), and the Corona Australis complex (CA, Alves et al., 2014).

for a strong magnetic field. The density gradients are smoother in comparison to the weaker field and the cloud is more compact, i.e. no clearly defined filaments condense out. At the same time the column density (in the face-on view) does not reach sufficiently large values.

The critical column density to become magnetically supercritical can be written as (see section 2.2.2, but also Vázquez-Semadeni et al., 2011)

$$N_{\text{crit}} \approx 2.92 \times 10^{20} \left(\frac{B}{1 \mu\text{G}} \right) \text{cm}^{-2}. \quad (4.2)$$

Although all different clouds assemble mass by accretion from the surrounding diffuse gas, the most striking difference is the complete lack of star formation for the higher magnetised clouds.

In order to quantify the gas dynamics at a specific evolutionary stage, figure 4.4 shows the probability distribution function of the column density (left, hereafter N-PDF) and the mass-to-flux ratio (right, from now on μ -PDF). As shown by Vázquez-Semadeni and Passot (2000), the statistics of a gas can be analysed by using a density PDF. For isothermal turbulence, this PDF develops a lognormal distribution with its variance depending on the Mach number of the gas. More recently it has been demonstrated that the width of the distribution also depends on the plasma- β as well as on the turbulent forcing parameter, i.e. if the driving of turbulence is purely

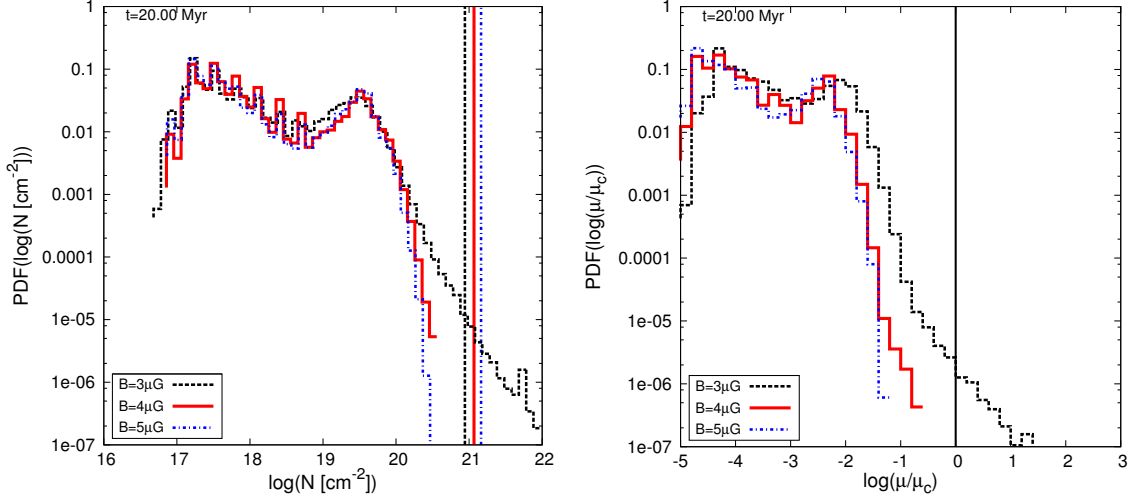


Figure 4.4: *Left:* Column density PDF for different initial magnetisations at 20 Myr. The weaker magnetic field allows for the development of a power-law tail, which indicates gravitational collapse. The vertical lines denote the respective threshold column densities for magnetic criticality after equation 4.2. *Right:* Corresponding μ -PDF. Here, the vertical line indicates the critical ratio.

solenoidal or compressive (see e.g., Federrath and Klessen, 2012, 2013). The same is also valid for the N-PDF, which is used in observational studies since the volume density is not accessible (e.g., Kainulainen et al., 2011; Schneider et al., 2013, 2015). The shape of the N-PDFs in figure 4.4 is not lognormal. The reason is the multi-phase nature of the ISM.

However, in the weaker magnetised case, a power-law tail at high column densities evolves, which is always seen in self-gravitating systems (Federrath and Klessen, 2013; Schneider et al., 2013), indicating the presence of gravitationally unstable regions. The vertical lines denote the threshold column densities according to equation 4.2. The thermally dominated case shows a transition to supercritical states, whereas the maximum column density in the magnetically dominated gas is approximately a factor of five lower. At this time the WNM flows vanished. Increases in column density are only due to mass accretion from the environment.

Since the column density and the mass-to-flux ratio are coupled via

$$\mu \approx \frac{\Sigma}{|B_{\text{LOS}}|}, \quad (4.3)$$

where Σ is the column density in g/cm^2 (Nakano and Nakamura, 1978), the overall shape of the μ -PDF should be very similar to the one of the N-PDF. This is indeed the case, as can be seen from figure 4.4, right. The modifications are due to the additional dependence on the magnetic

field. Here, again, the mass-to-flux ratio shows a similar distribution, but for the weaker field it is shifted towards higher values. Furthermore, the transition from subcritical to trans-critical regions is smoother, because of the lack of stiffness of the magnetic field. The dependence on column density then also implies the outcome of a power-law tail in the distribution, which continues up to values of $\log(\mu/\mu_c) \approx 1$, showing the presence of highly unstable, dynamically dominated regions. The mass-to-flux ratio for runs B₄Mo_{0.4}Io and B₅Mo_{0.5}Io is similar distributed. This indicates that initial dynamical processes should be more energetic than observed in the simulations, since dynamic compressions always result in increasing magnetic energy, which at some stage starts to dominate over thermal and gravitational energy. This yields a re-expansion of compressed regions and a simultaneous stabilisation of these.

The results from simulations with higher magnetisation now raise the question, how stars can form in such highly magnetised media.

4.3 Inclined WNM flows

Here we probe the influence of inclined colliding flows. Inclined collisions are easily justified by assuming the emergence of a supernova shock wave and its propagation through a Galactic spiral arm or by non-uniform large scale gravitational forces. The motion of the flow at an inclination with respect to the magnetic field results in an enhanced diffusivity of the latter and this process thus can be thought of as a non-ideal MHD process (e.g. [Heitsch et al., 2005](#); [Inoue and Inutsuka, 2008](#); [Heitsch et al., 2009](#), see also appendix A.1).

4.3.1 The Setup

The initial geometry can be seen in figure 4.5. The basics are the same as for the head-on case, but now one flow is inclined at an angle φ with respect to the x -axis. The initial background magnetic field is kept constant and aligned with the x -axis. The figure may imply that there might be a region where quiescent gas resides, but this is not the fact. The two flows still collide in the centre of the simulation box and since the magnetic field is still uniform, the collision will induce a normal shock. Table 4.1 lists the initial parameters for this study.

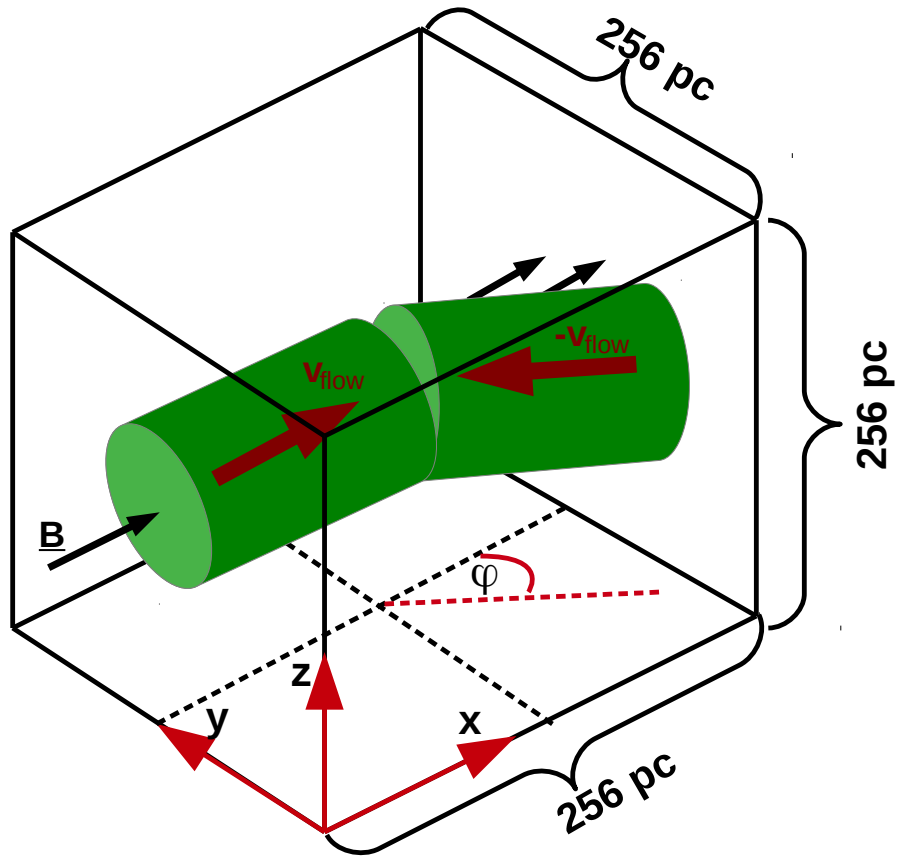


Figure 4.5: Setup of the initial conditions with inclined flow. The box and physical parameters are the same as in figure 3.3, but now one flow is inclined at an angle φ with respect to the background magnetic field. The inclined axis is shown as the red dashed line. Note, the collision still occurs at the centre of the simulation domain, in contrast to what is schematically shown here.

Table 4.1: Overview of the conducted simulations with varying flow and magnetic field parameters. ϕ is the inclination of one of the flows and \mathcal{M}_f is the isothermal Mach number of the converging WNM streams. \mathcal{M}_{RMS} denotes the Mach number of the turbulent fluctuations, \mathcal{M}_A is the turbulent Alfvén Mach number, β is the ratio of thermal to magnetic pressure and κ^* indicates the ratio of turbulent to numerical diffusion with the turbulent diffusion coefficient calculated according to [Lazarian et al. \(2012\)](#) (their equations (3) and (4)). Numerical diffusion is evaluated as $\kappa_{\text{num}} = \Delta x \times v_{\Delta x}$, where $v_{\Delta x}$ is the velocity at grid scale Δx . χ denotes the effective ratio of magnetic to numerical diffusion (see appendix A.1). μ/μ_{crit} is the normalised mass-to-magnetic flux ratio.

Run Name	ϕ	$ \underline{B} $	\mathcal{M}_f	\mathcal{M}_{RMS}	\mathcal{M}_A	κ^*	χ	β	μ/μ_{crit}^a	Min. Δx^b
	($^\circ$)	(μG)								(pc)
B ₃ Mo.4Io	0	3	2	0.4	0.39	2.53	0.00	1.93	0.79	0.03
B ₃ Mo.8Io	0	3	2	0.8	0.79	21.04	0.00	1.93	0.79	0.03
B ₃ MI.2Io	0	3	2	1.2	1.18	42.67	0.00	1.93	0.79	0.03
B ₄ Mo.4Io	0	4	2	0.4	0.29	1.04	0.00	1.08	0.59	0.03
B ₄ MI.5Io	0	4	2	1.5	1.10	42.67	0.00	1.08	0.59	0.03
B ₅ Mo.5Io	0	5	2	0.5	0.29	1.04	0.00	0.69	0.47	0.0075
B ₃ Mo.5I30	30	3	2	0.5	0.49	5.02	6.91	1.93	0.79	0.0075
B ₃ Mo.5I50	50	3	2	0.5	0.49	5.02	16.22	1.93	0.79	0.0075
B ₃ Mo.5I50a	50 ^{c)}	3	2	0.5	0.49	5.02	16.22	1.93	0.79	0.0075
B ₃ Mo.5I60	60	3	2	0.5	0.49	5.02	20.73	1.93	0.79	0.0075
B ₃ Mo.8I60	60	3	2	0.8	0.49	5.02	20.73	1.93	0.79	0.0075
B ₄ Mo.5I30	30	4	2	0.5	0.36	1.99	9.22	1.08	0.59	0.0075
B ₄ Mo.5I60	60	4	2	0.5	0.36	1.99	27.63	1.08	0.59	0.0075
B ₅ Mo.5I30	30	5	2	0.5	0.29	1.04	11.52	0.69	0.47	0.0075
B ₅ Mo.8I30	30	5	2	0.8	0.47	4.43	11.52	0.69	0.47	0.0075
B ₅ Mo.5I40	40	5	2	0.5	0.29	1.04	19.03	0.69	0.47	0.0075
B ₅ Mo.5I50	50	5	2	0.5	0.29	1.04	27.03	0.69	0.47	0.0075
B ₅ Mo.5I60	60	5	2	0.5	0.29	1.04	34.55	0.69	0.47	0.0075
B ₅ Mo.8I60	60	5	2	0.8	0.47	4.43	34.55	0.69	0.47	0.0075
B ₅ Mo.5I60Mf ₄	60	5	4	0.5	0.29	1.04	34.55	0.69	0.47	0.0075
B ₅ Mo.5I60AD ^{d)}	60	5	2	0.5	0.29	1.04	34.55	0.69	0.47	0.0075

Remarks:

a) According to the prescription by [Nakano and Nakamura \(1978\)](#) (i.e. $\mu_{\text{crit}} \simeq 0.16/\sqrt{G}$).

b) Maximum allowed resolution in the simulations.

c) Simulation with a different initial turbulent seed field.

d) Run with ambipolar diffusion. Simulation was stopped at $t \approx 12$ Myr.

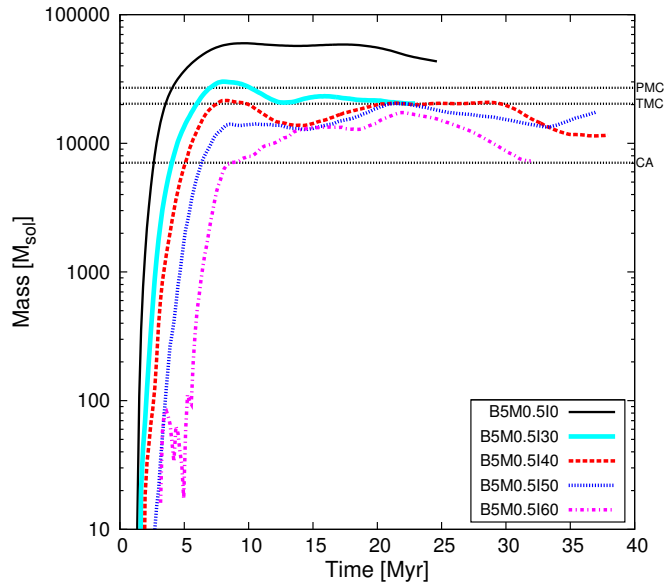


Figure 4.6: Temporal evolution of mass for runs B5M0.5I. . . . The horizontal black, dash-dotted lines have the usual meaning.

4.3.2 Magnetic Flux Reduction and Star Formation

We commence with the thermally dominated case, i.e. $|\underline{B}_0| = 3 \mu\text{G}$. The diffusivity increases with increasing inclination of the flow (see table 4.1 and appendix A.1). Figure 4.1 has already shown the evolution of the cloud mass as function of time. The mass crucially depends on the strength of the initial turbulent velocity fluctuations. In addition, if one applies an inclined flow, shearing motions and magnetic effects have to be taken into account. The magnetic field is able to slow down the inclined flow so that the collision will end soon and no gas is driven into the thermally unstable regime. But the final masses of the formed clouds are very similar, only varying by a factor of a few (see figure 4.6). This indicates that at later times, the information of the initial conditions is completely lost.

More interesting is the *way how the cloud evolves*. For small inclinations ($\varphi \leq 30^\circ$), no significant distortions occur and the mass accumulation and the final mass are comparable to cloud masses formed by purely head-on collisions (within factors of 2-3). The inclined flow is aligned with the magnetic field very fast. For highly inclined streams the condensation from the WNM to the CNM sets in later due to the above mentioned processes. At the same time, mass growth is stopped and a short phase of *mass loss* is evident as a direct consequence of strong shearing motions (see figure 4.6). But as soon as the strongest unstable fronts have vanished, the cloud turns back to a stabilised state with continuous accretion of matter. Figure 4.7 shows the resulting

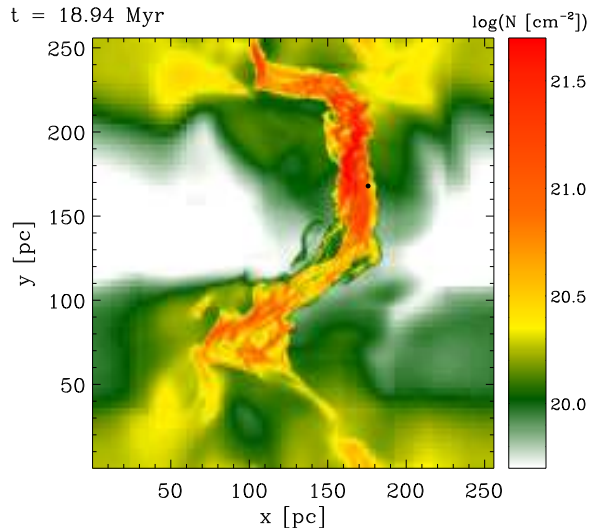


Figure 4.7: Column density map for run B3M0.5I50. The total integration length is 60 pc. The resulting global cloud structure is due to the initial compression by the flows.

molecular cloud structure for run B₃M_{0.5}I₅₀ (i.e. $B_0 = 3 \mu\text{G}$, $M_{\text{rms}} = 0.5$, $\Phi = 50^\circ$). Shown is the column density along the z -axis, that is, perpendicular to the background magnetic field. The black dot resembles a sink particle. The global morphology of the cloud is mainly influenced by the geometry of the colliding WNM streams with additional impact by the misalignment of the flow. It resembles a sheet-like shape with trailing arms with the one at the near side of the tilted flow being more elongated. This elongation is due to the later collision of the flows when the bulk of the mass has already been compressed. The resultant motion of the cloud yields that the still streaming gas interacts with the outer edges of the compressed gas by ‘pushing’ it away from the actual molecular cloud complex, thereby forming this observed elongated structure. At this time the flow is already too slow to significantly compress the gas, implying that the gas in the trailing arm is not able to sufficiently cool down by thermal instability. It is therefore not able to become gravitationally unstable. These shear flows and the resulting occurrence of trailing arms are possibly seen in observations of e.g. the Taurus molecular cloud, i.e. the non-star forming low column density arm (Alves et al., 2014).

In contrast to the evolution of the total mass of the molecular cloud, the evolution of the stellar (sink particle) mass is greatly influenced by inclining one flow. The most obvious indication is the delay of star formation with increasing misalignment (see figure 4.8). Due to the misalignment, magnetic pressure and magnetic tension act as opposing agent against gravity. In addition, the shear flows disrupt density enhancements and thus the transition from the WNM to dense,

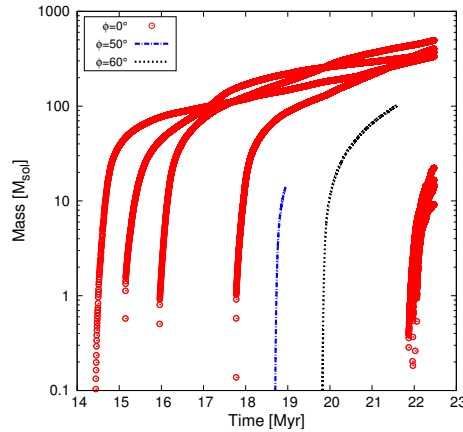


Figure 4.8: Evolution of individual sink particle masses for three inclinations of runs B3M. . . . The higher the inclination, the later star formation begins. In addition, the star formation rate and efficiency are strongly influenced (see also figure 4.1).

cold structures is hampered. Once, the turbulence has fully vanished, the cloud is still subject to its fast bulk motion. Clumps within the complex can only grow by accretion of matter from the immediate environment, because of the lack of turbulent compression, which could provide the seeds for gravitational unstable cores. The shear due to the misalignment also yields a less compact cloud. The material is not fully compressed by the two flows. Instead, a great amount is at first compressed and enters a phase of oscillating motions and dispersion due to shearing motions. The accumulation of enough Jeans masses to render the gas gravitationally unstable is delayed and also very inefficient, since the denser regions are greatly scattered and do not possess enough mass.

As can be seen from figure 4.7, there is at least one sink particle, indicating ongoing star formation. We stopped the simulation here, because star formation proceeds from there on (as can be seen e.g. from run B₃Mo.4Io).

4.3.3 Comparing Cloud Dynamics in Magnetically Differing Environments

Figure 4.9 shows the column density in the direction perpendicular to the background magnetic field for three initial magnetic field strengths ($|\underline{B}| = 3 \mu\text{G}$, $|\underline{B}| = 4 \mu\text{G}$, and $|\underline{B}| = 5 \mu\text{G}$) with an initial tilt of $\varphi = 60^\circ$. The weakest field case shows a strong distortion of magnetic field lines as well as the onset of star formation. In comparison, the stronger fields show a more ordered magnetic field, which shows no clear deviation from its initial uniform alignment. For $|\underline{B}| = 4 \mu\text{G}$ one can infer some large scale modulation of the field due to global dynamics as a resulting imprint of the large inclination. The morphology of all three molecular clouds is very

similar, although some local differences occur. The main cloud (having a sheet-like shape) is more compact for weaker fields, whereas the difference between the two strong magnetisations is negligible. This attribute results from the thermally dominated gas. The magnetic field does not control the gas dynamics and thus is forced to follow the motion of the fluid. Once, local density enhancements condense out, the magnetic field is dragged inwards together with accreting material. In the cases of more realistic fields, it is the magnetic field that dominates the fluid motion and that keeps the cloud coherent (see e.g., [Hennebelle, 2013](#)). At the same time the trailing arms now occur to be slightly denser. These arms are magnetically supported and thus more stable against shear flows and mixing by large scale fluid instabilities.

In contrast to a $3 \mu\text{G}$ -field, there is no star formation for the cases of $4 \mu\text{G}$ and $5 \mu\text{G}$, yet, although figure 4.3 indicates that these highly magnetised clouds are also more massive. The greater total masses and the lack of star formation combine to a picture of a fragmented cloud (see figure 4.13). Any intrinsically driven turbulence is subalfvénic and the magnetic field thus stays coherent. Such a field configuration has also been observed via polarised emission from CO (e.g. [Li et al., 2010, 2014](#)). So, what is the basic impact of the magnetic field on the star formation process? As long as accretion happens along the magnetic field, the influence of the latter can be safely ignored. Once, the gas begins to fragment, subcritical regions are produced, as long as the parental fragment was only slightly supercritical. Thus, accretion along field lines has to continue in order to generate supercritical fragments. Otherwise, magnetic pressure will drive the gas out of the potential well and the fragments stay subcritical and star formation stops.

The temporal evolution of the line-of-sight component of the magnetic field as function of column density is shown in figure 4.10. Different colours denote different evolutionary stages. The slanted straight lines indicate different criticality conditions according to various studies and using different approaches for deriving this condition ([McKee et al., 1993](#); [Shu et al., 1999](#); [Crutcher et al., 2010](#); [Li et al., 2014](#)). The horizontal black line denotes the initial value of the magnetic field. From left to right the initial magnetic field becomes stronger and from top to bottom the inclination increases in steps of 30° , starting at $\varphi = 0^\circ$. All cases have in common that the column density gradually increases at *constant* magnetic field magnitude, indicating gas accumulation along the field lines (see also [Crutcher et al., 2010](#)).

The thermally dominated case shows signs of early fragmentation and field compression, giving rise to an increase of the magnitude at relatively low column densities. These effects render the whole cloud magnetically subcritical. The clouds then undergo different dynamical phases with varying contribution of the magnetic field, i.e. times of pure accretion along the field lines,

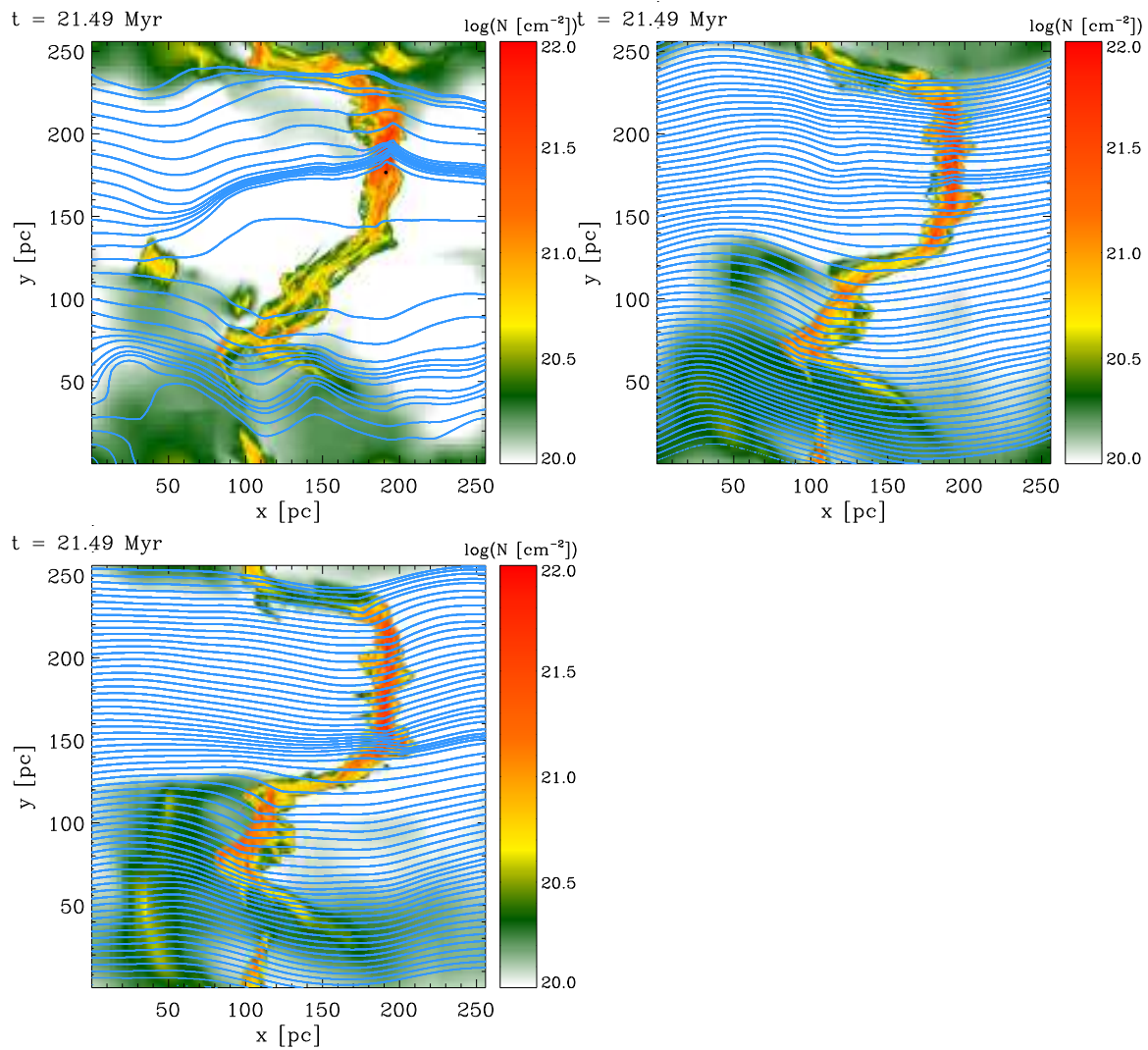


Figure 4.9: Column density map with overlaid magnetic field lines for $B = 3 \mu\text{G}$ (top left), $B = 4 \mu\text{G}$ (top right), and $B = 5 \mu\text{G}$ (bottom) from left to right. Initial inclination is $\Phi = 60^\circ$.

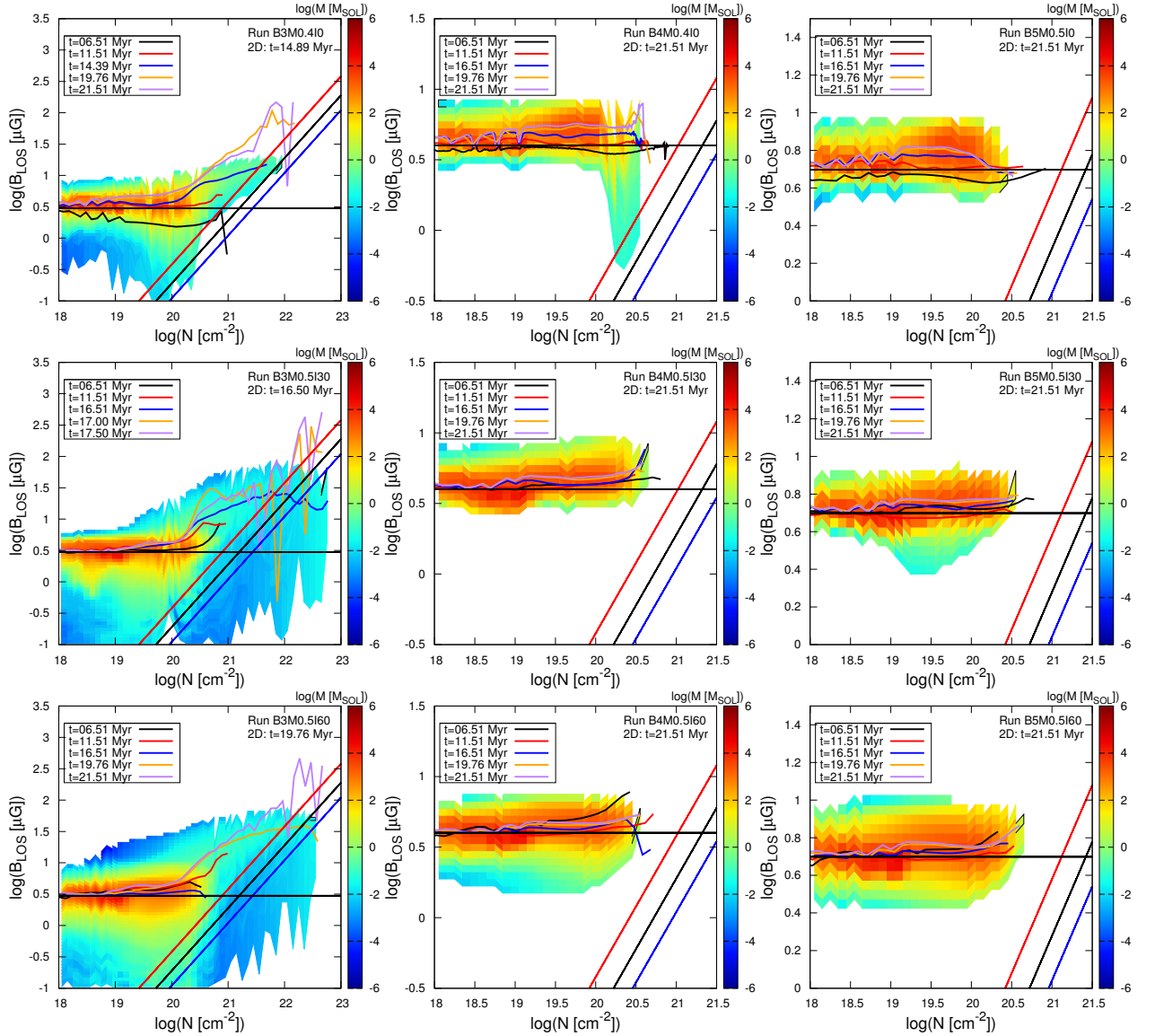


Figure 4.10: Evolutionary path of the cloud in $N - B_{\text{LOS}}$ space. In this case, $B_{\text{LOS}} = B_x$. From left to right: $B = 3\mu\text{G}$, $B = 4\mu\text{G}$, and $B = 5\mu\text{G}$, respectively. From top to bottom: $\Phi = 0^\circ$, $\Phi = 30^\circ$, $\Phi = 60^\circ$. Different colours denote different times. Note the different data range for the stronger fields. Also shown are the criticality condition (Crutcher et al., 2010; Crutcher, 2012, slanted red line), corrected for projection effects (Shu et al., 1999, slanted black line), and assuming equipartition of turbulent and magnetic fields (McKee et al., 1993, slanted blue line). Colour coded is the mass as function of column density, N , and line-of-sight magnetic field B_{LOS} .

twisting of the field by collapse and compression, and finally amplification of the field by large scale collapse and increasing column density. In between there exist stages, where the cloud shows signs of supercriticality. We here point out that the ordinate only shows the *average* line-of-sight component, i.e. there exist indeed supercritical regions that are not significant in terms of mass or volume fraction (see 2D histogram). Comparison with the weakest field shows that star formation is immediately initiated, when the gas becomes supercritical. The collapse proceeds and more material is dragged into the potential well. The resulting magnetic field amplification is still too low and finally it diffuses out of the central region. After the sink particle has formed, some of the field lines relax, thereby decreasing the density in some regions. As time proceeds the cloud becomes more compressed due to its global gravitational collapse. For better visualisation, the columns for $B = 5 \mu\text{G}$ and $B = 4 \mu\text{G}$ are shown in the column density range $19.5 \leq \log N \leq 21$ and $1 \mu\text{G} \leq |\underline{B}|_{\text{LOS}} \leq 25 \mu\text{G}$, since there occurs no significant amplification of the magnetic field during the evolution of the molecular cloud. This is indeed very intriguing, because observed magnetic fields are far larger in magnitude. We only see motion along the field lines, as has already been mentioned before, but we do also see *no sign of gravitational contraction*. Only some small modulations are seen, especially in the case of the cloud formed by head-on collision and $B = 4 \mu\text{G}$, but this amplification is less than a factor of two and thus not significant. At low column densities instead one can infer a slight 'global' amplification of a view percent. This can be accounted for accretion of mass from the diffuse halo surrounding the dense cloud. These data already indicate that the uniform component of the magnetic field is the leading component and no clear tangling of the field is observed. Furthermore, every process of gas accumulation perpendicular to the field lines is instantaneously balanced by magnetic forces (see figure 4.11). The flow cannot become dynamically important in order to bend the field lines and to render the magnetic field supercritical.

Even in the case of high diffusivity or large inclination, there is no amplification and/or tangling seen, indicating that diffusion processes might play only a minor role in rendering the field supercritical. If one takes a look at figure 4.12, it is obvious that the gas is highly subcritical. Shown are mass histograms as function of the normalised mass-to-flux ratio for the three magnetic fields at three late evolutionary stages. It is only for the weakest magnetic field that the gas shows some sign of evolution. One can clearly identify the power-law tail (which can be accounted for the N -PDF) and its growth as more mass enters the supercritical regime. In contrast, the higher magnetisation cases show roughly no evolution. Once a given distribution of the gas has developed it is seen to be globally stationary. The difference between the $4 \mu\text{G}$ and

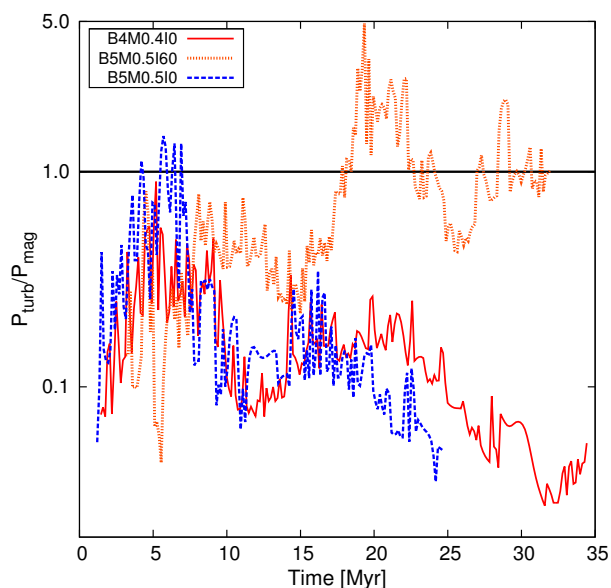


Figure 4.11: Temporal evolution of the ratio of turbulent ram pressure to magnetic pressure for three different runs. *On average* the magnetic field dominates and the ram pressure is not sufficient to induce motions perpendicular to the field lines.

$5 \mu\text{G}$ cases are small, i.e. the $4 \mu\text{G}$ case develops some larger mass-to-flux ratios. However, both regimes are far from being even critical.

4.3.4 Dynamics of Dense Cores

Due to turbulence, overdensities occur which become gravitationally bound. Figure 4.13 shows the evolution of the densest regions within the formed molecular clouds, i.e. of these with minimum density of $n = 1000 \text{ cm}^{-3}$. The left image shows the evolution of mass, the right panel the evolution of thermal and magnetic Jeans numbers. The temporal evolution is shown for the whole simulation, thus earlier ending graphs indicate the complete lack of gas with the respective minimum density from this time on.

For all runs with zero inclination, the compression by the two converging streams induces a transition to dense material with a few thousand solar masses. But as soon as the ram pressure of the confining flows becomes weaker these dense regions re-expand, showing that the regions were only pressure confined entities. For run B₃Mo.4I₀ a phase of increasing mass follows, which is mainly due to accretion of matter along the magnetic field lines. In the end the densest regions of the molecular cloud reach a total mass of a few hundred solar masses. Comparison with run

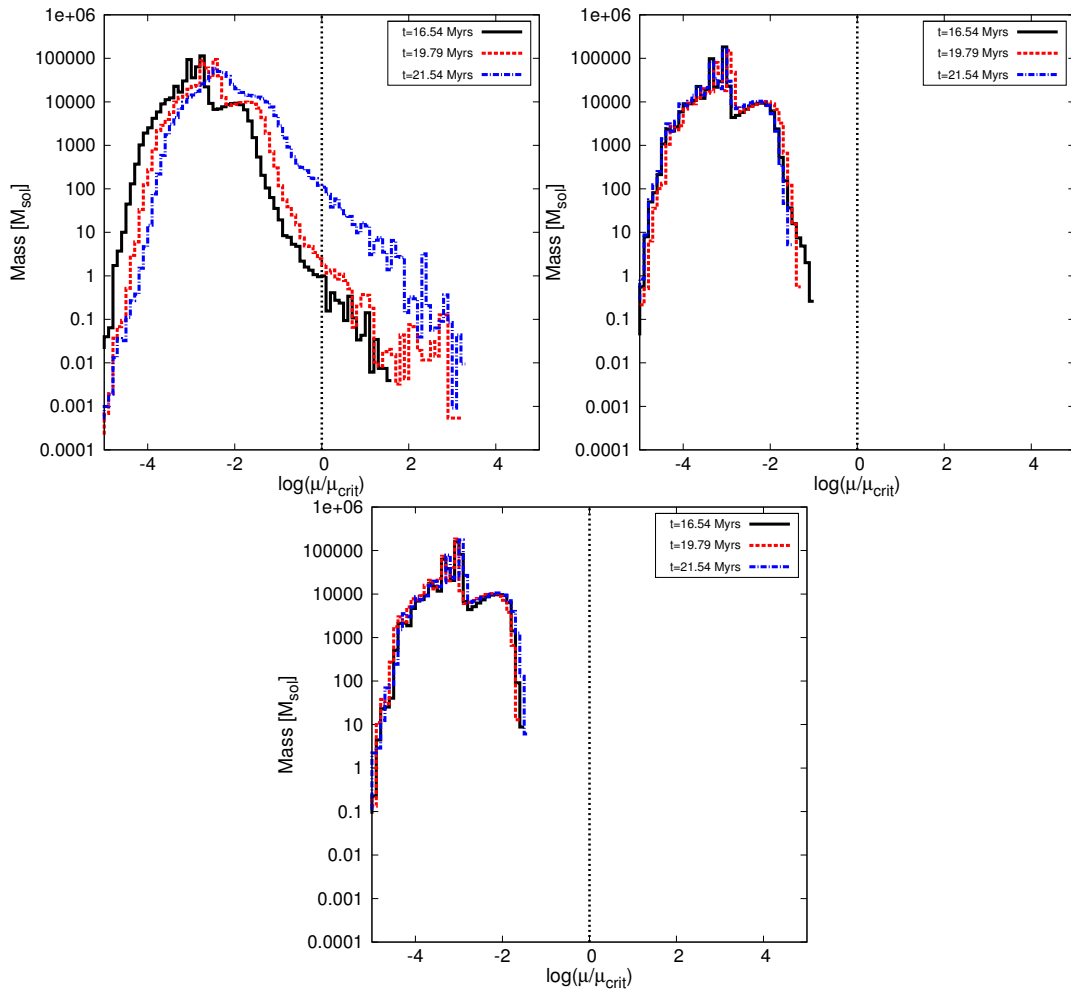


Figure 4.12: Mass as function of the mass-to-flux ratio for B3M0.5160 (top left), B4M0.5160 (top right), and B5M0.5160 (bottom). Different colours denote different times. The vertical line again indicates the critical value.

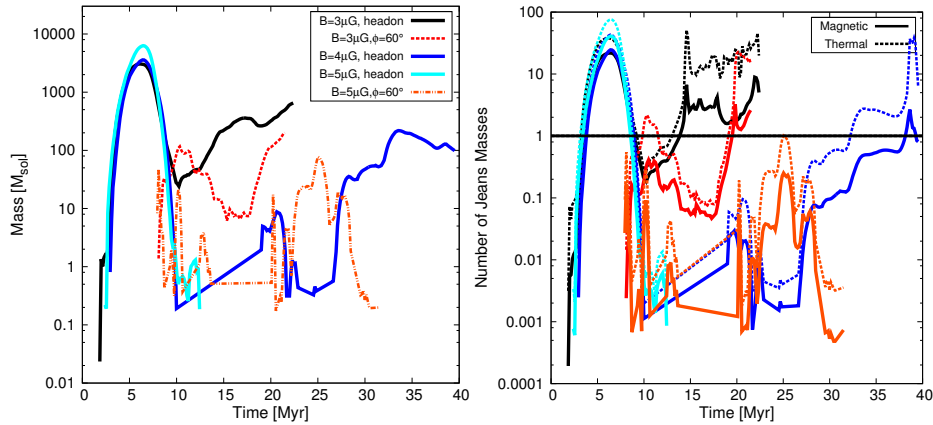


Figure 4.13: Temporal evolution of the gas with minimum density of $n = 1000 \text{ cm}^{-3}$, resembling the densest parts deeply embedded in the cloud. *Left:* Temporal evolution of mass. Note that for runs B4M0.4I0 and B5M0.5I60 there are stages where *no dense material exists* [indicated by the linear increasing (B4M0.4I0) and the non-varying stages (B5M0.5I60). The former is just the line connecting two data points!] between 10 and 20 Myr. *Right:* Evolution of the number of thermal and magnetic jeans masses. Colours correspond to the left figure.

B₃Mo.5I60 shows a difference of only a factor of a few in the end of the simulation.

The most striking difference is the first evolutionary phase, where the cores of run B₃Mo.5I60 undergo strong variations, because of the additional shearing motions, after they have firstly formed at far later times.

Run B₄Mo.5I0 already shows the influence of the stronger magnetic field. The decrease in external ram pressure by the converging flows also induces a re-expansion of the dense material within the cloud complex. But now the magnetic field is already strong enough to ensure a less efficient mass accretion. At around $t \approx 10 \text{ Myr}$ *no dense material exists*. This stage lasts until $t \approx 20 \text{ Myr}$, where the global collapse of the molecular cloud yielded strong enough compression to form dense material again³. Strong internal variations of the cloud then lead to a highly varying mass evolution. In the end, masses similar to run B₃Mo.4I0 are reached, and stars start to form. Interestingly it takes roughly 20 Myr for stars to form after the reoccurrence of dense cores. This already indicates that for shearing flows the onset of star formation with magnetic and thermal energies in equipartition is further delayed to far later times. But during such a long evolution, the clouds would then be subject to large scale Galactic processes and our setup would not be appropriate.

Further increase of the initial magnetic field strength shows even more dramatic changes in the overall evolution of the densest regions within the molecular clouds. In run B₅Mo.5I0 the exis-

³Note the linear increasing interval is simply the connecting line of two data points at 10 and 20 Myr.

tence of dense cores ends after $t \approx 12$ Myr, showing the complete lack of unstable cores after the compression by the bulk flows. Although a molecular cloud forms, it does not possess any region, which could possibly undergo gravitational contraction to form stars. However, the first evolutionary stages during the compression of the flows shows that the strong fields lead to higher masses of the dense gas due to the influence of the field. Inclining one WNM stream now shows striking difference. At first, the build up of dense cores starts out at later times as in the case of run B₃Mo.5I60. But the diffusive nature of this formation mechanism leads to the build-up of denser regions up to the end of the simulation, although there are stages where no dense cores exist. The evolutionary track of the dense gas is mainly influenced by the cloud motion and the magnetic forces. The whole dense material is thermally and magnetically highly stable, with the latter being the dominant aspect. Thus, although far more diffusive, the magnetic field is still able to suppress the formation of unstable cores and the subsequent star formation.

The stability of the dense regions is also indicated by the mass-to-flux ratio (see figure 4.14). Only if the magnetic field is sufficiently weak, gravitational energy dominates over magnetic energy and the inner regions of the molecular clouds are rendered magnetically supercritical. In case of a $4\mu\text{G}$ field a great spread of mass-to-flux ratios is observed with all being subcritical at the stages shown. During the further evolution of the cloud, magnetically supercritical cores form. Additionally, by inclining one stream, low-mass cores are generated, which have approximately the same mass-to-flux ratio as in the case of head-on colliding streams, indicating that the magnetic field diffuses out of the regions.

4.3.5 Analysis of the Densest Cores

Now we analyse the three densest cores in more detail. For simplicity, we have assumed that the cores are spherical entities. Figure 4.15 shows the normalised mass-to-flux ratio, the turbulent sonic and the turbulent Alfvén Mach number as function of radial distance from the centre of mass.

For run B₅Mo.5I0 the mass-to-flux ratio is subcritical and constant throughout the whole core. This has two implications: 1) Magnetic support is sufficient to keep the core stable and 2) there is no evidence for accretion of matter along the field lines (which would increase the ratio locally). Besides being higher, the mass-to-flux ratio for run B₃Mo.4I0 shows some variation as function of radial distance for all three cores. The centre of the densest core (solid line) is seen to make a transition to a supercritical state surrounded by a subcritical halo. Although the other two cores

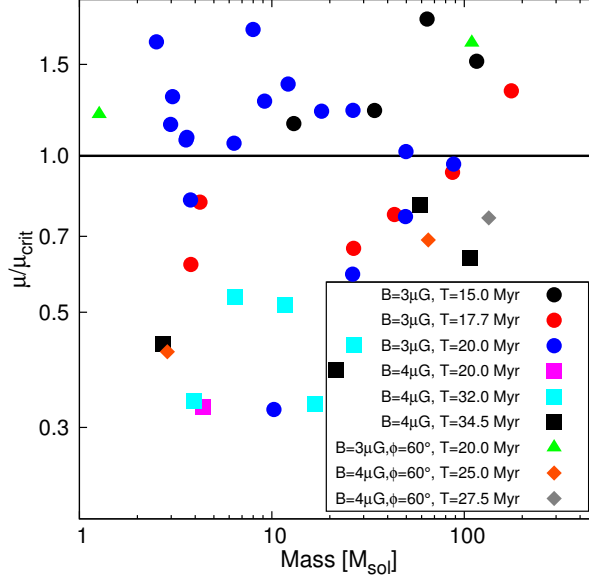


Figure 4.14: Normalised mass-to-flux ratio as function of core mass for runs B3M0.4I0 (circles), B3M0.5I60 (triangles), B4M0.4I0 (squares), and B4M0.4I60 (diamonds) at different evolutionary stages. Note that a comparison of equal temporal stages is not possible due to the lack of cores with densities of $n \geq 1000 \text{ cm}^{-3}$. For runs B5M. . . I. . . no such cores were found! The mass-to-flux ratio is normalised to $\mu_c = 0.16/\sqrt{G}$ (Nakano and Nakamura, 1978).

are subcritical as a whole, they show the same signature. The cores in run B₄Mo.4Io show a state between these of runs B₃Mo.4Io and B₅Mo.5Io. As expected, the mass-to-flux ratio of the densest core decreases with increasing radius. The two other cores show only a roughly constant ratio. The mass-to-flux ratio of the first core is still subcritical, but the transition to a supercritical state is achieved at slightly later times. Note that the location of the maximum mass-to-flux ratio in this core does not coincide with the centre of mass.

The dynamics of the cores can be analysed by looking at the turbulent Mach numbers (see middle and right panel). The cores are *subsonic* and *subalfvénic*, hence showing that 1) no strong compressions within the dense material occur and 2) the magnetic field prevents the gas from accumulating into denser unstable fragments. This is true for all clouds and can be interpreted as an imprint of the initial conditions. Only for the densest core in run B₃Mo.4Io, the outskirts are seen to be slightly supersonic and superalfvénic, indicating turbulent accretion onto the core. The difference between the two Mach numbers is less for the weakest field, since it is not able to fully prevent collapse. If the field strength is higher, magnetic tension will accelerate the gas, while relaxing the field lines. This is why the sonic Mach number is slightly higher, but nevertheless the motions only reach subsonic or at most transsonic states. At these densities ($n \approx 10^3 \text{ cm}^{-3}$), the

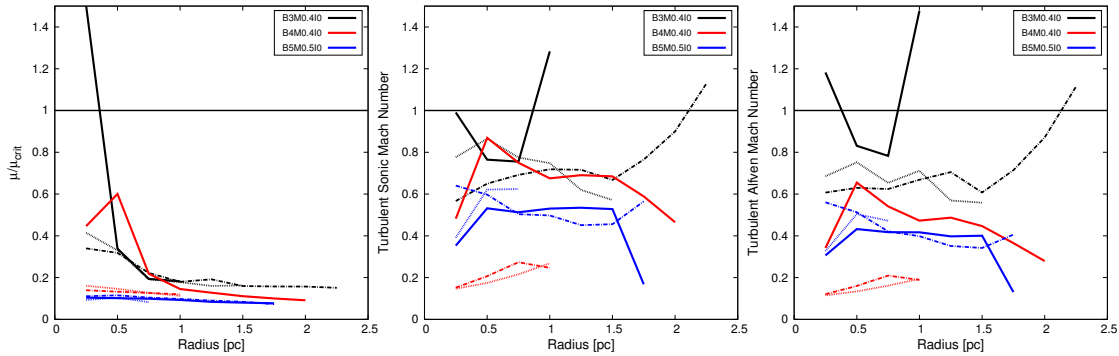


Figure 4.15: Radially averaged profiles of the three (indicated by different line styles) densest cores within the molecular clouds for runs B . . . M . . . IO. *Left:* Mass-to-flux ratio. *Middle:* Turbulent *isothermal* Mach number. *Right:* Turbulent Alfvén Mach number. The radial distance is evaluated with respect to the centre of mass. For runs B3M0.410 and B4M0.410, respectively, the data is shown shortly before the first star appears. The values for the turbulent Mach numbers mimic the initial conditions, i.e. that the turbulence is still subsonic and subalfvénic. Note, the masses of these cores range from $\approx 4 M_{\odot}$ (third massive in run B5M0.510) to $\approx 250 M_{\odot}$ (most massive in run B3M0.410).

flow seems to be mediated by the magnetic field lines, which in every case tends to suppress the build up of turbulent vortices.

4.4 Chapter Summary & Discussion

In the following, we discuss the role of ambipolar diffusion and show that the strong-coupling approximation is valid in case of our simulations. The discussion is followed by a summary of the main results.

4.4.1 Discussion: Influence of Ambipolar Diffusion

We have conducted one simulation including the non-ideal MHD effect of ambipolar diffusion. The AD module was implemented in FLASH and extensively tested by [Duffin and Pudritz \(2008\)](#). It uses the strong coupling approximation (like [Chen and Ostriker \(2012\)](#), see also [Chen and Ostriker \(2014\)](#))), which was shown to be valid in the physical regime we are analysing (see appendix in [Vázquez-Semadeni et al., 2011](#)). However, since we are using a slightly different density threshold than in [Vázquez-Semadeni et al. \(2011\)](#) and different turbulent Mach numbers, the validity has to be proven again:

Taking a typical length scale of $l = 0.0625$ pc (which corresponds to the accretion/softening radius of the sink particles in our simulation with 11 levels of refinement) and a typical velocity at

these scales of 0.5 km/s (taken from figure 4.1) the ratio

$$M_A^2/R_{AD}(l) \approx 1.5 \times 10^{-8}. \quad (4.4)$$

Here M_A is the Alfvén Mach number and $R_{AD}(l)$ is the AD Reynolds number at scale l . Hence, according to Li et al. (2006b, see also Vázquez-Semadeni et al. (2011)) the strong coupling approximation is satisfied very well in our simulations.

The fluxes are computed using a central differencing scheme and the numerical timestep is primarily controlled by AD. Note that the implementation by Chen and Ostriker (2012) uses super-timestepping to speed up the simulation (see also Choi et al., 2009).

A comparison of the influence of AD on molecular cloud evolution from Vázquez-Semadeni et al. (2011) is shown in figure 4.16. AD tends to smoothen filamentary structures within the cloud complex. The cloud centre reveals the highest densities, typical for AD (see also Crutcher et al., 2009). In contrast, the simulation without AD shows a highly filamentary molecular cloud. Note the cavities of diffuse gas with column densities $\lesssim 10^{20} \text{ cm}^{-2}$, which do not appear in the AD case. Stars form in both cases. However, in the case with AD, star formation is more localised to a distinct region near the centre of the cloud (which is the centre of the gravitational potential well). Furthermore, run B5Mo.5I6oAD includes the process of ambipolar diffusion in addition to an initial tilt. As was already mentioned in the remarks of table 4.1 the simulation was stopped at $t \approx 12 \text{ Myr}$. The subsequent evolution of the cloud showed no significant difference to the runs without ambipolar diffusion. In this case, the shear flows tend to suppress the formation of dense cores, where ambipolar diffusion would be most efficient.

4.4.2 Summary

We have presented the results of MHD simulations of colliding flows with varying initial conditions. The strength of the turbulent velocity fluctuations, of the background magnetic field as well as the alignment of one of the WNM streams with the magnetic field have been changed. We have shown that dense clouds can form *independent* of the initial conditions, but that their final mass and dynamics are mainly controlled by these (see table 4.2). Increasing initial turbulence lead to lower cloud masses due to less coherent gas streams. Oblique flows still lead to clouds with masses comparable to what has been observed recently and stronger magnetic fields will generally lead to more massive molecular clouds. The first point seems at first a contradiction

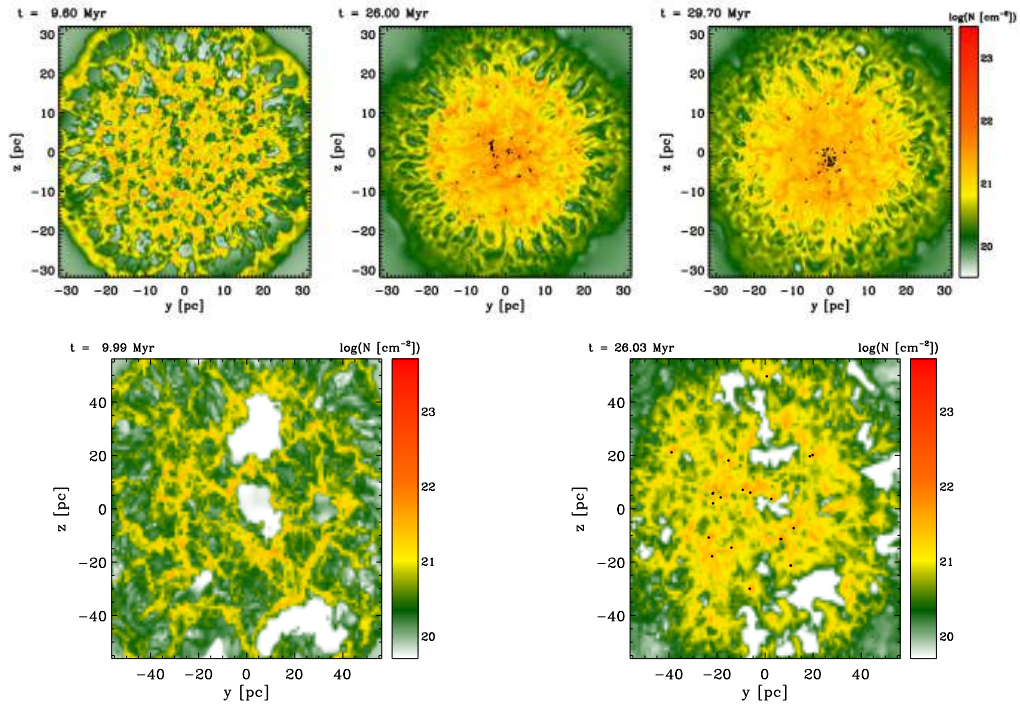


Figure 4.16: *Top:* Evolution of a molecular cloud subject to AD from [Vázquez-Semadeni et al. \(2011\)](#). *Bottom:* Simulation without AD. Despite different initial conditions, the appearance of the molecular cloud with AD is strikingly different. Here most of the filaments within the cloud tend to be smoothen by the action of AD. The whole molecular clouds appears to be more like a single complex, rather than being made of a filamentary network.

to [Inoue and Inutsuka \(2009\)](#) who stated that for larger inclined flows no dense, molecular clouds can form. However, here the cloud accretes mass and becomes molecular with time. As can be seen from figure 4.6, the onset of the formation of dense gas is delayed with increasing inclination. This is indeed consistent with [Inoue and Inutsuka \(2009\)](#), because the first few Myr are characterised by HI gas with densities below the threshold density of $n = 100 \text{ cm}^{-3}$.

Molecular clouds are able to condense out of the WNM, independent of the magnetic field strength. However, only in the cases of fairly weak initial magnetic fields, the formation of stars could be initiated. Starting with subcritical HI flows, the magnetic flux loss is in no cases sufficient to allow the build-up of supercritical cloud cores. The tendency of the magnetic field to realign itself with the initial direction is a crucial factor for the overall evolution. In order to circumvent this problem, non-ideal MHD was resembled by means of tilted collisions. Increasing inclination leads to increased diffusivity of the magnetic field. The variation of the inclination as well as the flow dynamics showed no tendency for faster accumulation of gas or

Table 4.2: Typical cloud parameters for gas with $n \geq 100 \text{ cm}^{-3}$ at the end of each simulation with equal turbulent and flow Mach number.

ϕ ($^\circ$)	$ \underline{B} $ (μG)	Time (Myr)	Cloud Mass ($10^3 M_\odot$)	SF? (yes/no)	Stellar Mass (M_\odot)	SFE (%)	E_{mag} (10^{46} erg)	Velocity Dispersion (km/s)	$N_{\text{jeans,mag}}$
0	3	21.79	40.81	yes	1346	3.2	23.59	0.99	23.99
30	3	18.29	21.84	yes	202	0.9	12.28	1.29	12.51
50	3	18.94	14.5	yes	14.20	0.1	6.39	0.73	9.86
50 ^a	3	21.04	17.9	yes	43.83	0.2	7.09	0.84	14.28
60	3	21.49	15.2	yes	95.68	0.6	7.02	1.45	10.68
0	4	39.52	18.33	yes	59.32	0.3	13.63	0.53	5.70
30	4	27.13	23.93	no	---	—	21.53	1.21	6.30
						—			
60	4	27.28	16.15	no	---	—	12.29	1.74	6.29
						—			
0	5	24.64	43.29	no	---	—	52.71	0.46	6.10
						—			
30	5	22.94	20.39	no	---	—	22.94	1.02	3.07
						—			
40	5	37.93	11.56	no	---	—	12.08	1.07	2.16
						—			
50	5	37.03	17.57	no	---	—	19.63	1.42	3.39
						—			
60	5	31.93	7.31	no	---	—	6.48	1.79	1.55
						—			

a: Different initial random seed for the turbulence.

faster transition to thermally dominated regions, since the flow dynamics is rather controlled by the appearing shear flows than magnetic diffusion.

We point out the complete lack of supercritical regions for realistic initial field strengths. As was shown in figure 4.14, the normalised mass-to-flux ratio ranges from 0.3–1.7 ($B = 3\mu\text{G}$) and 0.3–0.7 ($B = 4\mu\text{G}$), respectively. At least the former case for weak fields compares well with the results of [Chen and Ostriker \(2014\)](#), $\mu/\mu_c \sim 0.5 - 7.5$ as well as with observations ($\mu/\mu_c \approx 2$, [Troland and Crutcher, 2008](#)). From the observational side, HI clouds may be supercritical as a whole, but their observed, dense subregions be subcritical.

The question remains, how clouds achieve the transition from sub- to supercritical.

5

The Influence of Supernova Feedback on the Evolution and Lifetime of Molecular Clouds

Stellar feedback is an elemental part for the regulation of the dynamics of the ISM as well as of molecular clouds. One process is the end of a high-mass star's life, known as supernova. In the following I will describe the results of analyses dedicated to the impact of supernova feedback on the global dynamics and evolution of molecular clouds. Parts of the presented contents have been submitted to MNRAS in [Körtgen et al. \(2015\)](#).

My Contribution

[Körtgen et al. \(2015\)](#) is a multi-authored publication. I am the leading author. I performed the necessary simulations and implemented the feedback subgrid model. Here, help from the second author is acknowledged. I post-processed the results and carried out the interpretation of the results. I wrote the text for the paper. However, useful discussions by the co-authors and insightful comments are good reasons to make them appear on the publication.

5.1 Introduction

The formation of molecular clouds, dense clumps, and finally stars is regulated by the interplay of gravity, magnetic fields, turbulence, and stellar feedback. Magnetic fields provide support against gravity in addition to thermal and turbulent pressure.

The effect of turbulence is two-fold. Firstly, in the cold neutral medium (CNM) turbulent fluctuations are primarily supersonic. Thus, shocks occur, which compress the gas and hence provide the seeds for gravitationally unstable regions (e.g. [Mac Low and Klessen, 2004](#)). On the other hand, these supersonic motions constitute an effective pressure. This turbulent pressure acts as further support against gravity beside thermal and magnetic pressure. If this turbulence is also superalfvénic, it is the major support in molecular clouds ([Padoan et al., 1999](#); [Padoan and Nordlund, 1999](#); [Federrath and Klessen, 2012, 2013](#)).

The last component for the regulation of internal cloud dynamics is stellar feedback by jets/outflows, winds, ionising radiation, and supernovae. The role of jets and outflows is still being subject to strong debate. On the one hand, they are able to drive turbulence in the intra-clump medium ([Nakamura and Li, 2014](#); [Li et al., 2015](#)) and hence maintain the level of energy counterbalancing gravity. On the other hand, [Banerjee et al. \(2007\)](#) argue that the turbulent fluctuations, driven by a single source, are damped too fast as primarily compressive modes are excited. However, the combined effect of *multiple* outflows seems to be able to disperse (not disrupt) the parental clump ([Banerjee et al., 2007](#); [Wang et al., 2010](#); [Nakamura and Li, 2014](#)).

Stellar winds are believed to have a stronger impact on the massive star's environment and hence the parental cloud. As [Dale et al. \(2013\)](#) point out, winds are most efficient in dispersing dense, massive cores in which the stars are embedded. Their longrange impact, however, is not sufficient. [Dale et al. \(2014\)](#) compared simulations of idealised molecular clouds including stellar winds or ionisation feedback. The main driver of cloud dispersion is the massive star's ionising radiation, consistent with studies by [Vázquez-Semadeni et al. \(2010\)](#). Stellar winds in contrast only help to shape the emerging HII regions. In detail, winds yield more spherical HII regions, which are more stable against shell instabilities due to the smoothing influence of the expelled winds. However, the efficiency of dispersing entire (giant) molecular clouds by these two feedback mechanisms strongly depends on the cloud's mass and escape velocity. The degree of turbulence within the dense gas is only essential for the inhomogeneity of the cloud and hence the ability of the hot, ionised gas to escape through low-density channels. Concerning the impact of those mechanisms on the star formation process, [Dale et al. \(2014\)](#) and [Vázquez-Semadeni et al. \(2010\)](#) come

to similar conclusions in that ionisation feedback is most efficient in dispersing small regions. In addition, [Colin et al. \(2013\)](#) give a timescale for the dispersion of a 10 pc region of $t \approx 10 - 15$ Myr. On scales of entire molecular clouds ionisation feedback may also help to trigger the formation of new stars ([Walch et al., 2012, 2013](#)). However, the star formation efficiency is globally still being reduced by a factor of 10–20 % but not halted ([Dale et al., 2014](#)).

Finally, high-mass stars explode in a violent supernova event, thereby releasing $E_{\text{SN}} = 10^{51}$ erg in a short period of time. Preceding studies have focused either on Galactic scales, i.e. kpc-scales ([Korpi et al., 1999](#); [de Avillez, 2000](#); [de Avillez and Breitschwerdt, 2004](#); [Joung and Mac Low, 2006, 2007](#); [Shetty and Ostriker, 2008](#); [Joung et al., 2009](#); [Ostriker and Shetty, 2011](#); [Hill et al., 2012](#); [Shetty and Ostriker, 2012](#); [Gent et al., 2013a,b](#); [Walch et al., 2015](#); [Hennebelle and Iffrig, 2014](#); [Gatto et al., 2015](#)), or on scales of small clouds or even clumps with radii of a few pc ([Pittard and Rogers, 2012](#); [Rogers and Pittard, 2013](#); [Walch and Naab, 2015](#); [Iffrig and Hennebelle, 2015](#); [Geen et al., 2015](#)).

Recently, [Walch and Naab \(2015\)](#) have reported on supernova feedback in small-sized (radius $r = 16$ pc), massive ($M \approx 10^5 M_{\odot}$) and non-magnetised molecular clouds. The authors injected kinetic energy in a small sub-volume of the cloud in order to mimic the free-expansion phase of the supernova remnant (SNR). They resolved the different stages during the SNR evolution and analysed the influence of different physical mechanisms on this. For adiabatic expansion of the SNR in a homogeneous cloud, they yielded the complete dispersion of the latter on timescales of $t \leq 1$ Myr. However, the clouds – homogeneous or fractal – are *not being destroyed* if radiative cooling is included. The hot and shock-compressed gas cools too fast. Hence, the thermal energy supply, which can be converted into kinetic energy, shrinks on the same timescales. The net energy and momentum input are thus not sufficient to accelerate the gas to velocities greater than the cloud’s escape velocity. Similar results were obtained by [Iffrig and Hennebelle \(2015\)](#), who analysed the impact of supernova explosions within or near molecular clouds. The authors deduced that the impact of supernova feedback is primarily determined by the position of the progenitor star. Supernovae at the border of or near to a molecular cloud do not have a significant impact on a possible cloud dispersal as well as on the dynamics of the dense gas which is due to the lack of momentum transfer to the latter. The major part of the cloud is compressed and some regions are ablated. In the case of a supernova going off within a molecular cloud, the momentum transfer to the dense gas is much higher and hence the fraction of gas escaping the cloud. The results indicate a reduction of the cloud mass due to single supernova explosions of up to 50 % for clouds with masses of $M \approx 10^4 M_{\odot}$ and sizes of approximately

20–30 pc. However, the authors report no complete cloud dispersion.

In studies of Galactic scale simulations supernova feedback is usually taken into account since it is the main driver of Galactic fountain flows (e.g. Hill et al., 2012; Gent et al., 2013b; Walch et al., 2015). Usually, $E_{\text{SN}} = 10^{51}$ erg are injected during each individual supernova event. However, some approaches inject $E_{\text{SN}} = (2 - 3) \times 10^{51}$ erg in order to resemble additional energy input from ionisation and winds in one single event (P.Colín, priv. communication, 2012). Studies implementing more than one supernova are restricted to a certain supernova rate. For example, Joung and Mac Low (2006) use the *observed Galactic rate* of $\nu_{\text{SN,gal}} = 1/44 \text{ yr}^{-1}$ from Tammann et al. (1994). More recent studies by Walch et al. (2015) and Gatto et al. (2015) use a Kennicutt–Schmidt (KS) relation in order to extract the star formation rate surface density, Σ_{SFR} , and transform it to a supernova rate by convolution with an IMF.

Gatto et al. (2015) conducted a large parameter study of supernova feedback on Galactic scales. They investigated the influence of different supernova driving mechanisms on the thermal and dynamical state of the interstellar medium (ISM). Most relevant are their results from ‘peak driven’ supernovae – i.e. the supernovae exploded in regions of significantly enhanced density –, which state that this driving mechanism fails to explain the large fraction of molecular gas as well as the volume filling fraction of hot, ionised gas. The former is most likely due to disruption of dense, cold branches by the interaction of the SNR with the densest gas. The latter originates in very efficient cooling of hot gas in the shock–compressed regions within the dense clumps. The gas temperatures are cooled efficiently to $T < 10^6$ K. This is supported by Walch et al. (2015), who yield realistic disc structure and volume filling fractions of the hot gas for non–peak driven supernovae. Both studies underline the importance of feedback mechanisms prior to supernova feedback.

The results presented in this chapter try to bridge the gap between small–scale, i.e. 1 to a few 10 pc, simulations (Pittard and Rogers, 2012; Walch and Naab, 2015; Iffrig and Hennebelle, 2015) and large–scale (kpc) disc simulations (Korpi et al., 1999; Ostriker and Shetty, 2011; Walch et al., 2015; Tasker et al., 2015) by performing a set of simulations on intermediate scales of a few hundred pc. Section 5.2 gives the results of our study on supernova feedback, thereby focussing on the global evolution of the (dense) gas. In section 5.7.1 we briefly discuss missing physics. The chapter closes with a summary in section 5.7.

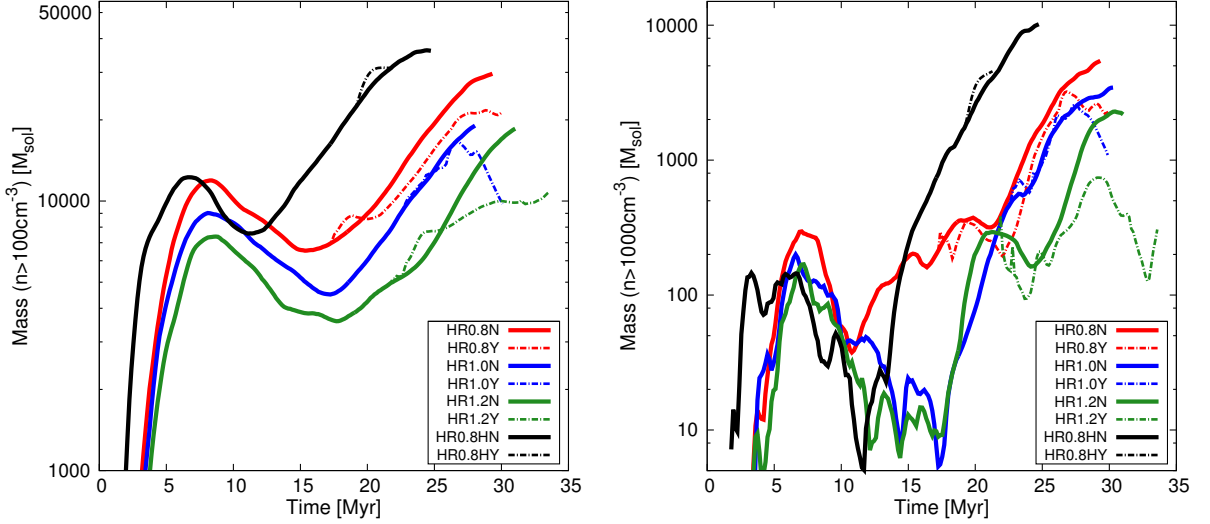


Figure 5.1: Temporal evolution of the mass of the cloud (left, $n \geq 100 \text{ cm}^{-3}$) and the densest parts in the cloud interior (right, $n \geq 1000 \text{ cm}^{-3}$). The data are evaluated within a cylindrical volume of radius $r = 50 \text{ pc}$ and height $h = 40 \text{ pc}$. Solid lines denote the runs without feedback, dash-dotted lines those with feedback. After the converging flows have vanished (at $t \approx 10 \text{ Myr}$) global collapse is initiated and the clouds become more massive. Note the different evolution of the cloud and the densest parts for HR0.8, respectively. Supernova feedback has a two-fold impact on the global evolution of the cloud mass (see text).

5.2 Evolution of Cloud Masses

The left panel in figure 5.1 shows the evolution of the mass of the *clouds*. The *clouds* are defined to consist of regions with density of $n \geq 100 \text{ cm}^{-3}$. They assemble mass by the compression of the WNM flows. The decrease of dense gas mass between 8 and 17 Myr in the MHD runs is a consequence of the re-expansion of the compressed material (see e.g. [Körtgen and Banerjee, 2015](#), and references therein). For the hydrodynamic runs this stage is from 5 to 12 Myr and is thus faster. This is because of the lack of a magnetic field, which would decelerate the gas. After this stage, global contraction of the cloud leads to an increase of mass. Generally the clouds are more massive for the hydrodynamic runs due to the lack of magnetic support. However, the accretion properties of the clouds seem very similar in the later stages from 20 Myr on. These stages are independent of the initial conditions since the flows have vanished and the initial turbulence has fully decayed. In the end, the clouds have masses between $M_{\text{cloud}} = 2 \times 10^4 - 4 \times 10^4 M_{\odot}$. The difference of the cloud masses between the MHD runs is due to the fact that initially the stronger turbulence disperses the gas more efficient. This also prevents the build up of a massive cloud. The impact of supernova feedback on the clouds is two-fold. The first supernova explosion results in a compression of the surrounding gas, thereby *increasing* the total mass of the cloud.

The efficiency in increasing the mass depends on where the supernova goes off (see also Iffrig and Hennebelle, 2015). For runs HR0.8Y and HR0.8HY, the cloud is dense enough to provide a significant obstacle to the emerging shock wave. An increase of mass is also seen in the cloud of run HR1.2Y, although the increase takes a longer time due to the more inhomogeneous cloud. In contrast, the supernova explosion in run HR1.0Y results in only a small increase of a few hundred solar masses. In this case, most of the injected energy can escape through low-density channels within the cloud. The denser regions are not significantly compressed. However, in all cases this phase of compression lasts only until the point, where parts of the clouds are heated up and dispersed by the transmitted shocks. From this stage on, the cloud mass stays lower in comparison to the clouds without feedback. If more and more stars explode, the growth in mass is either stopped or turned into a stage of decreasing mass (as in case HR1.0Y). The total decrease in cloud mass is between a factor of 1.5–2, in agreement with a previous study by Iffrig and Hennebelle (2015). However, the efficiency depends on the initial turbulence within the flows and thus the final cloud mass and (mean) density.

5.2.1 Evolution of the Densest Parts

In the right panel of figure 5.1 we present the evolution of the densest parts of the molecular cloud with densities of $n \geq 1000 \text{ cm}^{-3}$. The evolution of the densest parts essentially follows the evolution of the cloud. The strong fluctuations during the early stages indicate that these regions are diluted due to the energy injection from the WNM flows and turbulence. All clouds reveal stages of decreasing mass, because of the material expanding perpendicular to the WNM flows. The initial variations are due to (trans-alfvénic) turbulence. However, the densest regions in run HR0.8N do not show such variation. In this case, the turbulent fluctuations are sub-alfvénic. The more compact cloud interior is nearly unaffected by the re-expansion of the cloud and keeps on accreting. This indicates that the dispersion is primarily restricted to the outer edges of the cloud. The later evolutionary phases of all clouds – from 15 Myr on for the hydro case and from 20 Myr on for the MHD simulations – are dominated by global cloud contraction.

The supernova explosions now yield periods of varying total mass in the densest parts. This is due to dilatational and compressive phases and is seen in all MHD runs. In contrast, the hydro simulation only indicates a phase of compression. However, at this stage almost 10 % of the mass is contained in the dense parts. The energy cannot escape through low-density channels as the stellar environment is already too compact. In the end, the mass of the densest parts is reduced

by factors of about three for HR0.8Y and HR1.0Y to of about ten for HR1.2Y. Here, again, the low-density channels within the cloud play a major role for the net compression of the gas.

5.3 Cloud Dynamics

Figure 5.2 shows a temporal sequence of the column density, temperature and total velocity for run HR0.8Y. The first row shows the molecular cloud 30 kyr *before* the first supernova, the other two rows after supernovae have gone off. Prior to the first supernova, the cloud reveals a filamentary network and clumps as well as low-density cavities in between. This is a result of the interaction of turbulence and gravity, mediated by the ambient magnetic field (e.g. [Hennebelle, 2013](#); [Chen and Ostriker, 2014](#); [Körtgen and Banerjee, 2015](#)). The filaments are best being identified in the temperature slice as the cold branches with temperatures of about $T = 30$ K, immersed in a warm medium with $T = 1000 - 5000$ K. The filaments are also the places of lowest velocity. The supernovae act only locally since the shock terminates after ≈ 15 pc. The cold, dense gas is redistributed, as is best seen in the temperature slices. However, some part of the injected energy escapes through low-density channels within the molecular cloud. For comparison, the column density map before the first supernova and at the end of the simulation reveal different patterns at the cloud outskirts. Prior to supernova feedback, the outer border of the cloud is more spherical. After supernova feedback, the outskirts are more structured and the density of the WNM halo surrounding the cloud is higher – a clear indication for expelled material from the inner parts of the cloud. These parts of the molecular cloud do also reveal a slower inward-directed velocity now, as can be identified in the velocity pattern.

Figures 5.3 and 5.4 shows the final stage of runs HR1.0N, HR1.0Y, HR1.2N, and HR1.2Y in the xz -plane. The effect by the supernovae is more drastic for runs HR1.0N and HR1.0Y. This is because most of the high-mass stars have exploded within a distinct region in the centre of the molecular cloud. However, this effect is clearly seen only in the slices of the midplane ($y=0$). The column density shows a compact molecular cloud with a slightly tenuous region in its centre. Again, the supernovae result in a redistribution of matter, which is seen by the increased column density at the outer edges of the cloud.

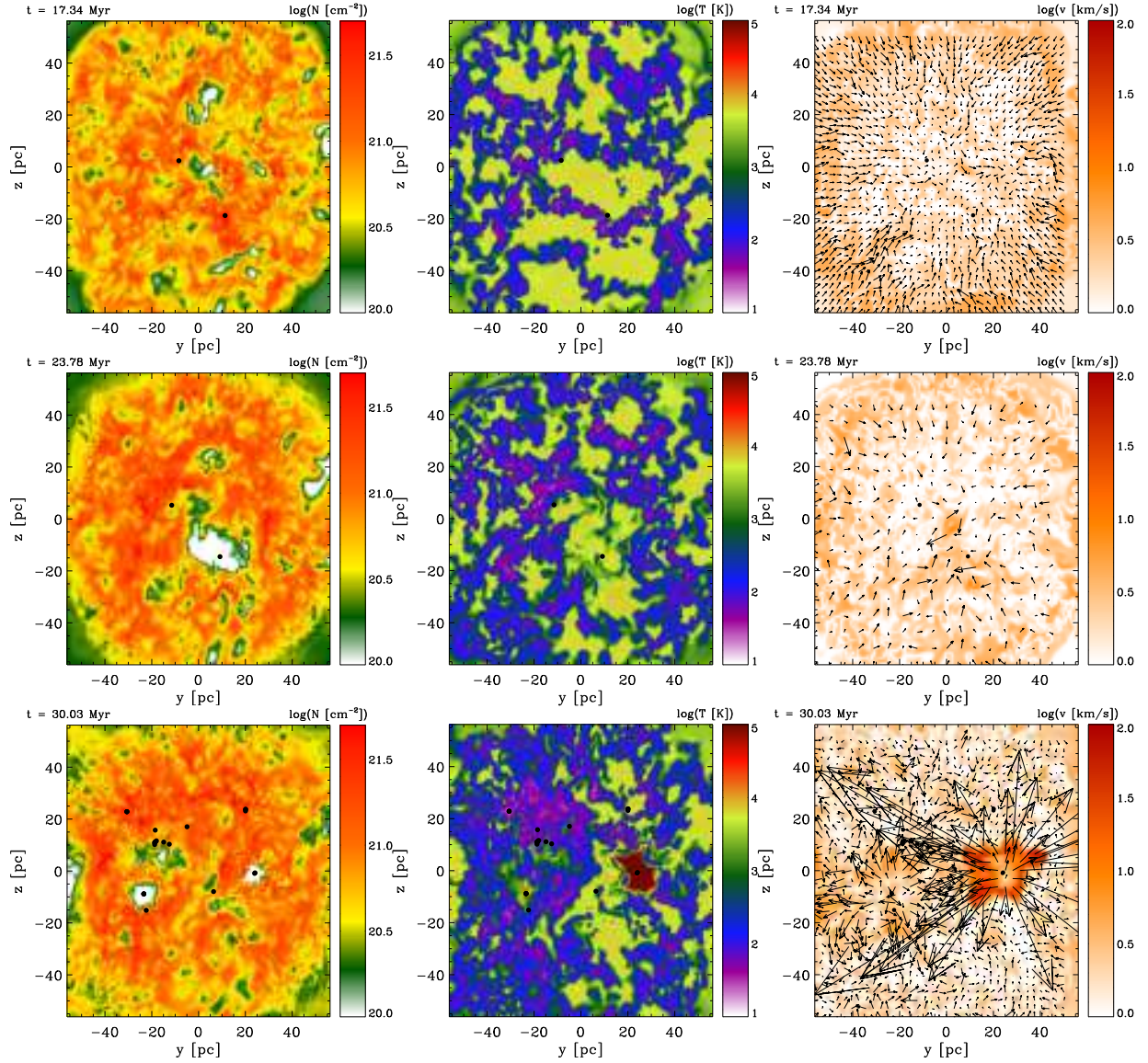
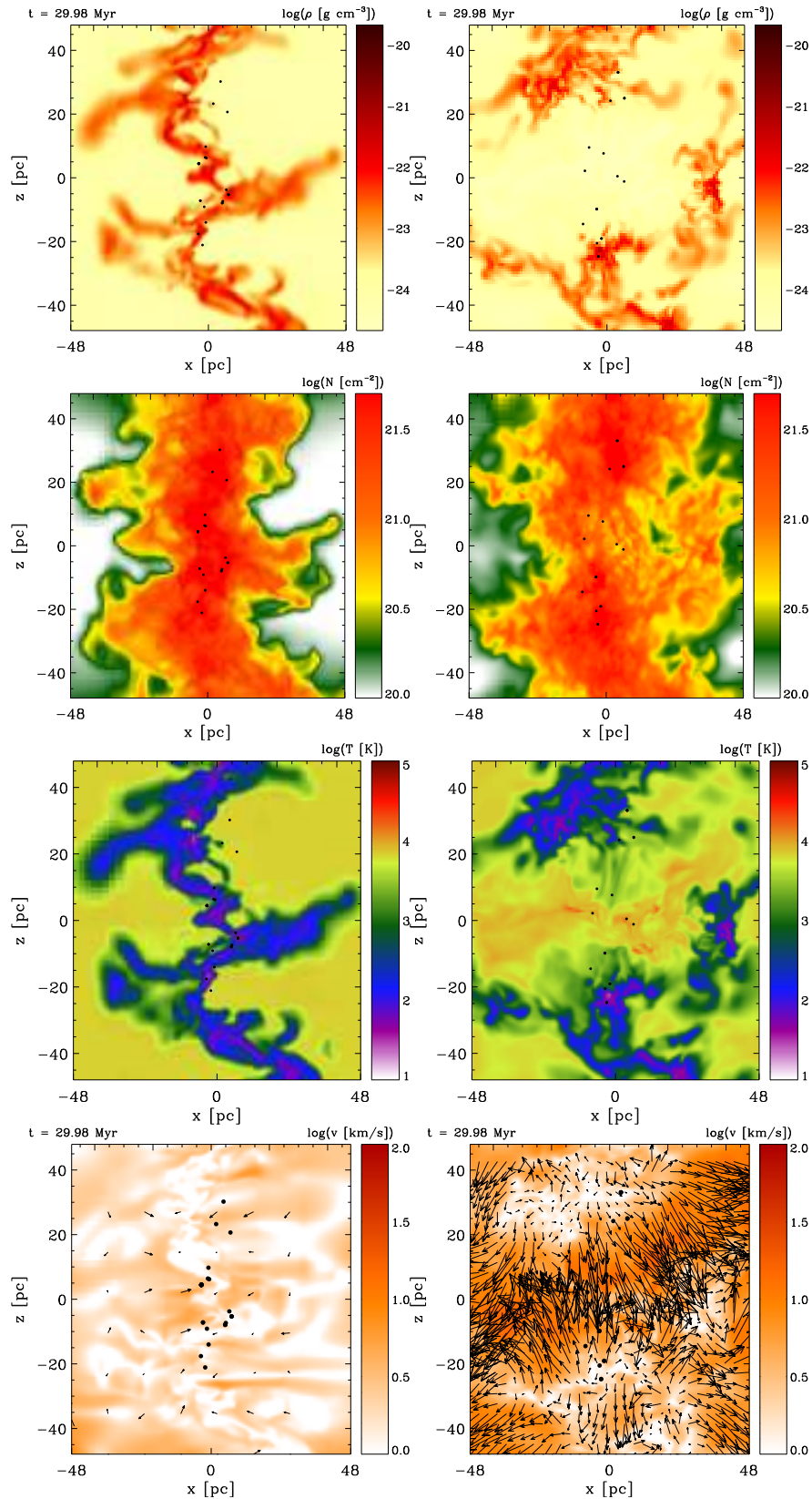


Figure 5.2: Data of run HR0.8Y. *Left to right:* Column density along the x -axis (parallel to the WNM streams, integration length is 40 pc), temperature, and absolute value of the velocity in the midplane ($x=0$). *Top to bottom:* Different evolutionary stages prior to and after supernova feedback. It is clearly seen that supernovae do not have a huge impact on the cloud dynamics and structure. The effects are only localised to some small regions of a few tens of parsec. In all cases, the typical vector in the velocity plots has a magnitude of $v_{\text{typ}} = 5 \text{ km/s}$. Note that the vector arrows are plotted with a linear scale. Stellar particles are represented by the black dots.



125

Figure 5.3: From top to bottom: Density in the $y=0$ -plane, column density along the y -axis (perpendicular to the WNM streams), temperature, and velocity magnitude. Left column for run HR1.0N, right one for HR1.0Y, respectively. The cloud is dispersed within a localised region. However, the column density map reveals a cloud with a tenuous region in its centre. The latter indicates that supernovae are not able to disrupt the whole cloud. The length of a typical vector is the same as in figure 5.2. Note that the vector arrows are plotted with a linear scale.

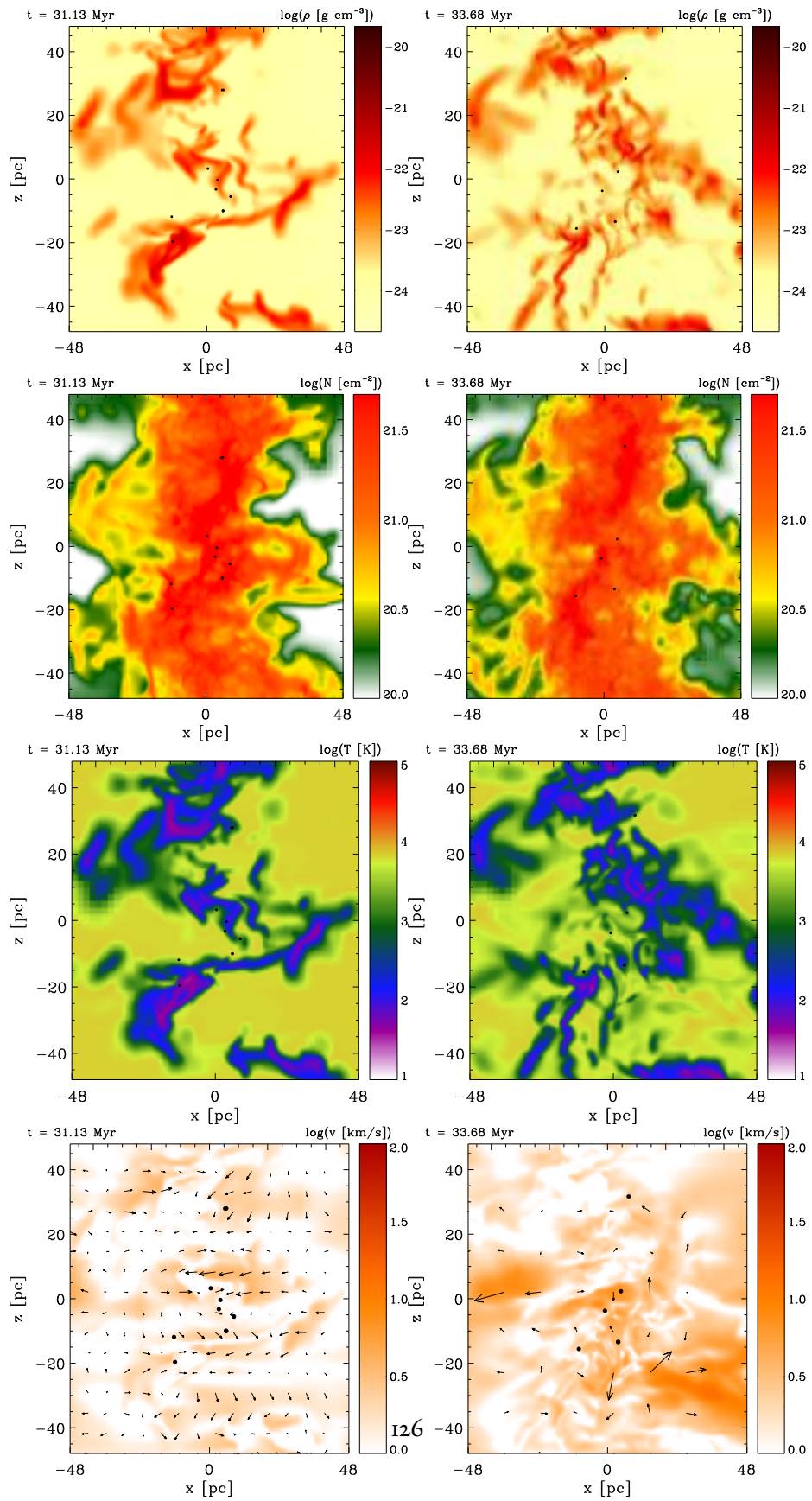


Figure 5.4: Same as figure 5.3, but for HR1.2N and HR1.2Y.

5.3.1 Thermal State of the Cloud

The redistribution of matter on large scales is accompanied by mixing of warm and cold gas on smaller scales. This is because of the turbulence generated by the multiple shock waves interacting with the substructures in the cloud as well as their interaction with each other.

The resulting increase of gas in the thermally unstable regime is seen in figure 5.5. We show the temporal evolution of phase space diagrams for runs HRo.8N, HRo.8Y, HRl.oN, and HRl.oY. The diagrams depict three times. The dynamical pressure of the converging flows terminated after about the dynamical flow time ($t_{\text{flow}} \approx 10 \text{ Myr}$) and is negligible at these temporal stages. In general, the gas evolves along the equilibrium curve. Most gas resides in the cold, stable regime. However, a significant part is also detected in the unstable regime. This material belongs to the halo surrounding the cloud. The scatter in the diagrams is due to ambient turbulent fluctuations that generate dilatational and compressive modes. Even in the case without feedback the pressure scatter increases with time. This is a result of global collapse and conversion of gravitational into (turbulent) kinetic energy.

The individual supernovae have a great, but short-lived impact on the phase space diagrams. The evolution of the supernova remnant creates over-pressurised volumes with high temperatures, as well as under-pressurised volumes with very low temperatures. Both phases are primarily seen in the low-density regime. However, the long-term evolution – indicated by large Δt in the plots – reveals that the gas is cooled faster than it is heated. This is best seen at $t = 24.3 \text{ Myr}$ in run HRo.8Y. There is only some scatter observed in the under-pressurised low-density regime. From $n \approx 10 \text{ cm}^{-3}$ the gas is in pressure equilibrium. For comparison, run HRo.8N reveals turbulent scatter in the same density regime.

The densest parts of the molecular cloud are barely affected. There only occurs a small decrease in mass, because the shock wave is not able to sufficiently disperse these regions. In the end of the simulation, the phase space diagrams look similar in the intermediate density regime for cases with and without feedback. That is, most of the gas mass evolves along the equilibrium curve. However, in the case of HRl.oN there is slightly more scatter.¹ All clouds affected by SN feedback reveal the emergence of low-density, hot material with temperatures of $10^3 - 10^4 \text{ K}$.

In figure 5.6 we show volume weighted and mass weighted temperature histograms. Most of the mass is in cold gas. The WNM instead contributes most to the volume fraction. The two

¹This density regime of HRo.8N cannot be compared with the corresponding case HRo.8Y since the latter is affected by a SN.

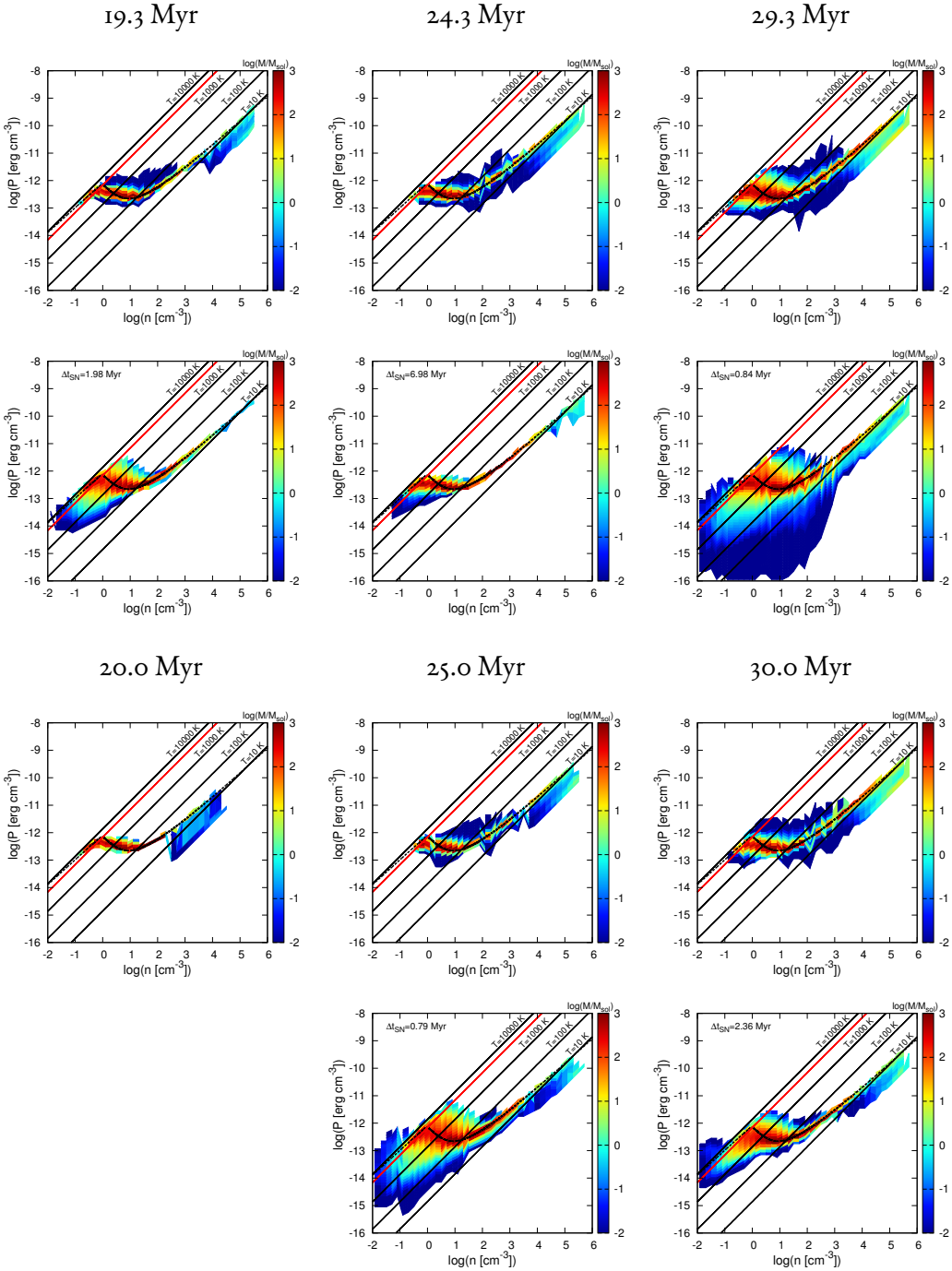


Figure 5.5: Phase space diagrams for the runs HR0.8N,HR0.8Y (top two rows) as well as HR1.0N and HR1.0Y (bottom two rows), respectively, without (upper row) and with (lower row) supernova feedback. Colour coded is the mass in each bin. Also shown are the isotherms for $T = 10, 100, 1000, 10000$ K (solid black lines) and the isotherm for $T = 5000$ K (solid red line). The dashed line marks the equilibrium pressure. The times within some of the plots denote the elapsed time since the last SN. Most of the mass is in the cold phase with the scatter being produced by turbulence. Interestingly, supernovae only produce short-lived strong deviations from pressure equilibrium. After a while the gas approaches equilibrium conditions again. The major difference at later times is the occurrence of a hot gas phase at low densities, which can be attributed to the cavity that has been created by the supernova explosion.

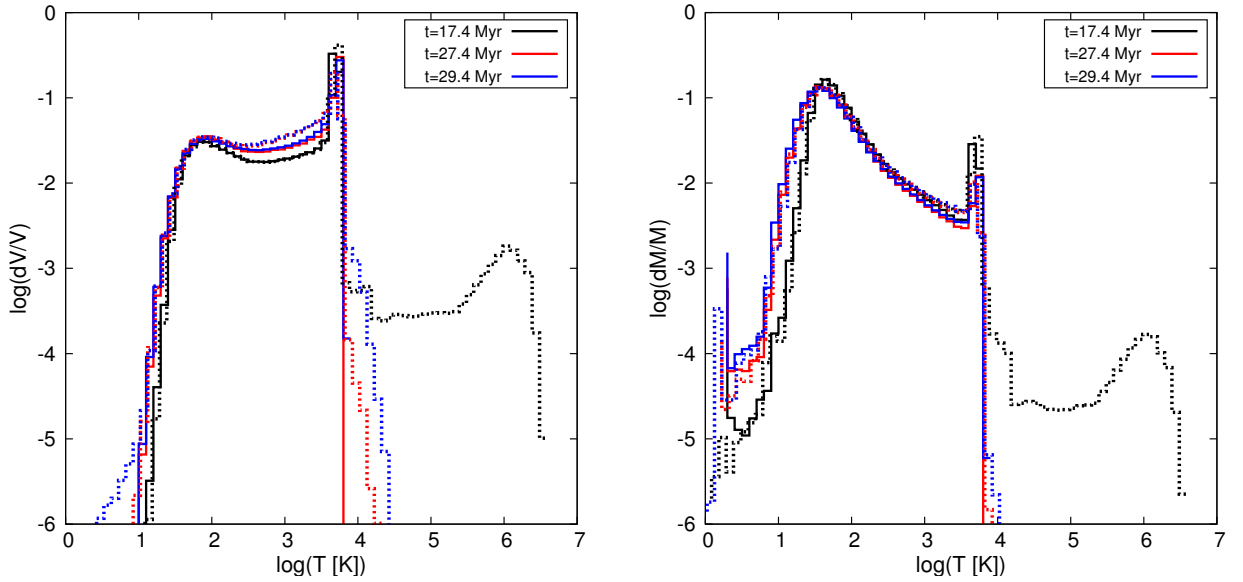


Figure 5.6: Temperature histogram for different evolutionary stages with (dotted) and without (solid) feedback for runs HR0.8. Note the large increase in temperature due to a supernova explosion (which went off shortly before the shown time). SN feedback results in an increased amount of material in the thermally unstable regime.

major thermodynamic phases of the ISM are clearly identified with temperatures of about $T = 40 - 50$ K for the cold gas and $T \approx 5500$ K for the WNM. A *three-phase* medium is only being generated for a transient period of time, with the additional phase being the hot gas (see also [McKee and Ostriker, 1977](#)). The volume- and/or mass-fraction is not significant and is only restricted to the supernova remnant. A more persistent effect is that supernova feedback converts cold gas to gas with moderate temperatures of $2.5 \leq \log(T/\text{K}) \leq 3.5$ with a net increase of $\approx 15\%$ in volume. The mass fraction, however, shows an increase of less than 1% in this temperature regime. We point out that an increase of gas in the thermally unstable regime can also be achieved via turbulent mixing alone (e.g. [Seifried et al., 2011](#)). However, in the case of supernova feedback it is a combination of (enhanced) turbulent mixing due to turbulence generated behind the shock fronts and efficient cooling of the gas. The latter is a result of moderate temperature and density enhancements in regions that are not directly affected by the hot stages of the SN, but rather by acoustic waves.

Interestingly, the mass-weighted histogram looks very similar to the one from [Hill et al. \(2012\)](#) in the range $|z| \leq 20$ pc, where z is the height above/below the disc midplane.

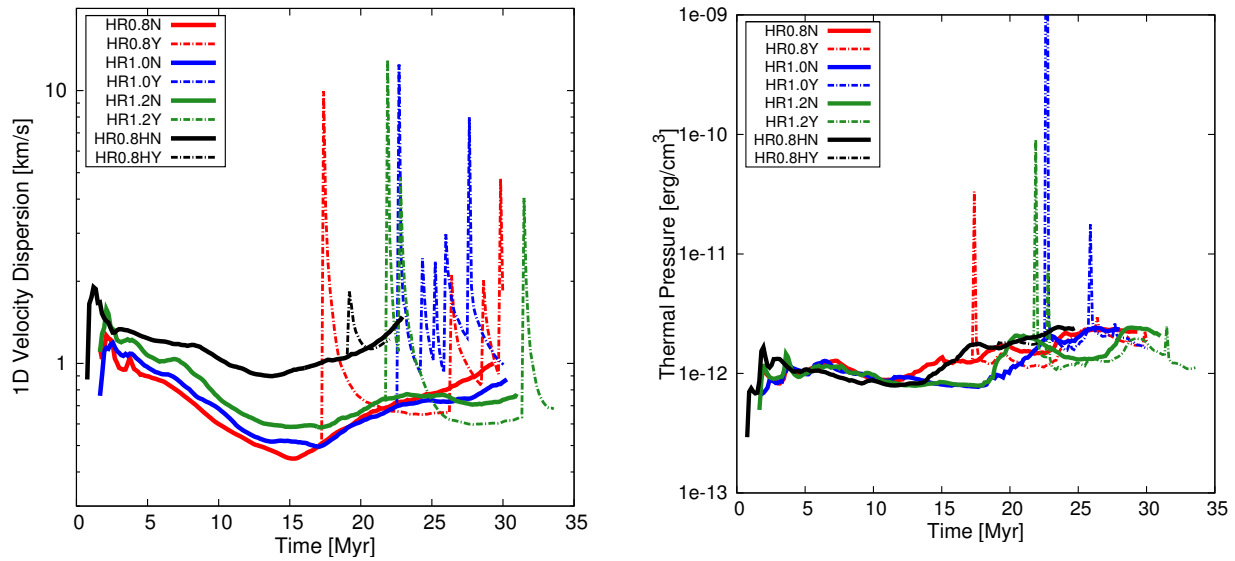


Figure 5.7: *Left:* Temporal evolution of the RMS velocity of the dense gas for all simulations. The supernovae only temporarily increase the velocity dispersion. This is due to the fact that the dense gas is even more compressed and most of the kinetic energy is hence converted into compressive work. Note that there occur stages where the RMS velocity in the SN runs falls below the no-SN values. Here, global collapse of dense regions towards the centre of the cloud is hampered. *Right:* Evolution of the dense gas’ thermal pressure. The densest parts of the molecular cloud show no significant increase of thermal pressure.

5.3.2 Long–Term Dynamical Evolution of the Dense Gas

In figure 5.7 we show the one–dimensional velocity dispersion (henceforth 1D–dispersion) and thermal pressure of the clouds. The former is calculated in accordance with [Gatto et al. \(2015\)](#), their eqs. (9) and (10)).

In general, the 1D–dispersion is higher for the hydro runs than for the MHD runs, roughly by a factor of 2–3. Hence the ambient magnetic field suppresses velocity fluctuations. The single supernova explosions are clearly seen by the sudden increase of the 1D–dispersion. Depending on the density of the region in which the supernovae go off, the 1D–dispersion reaches values of only 12 km/s. However, there are also peaks of only a few km/s in case the SN goes off in regions with high densities. This stage of increased velocity does not last long (up to ≈ 2 Myr), indicating the failure to transfer momentum to the dense gas. The compression of the gas also yields a decrease of the 1D–dispersion. The supernova shock front emanates outwards, while the molecular cloud gas collapses towards the centre of the cloud. When the shock hits the collapsing gas, a stagnation–like phase occurs. The velocities then fall below the values of the runs without supernova feedback (compare with the velocity pattern in figure 5.2). But, as can be seen, this effect again strongly depends on the number of supernovae going off, their individual position

to each other and their temporal sequence. Their relative position to each other is important because previous SN explosions clear the stellar environment from dense gas. For run HR1.oY there is an obvious net increase in 1D–dispersion by a factor of ≈ 2 . This is due to the formed supernova bubble, which is much more efficient in dispersing and driving mixing motions within the dense gas²(Sharma et al., 2014).

The evolution of the thermal pressure of the dense gas, P_{th} ($n > 100 \text{ cm}^{-3}$), is quite similar. The initial thermal pressure is $P_{\text{th,init}} \approx 7 \times 10^{-13} \text{ erg cm}^{-3}$. The compression by the flows and the turbulent fluctuations trigger thermal instability. The isobaric phase of this instability explains the occurrence of dense gas at pressures near the initial value. This phase does not last long and thermal pressure is increased over time. After the flows have decreased ($t \approx 10 \text{ Myr}$), the pressure almost stays constant, indicating the negligible influence of the flows on the thermodynamical state of the cloud.

The individual SN events are clearly identified by the sudden increase. However, most of the thermal energy is radiated away very rapidly. We point out that the cooling time of the dense gas is still 6–7 times longer than the sound crossing time within the injection region. Hence, we are not confronted with an over–cooling problem. The temporal decrease of the pressure, which is observed after SN events, is primarily due to efficient cooling. In the end, thermal pressure in the clouds subject to SN feedback approaches the one in the clouds without feedback.

5.3.3 Evolution of Energy Ratios of the Dense Gas

Figure 5.8 shows the evolution of the ratio of kinetic to gravitational energy as well as the ratio of total (thermal plus kinetic) to gravitational energy. The former ratio is being defined as

$$\alpha(\varrho > \varrho_{\text{thresh}}) = \frac{\frac{1}{2} \sum_i^N \mathcal{V}_i \varrho_i |v_i|^2}{\sum_i^N \mathcal{V}_i \varrho_i \Phi_i} = \frac{E_{\text{Kin}}(\varrho > \varrho_{\text{thresh}})}{E_{\text{Grav}}(\varrho > \varrho_{\text{thresh}})}, \quad (5.1)$$

with \mathcal{V}_i being the volume of the i –th cell and N being the number of cells with $\varrho > \varrho_{\text{thresh}}$. Φ_i is the gravitational potential in cell i . The first stage between 0 and 15 Myr is characterised by mass accretion. From 15 Myr on the ratio increases due to the conversion of gravitational energy into kinetic energy due to collapse (Vázquez-Semadeni et al., 2007). Feedback increases the ratio

²Please note that the formation of a supernova bubble is simply because of the clustered sink particles. In this sense, the efficiency of SN feedback in this simulation changes if no bubble is formed.

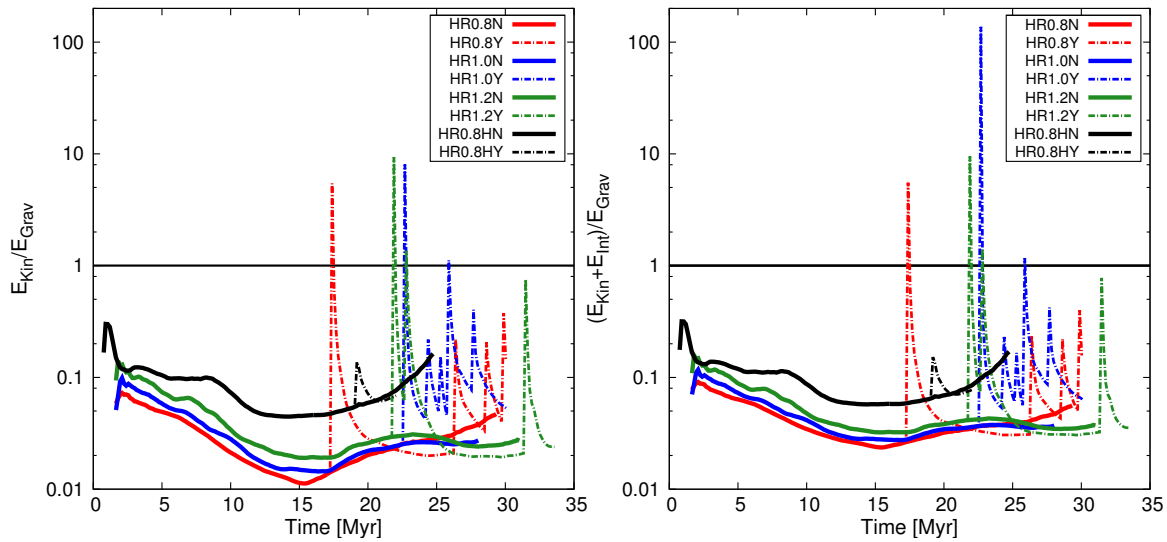


Figure 5.8: *Left:* Ratio of kinetic to gravitational energy. *Right:* Ratio of kinetic plus thermal to gravitational energy. Only at the time when a supernova goes off, kinetic and thermal dominate. The ratio tends to increase with increasing number of supernovae, but it seems to strongly depend on the cloud morphology or the environment where the supernova goes off.

for a small amount of time. During the supernovae the energy budget of the dense gas is purely controlled by kinetic (and thermal) energy. In this time interval, *the cloud seems to be rendered unbound* with virial parameters $\alpha \geq 2$. However, gravitational energy immediately dominates again. If the time between subsequent supernovae is too long, the ratio falls below the ratio in the cases without feedback. If the time between individual explosions is short (as in case HR1.0Y), the energy input yields a net increase of the ratio. However, there need to be far more supernova explosions in order to achieve (virial) equilibrium stages. Inspection of the density dependence of the energy ratios (not shown) reveals that equipartition is attained at densities of about $n \approx 10 \text{ cm}^{-3}$ for all runs, far below those that have been used to define the cloud.

5.4 Star Formation

5.4.1 Number and Mass of Sinks

Figure 5.9 shows the temporal evolution of the total stellar mass as well as of the number of particles. The stars accrete gas and the mass increases with time. A decrease in total mass is seen as the initial turbulence is increased, because the stellar accretion rates are influenced by the velocity fluctuations. Additionally, dense regions are more stable against collapse or they are dispersed very quickly. This also results in a smaller number of stars in the cloud. Also note the large dif-

ference of the stellar mass and number in the clouds of the hydrodynamic and MHD case with $\mathcal{M}_{\text{turb}} = 0.8$, indicating the balancing impact of the magnetic field (Vázquez-Semadeni et al., 2011; Hennebelle, 2013; Körtgen and Banerjee, 2015).

Now, in turn, if supernova feedback is included, the number of stars is reduced. Dense regions are evacuated and hence the seeds for star formation are missing. However, a closer look to runs HRo.8H shows that there are more stars in the clouds subject to feedback, than in the clouds without stellar feedback. This indicates the possible triggering of star formation. However, triggered star formation is not seen in the MHD runs, but analysis of this effect is beyond the scope of the underlying study.

The accretion rates are also being reduced by the supernova explosions. This leads to an overall reduction of the total stellar mass, which is of about a factor of two for the MHD runs, but less for the hydro run. The latter is due to the limited simulation duration. Further evolution should show a greater decrease in stellar mass. One interesting aspect concerning the total stellar mass is seen in the evolution. For runs HRo.8Y and HR1.2Y there is a period of nearly constant stellar mass, although there exist two stars in the cloud. Since only one star has gone off as a supernova, this indicates that the shock wave swept over the second star. The second star's mass supply is being dispersed, thus stopping the star's accretion either completely or reducing it to very low values. The increase of the mass at later times begins at roughly the same time as the formation of new stars.

5.4.2 Star Formation Efficiency & Rate

Figure 5.10 shows the star formation efficiency (SFE, see also section 2.4) and the temporal derivative of the *total* stellar mass, which we refer to as star formation rate (SFR), as function of time. In general, both quantities are seen to increase with time. The non-magnetised clouds show a steeper increase of the SFE, as well as of the SFR, at least during the later evolutionary stages. This difference is due to the lack of additional magnetic support against gravity (see e.g. Körtgen and Banerjee, 2015). The SFE for the magnetised clouds shows a decrease with increasing initial turbulent Mach number. The strong variation for run HR1.2N is due to the increase of the cloud's mass. This variation is also seen in the other two clouds (HRo.8 and HR1.0), but in a weaker fashion. In the end, values of 15–20 % are reached.

A similar trend is seen in the SFR. Here, the major difference compared to the hydrodynamic cases is the almost constant evolution for the first 5 to 10 Myr after star formation has begun. The

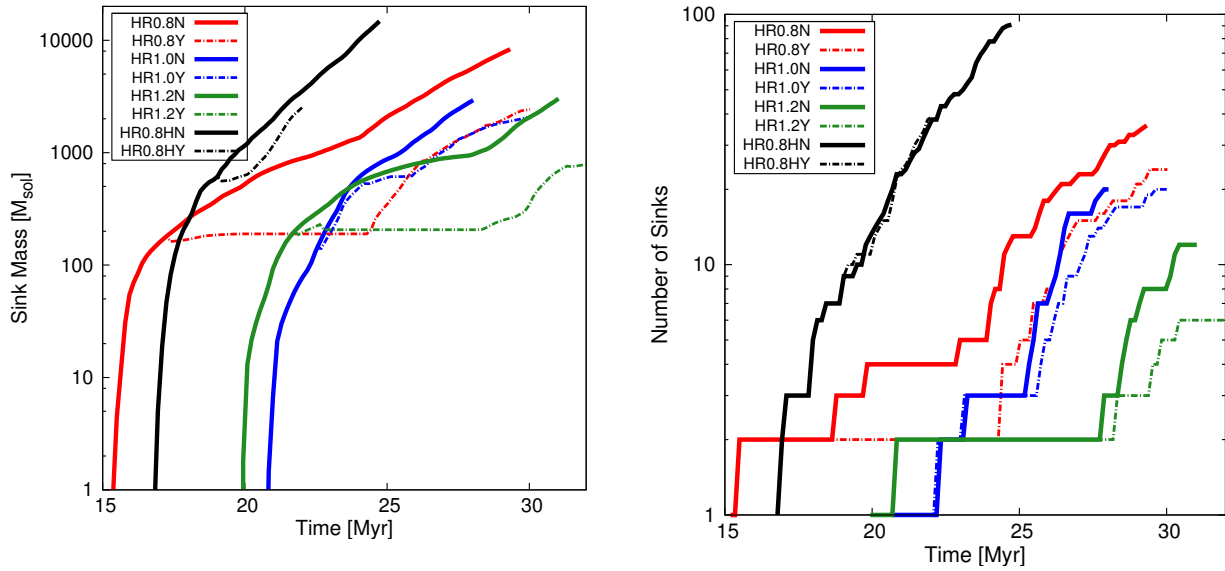


Figure 5.9: *Left:* Temporal evolution of sink particle mass (solid: without feedback, dash-dotted: with feedback). *Right:* Number of particles (solid: without feedback, dash-dotted: with feedback).

late increase of the SFR is due to global contraction of the cloud, where the magnetic field is not capable of counterbalancing gravity.

If feedback is included, both quantities are significantly decreased. Temporal variations in the accretion properties of both clouds and stars yield reduction efficiencies of factors 2–4. In the end of the simulations, the SFE is reduced by at most a factor of 2. The SFR shows a more pronounced evolution. The supernovae are obviously seen by the sudden decrease in the SFR. The overall impact of supernova feedback is firstly a reduction and secondly a roughly constant SFR. The former is due to less efficient accretion of the existing stars as well as suppressed formation of new stars. The latter is due to the evacuation of dense gas from the centre of the cloud, where most of the stars reside. This, in turn, affects the accretion behaviour of the stars. In the runs without feedback, global collapse increases the amount of gas that can (and will) be accreted by the individual stars. The SFR is finally being reduced by roughly a factor 2–4.

5.5 The One-Dimensional Velocity Dispersion

Observations of HI in emission indicate that the one-dimensional velocity dispersion of the WNM is $\sigma_{\text{HI}} \approx 10$ km/s (e.g. Heiles and Troland, 2003; Tamburro et al., 2009). SN feedback is thought of driving such velocities and models including driven turbulence in the ISM often

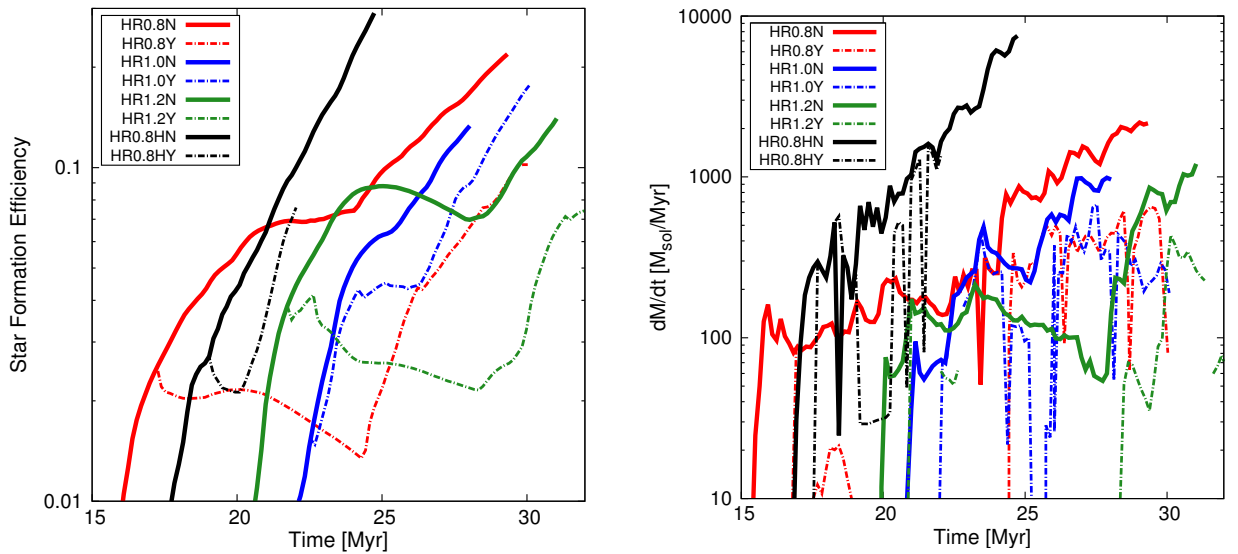


Figure 5.10: Temporal evolution of the star formation efficiency (left) and corresponding star formation rate (right). Supernova feedback decreases the SFR by about a factor of 2–4. The SFE is only reduced by at most a factor of 2.

use these values as the typical turbulent velocity (e.g. [Gatto et al., 2015](#), and references therein). However, as [Gatto et al. \(2015\)](#) report, SN feedback seems to be not capable of driving such high velocity dispersions in HI for longer timescales. Figure 5.11 shows the one-dimensional velocity dispersion as function of density at the end of each (MHD) simulation, using the recipe given in [Gatto et al. \(2015, their eqs. \(9\) and \(10\)\)](#)³. As can be seen, velocity dispersions can be as high as ≈ 20 km/s, but only for the low-density gas. The WNM with densities of $0.5 \leq n/\text{cm}^{-3} \leq 5$ reveal values of typically 1.5–5 km/s in clouds subject to SN feedback, far lower than the one observed. The large spread (also for the clouds without feedback) is due to the different accretion properties of the clouds themselves. For run HR0.8Y, there occurred a SN event shortly before the end of the simulation. That is why the velocity dispersion is higher compared to HR1.0Y and HR1.2Y. Even for the case of clustered supernovae, the one-dimensional velocity dispersion cannot reproduce observational results.

5.6 Lifetimes of Individual Regions within the Clouds

In order to evaluate the efficiency of SNe in disrupting small regions within molecular clouds, we give a comparative overview in table 5.1. SN feedback is much more efficient in disrupting

³Note that we do not include different chemical species. Thus the velocity dispersion is for one fluid and we compare our WNM regime with the HI emission results.

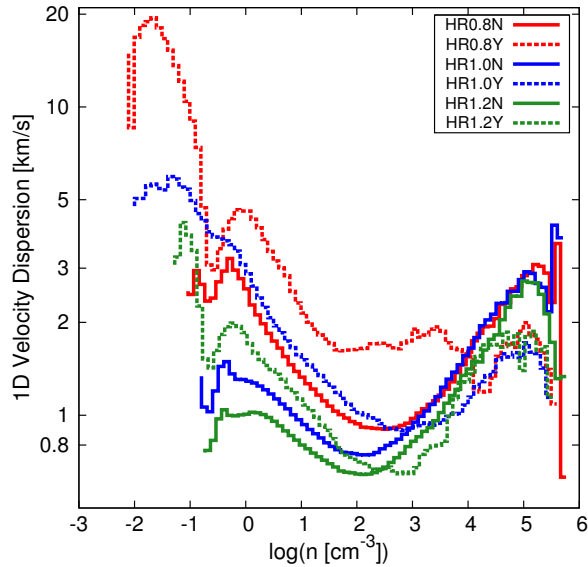


Figure 5.11: One-dimensional velocity dispersion as function of number density. As is shown, the values fail to reproduce observational results, indicating that SN feedback alone may not be the source of the observed HI dispersion. Note the lower velocity dispersion in the densest parts of the cloud due to stalled gas motions.

embedded structures like clumps and cores since the timescales (derived from simulation data: Estimate of cavity size at a timestep t after a SN has gone off.) for the disruption are roughly an order of magnitude smaller than for ionisation feedback. Our results are in good agreement with the study by [Martizzi et al. \(2015\)](#), who carried out simulations of individual SNe going off in an inhomogeneous medium. However, our achieved timescales are somewhat larger, because on the one hand, they did not include a magnetic field. On the other hand, the densities within our clumps, in which the massive stars explode, might be higher by up to two orders of magnitude. Hence, radiative cooling is much more efficient in our simulations. In contrast, [Rogers and Pittard \(2013\)](#) give larger timescales for the disruption of a clump by SN feedback of approximately 1.5 Myr, although the authors have included feedback mechanisms prior to the SN.

5.7 Chapter Summary and Discussion

5.7.1 Discussion: Missing Physics

We point out that our simulations lack the progenitor feedback mechanisms like stellar winds and the star's ionising radiation. In order to estimate the impact of progenitor feedback, one can

Table 5.1: Estimated diameter and destruction timescale for different feedback mechanisms.

Source	Diameter (pc)	Timescale	Form of Feedback
HR0.8Y ^a	4.8	29 kyr	SN
HR1.0Y ^a	9.7	50 kyr	SN
HR1.2Y ^a	6.5	14 kyr	SN
Rogers and Pittard (2013)	8	<1.5 Myr	SN
Colin et al. (2013)	10	10–20 Myr	Ionisation
Dale et al. (2014) ^b	10	10–20 Myr	Ionisation
Martizzi et al. (2015) ^c	10	15 kyr	SN

^aThis study.

^bDale et al. (2014) give the size of the region, but do not give a concrete destruction timescale. However, they argue that their timescales are comparable to Vázquez-Semadeni et al. (2010).

^cThe size of the region is read off by eye from their figure 1.

calculate the cooling timescale

$$t_c = \frac{3}{2} \frac{k_B T}{n \Lambda(T)}. \quad (5.2)$$

Here, k_B is Boltzmann’s constant, T is temperature, n is the number density of the heated gas, and $\Lambda(T)$ is the temperature dependent cooling function, respectively. t_c then gives the timescale when cooling starts to become dominant. For our simulations, typical densities in the stellar environment are in the range $n \in [10^2, 10^5] \text{ cm}^{-3}$ and the SN temperatures are as high as $T = 10^7 - 10^8 \text{ K}$. The cooling function at these temperatures is roughly constant ($\Lambda(T) \approx 5 \times 10^{-23} \text{ erg cm}^3 \text{ s}^{-1}$). These values give $t_c(T = 10^7 \text{ K}) = 1.3 \times 10^{-5} - 1.3 \times 10^{-2} \text{ Myr}$ and $t_c(T = 10^8 \text{ K}) = 1.3 \times 10^{-4} - 1.3 \times 10^{-1} \text{ Myr}$, which are still larger than the dynamical timescale, as stated in section 5.3.2. Hence, the major part of the injected thermal energy is radiated away within only a few timesteps. The resulting heating of parts of the molecular cloud is then due to shock heating and the dispersion of gas clumps is driven by momentum input. In contrast, if the high-mass star generates a large HII region, the SN will go off in a region of tenuous gas with densities of the order of $n_{\text{HII}} = 0.1 - 1 \text{ cm}^{-3}$. The cooling timescale then increases to $t_c(T = 10^7 \text{ K}) = 1.3 - 13 \text{ Myr}$ and $t_c(T = 10^8 \text{ K}) = 13 - 130 \text{ Myr}$, respectively. The SN remnant is hence only subject to adiabatic cooling and should expand much further due to its pressure-driven evolution up to the point where the SN remnant hits the shell that was being swept-up by the HII region. The combined effects of ionising radiation and SN should then be

able to disrupt entire molecular clouds on timescales less than that for pure ionising feedback, that is, of the order of a few Myr. This is also in agreement with the study by [Sharma et al. \(2014\)](#), who showed that superbubbles can retain up to 40 % of their energy over longer timescales, in stark contrast to the failure of individual SNe. Please note that our failure to fully disrupt the clouds with SNe alone, and our proposal that possibly the combined action of ionising radiation and SNe may accomplish this task, should not be confused with recent results by [Dale et al. \(2012\)](#) that ionising radiation alone is not capable of destroying very massive clouds ($\approx 10^6 M_{\odot}$). In their case, it is possible that the difficulty in destroying such clouds arises by the initial conditions considered by those authors (initially spherical clouds), since the spherical geometry causes the deepest possible potential wells, while real clouds are more likely sheetlike or filamentary (e.g. [Bally, 2001](#); [Heiles and Troland, 2003](#)) as is the case of the cloud in our simulations. In our case, the inability of the SNe alone to destroy the clouds is due more to its brief, impulsive nature, and the combination of this kind of feedback with ionising radiation may well be capable of destroying even very massive clouds.

5.7.2 Summary

In this study we have presented results from numerical simulations on molecular cloud evolution including supernova feedback from high-mass stars. The results suggest that supernova feedback alone is not sufficient to disrupt molecular clouds, consistent with previous studies. The dispersal is only restricted to some minor part of the parental cloud. Though the efficiency in disrupting the cloud is very low, supernovae still create regions of moderate temperature, which affects the thermodynamic behaviour of the gas. The efficiency also strongly depends on where the supernova goes off, on the number of supernova events, as well as on the porosity of the cloud. Single supernovae initially show signs of compression, which might lead to triggered star formation. With time, the shocks disperse those regions and the net effect is a negative feedback (disruption). If the supernovae are clustered, their combined energy and momentum input is sufficient to disrupt larger amounts of the parental cloud. However, even with clustered supernovae, the cloud is not fully destroyed. The supernovae are still able to remove up to 50 % of the total cloud mass. The inhomogeneity of the cloud due to initial turbulent fluctuations enables energy from the SN to escape through low-density channels. On the other hand, more turbulent clouds are also less compact and the substructures are hence dispersed more easily. The suppression of star formation, however, is quite effective with reduction of the SFE and

SFR by factors of 2–4, again consistent with previous studies on SN feedback. This is due to the fact that there occurs a short–period, but sufficient momentum transfer to the dense gas, which leads to their dispersion. However, our results indicate that star formation is not halted and continues throughout the simulation ($t \sim 35$ Myr) in all cases.

6

Summary and Outlook

The analysis of molecular cloud formation and evolution is a pivotal aspect for the understanding of the ISM and the eventual formation of stars. In the following, I will briefly recapitulate the main results of this study and give an outlook to future studies.

6.1 Summary: Magnetic Fields in the ISM

In chapter 4 I studied the influence of different initial magnetic field strengths in the ISM on the formation and evolution of molecular clouds. The clouds were formed in the shock-compressed layer of two converging cylindrical streams of diffuse H I gas. These flows were aligned with the background magnetic field and turbulent. The turbulent fluctuations were varied from subsonic to slightly supersonic. The magnetic field strength was adjusted to cover scenarios where the thermal energy dominates over magnetic energy ($B_0 = 3 \mu\text{G}$), where the fields are initially in equipartition ($B_0 = 4 \mu\text{G}$), and where magnetic energy dominates the energy budget ($B_0 = 5 \mu\text{G}$), respectively. I showed that supercritical and thus star forming cores can only form, when the initial magnetic field strength is sufficiently weak (that is, $B_0 = 3 \mu\text{G}$) or the magnetic energy initially

is at most in equipartition with the thermal energy of the gas. I discussed the morphology of the magnetic field and the dynamics of dense cores within the molecular clouds. The morphology of the field is coherent for $B_0 \geq 4 \mu\text{G}$ due to the restoring action of the Lorentz-force and twisted in case of $B_0 = 3 \mu\text{G}$ due to collapse. In the former case, cloud cores thus only undergo phases of compression and re-expansion.

In a second step I introduced an angle between one flow and the background magnetic field, which resembles non-ideal MHD effects. I highlighted that inclined collisions induce strong shear-flows that tend to decrease the cloud mass and density. The onset of star formation is delayed with increasing tilt in case of $B_0 = 3 \mu\text{G}$. In case of larger field strengths, I showed that dense cores can form in contrast to what is observed for head-on colliding flows. However, the formed cores were Jeans stable and subcritical. These results raise the question how star formation is achieved in strongly magnetised environments and how supercritical molecular clouds – as observations indicate – are being formed.

6.2 Summary: Supernova Feedback in Molecular Clouds

Chapter 5 was dedicated to the study of supernova feedback in molecular clouds. I showed that supernova feedback *alone* is not able to disrupt the entire parental molecular cloud. Instead, the influence of the feedback is restricted to a few tens of pc. However, supernovae are much more efficient in disrupting these small regions than other feedback mechanisms that occur already during the lifetime of the star. In detail, I showed that supernovae affect regions of sizes $\sim 10 - 20$ pc on timescales $\lesssim 1$ Myr, compared to e.g. dispersion by ionisation feedback with timescales a factor of ten larger. I argued that the transfer of energy and momentum to the dense gas (with densities $n \gtrsim 100 \text{ cm}^{-3}$) is not persistent. Most of the energy and momentum is lost due to either radiative cooling or compression of the surrounding gas. If, in addition, the initial WNM flows are trans- or mildly supersonic, the clouds are porous. I highlighted the importance of this porosity for the ability of the hot gas to escape through low-density channels. Due to this leakage, the efficiency of supernova feedback is reduced.

Furthermore, I analysed the impact of the feedback on the cloud's star formation rate and star formation efficiency. I showed that both quantities are reduced by roughly a factor of 2. However, the reduction of the star formation rate can be as high as a factor of 4, depending on the cloud morphology. Though, in all cases, star formation is not inhibited.

6.3 Outlook: Magnetic Fields in the ISM

What is the detailed role of ambipolar diffusion?

Vázquez-Semadeni et al. (2011) already pointed out that ambipolar diffusion is not fast enough to speed up the star formation process. I have argued in this study that inclined WNM flows induce the formation of dense cores within the molecular clouds, irrespective of the strength of the background magnetic field. Additionally, I have carried out a simulation with AD, but also with a large inclination. The result is that the shear-flows delay or suppress the formation of cores with high densities. In future studies, it is thus worth investigating the effects of small inclination and AD, which will further increase the diffusivity of the magnetic field. This will enable the formation of cores with densities, where AD is efficient and faster.

What is the impact of an external gravitational field?

The ISM is subject to an external gravitational acceleration resulting in e.g. gas falling into the potential well of a spiral arm. A future study aims at implementing such an external field. In simulations of the Galactic disc, it is already taken care of this potential (e.g. Walch et al., 2014; Gatto et al., 2015). The additional acceleration might help to bind the gas to the collision plane. Re-expansion of the gas is hampered and it might collapse. However, the parameter space for this kind of simulations increases due to the values of the stellar surface density as well as the functional form of the external potential.

What is the influence of shock-cloud interaction or multiple flow episodes?

The lack of star formation in clouds with realistic initial magnetic field strength might be due to too weak external pressure. The flows do not provide enough external compression so that the early re-expansion unbinds the clouds. This issue might be overcome due to larger coherent flows as suggested by Hartmann et al. (2001) and Vázquez-Semadeni et al. (2011). However, the coherence of WNM flows in a strongly turbulent ISM is questionable.

Molecular clouds can form in between colliding supernova shells. Multiple episodes of shock compression are then able to provide enough external pressure to keep the cloud material confined and drive it into gravitational collapse. Another, quite similar approach is the formation

of clouds in between flows with varying velocities/mass flux. Firstly, the cloud is compressed by high Mach number flows (e.g. SN) and is later on subject to further compression by lower Mach number flows (e.g. cooled SN remnants).

6.4 Outlook: Supernova Feedback in Molecular Clouds

What is the impact of multiple feedback mechanisms onto the cloud evolution?

As pointed out in this study and [Colin et al. \(e.g. 2013\)](#), the combined effect of ionisation and supernova feedback should disrupt the entire molecular cloud on timescales of ~ 10 Myr. This should indeed be analysed in the future since both feedback processes provide the major energy input from high-mass stars. However, one should take care of the influence of the initial conditions since the cloud morphology depends on the flow dynamics. In a second step, stellar winds can be included. Their influence helps to stabilise the evolution of the emerging H II regions and might help to faster disperse dense cores ([Dale et al., 2013](#)).

What is the impact on individual clumps and cores and the clump mass function?

Stellar feedback influences surrounding cores within the molecular cloud, but it remains to be evaluated to which extent. We aim to study the dynamics of dense cores. How are they disrupted, if they are disrupted at all? What happens to the mass spectrum of clumps in a certain molecular cloud? What is the influence on the spacing of fragments within the cloud?

Supernova-Flow Interaction

If the WNM streams are coherent over a large distance, high-mass star formation may have begun before the flows have vanished. In this study, the effect of high-mass stars onto the flow dynamics can be analysed. Specifically, what is the resulting mass-flux onto the cloud. Do supernovae terminate the flows completely due to the formation of supernova bubbles? A possible imprint of stellar feedback on the mass flux of coherent flows would indicate an upper limit for the masses of molecular clouds formed by converging streams, as is already being discussed in the literature.



Appendix

A.1 The Magnetised ISM: Estimate of the Effective Magnetic Diffusion

We here give a simple estimate for the dependence of the ambipolar diffusion coefficient on the magnetic field strength and the inclination of the flow. Specific numerical values are not of special interest here.

The AD diffusion parameter is $\eta_{AD} \propto B^2$. The respective numerical diffusivity is given by the product of the grid size and the Alfvén speed. The ratio η_{AD}/η_{num} estimates the influence of magnetic to numerical diffusion. In order to receive the diffusion for tilted flows, we make use of the fact that inclined flows will generate tilted field lines. This tilting can be interpreted as impact of magnetic diffusion. The perturbed field δB (which is here important for the diffusion coefficient) and the initial background field are then related by $\delta B = B_0 \sin(\varphi)$, where the tilting angle of the perturbed field, χ , and the inclination of the flows, φ , are related by $\chi = 90^\circ - \varphi$. The resultant ambipolar diffusion coefficient is then modified to $\eta_{AD} \propto B_0^2 \sin^2(\varphi)$, which gives zero diffusion for aligned flows and maximum diffusion for the perpendicular case

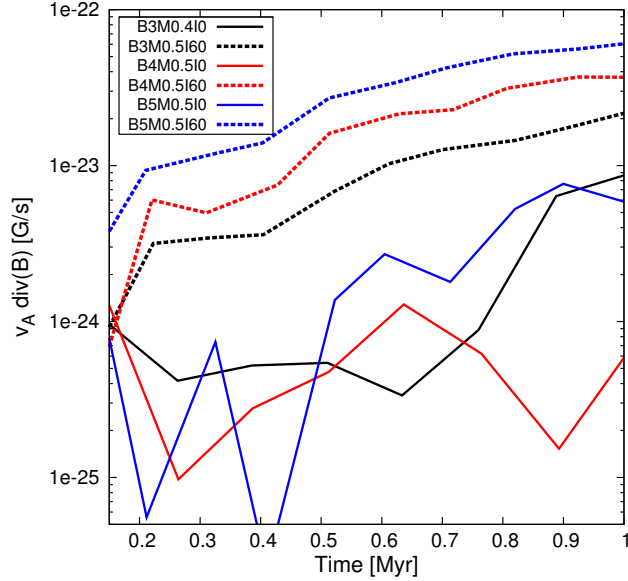


Figure A.1: Shown is the deviation from the induction equation due to diffusion in the ideal MHD limit for inclinations of 0° (solid) and 60° (dashed). Different colours indicate different initial magnetic field strengths.

(see fig. A.1).

A.2 SN Feedback: Resolution Study

As stated in section 3.4, supernova feedback is only enabled if the total sink particle mass exceeds $M_{\text{Kroupa}} = 160 M_\odot$. Figure A.2 shows the total mass of stars for three simulations with varying numerical resolution. The Kroupa–mass (horizontal solid black line) is reached at different times. However, the temporal difference is not significant for the global evolution of the cloud since it is only about 1 Myr. With time, the total stellar mass converges. It is thus independent of the numerical resolution. The usage of our IMF–fitting approach then gives the same supernova features for different resolutions. Note that the initial stages of the sink particle evolution differ due to different threshold densities. These densities influence the formation of sink particles as well as their accretion behaviour (gas is only accreted onto the sink particle, if the density in the respective cells exceeds the threshold density).

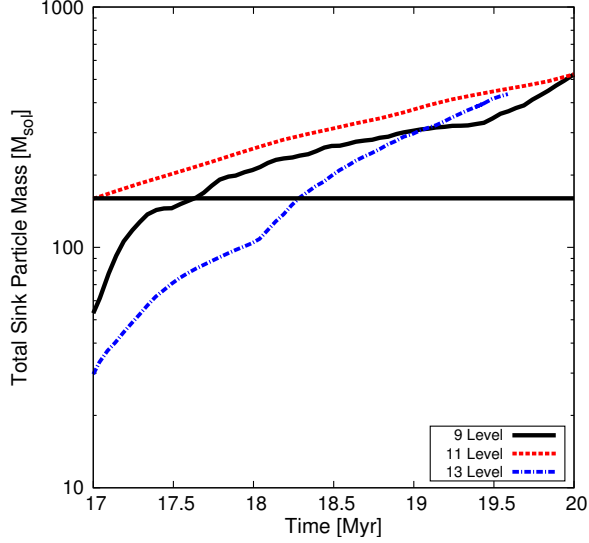


Figure A.2: Resolution study showing the mass of all sink particles as function of time for a time interval of $\Delta t \approx 3$ Myr. The horizontal black line denotes the critical cluster-mass for having at least one high-mass star. The temporal difference for reaching the critical mass is about $t_{\text{diff}} \approx 1.2$ Myr. It is thus not significant for the long-term dynamical evolution of the cloud. The total mass in all sink particles converges after some Myr of evolution.

A.3 Notes on the Supernova Rate

We use a supernova rate (in terms of *supernovae per solar mass*) as a combination of the observed supernova rate (in terms of *supernovae per year*) and the Galactic star formation rate (in terms of *solar mass per year*). This gives

$$\text{SNR}_M(\#/M_\odot) = \frac{\text{SNR}_{\text{yr}}(\#/yr)}{\text{SFR}(M_\odot/yr)}. \quad (\text{A.1})$$

Using values for $\text{SNR}_{\text{yr}} = (44 \text{ yr})^{-1}$ from (Tammann et al., 1994) and $\text{SFR} = 1 M_\odot \text{ yr}^{-1}$ from (Mac Low and Klessen, 2004), the supernova rate becomes

$$\text{SNR}_M = (44 M_\odot)^{-1}. \quad (\text{A.2})$$

This is analogous to a calculation of the supernova rate directly from an IMF. Using an IMF, SNR_M is just the number of high-mass stars per unit solar mass. For a Kroupa-IMF $\text{SNR}_M = (100 M_\odot)^{-1} - (160 M_\odot)^{-1}$, depending on the detailed numerical constants. The SNR in this study is hence three to four times higher than those from IMF estimates and thus gives an upper limit on the efficiency of cloud dispersion and disruption by supernovae.

For comparison, [Joung and Mac Low \(2006\)](#) and [Gatto et al. \(2015\)](#) use the rate from [Tammann et al. \(1994\)](#) and scale it down to the respective size of the simulation box (compared to the area of the Galaxy). This gives

$$\text{SNR}_{256 \times 256 \text{ pc}^2} = 2 \text{ SNe/Myr}. \quad (\text{A.3})$$

Knowing the number of SNe and the time interval in which they are going off, we are able to calculate a SN-rate in terms of *supernovae per Myr*. The results give $\text{SNR}_{\text{Myr}} \approx 1.7 \text{ SNe/Myr} - 2.1 \text{ SNe/Myr}$ in very good agreement with the above mentioned studies.

Acknowledgments

FIRST of all, I want to thank Robi Banerjee for giving me the opportunity to work on this fascinating topic. I want to thank him for his guidance, overall supervision, and sometimes also his patience. The discussions with him about star formation, magnetic fields and the latest Bundesliga–statistics were always extremely fruitful for me. His ongoing fascination and motivation have always been a new source of energy. Lastly, I want to thank him for giving me the opportunity to teach undergraduate students. It has been a great pleasure and experience for me to teach although students can sometimes be very cruel.

It is a great pleasure to have Stefanie Walch–Gassner as my second referee. I want to thank her for delightful discussions about the violent, but very interesting feedback from supernova.

I am also very grateful for stimulating discussions about MHD with Johannes Reppin and Jacques Wagstaff, and Volker Perdelwitz. Special thanks go to Christiane Diehl for discussions about astrophysics in general and for her extremely tasteful cakes and cookies. I further want to acknowledge FLASH and MPI support by Gunther Lukat. His deep wisdom on MPI–stuff was always a good help!

I thank Enrique Vázquez–Semadeni for stimulating discussions on molecular cloud formation and feedback and for his supervision during my stay at CRyA, Morelia in 2012 and Clare Dobbs for providing me the figure about the velocity dispersion – surface density scaling.

A very special thank you goes to Daniel Seifried. He always had time for discussions about FLASH, MHD, star formation, cloud formation, soccer, etc. I thank him for his expertise and his motivation to discuss about new ideas and old problems. Thanks!

DEAR Anja and Linus. Without you and your ongoing support, this work would have never been possible! I thank you for listening to essentially the same stuff every day, for never letting me down and for your ignorance when I was angry on physics! Thanks for the strong support in the last days and, Linus, thanks for teething at night. You both have always been a safe point during this sometimes harsh time! I love you both!

Bibliography

- Alves, J., Lombardi, M., and Lada, C. J. (2007). The mass function of dense molecular cores and the origin of the IMF. *A&A*, 462:L17–L21.
- Alves, J., Lombardi, M., and Lada, C. J. (2014). 2MASS wide-field extinction maps. V. Corona Australis. *A&A*, 565:A18.
- Alves, J. F., Lada, C. J., and Lada, E. A. (2001). Internal structure of a cold dark molecular cloud inferred from the extinction of background starlight. *Nature*, 409:159–161.
- André, P., Di Francesco, J., Ward-Thompson, D., Inutsuka, S.-I., Pudritz, R. E., and Pineda, J. E. (2014a). From Filamentary Networks to Dense Cores in Molecular Clouds: Toward a New Paradigm for Star Formation. *Protostars and Planets VI*, pages 27–51.
- André, P., Könyves, V., Arzoumanian, D., and Palmeirim, P. (2014b). Unraveling the Labyrinth of Star Formation with Herschel. In Stamatellos, D., Goodwin, S., and Ward-Thompson, D., editors, *Advances in Solid State Physics*, volume 36 of *Advances in Solid State Physics*, page 225.
- André, P., Men'shchikov, A., Bontemps, S., Könyves, V., Motte, F., Schneider, N., Didelon, P., Minier, V., Saraceno, P., Ward-Thompson, D., di Francesco, J., White, G., Molinari, S., Testi, L., Abergel, A., Griffin, M., Henning, T., Royer, P., Merín, B., Vavrek, R., Attard, M., Arzoumanian, D., Wilson, C. D., Ade, P., Aussel, H., Baluteau, J.-P., Benedettini, M., Bernard, J.-P., Blommaert, J. A. D. L., Cambrésy, L., Cox, P., di Giorgio, A., Hargrave, P., Hennemann, M., Huang, M., Kirk, J., Krause, O., Launhardt, R., Leeks, S., Le Penec, J., Li, J. Z., Martin, P. G., Maury, A., Olofsson, G., Omont, A., Peretto, N., Pezzuto, S., Prusti, T., Roussel, H., Russeil, D., Sauvage, M., Sibthorpe, B., Sicilia-Aguilar, A., Spinoglio, L., Waelkens, C., Woodcraft, A., and Zavagno, A. (2010). From filamentary clouds to prestellar cores to the stellar IMF: Initial highlights from the Herschel Gould Belt Survey. *A&A*, 518:L102.

Andre, P., Ward-Thompson, D., and Barsony, M. (2000). From Prestellar Cores to Protostars: the Initial Conditions of Star Formation. *Protostars and Planets IV*, pages 59–+.

Arzoumanian, D., André, P., Didelon, P., Könyves, V., Schneider, N., Men'shchikov, A., Soubie, T., Zavagno, A., Bontemps, S., di Francesco, J., Griffin, M., Hennemann, M., Hill, T., Kirk, J., Martin, P., Minier, V., Molinari, S., Motte, F., Peretto, N., Pezzuto, S., Spinoglio, L., Ward-Thompson, D., White, G., and Wilson, C. D. (2011). Characterizing interstellar filaments with Herschel in IC 5146. *A&A*, 529:L6.

Balfour, S. K., Whitworth, A. P., Hubber, D. A., and Jaffa, S. E. (2015). Star formation triggered by cloud-cloud collisions. *MNRAS*, 453:2471–2479.

Ballesteros-Paredes, J. and Hartmann, L. (2007). Remarks on Rapid vs. Slow Star Formation. *RMxAA*, 43:123–136.

Ballesteros-Paredes, J., Hartmann, L., and Vázquez-Semadeni, E. (1999). Turbulent Flow-driven Molecular Cloud Formation: A Solution to the Post-T Tauri Problem? *ApJ*, 527:285–297.

Ballesteros-Paredes, J., Hartmann, L. W., Vázquez-Semadeni, E., Heitsch, F., and Zamora-Avilés, M. A. (2011a). Gravity or turbulence? Velocity dispersion-size relation. *MNRAS*, 411:65–70.

Ballesteros-Paredes, J., Klessen, R. S., Mac Low, M.-M., and Vazquez-Semadeni, E. (2007). Molecular Cloud Turbulence and Star Formation. In Reipurth, B., Jewitt, D., and Keil, K., editors, *Protostars and Planets V*, pages 63–80.

Ballesteros-Paredes, J., Vázquez-Semadeni, E., Gazol, A., Hartmann, L. W., Heitsch, F., and Colín, P. (2011b). Gravity or turbulence? - II. Evolving column density probability distribution functions in molecular clouds. *MNRAS*, 416:1436–1442.

Bally, J. (2001). The Formation, Evolution, and Destruction of Molecular Clouds. In C. E. Woodward, M. D. Bica, & J. M. Shull, editor, *Tetons 4: Galactic Structure, Stars and the Interstellar Medium*, volume 231 of *Astronomical Society of the Pacific Conference Series*, pages 204–+.

Banerjee, R., Klessen, R. S., and Fendt, C. (2007). Can Protostellar Jets Drive Supersonic Turbulence in Molecular Clouds? *ApJ*, 668:1028–1041.

- Banerjee, R. and Körtgen, B. (2015). Formation of star-forming clouds from the magnetised, diffuse interstellar medium. *ArXiv e-prints*.
- Banerjee, R., Vázquez-Semadeni, E., Hennebelle, P., and Klessen, R. S. (2009). Clump morphology and evolution in MHD simulations of molecular cloud formation. *MNRAS*, 398:1082–1092.
- Basu, S. and Mouschovias, T. C. (1994). Magnetic braking, ambipolar diffusion, and the formation of cloud cores and protostars. 1: Axisymmetric solutions. *ApJ*, 432:720–741.
- Bate, M. R., Bonnell, I. A., and Price, N. M. (1995). Modelling accretion in protobinary systems. *MNRAS*, 277:362–376.
- Baumjohann, W. and Treumann, R. A. (1996). *Basic space plasma physics*.
- Bec, J., Frisch, U., Khanin, K., and Villone, B. (2001). A universal law for tails of density pdf's in multi-dimensional Burgers turbulence. *ArXiv Astrophysics e-prints*.
- Bec, J. and Khanin, K. (2007). Burgers turbulence. *Phys. Rep.*, 447:1–66.
- Beck, R. (2001). Galactic and Extragalactic Magnetic Fields. *Space Science Reviews*, 99:243–260.
- Beck, R. (2015). Magnetic Fields in Galaxies. In Lazarian, A., de Gouveia Dal Pino, E. M., and Melioli, C., editors, *Astrophysics and Space Science Library*, volume 407 of *Astrophysics and Space Science Library*, page 507.
- Berger, M. J. and Colella, P. (1989). Local adaptive mesh refinement for shock hydrodynamics. *Journal of Computational Physics*, 82:64–84.
- Beuther, H., Churchwell, E. B., McKee, C. F., and Tan, J. C. (2007). The Formation of Massive Stars. In Reipurth, B., Jewitt, D., and Keil, K., editors, *Protostars and Planets V*, pages 165–180.
- Biskamp, D. (2003). *Magnetohydrodynamic Turbulence*.
- Blandford, R. D. and Payne, D. G. (1982). Hydromagnetic flows from accretion discs and the production of radio jets. *MNRAS*, 199:883–903.
- Blitz, L. (1993). Giant molecular clouds. In Levy, E. H. and Lunine, J. I., editors, *Protostars and Planets III*, pages 125–161.

Blitz, L. and Shu, F. H. (1980). The origin and lifetime of giant molecular cloud complexes. *ApJ*, 238:148–157.

Bodenheimer, P. (2011). *Principles of Star Formation*. Springer-Verlag Berlin Heidelberg 2011.

Bonazzola, S., Heyvaerts, J., Falgarone, E., Perault, M., and Puget, J. L. (1987). Jeans collapse in a turbulent medium. *A&A*, 172:293–298.

Bonnell, I. A. and Bate, M. R. (2005). Binary systems and stellar mergers in massive star formation. *MNRAS*, 362:915–920.

Bonnell, I. A., Bate, M. R., Clarke, C. J., and Pringle, J. E. (2001). Competitive accretion in embedded stellar clusters. *MNRAS*, 323:785–794.

Bonnell, I. A., Bate, M. R., and Zinnecker, H. (1998). On the formation of massive stars. *MNRAS*, 298:93–102.

Bonnor, W. B. (1956). Boyle’s Law and gravitational instability. *MNRAS*, 116:351–+.

Bouchut, F., Klingenberg, C., and Waagan, K. (2007). A multiwave approximate Riemann solver for ideal MHD based on relaxation. I: theoretical framework. *Numerische Mathematik*, 108:7–42.

Brandenburg, A. and Subramanian, K. (2005). Astrophysical magnetic fields and nonlinear dynamo theory. *Phys. Rep.*, 417:1–4.

Carlhoff, P., Nguyen Luong, Q., Schilke, P., Motte, F., Schneider, N., Beuther, H., Bontemps, S., Heitsch, F., Hill, T., Kramer, C., Ossenkopf, V., Schuller, F., Simon, R., and Wyrowski, F. (2013). Large scale IRAM 30 m CO-observations in the giant molecular cloud complex W43. *A&A*, 560:A24.

Carroll-Nellenback, J. J., Frank, A., and Heitsch, F. (2014). The Effects of Flow-inhomogeneities on Molecular Cloud Formation: Local versus Global Collapse. *ApJ*, 790:37.

Chabrier, G. (2005). The Initial Mass Function: from Salpeter 1955 to 2005. In Corbelli, E., Palla, F., and Zinnecker, H., editors, *The Initial Mass Function 50 Years Later*, volume 327 of *Astrophysics and Space Science Library*, page 41.

- Chandrasekhar, S. (1951). The Gravitational Instability of an Infinite Homogeneous Turbulent Medium. *Royal Society of London Proceedings Series A*, 210:26–29.
- Chandrasekhar, S. (1967). *An introduction to the study of stellar structure*. New York: Dover, 1967.
- Chandrasekhar, S. and Fermi, E. (1953). Magnetic Fields in Spiral Arms. *ApJ*, 118:113.
- Chapman, N. L., Goldsmith, P. F., Pineda, J. L., Clemens, D. P., Li, D., and Krčo, M. (2011). The Magnetic Field in Taurus Probed by Infrared Polarization. *ApJ*, 741:21.
- Chen, C.-Y. and Ostriker, E. C. (2012). Ambipolar Diffusion in Action: Transient C Shock Structure and Prestellar Core Formation. *ApJ*, 744:124.
- Chen, C.-Y. and Ostriker, E. C. (2014). Formation of Magnetized Prestellar Cores with Ambipolar Diffusion and Turbulence. *ApJ*, 785:69.
- Choi, E., Kim, J., and Wiita, P. J. (2009). An Explicit Scheme for Incorporating Ambipolar Diffusion in a Magnetohydrodynamics Code. *ApJS*, 181:413–420.
- Colín, P., Avila-Reese, V., Vázquez-Semadeni, E., Valenzuela, O., and Ceverino, D. (2010). Low-mass Galaxy Formation in Cosmological Adaptive Mesh Refinement Simulations: The Effects of Varying the Sub-grid Physics Parameters. *ApJ*, 713:535–551.
- Colin, P., Vazquez-Semadeni, E., and Gomez, G. C. (2013). Molecular Cloud Evolution V. Cloud Destruction by Stellar Feedback. *ArXiv e-prints*.
- Cox, D. P. (1972). Cooling and Evolution of a Supernova Remnant. *ApJ*, 178:159–168.
- Crutcher, R. M. (2012). Magnetic Fields in Molecular Clouds. *ARA&A*, 50:29–63.
- Crutcher, R. M., Hakobian, N., and Troland, T. H. (2009). Testing Magnetic Star Formation Theory. *ApJ*, 692:844–855.
- Crutcher, R. M., Hakobian, N., and Troland, T. H. (2010). Self-consistent analysis of OH Zeeman observations. *MNRAS*, 402:L64–L66.
- Crutcher, R. M., Troland, T. H., Goodman, A. A., Heiles, C., Kazes, I., and Myers, P. C. (1993). OH Zeeman observations of dark clouds. *ApJ*, 407:175–184.

- Dale, J. E. (2015). The modelling of feedback in star formation simulations. *ArXiv e-prints*.
- Dale, J. E., Ercolano, B., and Bonnell, I. A. (2012). Ionizing feedback from massive stars in massive clusters - II. Disruption of bound clusters by photoionization. *MNRAS*, 424:377–392.
- Dale, J. E., Ngoumou, J., Ercolano, B., and Bonnell, I. A. (2013). Massive stars in massive clusters - IV. Disruption of clouds by momentum-driven winds. *MNRAS*, 436:3430–3445.
- Dale, J. E., Ngoumou, J., Ercolano, B., and Bonnell, I. A. (2014). Before the first supernova: combined effects of H II regions and winds on molecular clouds. *MNRAS*, 442:694–712.
- Dalgarno, A. and McCray, R. A. (1972). Heating and Ionization of HI Regions. *ARA&A*, 10:375.
- Dawson, J. R., Ntormousi, E., Fukui, Y., Hayakawa, T., and Fierlinger, K. (2015). A Young Giant Molecular Cloud Formed at the Interface of Two Colliding Supershells: Observations Meet Simulations. *ApJ*, 799:64.
- de Avillez, M. A. (2000). Disc-halo interaction - I. Three-dimensional evolution of the Galactic disc. *MNRAS*, 315:479–497.
- de Avillez, M. A. and Breitschwerdt, D. (2004). Volume filling factors of the ISM phases in star forming galaxies. I. The role of the disk-halo interaction. *A&A*, 425:899–911.
- Diehl, R., Halloin, H., Kretschmer, K., Lichti, G. G., Schönfelder, V., Strong, A. W., von Kienlin, A., Wang, W., Jean, P., Knödseder, J., Roques, J.-P., Weidenspointner, G., Schanne, S., Hartmann, D. H., Winkler, C., and Wunderer, C. (2006). Radioactive ^{26}Al from massive stars in the Galaxy. *Nature*, 439:45–47.
- Dobbs, C. L., Burkert, A., and Pringle, J. E. (2011). Why are most molecular clouds not gravitationally bound? *MNRAS*, 413:2935–2942.
- Dobbs, C. L., Krumholz, M. R., Ballesteros-Paredes, J., Bolatto, A. D., Fukui, Y., Heyer, M., Low, M.-M. M., Ostriker, E. C., and Vázquez-Semadeni, E. (2014). Formation of Molecular Clouds and Global Conditions for Star Formation. *Protostars and Planets VI*, pages 3–26.
- Dobbs, C. L., Pringle, J. E., and Duarte-Cabral, A. (2015). The frequency and nature of ‘cloud-cloud collisions’ in galaxies. *MNRAS*, 446:3608–3620.

Draine, B. T. (2011). *Physics of the Interstellar and Intergalactic Medium*.

Dubey, A., Fisher, R., Graziani, C., Jordan, IV, G. C., Lamb, D. Q., Reid, L. B., Rich, P., Sheeler, D., Townsley, D., and Weide, K. (2008). Challenges of Extreme Computing using the FLASH code. In Pogorelov, N. V., Audit, E., and Zank, G. P., editors, *Numerical Modeling of Space Plasma Flows*, volume 385 of *Astronomical Society of the Pacific Conference Series*, pages 145–+.

Duffin, D. F. and Pudritz, R. E. (2008). Simulating hydromagnetic processes in star formation: introducing ambipolar diffusion into an adaptive mesh refinement code. *MNRAS*, 391:1659–1673.

Ebert, R. (1955). Über die Verdichtung von H I-Gebieten. Mit 5 Textabbildungen. *ZAp*, 37:217–+.

Elmegreen, B. G. (1979). Magnetic diffusion and ionization fractions in dense molecular clouds - The role of charged grains. *ApJ*, 232:729–739.

Elmegreen, B. G. (1990). Theories of molecular cloud formation. In Blitz, L., editor, *The Evolution of the Interstellar Medium*, volume 12 of *Astronomical Society of the Pacific Conference Series*, pages 247–271.

Elmegreen, B. G. (2000). Star Formation in a Crossing Time. *ApJ*, 530:277–281.

Elmegreen, B. G. (2007). On the Rapid Collapse and Evolution of Molecular Clouds. *ApJ*, 668:1064–1082.

Elmegreen, B. G. and Scalo, J. (2004). Interstellar Turbulence I: Observations and Processes. *ARA&A*, 42:211–273.

Evans, II, N. J., Dunham, M. M., Jørgensen, J. K., Enoch, M. L., Merín, B., van Dishoeck, E. F., Alcalá, J. M., Myers, P. C., Stapelfeldt, K. R., Huard, T. L., Allen, L. E., Harvey, P. M., van Kempen, T., Blake, G. A., Koerner, D. W., Mundy, L. G., Padgett, D. L., and Sargent, A. I. (2009). The Spitzer c2d Legacy Results: Star-Formation Rates and Efficiencies; Evolution and Lifetimes. *ApJS*, 181:321–350.

Falgarone, E., Pety, J., and Hily-Blant, P. (2009). Intermittency of interstellar turbulence: extreme velocity-shears and CO emission on milliparsec scale. *A&A*, 507:355–368.

- Federrath, C. (2013). On the universality of supersonic turbulence. *ArXiv e-prints*.
- Federrath, C., Banerjee, R., Clark, P. C., and Klessen, R. S. (2010). Modeling Collapse and Accretion in Turbulent Gas Clouds: Implementation and Comparison of Sink Particles in AMR and SPH. *ApJ*, 713:269–290.
- Federrath, C. and Klessen, R. S. (2012). The Star Formation Rate of Turbulent Magnetized Clouds: Comparing Theory, Simulations, and Observations. *ApJ*, 761:156.
- Federrath, C. and Klessen, R. S. (2013). On the Star Formation Efficiency of Turbulent Magnetized Clouds. *ApJ*, 763:51.
- Federrath, C., Klessen, R. S., and Schmidt, W. (2008). The Density Probability Distribution in Compressible Isothermal Turbulence: Solenoidal versus Compressive Forcing. *ApJ*, 688:L79–L82.
- Fiedler, R. A. and Mouschovias, T. C. (1993). Ambipolar Diffusion and Star Formation: Formation and Contraction of Axisymmetric Cloud Cores. II. Results. *ApJ*, 415:680.
- Field, G. B. (1965). Thermal Instability. *ApJ*, 142:531–+.
- Field, G. B., Goldsmith, D. W., and Habing, H. J. (1969a). A Theoretical Model for the Interstellar Medium. In *Bulletin of the American Astronomical Society*, volume 1 of *Bulletin of the American Astronomical Society*, page 240.
- Field, G. B., Goldsmith, D. W., and Habing, H. J. (1969b). Cosmic-Ray Heating of the Interstellar Gas. *ApJ*, 155:L149+.
- Field, G. B. and Saslaw, W. C. (1965). A Statistical Model of the Formation of Stars and Interstellar Clouds. *ApJ*, 142:568.
- Finkbeiner, D. P. (2003). A Full-Sky $H\alpha$ Template for Microwave Foreground Prediction. *ApJS*, 146:407–415.
- Franco, J. and Cox, D. P. (1986). Molecular clouds in galaxies with different Z - Fragmentation of diffuse clouds driven by opacity. *PASP*, 98:1076–1079.
- Frank, A. and Mellema, G. (1996). Hydrodynamical Models of Outflow Collimation in Young Stellar Objects. *ApJ*, 472:684.

- Fryxell, B., Olson, K., Ricker, P., Timmes, F. X., Zingale, M., Lamb, D. Q., MacNeice, P., Rosner, R., Truran, J. W., and Tufo, H. (2000). FLASH: An Adaptive Mesh Hydrodynamics Code for Modeling Astrophysical Thermonuclear Flashes. *ApJS*, 131:273–334.
- Fujimoto, Y., Tasker, E. J., and Habe, A. (2014). Environmental dependence of star formation induced by cloud collisions in a barred galaxy. *MNRAS*, 445:L65–L69.
- Fukui, Y., Kawamura, A., Minamidani, T., Mizuno, Y., Kanai, Y., Mizuno, N., Onishi, T., Yonekura, Y., Mizuno, A., Ogawa, H., and Rubio, M. (2008). The Second Survey of the Molecular Clouds in the Large Magellanic Cloud by NANTEN. I. Catalog of Molecular Clouds. *ApJS*, 178:56–70.
- Galtier, S., Nazarenko, S. V., Newell, A. C., and Pouquet, A. (2000). A weak turbulence theory for incompressible magnetohydrodynamics. *Journal of Plasma Physics*, 63:447–488.
- Gatto, A., Walch, S., Mac Low, M.-M., Naab, T., Girichidis, P., Glover, S. C. O., Wünsch, R., Klessen, R. S., Clark, P. C., Baczynski, C., Peters, T., Ostriker, J. P., Ibáñez-Mejía, J. C., and Haid, S. (2015). Modelling the supernova-driven ISM in different environments. *MNRAS*, 449:1057–1075.
- Geen, S., Rosdahl, J., Blaizot, J., Devriendt, J., and Slyz, A. (2015). A detailed study of feedback from a massive star. *MNRAS*, 448:3248–3264.
- Gent, F. A., Shukurov, A., Fletcher, A., Sarson, G. R., and Mantere, M. J. (2013a). The supernova-regulated ISM - I. The multiphase structure. *MNRAS*, 432:1396–1423.
- Gent, F. A., Shukurov, A., Sarson, G. R., Fletcher, A., and Mantere, M. J. (2013b). The supernova-regulated ISM - II. The mean magnetic field. *MNRAS*, 430:L40–L44.
- Girichidis, P., Federrath, C., Banerjee, R., and Klessen, R. S. (2011). Importance of the initial conditions for star formation - I. Cloud evolution and morphology. *MNRAS*, 413:2741–2759.
- Girichidis, P., Federrath, C., Banerjee, R., and Klessen, R. S. (2012). Importance of the initial conditions for star formation - II. Fragmentation-induced starvation and accretion shielding. *MNRAS*, 420:613–626.
- Glover, S. C. O. and Clark, P. C. (2012). Is molecular gas necessary for star formation? *MNRAS*, 421:9–19.

- Glover, S. C. O., Clark, P. C., Micic, M., and Molina, F. (2015). Modelling [C I] emission from turbulent molecular clouds. *MNRAS*, 448:1607–1627.
- Goldreich, P. and Sridhar, S. (1995). Toward a theory of interstellar turbulence. 2: Strong alfvenic turbulence. *ApJ*, 438:763–775.
- Goodman, A. A., Barranco, J. A., Wilner, D. J., and Heyer, M. H. (1998). Coherence in Dense Cores. II. The Transition to Coherence. *ApJ*, 504:223–246.
- Gratier, P., Braine, J., Rodriguez-Fernandez, N. J., Schuster, K. F., Kramer, C., Corbelli, E., Combes, F., Brouillet, N., van der Werf, P. P., and Röllig, M. (2012). Giant molecular clouds in the Local Group galaxy M 33. *A&A*, 542:A108.
- Hacar, A. and Tafalla, M. (2011). Dense core formation by fragmentation of velocity-coherent filaments in L1517. *A&A*, 533:A34.
- Haro, G. (1952). Herbig’s Nebulous Objects Near NGC 1999. *ApJ*, 115:572.
- Hartmann, L., Ballesteros-Paredes, J., and Bergin, E. A. (2001). Rapid Formation of Molecular Clouds and Stars in the Solar Neighborhood. *ApJ*, 562:852–868.
- Hatchell, J., Richer, J. S., Fuller, G. A., Qualtrough, C. J., Ladd, E. F., and Chandler, C. J. (2005). Star formation in Perseus. Clusters, filaments and the conditions for star formation. *A&A*, 440:151–161.
- Haverkorn, M. (2015). Magnetic Fields in the Milky Way. In Lazarian, A., de Gouveia Dal Pino, E. M., and Melioli, C., editors, *Astrophysics and Space Science Library*, volume 407 of *Astrophysics and Space Science Library*, page 483.
- Heiles, C. and Crutcher, R. (2005). Magnetic Fields in Diffuse HI and Molecular Clouds. In R. Wielebinski & R. Beck, editor, *Cosmic Magnetic Fields*, volume 664 of *Lecture Notes in Physics*, Berlin Springer Verlag, pages 137–+.
- Heiles, C. and Troland, T. H. (2003). The Millennium Arecibo 21 Centimeter Absorption-Line Survey. II. Properties of the Warm and Cold Neutral Media. *ApJ*, 586:1067–1093.
- Heiles, C. and Troland, T. H. (2005). The Millennium Arecibo 21 Centimeter Absorption-Line Survey. IV. Statistics of Magnetic Field, Column Density, and Turbulence. *ApJ*, 624:773–793.

- Heitsch, F., Burkert, A., Hartmann, L. W., Slyz, A. D., and Devriendt, J. E. G. (2005). Formation of Structure in Molecular Clouds: A Case Study. *ApJ*, 633:L113–L116.
- Heitsch, F. and Hartmann, L. (2014). Accretion and diffusion time-scales in sheets and filaments. *MNRAS*, 443:230–240.
- Heitsch, F., Hartmann, L. W., and Burkert, A. (2008a). Fragmentation of Shocked Flows: Gravity, Turbulence, and Cooling. *ApJ*, 683:786–795.
- Heitsch, F., Hartmann, L. W., Slyz, A. D., Devriendt, J. E. G., and Burkert, A. (2008b). Cooling, Gravity, and Geometry: Flow-driven Massive Core Formation. *ApJ*, 674:316–328.
- Heitsch, F., Mac Low, M., and Klessen, R. S. (2001). Gravitational Collapse in Turbulent Molecular Clouds. II. Magnetohydrodynamical Turbulence. *ApJ*, 547:280–291.
- Heitsch, F., Slyz, A. D., Devriendt, J. E. G., Hartmann, L. W., and Burkert, A. (2007). Magnetized Nonlinear Thin-Shell Instability: Numerical Studies in Two Dimensions. *ApJ*, 665:445–456.
- Heitsch, F., Stone, J. M., and Hartmann, L. W. (2009). Effects of Magnetic Field Strength and Orientation on Molecular Cloud Formation. *ApJ*, 695:248–258.
- Heitsch, F., Zweibel, E. G., Slyz, A. D., and Devriendt, J. E. G. (2004). Turbulent Ambipolar Diffusion: Numerical Studies in Two Dimensions. *ApJ*, 603:165–179.
- Hennebelle, P. (2013). On the origin of non-self-gravitating filaments in the ISM. *A&A*, 556:A153.
- Hennebelle, P., Banerjee, R., Vázquez-Semadeni, E., Klessen, R. S., and Audit, E. (2008). From the warm magnetized atomic medium to molecular clouds. *A&A*, 486:L43–L46.
- Hennebelle, P. and Falgarone, E. (2012). Turbulent molecular clouds. *A&A Rev.*, 20:55.
- Hennebelle, P. and Iffrig, O. (2014). Simulations of magnetized multiphase galactic disc regulated by supernovae explosions. *A&A*, 570:A81.
- Hennebelle, P. and Péroul, M. (1999). Dynamical condensation in a thermally bistable flow. Application to interstellar cirrus. *A&A*, 351:309–322.

- Herbig, G. H. (1950). The Spectrum of the Nebulosity Surrounding T Tauri. *ApJ*, 111:11.
- Heyer, M., Krawczyk, C., Duval, J., and Jackson, J. M. (2009). Re-Examining Larson's Scaling Relationships in Galactic Molecular Clouds. *ApJ*, 699:1092–1103.
- Heyer, M. H. and Brunt, C. M. (2004). The Universality of Turbulence in Galactic Molecular Clouds. *ApJ*, 615:L45–L48.
- Heyer, M. H., Carpenter, J. M., and Snell, R. L. (2001). The Equilibrium State of Molecular Regions in the Outer Galaxy. *ApJ*, 551:852–866.
- Hill, A. S., Joung, M. R., Mac Low, M.-M., Benjamin, R. A., Haffner, L. M., Klingenberg, C., and Waagan, K. (2012). Vertical Structure of a Supernova-driven Turbulent, Magnetized Interstellar Medium. *ApJ*, 750:104.
- Hiltner, W. A. (1949). On the Presence of Polarization in the Continuous Radiation of Stars. II. *ApJ*, 109:471.
- Hoang, T. and Lazarian, A. (2008). Radiative torque alignment: essential physical processes. *MNRAS*, 388:117–143.
- Hubbard, A. and Brandenburg, A. (2012). Catastrophic Quenching in $\alpha\Omega$ Dynamos Revisited. *ApJ*, 748:51.
- Iffrig, O. and Hennebelle, P. (2015). Mutual influence of supernovae and molecular clouds. *A&A*, 576:A95.
- Inoue, T. and Inutsuka, S.-i. (2008). Two-Fluid Magnetohydrodynamic Simulations of Converging H I Flows in the Interstellar Medium. I. Methodology and Basic Results. *ApJ*, 687:303–310.
- Inoue, T. and Inutsuka, S.-i. (2009). Two-Fluid Magnetohydrodynamics Simulations of Converging H I Flows in the Interstellar Medium. II. Are Molecular Clouds Generated Directly from a Warm Neutral Medium? *ApJ*, 704:161–169.
- Inoue, T. and Inutsuka, S.-i. (2012). Formation of Turbulent and Magnetized Molecular Clouds via Accretion Flows of H I Clouds. *ApJ*, 759:35.

- Iroshnikov, P. S. (1964). Turbulence of a Conducting Fluid in a Strong Magnetic Field. *Soviet Ast.*, 7:566.
- Joung, M. K. R. and Mac Low, M.-M. (2006). Turbulent Structure of a Stratified Supernova-driven Interstellar Medium. *ApJ*, 653:1266–1279.
- Joung, M. K. R. and Mac Low, M.-M. (2007). Turbulent structure and star formation in a stratified, supernova-driven, interstellar medium. In Elmegreen, B. G. and Palous, J., editors, *IAU Symposium*, volume 237 of *IAU Symposium*, pages 358–362.
- Joung, M. R., Mac Low, M.-M., and Bryan, G. L. (2009). Dependence of Interstellar Turbulent Pressure on Supernova Rate. *ApJ*, 704:137–149.
- Kahn, F. D. (1974). Cocoons around early-type stars. *A&A*, 37:149–162.
- Kainulainen, J., Beuther, H., Banerjee, R., Federrath, C., and Henning, T. (2011). Probing the evolution of molecular cloud structure. II. From chaos to confinement. *A&A*, 530:A64.
- Kawamura, A., Mizuno, Y., Minamidani, T., Filipović, M. D., Staveley-Smith, L., Kim, S., Mizuno, N., Onishi, T., Mizuno, A., and Fukui, Y. (2009). The Second Survey of the Molecular Clouds in the Large Magellanic Cloud by NANTEN. II. Star Formation. *ApJS*, 184:1–17.
- Kim, J., Hong, S. S., Ryu, D., and Jones, T. W. (1998). Three-dimensional Evolution of the Parker Instability under a Uniform Gravity. *ApJ*, 506:L139–L142.
- Kim, J., Ryu, D., and Jones, T. W. (2001). Three-dimensional Simulations of the Parker Instability in a Uniformly Rotating Disk. *ApJ*, 557:464–474.
- Kim, W.-T., Ostriker, E. C., and Stone, J. M. (2002). Three-dimensional Simulations of Parker, Magneto-Jeans, and Swing Instabilities in Shearing Galactic Gas Disks. *ApJ*, 581:1080–1100.
- Kleinmann, S. G., Lysaght, M. G., Pughe, W. L., Schneider, S. E., Skrutskie, M. F., Weinberg, M. D., Price, S. D., Matthews, K., Soifer, B. T., and Huchra, J. P. (1994a). The Two Micron All Sky Survey. *Ap&SS*, 217:11–17.
- Kleinmann, S. G., Lysaght, M. G., Pughe, W. L., Schneider, S. E., Skrutskie, M. F., Weinberg, M. D., Price, S. D., Matthews, K. Y., Soifer, B. T., and Huchra, J. P. (1994b). The Two Micron All Sky Survey. *Experimental Astronomy*, 3:65–72.

- Klessen, R. S. and Glover, S. C. O. (2014). Physical Processes in the Interstellar Medium. *ArXiv e-prints*.
- Klessen, R. S., Heitsch, F., and Mac Low, M.-M. (2000). Gravitational Collapse in Turbulent Molecular Clouds. I. Gasdynamical Turbulence. *ApJ*, 535:887–906.
- Koda, J., Scoville, N., Sawada, T., La Vigne, M. A., Vogel, S. N., Potts, A. E., Carpenter, J. M., Corder, S. A., Wright, M. C. H., White, S. M., Zauderer, B. A., Patience, J., Sargent, A. I., Bock, D. C. J., Hawkins, D., Hodges, M., Kembball, A., Lamb, J. W., Plambeck, R. L., Pound, M. W., Scott, S. L., Teuben, P., and Woody, D. P. (2009). Dynamically Driven Evolution of the Interstellar Medium in M51. *ApJ*, 700:L132–L136.
- Kolmogorov, A. (1941). The Local Structure of Turbulence in Incompressible Viscous Fluid for Very Large Reynolds' Numbers. *Akademiia Nauk SSSR Doklady*, 30:301–305.
- Königl, A. (1999). Theory of bipolar outflows from high-mass young stellar objects. *New Astronomy Review*, 43:67–77.
- Korpi, M. J., Brandenburg, A., Shukurov, A., Tuominen, I., and Nordlund, Å. (1999). A Supernova-regulated Interstellar Medium: Simulations of the Turbulent Multiphase Medium. *ApJ*, 514:L99–L102.
- Körtgen, B. and Banerjee, R. (2015). Impact of magnetic fields on molecular cloud formation and evolution. *MNRAS*, 451:3340–3353.
- Körtgen, B., Seifried, D., Banerjee, R., Vázquez-Semadeni, E., and Zamora-Avilés, M. (2015). Supernova feedback in molecular clouds: Global evolution and dynamics. *Submitted to MNRAS*.
- Krasnopolsky, R., Li, Z., and Shang, H. (2011). Disk Formation in Magnetized Clouds Enabled by the Hall Effect. *ArXiv e-prints*.
- Krasnopolsky, R., Li, Z.-Y., and Shang, H. (2010). Disk Formation Enabled by Enhanced Resistivity. *ApJ*, 716:1541–1550.
- Kritsuk, A. G., Lee, C. T., and Norman, M. L. (2013). A supersonic turbulence origin of Larson's laws. *MNRAS*, 436:3247–3261.

- Kritsuk, A. G., Norman, M. L., Padoan, P., and Wagner, R. (2007). The Statistics of Supersonic Isothermal Turbulence. *ApJ*, 665:416–431.
- Kroupa, P. (2001). On the variation of the initial mass function. *MNRAS*, 322:231–246.
- Krumholz, M. R., Bate, M. R., Arce, H. G., Dale, J. E., Gutermuth, R., Klein, R. I., Li, Z.-Y., Nakamura, F., and Zhang, Q. (2014). Star Cluster Formation and Feedback. *Protostars and Planets VI*, pages 243–266.
- Krumholz, M. R. and McKee, C. F. (2005). A General Theory of Turbulence-regulated Star Formation, from Spirals to Ultraluminous Infrared Galaxies. *ApJ*, 630:250–268.
- Krumholz, M. R., McKee, C. F., and Klein, R. I. (2005). How Protostellar Outflows Help Massive Stars Form. *ApJ*, 618:L33–L36.
- Krumholz, M. R. and Tan, J. C. (2007). Slow Star Formation in Dense Gas: Evidence and Implications. *ApJ*, 654:304–315.
- Kudoh, T. and Basu, S. (2011). Formation of Collapsing Cores in Subcritical Magnetic Clouds: Three-dimensional Magnetohydrodynamic Simulations with Ambipolar Diffusion. *ApJ*, 728:123.
- Kudoh, T., Basu, S., Ogata, Y., and Yabe, T. (2007). Three-dimensional simulations of molecular cloud fragmentation regulated by magnetic fields and ambipolar diffusion. *MNRAS*, 380:499–505.
- Kwan, J. (1979). The mass spectrum of interstellar clouds. *ApJ*, 229:567–577.
- Lada, C. J. (2006). Stellar Multiplicity and the Initial Mass Function: Most Stars Are Single. *ApJ*, 640:L63–L66.
- Lada, C. J. and Lada, E. A. (2003). Embedded Clusters in Molecular Clouds. *ARA&A*, 41:57–115.
- Lamers, H. J. G. L. M. and Cassinelli, J. P. (1999). *Introduction to Stellar Winds*.
- Landau, L. D. and Lifshitz, E. M. (1959). *Fluid mechanics*.

- Larson, R. B. (1969). Numerical calculations of the dynamics of collapsing proto-star. *MNRAS*, 145:271–+.
- Larson, R. B. (1981). Turbulence and star formation in molecular clouds. *MNRAS*, 194:809–826.
- Lazarian, A. (2007). Tracing magnetic fields with aligned grains. *J. Quant. Spec. Radiat. Transf.*, 106:225–256.
- Lazarian, A., Esquivel, A., and Crutcher, R. (2012). Magnetization of Cloud Cores and Envelopes and Other Observational Consequences of Reconnection Diffusion. *ApJ*, 757:154.
- Lazarian, A. and Vishniac, E. T. (1999). Reconnection in a Weakly Stochastic Field. *ApJ*, 517:700–718.
- LeBlanc, F. (2010). *An Introduction to Stellar Astrophysics*.
- Lee, S. M. and Hong, S. S. (2011). Parker Instability in a Self-gravitating Magnetized Gas Disk. III. Nonlinear Development of the Parker Instability. *ApJ*, 734:101.
- Li, H., Blundell, R., Hedden, A., Kawamura, J., Paine, S., and Tong, E. (2010). Evidence for dynamically important magnetic fields in molecular clouds. *MNRAS*, pages 1823–+.
- Li, H., Dowell, C. D., Goodman, A., Hildebrand, R., and Novak, G. (2009). Anchoring Magnetic Field in Turbulent Molecular Clouds. *ApJ*, 704:891–897.
- Li, H., Griffin, G. S., Krejny, M., Novak, G., Loewenstein, R. F., Newcomb, M. G., Calisse, P. G., and Chuss, D. T. (2006a). Results of SPARO 2003: Mapping Magnetic Fields in Giant Molecular Clouds. *ApJ*, 648:340–354.
- Li, H., Li, D., Qian, L., Xu, D., Goldsmith, P. F., Noriega-Crespo, A., Wu, Y., Song, Y., and Nan, R. (2015). Outflows and Bubbles in Taurus: Star-formation Feedback Sufficient to Maintain Turbulence. *ArXiv e-prints*.
- Li, H.-B., Goodman, A., Sridharan, T. K., Houde, M., Li, Z.-Y., Novak, G., and Tang, K. S. (2014). The Link Between Magnetic Fields and Cloud/Star Formation. *Protostars and Planets VI*, pages 101–123.

- Li, P. S., McKee, C. F., and Klein, R. I. (2006b). The Heavy-Ion Approximation for Ambipolar Diffusion Calculations for Weakly Ionized Plasmas. *ApJ*, 653:1280–1291.
- Lombardi, M., Lada, C. J., and Alves, J. (2010). 2MASS wide field extinction maps. III. The Taurus, Perseus, and California cloud complexes. *A&A*, 512:A67.
- Mac Low, M.-M. and Klessen, R. S. (2004). Control of star formation by supersonic turbulence. *Reviews of Modern Physics*, 76:125–194.
- Martizzi, D., Faucher-Giguère, C.-A., and Quataert, E. (2015). Supernova feedback in an inhomogeneous interstellar medium. *MNRAS*, 450:504–522.
- Matzner, C. D. and McKee, C. F. (2000). Efficiencies of Low-Mass Star and Star Cluster Formation. *ApJ*, 545:364–378.
- McClure-Griffiths, N. M., Dickey, J. M., Gaensler, B. M., Green, A. J., and Haverkorn, M. (2006). Magnetically Dominated Strands of Cold Hydrogen in the Riegel-Crutcher Cloud. *ApJ*, 652:1339–1347.
- McKee, C. F. and Ostriker, E. C. (2007). Theory of Star Formation. *ARA&A*, 45:565–687.
- McKee, C. F. and Ostriker, J. P. (1977). A theory of the interstellar medium - Three components regulated by supernova explosions in an inhomogeneous substrate. *ApJ*, 218:148–169.
- McKee, C. F. and Tan, J. C. (2002). Massive star formation in 100,000 years from turbulent and pressurized molecular clouds. *Nature*, 416:59–61.
- McKee, C. F. and Tan, J. C. (2003). The Formation of Massive Stars from Turbulent Cores. *ApJ*, 585:850–871.
- McKee, C. F., Zweibel, E. G., Goodman, A. A., and Heiles, C. (1993). Magnetic Fields in Star-Forming Regions - Theory. In Levy, E. H. and Lunine, J. I., editors, *Protostars and Planets III*, pages 327–+.
- McLeod, A., Palouš, J., and Whitworth, A. (2011). Collisions of supersonic clouds. In Alves, J., Elmegreen, B. G., Girart, J. M., and Trimble, V., editors, *Computational Star Formation*, volume 270 of *IAU Symposium*, pages 355–358.

- Mellema, G. and Frank, A. (1997). Outflow collimation in young stellar objects. *MNRAS*, 292:795.
- Mestel, L. (1968). Magnetic braking by a stellar wind-I. *MNRAS*, 138:359.
- Mestel, L. and Spitzer, Jr., L. (1956). Star formation in magnetic dust clouds. *MNRAS*, 116:503.
- Miller, G. E. and Scalo, J. M. (1979). The initial mass function and stellar birthrate in the solar neighborhood. *ApJS*, 41:513–547.
- Moeckel, N. and Clarke, C. J. (2011). Collisional formation of very massive stars in dense clusters. *MNRAS*, 410:2799–2806.
- Mouschovias, T. C. (1979). Magnetic braking of self-gravitating, oblate interstellar clouds. *ApJ*, 228:159–162.
- Mouschovias, T. C. and Ciolek, G. E. (1999). Magnetic Fields and Star Formation: A Theory Reaching Adulthood. In C. J. Lada & N. D. Kylafis, editor, *NATO ASIC Proc. 540: The Origin of Stars and Planetary Systems*, pages 305–+.
- Mouschovias, T. C., Kunz, M. W., and Christie, D. A. (2009). Formation of interstellar clouds: Parker instability with phase transitions. *MNRAS*, 397:14–23.
- Mouschovias, T. C. and Paleologou, E. V. (1980). Magnetic braking of an aligned rotator during star formation - an exact, time-dependent solution. *ApJ*, 237:877–899.
- Mouschovias, T. C. and Spitzer, Jr., L. (1976). Note on the collapse of magnetic interstellar clouds. *ApJ*, 210:326–+.
- Müller, J., Simon, S., Motschmann, U., Glassmeier, K.-H., Saur, J., Schüle, J., and Pringle, G. J. (2010). Magnetic field fossilization and tail reconfiguration in Titan’s plasma environment during a magnetopause passage: 3D adaptive hybrid code simulations. *Planet. Space Sci.*, 58:1526–1546.
- Myers, P. C. (2009). Filamentary Structure of Star-forming Complexes. *ApJ*, 700:1609–1625.
- Nakamura, F. and Li, Z.-Y. (2014). Confronting the Outflow-regulated Cluster Formation Model with Observations. *ApJ*, 783:115.

- Nakano, T. and Nakamura, T. (1978). Gravitational Instability of Magnetized Gaseous Disks 6. *PASJ*, 30:671–680.
- Ntormousi, E., Burkert, A., Fierlinger, K., and Heitsch, F. (2011). Formation of Cold Filamentary Structure from Wind-blown Superbubbles. *ApJ*, 731:13.
- Ntormousi, E., Burkert, A., Fierlinger, K., and Heitsch, F. (2014). Filamentary Cold Structure from Colliding Shells. *Astrophysics and Space Science Proceedings*, 36:185.
- Offner, S. S. R., Clark, P. C., Hennebelle, P., Bastian, N., Bate, M. R., Hopkins, P. F., Moraux, E., and Whitworth, A. P. (2014). The Origin and Universality of the Stellar Initial Mass Function. *Protostars and Planets VI*, pages 53–75.
- Ossenkopf, V. and Mac Low, M.-M. (2002). Turbulent velocity structure in molecular clouds. *A&A*, 390:307–326.
- Ostriker, E. C. and Shetty, R. (2011). Maximally Star-forming Galactic Disks. I. Starburst Regulation Via Feedback-driven Turbulence. *ApJ*, 731:41.
- Padmanabhan, T. (2001). *Theoretical Astrophysics - Volume 2, Stars and Stellar Systems*.
- Padoan, P., Bally, J., Billawala, Y., Juvela, M., and Nordlund, Å. (1999). Supersonic Turbulence in the Perseus Molecular Cloud. *ApJ*, 525:318–329.
- Padoan, P., Federrath, C., Chabrier, G., Evans, II, N. J., Johnstone, D., Jørgensen, J. K., McKee, C. F., and Nordlund, Å. (2014). The Star Formation Rate of Molecular Clouds. *Protostars and Planets VI*, pages 77–100.
- Padoan, P., Jimenez, R., Juvela, M., and Nordlund, Å. (2004). The Average Magnetic Field Strength in Molecular Clouds: New Evidence of Super-Alfvénic Turbulence. *ApJ*, 604:L49–L52.
- Padoan, P., Juvela, M., Goodman, A. A., and Nordlund, Å. (2001). The Turbulent Shock Origin of Proto-Stellar Cores. *ApJ*, 553:227–234.
- Padoan, P., Lunttila, T., Juvela, M., Nordlund, Å., Collins, D., Kritsuk, A., Normal, M., and Ustyugov, S. (2011). Magnetic Fields in Molecular Clouds. In Brummell, N. H., Brun, A. S., Miesch, M. S., and Ponty, Y., editors, *IAU Symposium*, volume 271 of *IAU Symposium*, pages 187–196.

- Padoan, P. and Nordlund, Å. (1999). A Super-Alfvénic Model of Dark Clouds. *ApJ*, 526:279–294.
- Padoan, P., Pan, L., Haugboelle, T., and Nordlund, A. (2015). The Origin of Molecular Cloud Turbulence. *ArXiv e-prints*.
- Parker, E. N. (1958). Dynamics of the Interplanetary Gas and Magnetic Fields. *ApJ*, 128:664.
- Parker, E. N. (1966). The Dynamical State of the Interstellar Gas and Field. *ApJ*, 145:811.
- Pelletier, G. and Pudritz, R. E. (1992). Hydromagnetic disk winds in young stellar objects and active galactic nuclei. *ApJ*, 394:117–138.
- Penston, M. V. (1969). Dynamics of self-gravitating gaseous spheres-II. Collapses of gas spheres with cooling and the behaviour of polytropic gas spheres. *MNRAS*, 145:457–+.
- Peters, T., Mac Low, M., Banerjee, R., Klessen, R. S., and Dullemond, C. P. (2010). Understanding Spatial and Spectral Morphologies of Ultracompact H II Regions. *ApJ*, 719:831–843.
- Pillai, T., Kauffmann, J., Tan, J. C., Goldsmith, P. F., Carey, S. J., and Menten, K. M. (2015). Magnetic Fields in High-mass Infrared Dark Clouds. *ApJ*, 799:74.
- Pinto, C., Galli, D., and Bacciotti, F. (2008). Three-fluid plasmas in star formation. I. Magneto-hydrodynamic equations. *A&A*, 484:1–15.
- Pittard, J. M. and Rogers, H. (2012). Feedback from Winds and Supernovae in Massive Stellar Clusters. In Drissen, L., Rubert, C., St-Louis, N., and Moffat, A. F. J., editors, *Astronomical Society of the Pacific Conference Series*, volume 465 of *Astronomical Society of the Pacific Conference Series*, page 398.
- Planck Collaboration, Adam, R., Ade, P. A. R., Aghanim, N., Alves, M. I. R., Arnaud, M., Arzoumanian, D., Ashdown, M., Aumont, J., Baccigalupi, C., Banday, A. J., Barreiro, R. B., Bartolo, N., Battaner, E., Benabed, K., Benoit-Lévy, A., Bernard, J.-P., Bersanelli, M., Bielewicz, P., Bonaldi, A., Bonavera, L., Bond, J. R., Borrill, J., Bouchet, F. R., Boulanger, F., Bracco, A., Burigana, C., Butler, R. C., Calabrese, E., Cardoso, J.-F., Catalano, A., Chamballu, A., Chiang, H. C., Christensen, P. R., Colombi, S., Colombo, L. P. L., Combet, C., Couchot, F., Crill, B. P., Curto, A., Cuttaia, F., Danese, L., Davies, R. D., Davis, R. J., de Bernardis, P., de Rosa, A., de Zotti,

G., Delabrouille, J., Dickinson, C., Diego, J. M., Dole, H., Donzelli, S., Doré, O., Douspis, M., Ducout, A., Dupac, X., Efstathiou, G., Elsner, F., Enßlin, T. A., Eriksen, H. K., Falgarone, E., Ferrière, K., Finelli, F., Forni, O., Frailis, M., Fraisse, A. A., Franceschi, E., Frejsel, A., Galeotta, S., Galli, S., Ganga, K., Ghosh, T., Giard, M., Gjerløw, E., González-Nuevo, J., Górski, K. M., Gregorio, A., Gruppuso, A., Guillet, V., Hansen, F. K., Hanson, D., Harrison, D. L., Henrot-Versillé, S., Hernández-Monteagudo, C., Herranz, D., Hildebrandt, S. R., Hivon, E., Holmes, W. A., Hovest, W., Huppenberger, K. M., Hurier, G., Jaffe, A. H., Jaffe, T. R., Jones, W. C., Keihänen, E., Keskitalo, R., Kisner, T. S., Kneissl, R., Knoche, J., Kunz, M., Kurki-Suonio, H., Lagache, G., Lamarre, J.-M., Lasenby, A., Lattanzi, M., Lawrence, C. R., Leonardi, R., Levrier, F., Liguori, M., Lilje, P. B., Linden-Vørnle, M., López-Cañiego, M., Lubin, P. M., Macías-Pérez, J. F., Maffei, B., Maino, D., Mandolesi, N., Maris, M., Marshall, D. J., Martin, P. G., Martínez-González, E., Masi, S., Matarrese, S., Mazzotta, P., Melchiorri, A., Mendes, L., Mennella, A., Migliaccio, M., Miville-Deschênes, M.-A., Moneti, A., Montier, L., Morgante, G., Mortlock, D., Munshi, D., Murphy, J. A., Naselsky, P., Natoli, P., Nørgaard-Nielsen, H. U., Noviello, F., Novikov, D., Novikov, I., Oppermann, N., Oxborrow, C. A., Pagano, L., Pajot, F., Paoletti, D., Pasian, F., Perdureau, O., Perotto, L., Perrotta, F., Pettorino, V., Piacentini, F., Piat, M., Plaszczynski, S., Pointecouteau, E., Polenta, G., Ponthieu, N., Popa, L., Pratt, G. W., Prunet, S., Puget, J.-L., Rachen, J. P., Reach, W. T., Reinecke, M., Remazeilles, M., Renault, C., Ristorcelli, I., Rocha, G., Roudier, G., Rubiño-Martín, J. A., Rusholme, B., Sandri, M., Santos, D., Savini, G., Scott, D., Soler, J. D., Spencer, L. D., Stolyarov, V., Sudiwala, R., Sunyaev, R., Sutton, D., Suur-Uski, A.-S., Sygnet, J.-F., Tauber, J. A., Terenzi, L., Toffolatti, L., Tomasi, M., Tristram, M., Tucci, M., Umaga, G., Valenziano, L., Valiviita, J., Van Tent, B., Vielva, P., Villa, F., Wade, L. A., Wandelt, B. D., Wehus, I. K., Wiesemeyer, H., Yvon, D., Zacchei, A., and Zonca, A. (2014a). Planck intermediate results. XXXII. The relative orientation between the magnetic field and structures traced by interstellar dust. *ArXiv e-prints*.

Planck Collaboration, Ade, P. A. R., Aghanim, N., Alves, M. I. R., Arnaud, M., Arzoumanian, D., Ashdown, M., Aumont, J., Baccigalupi, C., Banday, A. J., Barreiro, R. B., Bartolo, N., Battaner, E., Benabed, K., Benoît, A., Benoit-Lévy, A., Bernard, J.-P., Bersanelli, M., Bielewicz, P., Bock, J. J., Bonavera, L., Bond, J. R., Borrill, J., Bouchet, F. R., Boulanger, F., Bracco, A., Burigana, C., Calabrese, E., Cardoso, J.-F., Catalano, A., Chiang, H. C., Christensen, P. R., Colombo, L. P. L., Combet, C., Couchot, F., Crill, B. P., Curto, A., Cuttaia, F., Danese, L., Davies, R. D., Davis, R. J., de Bernardis, P., de Rosa, A., de Zotti, G., Delabrouille, J., Dickin-

son, C., Diego, J. M., Dole, H., Donzelli, S., Doré, O., Douspis, M., Ducout, A., Dupac, X., Efstathiou, G., Elsner, F., Enßlin, T. A., Eriksen, H. K., Falceta-Gonçalves, D., Falgarone, E., Ferrière, K., Finelli, F., Forni, O., Frailis, M., Fraisse, A. A., Franceschi, E., Frejsel, A., Galeotta, S., Galli, S., Ganga, K., Ghosh, T., Giard, M., Gjerløw, E., González-Nuevo, J., Górski, K. M., Gregorio, A., Gruppuso, A., Gudmundsson, J. E., Guillet, V., Harrison, D. L., Helou, G., Hennebelle, P., Henrot-Versillé, S., Hernández-Monteagudo, C., Herranz, D., Hildebrandt, S. R., Hivon, E., Holmes, W. A., Hornstrup, A., Huffenberger, K. M., Hurier, G., Jaffe, A. H., Jaffe, T. R., Jones, W. C., Juvela, M., Keihänen, E., Keskitalo, R., Kisner, T. S., Knoche, J., Kunz, M., Kurki-Suonio, H., Lagache, G., Lamarre, J.-M., Lasenby, A., Lattanzi, M., Lawrence, C. R., Leonardi, R., Levrier, F., Liguori, M., Lilje, P. B., Linden-Vørnle, M., López-Caniego, M., Lubin, P. M., Macías-Pérez, J. F., Maino, D., Mandolesi, N., Mangilli, A., Maris, M., Martin, P. G., Martínez-González, E., Masi, S., Matarrese, S., Melchiorri, A., Mendes, L., Mennella, A., Migliaccio, M., Miville-Deschênes, M.-A., Moneti, A., Montier, L., Morgante, G., Mortlock, D., Munshi, D., Murphy, J. A., Naselsky, P., Nati, F., Netterfield, C. B., Noviello, F., Novikov, D., Novikov, I., Oppermann, N., Oxborrow, C. A., Pagano, L., Pajot, F., Paladini, R., Paoletti, D., Pasian, F., Perotto, L., Pettorino, V., Piacentini, F., Piat, M., Pierpaoli, E., Pietrobon, D., Plaszczynski, S., Pointecouteau, E., Polenta, G., Ponthieu, N., Pratt, G. W., Prunet, S., Puget, J.-L., Rachen, J. P., Reinecke, M., Remazeilles, M., Renault, C., Renzi, A., Ristorcelli, I., Rocha, G., Rossetti, M., Roudier, G., Rubiño-Martín, J. A., Rusholme, B., Sandri, M., Santos, D., Savellainen, M., Savini, G., Scott, D., Soler, J. D., Stolyarov, V., Sudiwala, R., Sutton, D., Suur-Uski, A.-S., Sygnet, J.-F., Tauber, J. A., Terenzi, L., Toffolatti, L., Tomasi, M., Tristram, M., Tucci, M., Umana, G., Valenziano, L., Valiviita, J., Van Tent, B., Vielva, P., Villa, F., Wade, L. A., Wandelt, B. D., Wehus, I. K., Ysard, N., Yvon, D., and Zonca, A. (2015). Planck intermediate results. XXXV. Probing the role of the magnetic field in the formation of structure in molecular clouds. *ArXiv e-prints*.

Planck Collaboration, Ade, P. A. R., Aghanim, N., Alves, M. I. R., Arnaud, M., Arzoumanian, D., Aumont, J., Baccigalupi, C., Banday, A. J., Barreiro, R. B., Bartolo, N., Battaner, E., Benabed, K., Benoit-Lévy, A., Bernard, J.-P., Berné, O., Bersanelli, M., Bielewicz, P., Bonaldi, A., Bonavera, L., Bond, J. R., Borrill, J., Bouchet, F. R., Boulanger, F., Bracco, A., Burigana, C., Calabrese, E., Cardoso, J.-F., Catalano, A., Chamballu, A., Chiang, H. C., Christensen, P. R., Clements, D. L., Colombi, S., Combet, C., Couchot, F., Crill, B. P., Curto, A., Cuttaia, F., Danese, L., Davies, R. D., Davis, R. J., de Bernardis, P., de Rosa, A., de Zotti, G., Delabrouille,

J., Dickinson, C., Diego, J. M., Donzelli, S., Doré, O., Douspis, M., Ducout, A., Dupac, X., Elsner, F., Enßlin, T. A., Eriksen, H. K., Falgarone, E., Ferrière, K., Forni, O., Frailis, M., Fraise, A. A., Franceschi, E., Frejsel, A., Galeotta, S., Galli, S., Ganga, K., Ghosh, T., Giard, M., Giraud-Héraud, Y., Gjerløw, E., González-Nuevo, J., Gregorio, A., Gruppuso, A., Guillet, V., Hansen, F. K., Hanson, D., Harrison, D. L., Hernández-Monteaudo, C., Herranz, D., Hildebrandt, S. R., Hivon, E., Hobson, M., Holmes, W. A., Huffenberger, K. M., Hurier, G., Jaffe, A. H., Jaffe, T. R., Jones, W. C., Juvela, M., Keskitalo, R., Kisner, T. S., Knoche, J., Kunz, M., Kurki-Suonio, H., Lagache, G., Lamarre, J.-M., Lasenby, A., Lawrence, C. R., Leonardi, R., Levrier, F., Liguori, M., Lilje, P. B., Linden-Vørnle, M., López-Caniego, M., Lubin, P. M., Macías-Pérez, J. F., Maffei, B., Mandolesi, N., Mangilli, A., Maris, M., Martin, P. G., Martínez-González, E., Masi, S., Matarrese, S., Mazzotta, P., Melchiorri, A., Mendes, L., Mennella, A., Migliaccio, M., Mitra, S., Miville-Deschênes, M.-A., Moneti, A., Montier, L., Morgante, G., Mortlock, D., Munshi, D., Murphy, J. A., Naselsky, P., Nati, F., Natoli, P., Nørgaard-Nielsen, H. U., Noviello, F., Novikov, D., Novikov, I., Oppermann, N., Pagano, L., Pajot, F., Paladini, R., Paoletti, D., Pasian, F., Perrotta, F., Pettorino, V., Piacentini, F., Piat, M., Pierpaoli, E., Pietrobon, D., Plaszczynski, S., Pointecouteau, E., Polenta, G., Pratt, G. W., Puget, J.-L., Rachen, J. P., Rebolo, R., Reinecke, M., Remazeilles, M., Renault, C., Renzi, A., Ricciardi, S., Ristorcelli, I., Rocha, G., Rosset, C., Rossetti, M., Roudier, G., Rubiño-Martín, J. A., Rusholme, B., Sandri, M., Savelainen, M., Savini, G., Scott, D., Soler, J. D., Stolyarov, V., Sutton, D., Suur-Uski, A.-S., Sygnet, J.-F., Tauber, J. A., Terenzi, L., Toffolatti, L., Tomasi, M., Tristram, M., Tucci, M., Valenziano, L., Valiviita, J., Van Tent, B., Vielva, P., Villa, F., Wade, L. A., Wandelt, B. D., Yvon, D., Zacchei, A., and Zonca, A. (2014b). Planck intermediate results. XXXIII. Signature of the magnetic field geometry of interstellar filaments in dust polarization maps. *ArXiv e-prints*.

Price, D. J. and Bate, M. R. (2008). The effect of magnetic fields on star cluster formation. *MNRAS*, 385:1820–1834.

Price, D. J. and Bate, M. R. (2009). Inefficient star formation: the combined effects of magnetic fields and radiative feedback. *MNRAS*, 398:33–46.

Pudritz, R. E. and Norman, C. A. (1983). Centrifugally driven winds from contracting molecular disks. *ApJ*, 274:677–697.

Pudritz, R. E. and Norman, C. A. (1986). Bipolar hydromagnetic winds from disks around protostellar objects. *ApJ*, 301:571–586.

- Reipurth, B. and Bally, J. (2001). Herbig-Haro Flows: Probes of Early Stellar Evolution. *ARA&A*, 39:403–455.
- Robitaille, T. P. and Whitney, B. A. (2010). The Present-Day Star Formation Rate of the Milky Way Determined from Spitzer-Detected Young Stellar Objects. *ApJ*, 710:L11–L15.
- Rogers, H. and Pittard, J. M. (2013). Feedback from winds and supernovae in massive stellar clusters - I. Hydrodynamics. *MNRAS*, 431:1337–1351.
- Roman-Duval, J., Jackson, J. M., Heyer, M., Rathborne, J., and Simon, R. (2010). Physical Properties and Galactic Distribution of Molecular Clouds Identified in the Galactic Ring Survey. *ApJ*, 723:492–507.
- Rosolowsky, E. and Blitz, L. (2005). Giant Molecular Clouds in M64. *ApJ*, 623:826–845.
- Salpeter, E. E. (1955). The Luminosity Function and Stellar Evolution. *ApJ*, 121:161.
- Santos-Lima, R., de Gouveia Dal Pino, E. M., and Lazarian, A. (2011). The role of turbulent magnetic reconnection on the formation of rotationally supported protostellar disks. *ArXiv e-prints*.
- Scalo, J. and Elmegreen, B. G. (2004). Interstellar Turbulence II: Implications and Effects. *ARA&A*, 42:275–316.
- Schneider, N., André, P., Könyves, V., Bontemps, S., Motte, F., Federrath, C., Ward-Thompson, D., Arzoumanian, D., Benedettini, M., Bressert, E., Didelon, P., Di Francesco, J., Griffin, M., Hennemann, M., Hill, T., Palmeirim, P., Pezzuto, S., Peretto, N., Roy, A., Rygl, K. L. J., Spinoglio, L., and White, G. (2013). What Determines the Density Structure of Molecular Clouds? A Case Study of Orion B with Herschel. *ApJ*, 766:L17.
- Schneider, N., Ossenkopf, V., Csengeri, T., Klessen, R. S., Federrath, C., Tremblin, P., Girichidis, P., Bontemps, S., and André, P. (2015). Understanding star formation in molecular clouds. I. Effects of line-of-sight contamination on the column density structure. *A&A*, 575:A79.
- Sedov, L. I. (1959). *Similarity and Dimensional Methods in Mechanics*.

- Seifried, D., Banerjee, R., Pudritz, R. E., and Klessen, R. S. (2012). Disc formation in turbulent massive cores: Circumventing the magnetic braking catastrophe. *ArXiv e-prints*.
- Seifried, D., Banerjee, R., Pudritz, R. E., and Klessen, R. S. (2013). Turbulence-induced disc formation in strongly magnetized cloud cores. *MNRAS*, 432:3320–3331.
- Seifried, D., Schmidt, W., and Niemeyer, J. C. (2011). Forced turbulence in thermally bistable gas: a parameter study. *A&A*, 526:A14.
- Seifried, D. and Walch, S. (2015). The impact of turbulence and magnetic field orientation on star-forming filaments. *MNRAS*, 452:2410–2422.
- Sharma, P., Roy, A., Nath, B. B., and Shchekinov, Y. (2014). In a hot bubble: why does super-bubble feedback work, but isolated supernovae do not? *MNRAS*, 443:3463–3476.
- Shetty, R. and Ostriker, E. C. (2008). Cloud and Star Formation in Disk Galaxy Models with Feedback. *ApJ*, 684:978–995.
- Shetty, R. and Ostriker, E. C. (2012). Maximally Star-forming Galactic Disks. II. Vertically Resolved Hydrodynamic Simulations of Starburst Regulation. *ApJ*, 754:2.
- Shu, F. H. (1977). Self-similar collapse of isothermal spheres and star formation. *ApJ*, 214:488–497.
- Shu, F. H. (1983). Ambipolar diffusion in self-gravitating isothermal layers. *ApJ*, 273:202–213.
- Shu, F. H. (1992). *The physics of astrophysics. Volume II: Gas dynamics*.
- Shu, F. H., Adams, F. C., and Lizano, S. (1987). Star formation in molecular clouds - Observation and theory. *ARA&A*, 25:23–81.
- Shu, F. H., Allen, A., Shang, H., Ostriker, E. C., and Li, Z.-Y. (1999). Low-Mass Star Formation: Theory. In Lada, C. J. and Kylafis, N. D., editors, *NATO ASIC Proc. 540: The Origin of Stars and Planetary Systems*, page 193.
- Shu, F. H., Najita, J., Ostriker, E. C., and Shang, H. (1995). Magnetocentrifugally Driven Flows from Young Stars and Disks. V. Asymptotic Collimation into Jets. *ApJ*, 455:L155+.

- Simon, S., Boesswetter, A., Bagdonat, T., Motschmann, U., and Schuele, J. (2007). Three-dimensional multispecies hybrid simulation of Titan's highly variable plasma environment. *Annales Geophysicae*, 25:117–144.
- Smith, M. D. (2004). *The origin of stars*.
- Solomon, P. M., Rivolo, A. R., Barrett, J., and Yahil, A. (1987). Mass, luminosity, and line width relations of Galactic molecular clouds. *ApJ*, 319:730–741.
- Spitzer, L. (1978). *Physical processes in the interstellar medium*.
- Sridhar, S. and Goldreich, P. (1994). Toward a theory of interstellar turbulence. I: Weak Alfvénic turbulence. *ApJ*, 432:612–621.
- Stahler, S. W. and Palla, F. (2005). *The Formation of Stars*. Wiley-VCH, ISBN 3-527-40559-3, 2005.
- Stanchev, O., Veltchev, T. V., Kauffmann, J., Donkov, S., Shetty, R., Körtgen, B., and Klessen, R. S. (2015). Tracing the general structure of Galactic molecular clouds using Planck data - I. The Perseus region as a test case. *MNRAS*, 451:1056–1069.
- Strömgren, B. (1939). The Physical State of Interstellar Hydrogen. *ApJ*, 89:526.
- Tamburro, D., Rix, H.-W., Leroy, A. K., Mac Low, M.-M., Walter, F., Kennicutt, R. C., Brinks, E., and de Blok, W. J. G. (2009). What is Driving the H I Velocity Dispersion? *AJ*, 137:4424–4435.
- Tammann, G. A., Loeffler, W., and Schroeder, A. (1994). The Galactic supernova rate. *ApJS*, 92:487–493.
- Tan, J. C. (2000). Star Formation Rates in Disk Galaxies and Circumnuclear Starbursts from Cloud Collisions. *ApJ*, 536:173–184.
- Tan, J. C. (2005). Clustered massive star formation in molecular clouds. In Cesaroni, R., Felli, M., Churchwell, E., and Walmsley, M., editors, *IAU Symposium*, pages 318–327.
- Tan, J. C., Beltrán, M. T., Caselli, P., Fontani, F., Fuente, A., Krumholz, M. R., McKee, C. F., and Stolte, A. (2014). Massive Star Formation. *Protostars and Planets VI*, pages 149–172.

- Tan, J. C., Shaske, S. N., and Van Loo, S. (2013). Molecular Clouds: Internal Properties, Turbulence, Star Formation and Feedback. In Wong, T. and Ott, J., editors, *IAU Symposium*, volume 292 of *IAU Symposium*, pages 19–28.
- Tasker, E. J. (2011). Star Formation in Disk Galaxies. II. The Effect Of Star Formation and Photoelectric Heating on the Formation and Evolution of Giant Molecular Clouds. *ApJ*, 730:11.
- Tasker, E. J. and Tan, J. C. (2009). Star Formation in Disk Galaxies. I. Formation and Evolution of Giant Molecular Clouds via Gravitational Instability and Cloud Collisions. *ApJ*, 700:358–375.
- Tasker, E. J., Wadsley, J., and Pudritz, R. (2015). Star Formation in Disk Galaxies. III. Does Stellar Feedback Result in Cloud Death? *ApJ*, 801:33.
- Tielens, A. G. G. M. (2005). *The Physics and Chemistry of the Interstellar Medium*.
- Toro, E. F. (2009). *Riemann Solvers and Numerical Methods for Fluid Dynamics*. Springer, 2009.
- Troland, T. H. and Crutcher, R. M. (2008). Magnetic Fields in Dark Cloud Cores: Arecibo OH Zeeman Observations. *ApJ*, 680:457–465.
- Truelove, J. K., Klein, R. I., McKee, C. F., Holliman, J. H., Howell, L. H., and Greenough, J. A. (1997). The Jeans Condition: A New Constraint on Spatial Resolution in Simulations of Isothermal Self-gravitational Hydrodynamics. *ApJ*, 489:L179+.
- van Dishoeck, E. F. and Black, J. H. (1988). The photodissociation and chemistry of interstellar CO. *ApJ*, 334:771–802.
- Vázquez-Semadeni, E. (2015). Interstellar MHD Turbulence and Star Formation. In Lazarian, A., de Gouveia Dal Pino, E. M., and Melioli, C., editors, *Astrophysics and Space Science Library*, volume 407 of *Astrophysics and Space Science Library*, page 401.
- Vázquez-Semadeni, E., Banerjee, R., Gomez, G., Hennebelle, P., Duffin, D., and Klessen, R. S. (2011). Molecular Cloud Evolution IV: Magnetic Fields, Ambipolar Diffusion, and the Star Formation Efficiency. *MNRAS in press*, *ArXiv e-prints*:1101.3384.

Vázquez-Semadeni, E., Colín, P., Gómez, G. C., Ballesteros-Paredes, J., and Watson, A. W. (2010). Molecular Cloud Evolution. III. Accretion Versus Stellar Feedback. *ApJ*, 715:1302–1317.

Vázquez-Semadeni, E. and García, N. (2001). The Probability Distribution Function of Column Density in Molecular Clouds. *ApJ*, 557:727–735.

Vázquez-Semadeni, E., Gómez, G. C., Jappsen, A., Ballesteros-Paredes, J., and Klessen, R. S. (2009). High- and Low-Mass Star-Forming Regions from Hierarchical Gravitational Fragmentation. High Local Star Formation Rates with Low Global Efficiencies. *ApJ*, 707:1023–1033.

Vázquez-Semadeni, E., Gómez, G. C., Jappsen, A. K., Ballesteros-Paredes, J., González, R. F., and Klessen, R. S. (2007). Molecular Cloud Evolution. II. From Cloud Formation to the Early Stages of Star Formation in Decaying Conditions. *ApJ*, 657:870–883.

Vázquez-Semadeni, E. and Passot, T. (2000). The Density Probability Distribution Function in Turbulent, Isothermal, Magnetized Flows in Slab Geometry. *ArXiv Astrophysics e-prints*.

Vázquez-Semadeni, E., Ryu, D., Passot, T., González, R. F., and Gazol, A. (2006). Molecular Cloud Evolution. I. Molecular Cloud and Thin Cold Neutral Medium Sheet Formation. *ApJ*, 643:245–259.

Vishniac, E. T. (1994). Nonlinear instabilities in shock-bounded slabs. *ApJ*, 428:186–208.

von Weizsäcker, C. F. (1951a). Turbulence in Interstellar Matter (Part 1). In *Problems of Cosmical Aerodynamics*, page 158.

von Weizsäcker, C. F. (1951b). Turbulence in Interstellar Matter (Part 2). In *Problems of Cosmical Aerodynamics*, page 200.

Waagan, K., Federrath, C., and Klingenberg, C. (2011). A robust numerical scheme for highly compressible magnetohydrodynamics: Nonlinear stability, implementation and tests. *Journal of Computational Physics*, 230:3331–3351.

Walch, S., Girichidis, P., Naab, T., Gatto, A., Glover, S. C. O., Wünsch, R., Klessen, R. S., Clark, P. C., Peters, T., Derigs, D., and Baczynski, C. (2015). The SILCC (SIMulating the LifeCycle of molecular Clouds) project - I. Chemical evolution of the supernova-driven ISM. *MNRAS*, 454:238–268.

- Walch, S. and Naab, T. (2015). The energy and momentum input of supernova explosions in structured and ionized molecular clouds. *MNRAS*, 451:2757–2771.
- Walch, S., Whitworth, A. P., Bisbas, T. G., Wünsch, R., and Hubber, D. A. (2013). Clumps and triggered star formation in ionized molecular clouds. *MNRAS*, 435:917–927.
- Walch, S. K., Girichidis, P., Naab, T., Gatto, A., Glover, S. C. O., Wünsch, R., Klessen, R. S., Clark, P. C., Peters, T., and Baczynski, C. (2014). The SILCC (Simulating the LifeCycle of molecular Clouds) project: I. Chemical evolution of the supernova-driven ISM. *ArXiv e-prints*.
- Walch, S. K., Whitworth, A. P., Bisbas, T., Wünsch, R., and Hubber, D. (2012). Dispersal of molecular clouds by ionizing radiation. *MNRAS*, 427:625–636.
- Wang, P., Li, Z., Abel, T., and Nakamura, F. (2010). Outflow Feedback Regulated Massive Star Formation in Parsec-Scale Cluster-Forming Clumps. *ApJ*, 709:27–41.
- Weigert, A., Wendker, H. J., and Wisotzki, L. (2009). *Astronomie und Astrophysik*. Wiley-VCH 2009.
- Wolfire, M. G., Hollenbach, D., McKee, C. F., Tielens, A. G. G. M., and Bakes, E. L. O. (1995). The neutral atomic phases of the interstellar medium. *ApJ*, 443:152–168.
- Wu, B., Van Loo, S., Tan, J. C., and Bruderer, S. (2015). GMC Collisions as Triggers of Star Formation. I. Parameter Space Exploration with 2D Simulations. *ArXiv e-prints*.
- Wu, Y., Wei, Y., Zhao, M., Shi, Y., Yu, W., Qin, S., and Huang, M. (2004). A study of high velocity molecular outflows with an up-to-date sample. *A&A*, 426:503–515.
- Yorke, H. W. and Sonnhalter, C. (2002). On the Formation of Massive Stars. *ApJ*, 569:846–862.
- Zinnecker, H. and Yorke, H. W. (2007). Toward Understanding Massive Star Formation. *ARA&A*, 45:481–563.
- Zuckerman, B. and Evans, II, N. J. (1974). Models of massive molecular clouds. *ApJ*, 192:L149–L152.
- Zuckerman, B. and Palmer, P. (1974). Radio radiation from interstellar molecules. *ARA&A*, 12:279–313.

Eidesstattliche Versicherung

Hiermit erkläre ich an Eides statt, dass ich die vorliegende Dissertationsschrift selbst verfasst und keine anderen als die angegebenen Quellen und Hilfsmittel benutzt habe.

Hamburg, den

(Bastian Körtgen)